Alexandra Cristina Rodrigues Loupas

Master of Science

Study of Low-energy Electron Collisions with Molecules of Biological Relevance

Thesis submitted in partial fulfillment
of the requirements for the degree of

Doctor of Philosophy in
Radiation Biology and Biophysics
Applied Atomic and Molecular Physics

Adviser: Jimena Diaz Gorfinkiel, Senior Lecturer, The Open University

Co-adviser: Paulo Manuel Assis Loureiro Limão-Vieira, Full Professor, Faculdade de Ciências e Tecnologia da Universidade Nova de Lisboa

Examination Committee

Chairperson: Professor João Carlos da Palma Goes
Raporteurs: Professor Márcio Varella
Professor Filipe Ribeiro Ferreira da Silva
Members: Professor Gustavo García Gomez-Tejedor
Professor Pedro António de Brito Tavares
Dr. Jimena Diaz Gorfinkiel

FACULDADE DE CIÊNCIAS E TECNOLOGIA
UNIVERSIDADE NOVA DE LISBOA

December, 2019

Study of Low-energy Electron Collisions with Molecules of Biological Relevance

This document was created using the (pdf)LaTeX processor, based in the "novathesis" template[1], developed at the Dep. Informática of FCT-NOVA [2].
[1] https://github.com/joaomlourenco/novathesis [2] http://www.di.fct.unl.pt

To Carlos and Madalena

ACKNOWLEDGEMENTS

First of all, to Dr. Jimena Diaz Gorfinkiel, to whom there are not enough words to thank. For her absolute commitment to me and this project, her support, understanding and friendship, that drove me much further than I ever expected. It was an honour to learn from you through all these three years, and I feel very lucky. My sincere thank you.

To Professor Paulo Limão-Vieira, for the opportunity to be part of such an incredible Doctoral Programme as RaBBiT, and for believing in me.

I would also like to thank Portuguese National Funding Agency, New University of Lisbon, ARCHER (UK National Supercomputing Service) and The Open University for providing me financial support. This work was also supported by Radiation Biology and Biophysics Doctoral Training Programme (RaBBiT, PD/00193/2012) through scholarship PD/BD/106031/2015, UID/FIS/00068/2019 (CEFITEC) and UID/Multi/04378/2019 (UCIBIO).

To my family, specially my parents, who suffered the most with my departure to the UK, but never tried to cut my wings. For their unconditional love and support, thank you.

To all of my Portuguese friends. Even 1600km apart you guys were always there for me. I could not ask for better ones! To the English friends: thank you for making my stay in the UK much more enjoyable; I will miss you.

To Yolanda, Tia Fátima e Tio Barata. Part of my accomplishments are yours. For receiving me with arms wide open and making me feel like family, I could never thank you enough.

Finally, to Carlos. My husband, my partner and my source of strength. The one who showed me many times I was where I should, and never questioned my choices. For all the motivation during my PhD, and for giving me the most beautiful daughter in between, thank you.

ABSTRACT

This thesis is focused on the application of the R-matrix method, as implemented in the UKRmol and UKRmol+ suites, to study low-energy electron collisions with three medium-sized molecules of biological relevance: *para*-benzoquinone, thiophene and alanine. Our goals for all the targets are mainly three: (i) to identify and characterize respective resonances; (ii) to calculate elastic and inelastic integral and elastic differential cross sections; and (iii) compare our results with the literature. To do so, we use several scattering models, choosing the most suitable on the basis of the characteristics being investigated: Static Exchange, Static Exchange plus Polarization and/or Close-Coupling approximation.

Specially at higher energies, we find an unexpectedly large number of resonances for the three targets, most of them of core-excited and core-excited shape character. We compare our results with other calculations and/or experiments in the literature, but the absence of detailed experimental results for many targets at these energies precludes a meaningful comparison. Nonetheless, three scenarios are then obtained: in the first one, for *para*-benzoquinone, the agreement with previous results is satisfactory; in the second, for thiophene, is excellent; and finally, for alanine, there is not much prior information on the literature to make decisive conclusions.

This work was all published in peer-reviewed journals.

Keywords: Low-energy electron-collisions, elastic and inelastic scattering, R-matrix method, organic molecules.

RESUMO

Esta tese é centrada na aplicação do método da matriz-R, tal como implementada nos programas UKRmol and UKRmol+, no estudo de colisões entre electrões de baixa energia e três diferentes moléculas de interesse biológico: *para*-benzoquinona, tiofeno e alanina. Os objectivos para todos os alvos são essencialmente três: (i) identificar e caracterizar as respectivas ressonâncias; (ii) calcular as secções cde choque eficazes elásticas e inelásticas integrais e elásticas diferenciais. Para tal, utiliza-se vários modelos de dispersão, escolhendo o mais adequado em função do que se pretende calcular: *Static Exchange*, *Static Exchange plus Polarization* e/ou *Close-Coupling*.

Especialmente a energias mais elevadas, encontramos um inesperado número de resonâncias para todas as três moléculas estudadas, maioritariamente com carácter *core-excited shape*. Os resultados obtidos são comparados a literatura disponível, obtidos tanto a nível teórico como experimental. No entanto, a falta de resultados experimentais para algumas moléculas, especialmente para estes valores de energia, dificulta a comparação.

Três cenários são então obtidos: no primeiro, *para*-benzoquinona, o consenso com a literatura é satisfatório; no caso do tiofeno, excelente; e finalmente, para a alanine, não existe informação suficiente na literatura para se poder fazer comparações conclusivas.

Todo o trabalho apresentado nesta tese foi publicado em revistas científicas.

Palavras-chave: Colisões com electrões de baixa energia, dispersão elástica e inelástica, método da matriz-R, moléculas orgânicas.

CONTENTS

LIST OF FIGURES

LIST OF TABLES

ACRONYMS

CAS Complete Active Space.

CC Close-Coupling approximation.

CE Core-excited resonance.

CSF Configuration state function.

DCS Differential Cross Section.

DEA Dissoactive Electron Attachment.

DSB Double strand breaks.

EEL Electron Energy Loss.

ES Excited state.

ETS Electron Transmission Spectroscopy.

GS Ground state.

HF Hartree-Fock approximation.

HOMO Highest occupied molecular orbital.

ICS Integral Cross Section.

LEE Low energy electrons.

LUMO Lowest unoccupied molecular orbital.

SA-CASSCF State-Averaged Complete Active Space Self Consistent Field approximation.

SE Static Exchange approximation.

SEP Static Exchange plus Polarization approximation.

SSB Single strand breaks.

VE Vertical excitation.

VO Virtual orbital.

CHAPTER 1

INTRODUCTION

One of the biggest challenges of this century is to respond to the medical needs of a growing and ageing population. Every day we assist to the appearance of more resistant diseases, in addition to several types of cancer that continue to affect a significant part of the world population (in 2017, 8.8 millions of people died from cancer [1]). The improvement and development of new treatments is therefore a major scientific concern. Highly energetic, ionising radiation (or *primary* radiation) has been applied in cancer treatment (radiotherapy) to around 50% of cancer patients [2]. Besides the direct effect of the primary radiation in human tissue, there are other processes involved, caused by the secondary species that are formed as a consequence of this first interaction. These processes cannot be disregarded, as we shall explain in this chapter.

Biological radiation damage (see figure 1.1 for an overview of the whole process) has been a very popular topic over the last decades, mainly from the physical-chemical perspective. The origin of this radiation can be natural or man made: a constant background of low intensity (but high energy) radiation is present all over the Earth, and comes essentially from cosmic radiation and due to the presence of radioactive Radon (222Rn) in the air, itself a product of the decay of radioactive uranium isotopes. With the rapid decrease of the ozone concentration in the stratosphere over the last decades, there has been an increased human exposure to ultraviolet background (UVB) radiation. The energy quanta of UVB radiation (3.9-4.4 eV), although non-ionising, is capable of inducing molecular changes when interacting with biomolecular systems [3], as we will explain later on.

Besides the natural sources, human exposure to radiation can also occur for medical reasons: radiotherapy or medical imaging. Radiotherapy, as mentioned previously, is used to treat several types of cancer and it is relatively low cost compared to other treatments. Therefore, it is the more suitable procedure to use in developing countries, where cancer-survival rates are still very discouraging. Medical imaging consists mainly of tests that allow medical professionals to

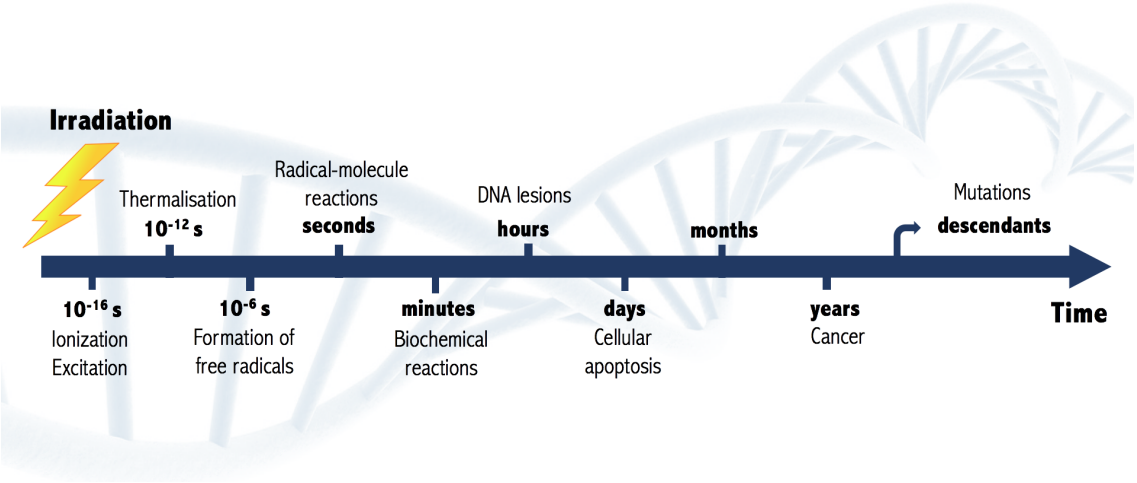

Figure 1.1: Chronological diagram of radiation induced damage, adapted from [6].

"see inside the body"in order to diagnose, treat, and monitor health conditions. Medical imaging procedures are often used as a tool to determine the best treatment options for patients. The type of imaging procedure used depends on the health concern and the part of the body that is being examined. Some common examples of imaging tests include X-rays, computed tomography (CT), fluoroscopy and positron emission tomography (PET) [4, 5].

Over the last decades, there has been a lot of experimental and theoretical (see reference [7] and references therein, mainly in part I) work on quantification of the interaction of primary and secondary radiation with cell components and respective molecules. The radiation can be electromagnetic, electrons, positrons, protons, α-particles, neutrons and heavy charged ions. However, electrons (called *secondary*) are the major product of the interaction between ionizing radiation and a surrounding medium: around 10^4 electrons with energies below 30 eV are generated per MeV of deposited radiation [8, 9]. As expected, and motivated by the pioneering work from Boudaïffa *et al.* from Leon Sanche's group [10], the interaction between biomolecules and secondary electrons started receiving the attention of several groups all over the world [11, 12, 13, 14] (for a review see reference [3]). The experiments of Boudaïffa *et al.* were focused on DNA, and proved that electrons below the ionization threshold can produce single and double-strand breaks (SSBs and DBSs, respectively), through the Dissoactive Electron Attachment (DEA) process.

It is important to keep in mind that apart from DNA, cells contain a huge number of other important molecules, for example proteins and water, that are also potential targets for the incoming radiation, as we explain in the next section.

1.1 Radiation damage in biological systems

As mentioned earlier, when high-energy radiation interacts (or *collides*) with living tissue, it produces a range of structural and chemical modifications that can affect biological function. These modifications can occur directly (when the primary radiation particle ionizes the molecules

directly, initiating a chain of events that leads to structural changes) or indirectly, through the production of intermediate species (free radicals and other particles like electrons, protons, etc.) that will damage the molecules. Our focus here is low energy electrons (LEEs, or *secondary*, as called before), the most abundant species produced during this interaction. The LEEs are generated by ionization processes, or formed by intermolecular Coulombic decay, which is a kind of non-local autoionization process [15]. They can also be formed by water radiolysis (dissociation of water molecules by ionizing radiation). Independent of their source, these LEEs can drive severe damage to biomolecules, which may lead to mutagenic, genotoxic and other lesions, in the case of DNA. After their production, these electrons gradually lose their kinetic energy through a series of inelastic interactions with the surroundings, until they reach near-zero energy, where we say they have been thermalised, or become solvated by the surrounding water [16].

The aim of studying LEEs collisions with biologically relevant molecules is to understand the mechanism of electron induced damage in these systems, and produce quantitative data to be used in modelling the radiation effects. Although the majority of the work has been performed in the gas phase (or as isolated molecules, in the case of computational studies), the reality is not that simple - in the cell, the target molecules are embedded in a specific environment that will affect the electron-molecule interaction and its outcome. The surroundings are mainly composed by water molecules, which triggered studies in pure and hydrated clusters [17, 18, 19]; studies in the condensed phase have also been performed (e.g. references [20, 21]).

There are plenty of other biologically relevant target molecules besides the extensively studied nucleobases: sugars, aminoacids and smaller molecules that could serve as a model for more complex systems - e.g. proteins, that due to their size are impossible to model at the levels of accuracy required in our calculations. Therefore, the strategy used by theoreticians is to study the target's central moiety, or smaller molecules that are similar enough, keeping the calculations within the computational limits. We will present some illustrative examples of this approach in section 1.5.

Beyond the importance of studying the interaction between LEEs and biological targets, electrons also play a crucial role outside the human context. Processes like photosynthesis, where electron transfer reactions have the most crucial role, are also attention worthy. Therefore, understanding the effects of electron collisions with the molecules that participate in these kind of processes is not only important, but needed. *Para*-benzoquinone (see chapter 3), (the prototypical member of the quinone's family) is known to be involved in photosynthesis and respiration [22], and is one of the targets we studied during this thesis.

1.2 Electron-molecule collisions

As we have been discussing, a collision between an electron and a molecule can have serious implications on molecular structure and functioning. In this section we will present a brief overview of the electron-molecule collision process and its applications.

Electron-molecule collisions have been studied extensively by both experimentalists and theoreticians, especially over the last two decades. This was stimulated by mainly two factors: (i) the emergence of more powerful computers that allow the study of more complex targets and more collision processes more accurately; and (ii) the increasing development of experimental instrumentation (improved electron spectrometers, intense sources of spin-polarised electrons, position-sensitive detectors, etc.) [23].

Electrons, particularly, play a central role in atomic and molecular physics, as their small mass makes them much more mobile than the nuclei. The understanding of their behaviour is essential to understand a large variety of problems in many areas of physics (such as gas lasers, laboratory plasmas, ionospheres, auroras, stellar atmospheres, interstellar gases and more recently, and more relevant to this thesis, radiation induced damage) whose advance is dependent on the availability of data on collision processes between electrons, ions, and neutral atoms and molecules. The subject of atomic and molecular collisions is itself of great intrinsic interest, having played a leading role in the establishment of quantum theory [23].

Electron-molecule collisions are significantly more difficult to study than electron-atom collisions, due to the following reasons:

- Molecules have rotational and vibrational degrees of freedom. Those can be excited by a much smaller amount of energy than electronic excitations. As a result, rotational and vibrational excitations are the dominant energy-loss processes below the electronic excitation threshold of the target molecule;
- The electron-molecule short-range interaction is essentially multi-centred and non-spherical because molecules are characterised by the presence of more than one nucleus. Even at large separations, the interaction is often strong and orientation dependent since molecules have various permanent electric multipole moments. Furthermore, the polarisability of the target molecule, which determines the polarisation force is also anisotropic;
- Molecular targets can dissociate in collision with an electron, as we will explain later on.

1.2.1 Low-energy electron processes

In section 1.1, we expressed our interest in electron-molecule collisions with electrons defined as "low-energy", as their energy lay below the ioniastion threshold of the target molecule (around 10-15 eV). In this energy range, any of the following processes can happen [24] (the processes are listed in approximate order of increasing kinetic energy of the projectile):

- **Elastic scattering**: where the internal state of the target and the kinetic energy of the incoming electron are not affected.

$$AB + e^- \rightarrow AB + e^-$$

- **Rotational excitation**: the rotational state of the target (denoted by j) is changed, as well as the energy of the incoming electron.

$$AB_j + e^- \rightarrow AB_{j'} + e^-$$

- **Vibrational excitation**: the vibrational state of the target (denoted by v) is changed, as well as the energy of the incoming electron.

$$AB_v + e^- \rightarrow AB_{v'} + e^-$$

- **Electronic excitation**: the electronic state of the target (denoted by i) is changed, as well as the energy of the incoming electron.

$$AB_i + e^- \rightarrow AB_{i'} + e^-$$

- **Electron impact dissociation**: the target is excited into a dissoactive state, leading to its neutral fragmentation. The formation of the intermediate AB^{*-} (also known by temporary negative ion, TNI^-, or resonance) is not necessary.

$$AB + e^- \rightarrow [AB^{*-}] \rightarrow A + B + e^-$$

- **Dissoactive electron attachment (DEA)**: the incoming electron is trapped in a resonant state, cleaves one molecular bond (or more) and remains attached to one of the fragments, whereas the other (or others) are neutral.

$$AB + e^- \rightarrow AB^{*-} \rightarrow A + B^- + e^- \text{ (or } A^- + B + e^-)$$

The DEA process is responsible for molecular bonds cleavage in biological targets, as explained (although the electron impact dissociation also leads to molecular break-up). The first step of the whole process is the formation of a resonance (AB^{*-}). To fully comprehend the DEA mechanism, it is crucial to understand the behaviour and the characteristics of resonances, as they determine the fate of the target molecule. The DEA process will be discussed in more detail later on this chapter.

1.3 Resonances

Resonances are electronic states embedded in a continuum (except vibrational Feshbach resonances - VFRs, as we will explain later) and, as a consequence, are always susceptible to spontaneous electron loss (autodetachment). Although electron loss can happen very quickly, a potential energy barrier prevents the electron from leaving instantly [25]. An atom or a molecule can have many different electronic resonances, but each of those can only occur for a particular energy of the incoming electron. By definition, a resonance has a negative electron affinity and is characterized by its energy E and width Γ, where the latter is related to its half-time (or lifetime) τ, through the expression below:

$$\Gamma = \hbar/\tau$$

Resonances can be observed in a number of calculated and/or measured scattering quantities. For example, they manifest themselves as peaks in the integral cross section for elastic and inelastic scattering and as sudden changes of approximately π in the eigenphase sum (see chapter 2). They are also visible as peaks in the time-delay (also defined in chapter 2).

Resonances can be classified according to whether they involve fundamentally the electronic states of the target or they involve nuclear (vibrational) degrees of freedom. The electronic resonances can be classified as:

- **Shape resonances**: The electron attaches to the target molecule in its ground electronic state (that is then described as the parent state of the resonance), usually at low incident electron energies (approximately up to the energy of the first excited threshold of the target - above this energy most resonances usually have core-excited character). These resonances are seen as trapping of the incoming electron in one of the unoccupied orbitals of the target molecule - they are 1 particle 0 hole states. The potential energy curve of a shape resonance lies above the one of the neutral molecule. However when this resonance has energy close to the ground state energy, the potential energy curve may be below the ground state energy for some geometries and the resonant state becomes bound [26]. The lifetime differs between molecules and between resonances in the same molecule, and can be of the order of ten femtoseconds to milliseconds. Because they tend to be relatively close in energy to the ground state, these resonances are usually short-lived.

- **Core-excited resonances**: The resonance is formed when the incoming electron electronically excites the target molecule to an excited state (the parent state), and at the same time, it is temporarily trapped in one of the unoccupied orbitals. The description of the core-excited resonances usually involves single excitations of the target molecule, i.e. they are 2 particle 1 hole states. These resonances usually occur at higher incident electron energies than shape resonances (since some energy is needed to excite the target first). We can divide core-excited resonances into two different types: Feshbach and core-excited-shape resonances [27].

    1. *Feshbach resonances*: These resonances lie energetically below the parent state and are typically weakly bound. They tend to have much longer lifetimes than both shape and core-excited shape resonances, and therefore are very narrow which makes them very hard to detect experimentally, due to the experimental instrumentation resolution. This is because the autodetachment channel to the parent state is closed i.e., the decay to the parent state is energetically forbidden, and consequently, its decay occurs into some nonparent state(s).
    2. *Core-excited shape resonances*: The approaching electron has enough energy to electronically excite the molecule to which the electron is concurrently trapped. These resonances lie above the parent state into which they can decay through the autodetachment process that is usually short. The name itself implies similarities to

the shape resonances, as their mechanism of formation is the same except that the attractive part of effective potential arises between the incoming electron and the target molecule in an electronically excited state.

Other type of Feshbach resonances are VFRs: they involve nuclear motion and usually occur at very low energies when the electron is trapped into a diffuse (dipole-bound) state and its energy is transferred to the molecular vibrations. VFRs are likely to occur in molecules with large polarizabilities and/or a very large dipole moment, and can be found just below the thresholds for vibrational excitation of the target molecule.

Figure 1.2 summarizes the types of resonances we just described, their usual lifetimes and where their relative positions are with respect to electronic states of the target.

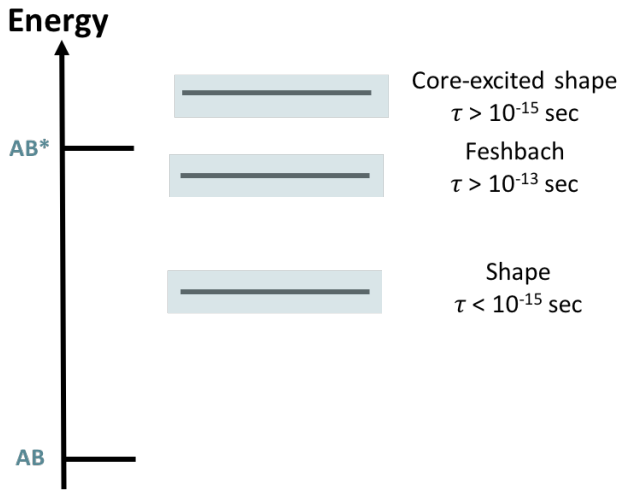

Figure 1.2: Schematic figure of the relative position of shape, core-excited shape and Feshbach resonances and respective usual lifetimes. The size of the grey boxes is not representing their width. AB stands for a generic target molecule. The horizontal lines in the energy axis correspond to the ground state (AB) and an excited state (AB*) energies.

In our calculations we have identified several resonances that we characterize as of *mixed* character. These resonances do not have a shape or core-excited character, but are, in fact, a mix of both. They possess more than one parent state (state the electron attaches to in the scattering process), one of them the ground state, and the remaining an electronically excited state(s).

As metastable states, resonances can decay very easily (unless they become bound, as mentioned previously). This decay depends on several factors as: the lifetime of the resonances, if the resonance formed is dissoactive, how fast the nuclei moves, how far from the equilibrium geometry the anion becomes bound, etc.; we can have mainly two types of decay, schematized in figure 1.3:

- **Autodetachment** (AD)
  It is the most probable channel leading to decay of a shape resonance, where the autodetached electron has the same energy as the incoming electron. In the case of core-excited

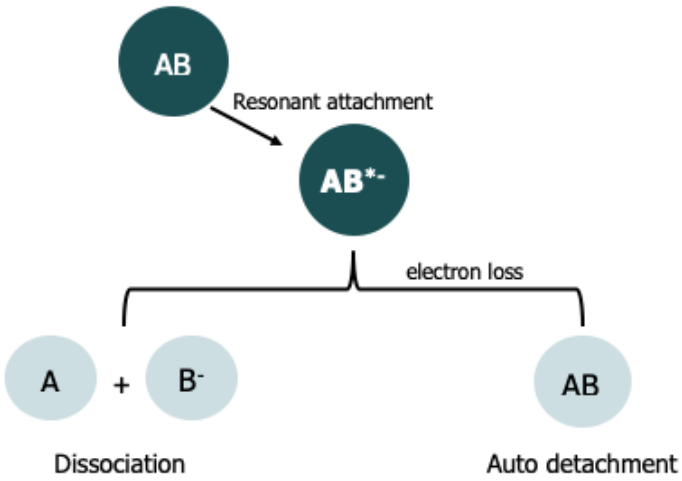

Figure 1.3: Possible pathways for a resonance decay. After its formation, electron loss through autodetachment can occur or DEA into fragments, one of them negatively charged.

resonances, some part of the initial kinetic energy of the electron can be left within the molecule (i.e. to use in the rotational, vibrational, electronic degrees of freedom excitation).

- **Dissociative electron attachment** (DEA)
  It is the most likely decaying channel for resonances with a long lifetime. The dissociation process is bond selective, that is, the bonds that break in a molecule are dependent on the incident electron energy, as shown in the work of Denifl *et al.* [14] and many others. Multiple bond cleavages and new bond formation are also possible as a result of DEA. Figure 1.4 (adapted from [28]) illustrates the potential energy diagram for the DEA process of a diatomic molecule.

This process requires a bit more of our attention as it is one of the main reasons why we are interested in identifying and characterizing resonances. As the anionic product can be detected straight after molecule cleavage by conventional mass spectrometry, DEA has become very popular and extensive studies have been performed. The kinetic energy of the fragments is determined by the asymptotic behavior of the potential energy curves and the internal energies of the products. DEA dynamics involves a strong interaction between the electron motion and nuclear motion, and this makes its the theoretical description particularly challenging [29].

Despite its importance in electron-induced fragmentation of biomolecules, DEA has also important applications in industry (like FEBID [30] - Focused Electron Beam Induced Deposition - and industrial plasmas) as well as occurring naturally, for example, in the Earth ionosphere where oxygen radical anions are formed by DEA from molecular oxygen.

However, dissociation and autodetachment are not the only possible fates of a resonance. As we will present and discuss in chapter 3, there are molecules (as *p*-BQ) capable of accept and retain electrons. This means that their resonances are fairly stable, and their energy is

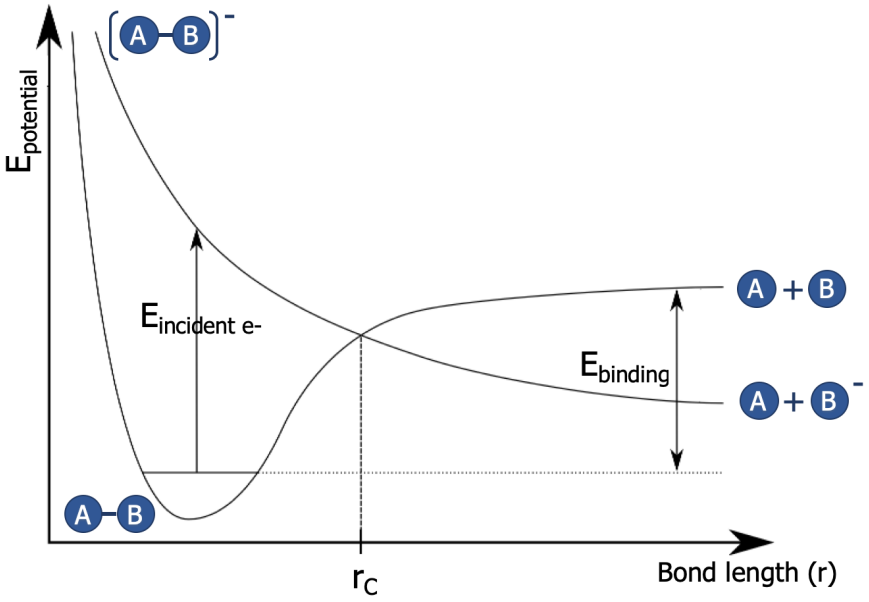

Figure 1.4: Scheme of the DEA process for a diatomic molecule AB, representing the potential energy $E_{potential}$ as a function of the bond length (r). The A-B and $[A\text{-}B]^-$ curves are the potential energy of the neutral and anion molecules, respectively. $E_{incident}$ is the energy of the incident electron; $E_{binding}$ the energy needed to dissociate the bond. The dashed horizontal line represents the vibrational energy. For $r > r_C$, the anion becomes bound, and stable against autoionization. Therefore, if the molecule reaches this point before autoionizing, DEA will occur.

dissipated through the nuclear degrees of freedom of the molecule, until it reaches the bound anionic state, that is more stable than the neutral ground state.

1.3.1 Cross sections

One of the main ways of quantifying the effect of a collision is by measuring (or calculating) a cross section: they can be defined as a measure of probability that a specific process will take place in a collision of two targets.

Cross sections can be classified in several ways: as an integrated quantity over all parameters, and therefore called **integral cross sections** (or ICS); or as **differential cross sections** (DCS), when it is specified as a function of some final-state variable, in our case the scattering angle. The former depends only on the scattering energy, whereas the latter can be presented as angular DCS - provided for a specific scattering energy as a function of the scattering angle; or what we usually call excitation functions - provided for a specific scattering angle as a function of scattering energy.

Cross sections can either be determined for a specific process or for a sum of these, referred to as total cross sections (TCS), that quantify the probability that all scattering processes take place and are easily measured. Elastic cross sections (ECS) quantify the probability of the

incoming electron interacting with the target molecule without modifying its internal state. Experimentally, it is impossible to measure "purely"elastic cross sections, as they usually include some rotational excitation contributions. Momentum transfer cross sections can be determined straightforwardly from elastic DCS, although their publication is not common. Vibration and electron excitation cross sections can be measured and calculated. However, it is not always possible to provide state-to-state experimental results so cross sections are regularly provided for excitation to a group of states. The DEA cross sections can also be measured and calculated, although the latter is fairly difficult. As for the experiments, it is more usual in publications to see ion yields as a function of scattering energy, given the difficulty in turning these into absolute values (and consequently cross sections).

The modelling of a number of physical phenomena requires the availability of cross sections for all possible electron induced processes (elastic scattering, target excitation, DEA, ionization, neutral and dipolar dissociation, etc.) for a broad energy range. For example, Monte Carlo simulations of track structures to model radiation induced damage in the cell, in which the interaction history of the incident and released particles is followed step-by-step until their energy falls below a specified threshold [31], requires knowledge of a large number of cross sections.

Modelling of plasmas and transport processes of charged particles (electrons, positrons, protons) in gaseous and liquid media to obtain electron densities, average velocities, etc. [32, 33] also require cross section data as input. These studies have applications in fields as diverse as gas discharge physics, atmospheric and astrophysical environments, environmental science and most recently, radiation damage in living tissues.

1.3.2 Photodetachment

As mentioned in section 1.1, one of the systems studied is *p*-BQ, specifically its resonance spectrum and its link to the photodetachment process (that has been studied by many experimental groups over the years - see chapters 3 and 6). Therefore, we will briefly describe this process here.

Photodetachment (if the target is neutral, the process is called *photoionization*) is the processes where a photon of specific energy interacts with a negative ion, leading to the neutral molecule and a free electron, represented by the expression below.

$$A^- + \gamma \rightarrow A + e^- \tag{1.1}$$

Normally, the ionized electron is promoted directly to the continuum. However, if resonances are present in the system (which is the case of *p*-BQ), they can provide pathways for the system to return to its ground state, although, like all resonances, they are subject to decay *via* the spontaneous process of autodetachment. This decay manifests as a resonance structure in the detachment cross section. Identifying and characterizing these species is therefore essential to accurately describe the mechanism of photodetachment.

All information about the structure and dynamics of negative ions comes from controlled experiments in which electrons are detached from the ions after they interact with photons (in the case of photodetachment) or other particles. Photodetachment is the preferred method to study negative ion structure and dynamics, since the energy resolution associated with such measurements is typically much higher than that achieved in any particle-induced detachment process. Cross sections for this process start at zero at threshold, increase to a maximum a few eV above threshold, and then decrease. Threshold behaviour and resonance structure in detachment cross sections are of particular interest, since they both involve a high degree of correlation between the electrons.

Other examples where electronic excitation of light absorbing molecules are the trigger for the upcoming processes are the primary processes of photosynthesis and vision [34, 35].

1.4 Theoretical approaches to electron-molecule collisions

In the early days, the goal of theoretical studies was to explain the experimental discoveries, or to approximately reproduce their results. However, due to the fast development of computational techniques and facilities, it is sometimes possible to obtain physical quantities theoretically, like cross sections, which can be more accurate than the observed data.

The low energy region is the most complicated to model, as effects of target polarisation and electron correlation play a strong part. Many *ab initio* methods have been used, both for scattering studies in general or resonances identification, divided basically into two types: calculations based on purely quantum chemistry methods, like Density Functional Theory (DFT), and scattering calculations.

In principle, for very low electron energies or for energies close to a resonance, calculations should take into account the coupling of electronic and nuclear motions. However, the resulting scattering calculations would be very computational demanding. Therefore, scattering methods tend to use the the well known Fixed-Nuclei approximation, in the energy region of its validity.. As a result, many scattering calculations focus only on the accurate description of the electron dynamics.

Several many-electron *ab initio* methods have been developed for calculations of low-energy electron-molecule collisions. Among these [36]:

- The R-matrix method [37];
- The Schwinger Multichannel (SMC) and the Schwinger Multichannel with Pseudo-Potentials (SMCPP) methods [38, 39];
- The Kohn variational method [40].

Modelling electron-molecule interactions is considerably more difficult than calculations of the electronic structure of the isolated molecule for three main reasons: (i) the polarization/-correlation effects between the scattering electron and the electrons of the target have to be

taken into account; (ii) the (N+1) wavefunctions need to be described at a similar level of quality to the one describing the target states; and (iii), the most significant difficulty, is the fact that the unbound electron needs to be described for all the space, since it is not "confined"as the electrons of the target.

Obtaining a reasonable description of both bound and continuum electrons and their interactions in the energy range of interest requires significantly more computational resources compared with quantum chemistry calculations of bound-state solutions of the Schrödinger equation. This is particularly true for electron-rich targets, like the molecules studied in this thesis.

1.5 Low-energy electron collisions from model molecules

Apart from the DNA nucleobases that have already been extensively studied using a variety of techniques and experimental methods (see [17] and references therein), there are several other molecules catching the attention of the scientific community. These are small to medium-sized molecules, that might not be contained within living organisms, but that serve as models for more complex biological systems, similarly to what we expect for the individual study of nucleobases: their study can provide insights into the general behaviour of the DNA molecule. In this section we will present two illustrative examples of these smaller molecules that have been widely studied: pyrimidine and tetrahydrofuran (THF).

Pyrimidine (see upper structure in figure 1.5) is the precursor of the pyrimidinic nucleobases (cytosine, thymine and uracil, see bottom structures in figure 1.5) and as such has received significant experimental and theoretical attention. Given the higher symmetry of pyrimidine, accurate calculations are easier to perform. Several electron collisions studies have been performed for pyrimidine: a detailed review can be found in reference [17].

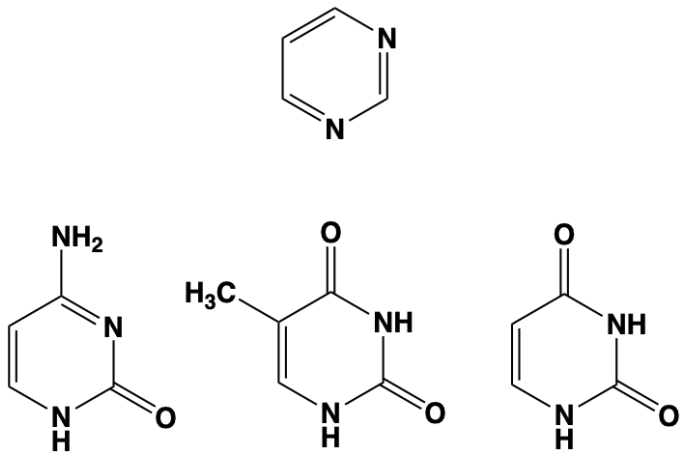

Figure 1.5: Chemical structure of pyrimidine (top) and cytosine, thymine and uracil (bottom structures, respectively).

The work from Bug *et al.* [31] provided the first cross section data set of DNA constituents for electron impact in the energy range between 10 eV-1 keV. These data set was designed for

an implementation in Monte Carlo simulations and consists of model functions, taking into account elastic scattering, ionization and excitation interactions with DNA constituents, among them pyrimidine. Their work was developed on the basis of determining absolute differential and total scattering cross sections, using the available theoretical and experimental data from literature, and can be readily used for track structure simulations of electrons with energies between 30 eV-1 KeV. The same study was performed for THF [41].

THF is the simplest model for the deoxyribose building block of DNA (illustrated on the left and right sides of figure 1.6, respectively), and has been widely studied theoretical and experimentally, as a route to understand electron interaction with the DNA backbone (see a summary of these studies in [17]).

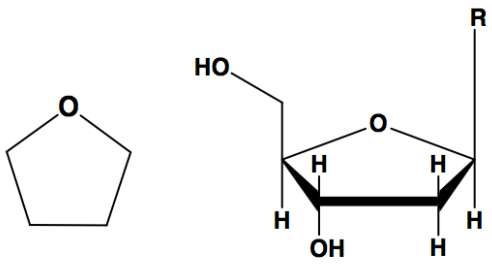

Figure 1.6: Chemical structure of THF (left) and the deoxyribose moiety (right) of DNA. R stands for any nucleobase.

As seen for these two examples, the study of simpler molecules as a model for more complex biosystems (and as input for other types of studies) has been the focus of significant research.

1.6 Objectives and layout of the thesis

In this work we performed low energy electron collision calculations for three small molecules of biological relevance (see chemical structures in figure 1.7): *para*-benzoquinone, a prototypical member of the quinone family that are involved in electron transfer reactions during photosynthesis [22]; thiophene, one of the most used building blocks of anti-inflammatory drugs, and often used in substitution of benzene ring in pharmaceuticals [42]; and alanine, the second smallest aminoacid that could help providing information into the behaviour of proteins, as one of theirs building blocks.

Our aim was to look into different types of targets, in order to analyse the main differences in the resonant behaviour of their respective families, although all of them have biological interest. Particularly, we have chosen to study *p*-BQ because, despite the fact it is extremely interesting as we will show and has been extensively studied (both experimental and theoretically), no consensus on its resonance spectrum is found in the literature. Thiophene was chosen due to the number of experiments that were available, and the lack of calculations to compare them with. Finally, alanine was selected mainly because there was no information on core-excited resonances for it, and very little on other aminoacids.

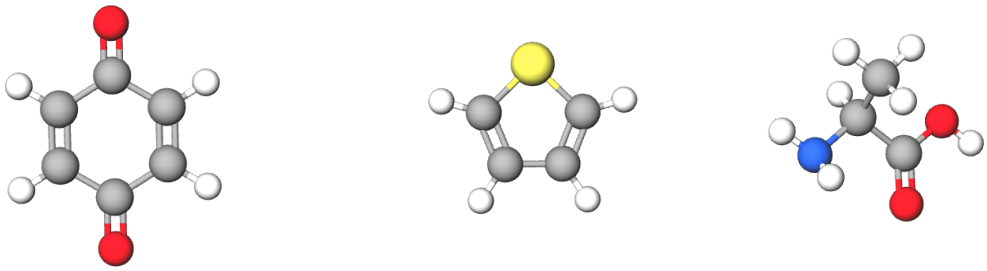

Figure 1.7: 3D chemical structure of *para*-benzoquinone, thiophene and alanine. The colours represent: grey- carbon atoms, white- hydrogen atoms, red- oxygen atoms, yellow- sulphur atoms and blue- nitrogen atoms.

The most interesting question regarding electron collisions with these types of molecules is related to the large number of resonances they possess, their character and respective mechanism of formation. As we will show later on, this does not always have a straightforward answer. The focus of this thesis is mainly the identification and characterisation of resonances, specially of core-excited character, which are less well understood and studied than shape ones, as they are much harder both to identify experimentally and characterise theoretically. Although all of the systems we looked at in this work have been studied before using other methodologies (and some using the R-matrix method), there were many questions that still needed to be answered.

In order to carry out our electron collision calculations we used the R-matrix method [24], as implemented in the UKRmol [43] and UKRmol+ suite of codes [44, 45]. The main objectives of our research were:

1. Describe, as accurately as possible, the resonances in our three target systems. This includes:
    - Evaluate and analyse in detail the position of the higher energy resonances, link them to DEA studies (if available), and provide information about their character;
    - Identify the parent states of high-energy resonances, whenever is possible.
2. Obtain elastic and inelastic cross sections, that can be used in further studies (e.g. track structure modelling). This includes:
    - Compare the obtained cross sections (integral and differential) with experiments and other calculations, whenever available;
    - Provide information about the excitation function for some of the targets;

This thesis is organised in the following way: after this introduction chapter, in chapter 2, we will describe in detail the methods and techniques we have used to perform our calculations. Both computational tools used - UKRmol and UKRmol+ - will also be described, as well as external programs that were used, like *polydcs*. In chapter 3, dedicated to *p*-BQ, we will present our scattering models, results and conclusions, as well as a detailed discussion and comparison with literature. One publication emerged from these studies [46]. Chapter 4 is focused on thiophene.

We performed calculations on the excitation cross sections and compare with the experiments from Regeta [47]. Integral and differential cross sections are also presented and discussed along with other experiments and calculations [48, 49]. In chapter 5 we present our results for alanine, where an improved scattering model for R-matrix calculations with this target is discussed. With this new model we determine a detailed resonant spectrum and cross sections data. For *p*-BQ, thiophene and alanine, an attempt to link our results with DEA experiments is presented and discussed. Chapter 6 presents some preliminary results for two different studies involving the *p*-BQ molecule: (i) an attempt to model its photodetachment process, where we will explain our modifications to the code used previously to perform photoionisation calculations, and a description of our model; comparison with the experimental data is also discussed; and (ii) scattering calculations with the complex *p*-BQ-H_2O, where we look at the effect of a single water molecule in the resonance positions of *p*-BQ, and in the transition energies of the *p*-BQ anion, motivated by the experimental work of Stockett and Nielsen [50].

Our main conclusions and suggestions for future work are presented in chapter 7.

CHAPTER 2

THEORETICAL METHODS

This chapter deals with the theoretical method used throughout this thesis, the R-matrix method. Using this method, we can obtain the cross sections and other quantities relevant for the analysis of the electron-molecule collision problem. Therefore, its description constitutes the main part of this chapter.

We will start by briefly presenting the two electronic structure methods used in this work to generate the target orbitals and wavefunctions needed in our calculations: the Hartree-Fock Self-Consistent Field (HF-SCF) and the Complete Active Space Self-Consistent Field (CASSCF) quantum chemistry methods. The following section is devoted to a brief introduction to the scattering event, followed by a description of the R-matrix theory. Within this section we present the main principles of each of the parts in which the calculation is divided. Section 2.4 focuses on the time-delay analysis, a very useful technique used to identify resonances, focusing on its advantages and the theory behind it. We will also introduce the three scattering models used during this work, and finally, present a description of the computational tools we used: the UKRmol and UKRmol+ suites and the programs that are not part of the suites that have also been used. The former are both implementations of the R-matrix method for electron and positron-molecule collisions. Their application in photoionization (and attempt to photodetachment) process will be briefly described later.

Most of the sections give a general overview of the method used in this thesis, which aims to aid the understanding of the motivation and language of the R-matrix theory. No attempt at mathematical rigour will be made, but can be found in references [25, 37].

The scattering approach presented in this chapter is time-independent and all the calculations will be performed within the Fixed-Nuclei approximation. This approximation considers that, because the nuclei are much heavier than the electrons, their motion should be much slower and they remain fixed (the molecule does not rotate or vibrate) during the time of the collision. Therefore it is reasonable to neglect the nuclear kinetic energy [51].

2.1 Electronic structure theory: HF and CASSCF methods

Electronic structure theory describes the motions of electrons (in atoms and molecules) in an electrostatic field created by the nuclei, and comprises the calculation of the electronic wavefunctions and their associated energies. The Born-Oppenheimer approximation underlies this theory: its basic principle is to separate the motion of the atomic nuclei and the electrons in a molecule. As the nuclei are much heavier, and therefore much slower compared to electrons, its kinetic energy can be neglected, and we have to treat only the electronic problem [52].

To solve the electronic problem, it is usual to start with the HF approximation. This approximation is based on the idea that each electron feels an average potential, ie. it moves in a field generated by the remaining electrons. The HF approximation assumes that the exact wavefunction of the system can be approximated by a single Slater determinant (named after John Slater), which is a normalized antisymmetrized (and therefore satisfies the Pauli exclusion principle) product of molecular orbitals. The use of determinants to express the wavefunction of a N-body system turns the computational treatment much easier. Each of the entries of the Slater determinant are functions that represent a spin-orbital for each electron of the N-electron system. To determine spin-orbital $\phi_\alpha(1)$, where we have arbitrarily assigned electron 1 to spin-orbital ϕ_α, we need to solve the following equation:

$$f_1\phi_\alpha(1) = \epsilon_\alpha\phi_\alpha(1) \tag{2.1}$$

- ϵ_α is the spin-orbital energy;
- f_i is the Fock operator for electron i given by:

$$f_i = -\frac{\nabla_i^2}{2} - \sum_{k=1}^{Nuclei}\frac{Z_k}{\rho_{ki}} + v_i^{HF} \tag{2.2}$$

- Z_k is the charge of the nuclei k;
- ρ_{kj} is the distance between nuclei k and the ith electron;
- v_i^{HF} is the average potential experienced by the ith electron due to the presence of the other $N-1$ electrons.

Each spin-orbital ϕ_α must be obtained by solving an equation of the form of equation 2.1, with the corresponding Fock operator f_i. However, because each Fock operator depends on the spin-orbitals of all the other $N-1$ electrons (via v_i^{HF}), it appears that to set up the HF equations, one must already know the solutions beforehand. This is a known dilemma in electronic structure calculations, and it is commonly solved using an iterative style of solution, stopping when the solutions are self-consistent - hence the name self-consistent field (SCF) is given to this approach, and therefore HF-SCF to the whole approximation. In a self-consistent procedure, a trial set of spin-orbitals is chosen and used to construct an initial Fock operator, then

the HF equations are solved to obtain a new set of spin-orbitals that are consequently used to construct a revised Fock operator, and so on. The cycle of calculations is repeated until the solutions converge [53].

Although the HF-SCF method does not consider the instantaneous Coulombic interactions between electrons, the electron-electron repulsion can be taken into account by using a linear combination of Slater determinants; this is what is known as the configuration interaction (CI) approach. A convenient way to build those other determinants is by taking the HF ground state as a reference determinant and promote each electron from an occupied orbital to an unoccupied orbital (called virtual orbital). Each of the determinants (or a linear combination of a small number of them) constructed so as to have the correct space-spin symmetry, is called a configuration state function (CSF). These CSFs are used to construct the Hamiltonian matrix, which eigenvalues correspond to the energy of each CSF particularly. Therefore, the Hamiltonian matrix needs to be diagonalized to obtain their energy, which is the most computational demanding part of our calculations. Nowadays we can find several methods to limit the size and computational resources of these calculations.

The other method we used to perform our calculations is the more sophisticated **Complete Active Space Self Consistent Field** (CASSCF) method. Here, the orbitals and the CI expansion coefficients are optimized at the same time, so we obtain the set of orbitals that best describe the states of interest, using the specific configurations we generated (i.e. the target electronic states are represented using multiple CSFs). A CASSCF calculation can be carried out in two ways: state-specific or state-averaged mode. Both have the same principle, which is to carry out the calculation on a small sub-set of chosen orbitals, but during this thesis we have only used the latter. A state-averaged calculation minimizes a weighted average of energies of several chosen states. These weights can be chosen arbitrarily, but it is common practice to give the largest weight to the ground state. The main advantage of this method is that it produces a set of orthogonal orbitals describing all chosen electronic states in the best way possible. The disadvantage is that usually the quality of the description of a specific state using orbitals optimized to describe large number of electronic states with a common set of orbitals is poorer than the description of one given state using orbitals optimised only for that particular state. Nonetheless, this is our best approximation when several states need to be described simultaneously.

A CASSCF calculation starts with a set of orbitals as a starting guess (usually generated at HF level). Next, the frozen orbitals are chosen; these orbitals correspond to the inner shell ones that normally do not participate in (or its contribution is very small to) the scattering process. As a consequence, these orbitals are not optimised. After that, and most importantly, a set of active orbitals (also called the Complete Active Space (CAS)) is chosen, for which the orbital optimisation will be performed.

The choice of the correct active space is crucial to the success of the method, because electrons occupying the active orbitals are the ones involved in the collision process. This choice depends on the electronic states being described as well as the computational resources available, so there are a wide range of possibilities. The CASSCF model is usually denoted by a pair of numbers (n, m), where n indicates the number of electrons being distributed among the

m active orbitals. The other $(N-n)$ electrons occupy the frozen orbitals. Once these two types of orbitals are picked, the CASSCF orbital optimisation is performed.

In order to carry on the calculations, a basis set is required. A basis set is defined as a set of functions used to create the molecular orbitals, which are expanded as a linear combination with coefficients that need to be determined. There are many types of basis sets (minimal, split-valence, correlation-consistent, etc.) that are picked according to the type of processes we are trying to describe.

A basis set can either be composed of atomic orbitals (yielding the linear combination of atomic orbitals approach, the most usual choice in quantum chemistry calculations), or plane waves in the case of solid state calculations. There are several type of atomic orbitals: Gaussian-type orbitals (GTOs), Slater-type orbitals or numerical orbitals. The former ones are, by far, the most used as they are easier to treat computationally.

2.2 Introduction to scattering processes

Scattering studies have been the focus of many experimental and theoretical work for almost 100 years. A very early example of their use is the formulation by Rutherford of his nuclear model of the atom, which resulted from his famous experiments with $\alpha-$particles scattered by platinum and gold foils.

Scattering events can be classified into two types: **elastic** scattering, when the total kinetic energy of the particles remains unchanged, as only translational kinetic energy is transferred between the two particles; and **inelastic** scattering, when the total translational kinetic energy changes and some of it is used to excite internal modes of the projectile or the target.

A collision of two particles can have different outcomes. Each of the final possible products of the collision is called a *channel*, defined by the states of both target and projectile. Therefore, a scattering process is called a *multichannel collision*, whenever there are many different possible states in which the target and projectile can emerge after collision. Nevertheless, there are certain simple processes (e.g. very low energy scattering of an electron off a proton) in which only one channel needs to be considered. This case is called a *single channel* process and it happens when all the other channels are either closed (energetically inaccessible) or can be neglected. The formalism of single-channel scattering is much simpler than the general case of the multichannel process, but it includes almost all the basic scattering concepts. A brief description of the formalism of single and multichannel collisions can be found elsewhere [25].

A standard approach to the scattering problem is to solve the time-independent Schrödinger equation, in order to obtain the quantity S_l (after a series of mathematical transformations that we will not describe in this thesis) defined as the ***S*-matrix element**. The S-matrix is closely related to other scattering quantities, as we will show later on this chapter, from which we can obtain observables and resonance information (position, widths, etc.). A full description of the S-matrix theory can be found elsewhere [25].

2.3 R-matrix theory

There are several methods to solve the scattering problem. In this work we use the R-matrix approach, devised by Wigner and Eisenbud in 1947 [54], to solve scattering problems in nuclear physics. Through the years, it has been further developed and extended by many scientists and many complete reviews of the theory and their applications in atomic and molecular physics have been written [24, 55, 56, 57].

Briefly, the basic idea of the R-matrix method is the division of the configuration space into two regions: inner and outer region (see schematic representation in figure 2.1). The boundary between these regions is a sphere of radius a, that we call the R-matrix radius, centred on the center of mass of the target molecule. In the inner region ($r \leq a$), the scattering electron becomes indistinguishable from the electrons of the target, therefore we need to take into account both exchange and correlation effects and the calculation gets very complex and can only be solved numerically. The inner region must contain all the electronic densities of the target states included in the calculation and that of the orbitals used to build the L^2 functions.

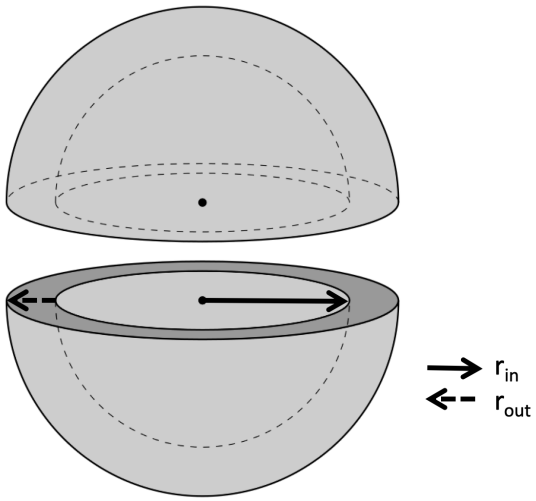

Figure 2.1: Schematic representation of the R-matrix method (figure adapted from reference [58]). The inner and the outer region are separated by the R-matrix radius r_{in}. r_{out} is the radius up to which the propagation is performed, where the outer and the asymptotic region match (the propagation process is explained later in this chapter). Despite the scale of the figure, r_{out} is usually much larger than r_{in}.

On the other hand, in the outer region ($r > a$) the scattering electron is distinguishable from the target electrons. Exchange and correlation effects are weak, and therefore can be neglected, which makes the calculation much simpler. The inner region data is used as boundary conditions to solve the outer region problem. From the known asymptoptic solution in the outer region, the **S**-matrix and its derivatives **K**- and **T**-matrices can be calculated and from all these we can extract observable quantities. The time-delay (see section 2.4) can also be obtained, which allows us to determine resonance parameters (these can also be obtain directly from the **K**-matrix).

In the following sections we will describe the R-matrix method applied to electron-molecule scattering.

2.3.1 Inner region calculation

The starting point of the R-matrix theory for electron-molecule collisions is the expansion of the full scattering wavefunction $\Psi_E^\Gamma(\mathbf{x}_1,\mathbf{x}_2,...,\mathbf{x}_N,\mathbf{x}_{N+1})$ in terms of a basis set, denoted $\Psi_k^\Gamma(\mathbf{x}_1,\mathbf{x}_2,...,\mathbf{x}_N,\mathbf{x}_{N+1})$ defined in the inner region: [24]

$$\Psi_E^\Gamma(\mathbf{x}_1,\mathbf{x}_2,...,\mathbf{x}_N,\mathbf{x}_{N+1}) = \sum_k A_k^E \Psi_k^\Gamma(\mathbf{x}_1,\mathbf{x}_2,...,\mathbf{x}_N,\mathbf{x}_{N+1}) \tag{2.3}$$

- Ψ_k^Γ are the basis functions and do not depend on the scattering energy E;
- Ψ_E^Γ is the total wavefunction and the energy dependence is contained only in the coefficients A_k^E
- $\mathbf{x}_i$ corresponds to the spin and space coordinates of the ith electron;
- N is the number of electrons.

The superscripts Γ represent each irreducible representation of the point-group of the molecule. They are used in the functions Ψ and χ below to indicate that these are constructed to transform according to the chosen irreducible representation and have the appropriate total spin. Due to the presence of many indistinguishable electrons and scattering channels, solving this region requires a lot of computational resources.

The choice of the basis functions is made to reflect as closely as possible the underlying electronic processes taking place during the collision and is therefore the most important step in the scattering calculation. The basis functions for the inner region are written in the so-called *Close-coupling approximation*:

$$\Psi_k^\Gamma(\mathbf{x}_1,...,\mathbf{x}_{N+1}) = \mathscr{A} \sum_{i=1}^{n_b} \sum_{j=1}^{n_c} \Phi_i(\mathbf{x}_N,...,\mathbf{x}_{N+1}) \gamma_{ij}(\mathbf{x}_{N+1}) a_{ijk} + \sum_{i=1}^{m} \chi_i^\Gamma(\mathbf{x}_1,...,\mathbf{x}_{N+1}) b_{ik} \tag{2.4}$$

- $\Phi_i(\mathbf{x}_1,...,\mathbf{x}_{N+1})$ describes the ith electronic state;
- $\chi_i^\Gamma(\mathbf{x}_1,...,\mathbf{x}_{N+1})$ in the second sum are the L^2 integrable functions;
- $\gamma_{ij}(\mathbf{x}_{N+1})$ are the continuum functions that represent the unbound scattering electron, and are the only ones with a nonzero amplitude in the R-matrix sphere;
- $\mathscr{A}$ is the antisymmetrization operator.

The target states Φ_i in equation 2.4 are coupled only with the continuum orbitals γ_{ij} that together form products transforming according to the irreducible representation Γ. Only one

set of continuum functions is generated (represented by the index i) to couple with a given target state, for the symmetry reasons explained above.

To obtain correct results, the density of the L^2 functions χ_i^Γ needs to be fully contained within the R-matrix sphere (the charge densities can be calculated using the program *radden* as function of the radial coordinate- see section 2.6). In fact, the maximum spatial extent of the target states and the L^2 functions is what determines the R-matrix radius a. These latter functions along with the target states Φ_i are constructed as linear combinations of antisymmetrized products of the orthogonalised orbitals of the target molecule. The particular type and number of target states and L^2 functions included in the Close-Coupling expansion (equation 2.4) constitutes a scattering model. The functions χ_i^Γ allow for the description of the short-range correlation and polarisation effects as well as that of electron resonances, and their form is therefore one of the most important properties of the scattering model.

The continuum orbitals γ_{ij}, describing the unbound scattering electron, are generally built combining GTOs sitting on the centre of mass and on the atoms. These continuum basis are built for a specific R-matrix radius, using the procedure described in reference [59]. To obtain the final set of orthogonal orbitals that are actually going to be used in the scattering calculation, the continuum orbitals are first Schmidt orthogonalised [1] to the target molecule's orbitals and then symmetrically orthogonalized among themselves: the orbitals with eigenvalues of the overlap matrix smaller than a pre-defined threshold are deleted. The remaining orthogonal orbitals correspond to the γ_{ij} in equation 2.4.

The inclusion of continuum GTOs corresponds to the use of a partial wave expansion (represented by equation 2.5) for the wavefunction of the scattering electron.

$$\Psi(r,\theta,\varphi) = \sum_{l,m} = \frac{F_l(r)}{r} Y_{l,m}(\theta,\varphi) \tag{2.5}$$

- $Y_l^m(\theta,\varphi) = (-1)^m \sqrt{\frac{(2l+1)}{4\pi}\frac{(l-m)!}{(l+m)!}} P_l^m(cos\theta) e^{im\varphi}$ are the spherical harmonics of degree l and order m;
- P_l^m are the Legendre polynomials;
- $F_l(r)$ are the reduced radial wavefunctions.

The coefficients a_{ijk} and b_{ik} in equation 2.4 are determined by the requirement the functions Ψ_k^Γ diagonalize the hermitian $N+1$ Hamiltonian, $\tilde{H}_{N+1}$, in the inner region. That is:

[1] Procedure that consists in taking a non-orthogonal set of linearly independent functions and constructs an orthogonal basis, over an arbitrary interval with respect to an arbitrary weighting function. [60]

$$\left(\Psi^{\Gamma}_{k'}|\tilde{H}_{N+1}|\Psi^{\Gamma}_{k}\right) = (\Psi^{\Gamma}_{k'}|H_{N+1}+L|\Psi^{\Gamma}_{k}) = E_k\delta_{k'k} \tag{2.6}$$

$$H_{N+1} = \sum_{i=1}^{N+1}\left(-\frac{\nabla_i^2}{2} - \sum_{k=1}^{Nuclei}\frac{Z_k}{\rho_{ki}}\right) + \sum_{i>j}^{N+1}\frac{1}{r_{ij}} + \sum_{k>l}^{Nuclei}\frac{Z_k Z_l}{R_{kl}} \tag{2.7}$$

- E_k corresponds to the energy of each solution of Ψ^{Γ}_{k};
- Z_k is the charge of nuclei k;
- ρ_{ki} is the distance between the nuclei k and electron i;
- r_{ij} is the distance between electrons i and j;
- R_{kl} is the distance between nuclei k and nuclei l;
- L is the Bloch operator (described below).

Note that we are using round brackets instead of the usual angled brackets to indicate that the integration is carried out only in the inner region, and not over all the configuration space.

As we are using the fixed-nuclei approximation, the nuclei kinetic energy terms can be ignored and the final Hamiltonian for the system includes only the electronic part. To calculate the matrix elements of the Hamiltonian we use the Bloch operator (L) described by:

$$L = \frac{1}{2}\sum_{i=1}^{N+1}\sum_{j=1}^{n_{ch}}|\Phi_j Y_{l_j,m_j}(\hat{\mathbf{x}}_i)\delta(r_i-a)\left(\frac{d}{dr_i}-\frac{b-1}{r_i}\right)(\Phi_j Y_{l_j,m_j}(\hat{\mathbf{x}}_i)| \tag{2.8}$$

- the index j runs over all n_{ch} scattering channels;
- $\delta(r-a)$ is the Delta function;
- b is an arbitrary constant;

The purpose of this operator is to ensure the hermicity of the Hamiltonian $\tilde{H}_{N+1}$.

We shall now move to the derivation of the R-matrix, which provides the link between the radial functions of the scattering electron in the inner and the outer regions. In our notation, the expression for the channels reads: $|\Phi_i Y_{l_i,m_i}(\hat{\mathbf{x}}_{N+1})\frac{1}{r_{N+1}})$. In the first step we rewrite the Schrödinger equation using the Bloch operator to obtain:

$$(H_{N+1} + L)\Psi_E^\Gamma(\mathbf{x}_1, ..., \mathbf{x}_{N+1}) = (E + L)\Psi_E^\Gamma(\mathbf{x}_1, ..., \mathbf{x}_{N+1}) \Leftrightarrow \tag{2.9}$$

$$\Psi_E^\Gamma(\mathbf{x}_1, ..., \mathbf{x}_{N+1}) = (H_{N+1} + L - E)^{-1} L \Psi_E^\Gamma(\mathbf{x}_1, ..., \mathbf{x}_{N+1}) \tag{2.10}$$

We insert the complete set of states Ψ_k^Γ for the inner region between the two operators on the right hand side, project the equation on the channels $|\Phi_i Y_{l_i,m_i}(\hat{\mathbf{x}}_{N+1})\frac{1}{r_{N+1}})$ and use equation 2.6 to obtain:

$$\left(\Phi_i Y_{l_i,m_i}(\hat{\mathbf{x}}_{N+1})\frac{1}{r_{N+1}}\middle|\Psi_E^\Gamma\right) = \sum_k (E_k - E)^{-1}\left(\Phi_i Y_{l_i,m_i}(\hat{\mathbf{x}}_{N+1})\frac{1}{r_{N+1}}\middle|\Psi_k^\Gamma\right)(\Psi_k^\Gamma|L|\Psi_E^\Gamma) \tag{2.11}$$

Projection on the channels $|\Phi_i Y_{l_i,m_i}(\hat{\mathbf{x}}_{N+1})\frac{1}{r_{N+1}})$ guarantees that the function on the left side is a function of r_{N+1} only and that it does not contain the term $\frac{1}{r_{N+1}}$. We want to evaluate this function on the boundary $r = a$, because this is where we want to start the calculation for the outer region.

The reduced radial wavefunctions $F_i(a)$ and the surface amplitudes $w_{ik}(a)$ can be defined as:

$$F_i(a) = \left(\Phi_i Y_{l_i,m_i}\frac{1}{r_{N+1}}\middle|\Psi_E^\Gamma\right)_{r=a} \tag{2.12}$$

$$w_{ik}(a) = \left(\Phi_i Y_{l_i,m_i}\frac{1}{r_{N+1}}\middle|\Psi_k^\Gamma\right)_{r=a} \tag{2.13}$$

For simplicity, we omit the dependence of the $\Psi_E^\Gamma(\mathbf{x}_1, ..., \mathbf{x}_{N+1})$ wavefunctions on the $(\hat{\mathbf{x}}_i)$ variables.

Rewriting equation 2.9 and evaluating it at $r = a$, we get the following expression for the reduced radial wavefunction:

$$F_i(a) = \sum_k \frac{w_{ik}(a)}{E_k - E} (\Psi_k^\Gamma | L | \Psi_E^\Gamma) \tag{2.14}$$

Where $(\Psi_k^\Gamma | L | \Psi_E^\Gamma)$ is defined by the equation below, and which evaluation can be seen elsewhere [61].

$$(\Psi_k^\Gamma | L | \Psi_E^\Gamma) = \frac{1}{2a} \sum_{j=1}^{n_{ch}} w_{jk}(a) \left(a \left[\frac{df_j}{dr} \right]_a - bF_j(a) \right) \tag{2.15}$$

After inserting this result back into equation 2.14 we obtain:

$$F_i(a) = \sum_{j=1}^{n_{ch}} \sum_k R_{ij} \left(a \frac{dF_j}{dr} \Big|_a - bF_j(a) \right) \tag{2.16}$$

And the R-matrix elements are defined as:

$$R_{ij}(E) = \frac{1}{2a} \sum_k \frac{w_{ik}(a) w_{jk}(a)}{E_k - E} \tag{2.17}$$

Equation 2.16 explicitly demonstrates the role of the R-matrix as the quantity linking the inner and the outer region, as it relates the radial scattering wavefunction at $r = a$ to the quantity $R(E)$ which is obtained by solving the inner region, and matching with the known solution of the outer region (seen in the following subsection) at $r = a$.

2.3.2 Outer region calculation

The outer region calculation is significantly simpler than the inner region calculation, as the incoming electron is distinguishable from the N electrons of the target molecule, and therefore we can approximate its interaction with the target molecule by a generally nonspherical single centre potential. Therefore the full scattering wavefunction in the outer region can be written in the following, simpler, form:

$$\Psi_E^\Gamma(\mathbf{x}_1, ..., \mathbf{x}_{N+1}) = \sum_{j=1} \Phi_j(\mathbf{x}_N, \hat{\mathbf{r}}_{N+1}, \sigma_{N+1}) \frac{F_j(r_{N+1})}{r_{N+1}}, r_{N+1} \geq a \tag{2.18}$$

$F_j(r_{N+1})$ are at $r_{N+1} = a$ the reduced radial wavefunctions and correspond to the radial part of the partial waves of the scattering electron.

The equations determining the radial functions $F_j(r_{N+1})$ for $r_{N+1} > a$ are obtained by projecting the appropriate Schrödinger equation on the channel functions $|\Phi_i Y_{l_i,m_i}(\hat{\mathbf{x}}_{N+1}) \frac{1}{r_{N+1}})$; after some algebra one obtains the following equation [61]:

$$E_i F_i(r) + \left(-\frac{1}{2}\frac{d^2}{dr^2} + \frac{l_i(l_i+1)}{2r^2} \right) F_i(r) + \sum_{j=1}^{n_{ch}} V_{ij}(r) F_j(r) = E F_i(r) \tag{2.19}$$

- $V_{ij}(r)$ are the coupling potentials, and can be written using the single-centre expansion of the Coulomb interaction of the form:

$$V_{ij}(r) = \sum_{\lambda=0}^{\infty} a_{ij\lambda} r^{-\lambda-1}, i, j = 1, ..., n_{ch}, r \geq a \tag{2.20}$$

- a_{ij} are coefficients linked to the permanent ($i = j$) and the transition ($i \neq j$) multiple moments of the target electronic states.
- E_i is the channel energy, corresponding to the energy of a target state included in the calculation.

For simplicity, we removed the index $N+1$ from the radial coordinate of the scattering electron, because r_{N+1} is the only radial coordinate in the equations above.

The previous equation for the coupling potentials (equation 2.20) can now be inserted in expansion 2.19 to obtain the final form of the single-centre no-exchange close-coupling equations:

$$\left(\frac{d^2}{dr^2} - \frac{l_i(l_i+1)}{r^2} + k_i^2 \right) F_i(r) = 2 \sum_{j=1}^{n_{ch}} \sum_{\lambda=0} a_{ij\lambda} r^{-\lambda-1} F_j(r) \tag{2.21}$$

- $k_i = \sqrt{2(E - E_i)}$ are the channel momenta.

This set of equations allow us to find the $F_i(r)$ in the outer region for each energy E using the R-matrix (equations 2.16 and 2.17) from the inner region calculation. These equations represent a multichannel radial scattering problem.

In order to solve the set of differential equations 2.21, that can only be solved numerically, we use the R-matrix propagation and asymptotic expansions. The propagation is described in detail elsewhere [62], and significantly decreases the computational cost. The main principle is the division of the propagation space into small regions, where the Hamiltonian is kept constant, up to a radius large enough to allow for the use of the asymptotic expansion[2] of the radial wavefunctions $F_i(r)$ (this also decreases the computational resources).

For open channels, each radial wavefunction $F_i(r)$ solution of 2.21, can be written in the asymptotic region as a linear combination of the following linearly independent functions, known as asymptotic expressions:

[2] The asymptotic expansion used in the UKRmol and UKRmol+ suites of codes is the one described by Gailitis [63] (see reference [61] for a more detailed description).

$$R_i^s(r) = \frac{1}{\sqrt{k_i}} \sin(k_i r - l_i\pi/2 + \eta ln2k_i r + \sigma_{l_i}) \tag{2.22}$$

$$R_i^c(r) = \frac{1}{\sqrt{k_i}} \cos(k_i r - l_i\pi/2 + \eta ln2k_i r + \sigma_{l_i}) \tag{2.23}$$

- $\eta = \frac{Z}{k_i}$ is the Coulomb parameter;
- $\sigma_{l_i} = \Gamma(l_i + 1 - i\eta)$ corresponds to the Coulomb phase;
- R_i^s and R_i^c can be seen as the free and the scattered radial waves, respectively.

Using these two independent functions and the solutions of the differential equations 2.21 allow us to express the general solution $F_{\gamma_{i,l_i,m_i}}^{\gamma_{j,l_j,m_j}}$ of equation 2.21 (and therefore obtain the **K**-matrix) in the asymptotic region as their linear combination:

$$F_{\gamma_{i,l_i,m_i}}^{\gamma_{j,l_j,m_j}} = \delta_{i,j}\delta_{l_i,l_j}\delta_{m_i,m_j} R_{i,l_i}^-(r) + K_{i,l_i,m_i;j,l_j,m_j}^{\Gamma} R_{j,l_j}^+(r), r \to \infty \tag{2.24}$$

- $K_{i,l_i,m_i;j,l_j,m_j}^{\Gamma}$ are the elements of the real-valued **K**-matrix;
- The indices of the radial wavefunction $F_{\gamma_{i,l_i,m_i}^{\gamma}}^{\gamma_{j,l_j,m_j}}$ denote a solution corresponding to the electron incoming in the channel γ_{i,l_i,m_i} and outgoing in the channel γ_{j,l_j,m_j}.

For closed channels we set the radial functions to zero, as the solution of equation 2.21 decreases exponentially.

The link between the **K**-matrix and the **T**- and **S**- matrix can be made as follows:

$$\mathbf{T}^{\Gamma} = 2i\mathbf{K}^{\Gamma}(1 - i\mathbf{K}^{\Gamma})^{-1} \tag{2.25}$$

$$\mathbf{S}^{\Gamma} = (1 + i\mathbf{K}^{\Gamma})(1 - i\mathbf{K}^{\Gamma})^{-1} \tag{2.26}$$

The **T**-matrix can be used to calculate the cross section for transitions from state i to state j:

$$\sigma_{i\to j}(E) = \frac{\pi}{k_i^2} \sum_{\Gamma} \sum_{S} \sum_{l_i,l_j} \sum_{m_i,m_j} \frac{2S+1}{2(2s_i+1)} |T_{i,l_i,m_i;l_j,m_j}(E)|^2 \tag{2.27}$$

- S is the total spin of the system;
- s_i is the spin of the target state i;
- Γ indicates the irreducible representation of the point group of the molecule.

Finally, we can present a summary for a practical R-matrix calculation:

- Choose the wavefunctions orbitals that go in equation 2.4;
- Obtain the basis functions Ψ_k^Γ by diagonalizing $\tilde{H}_{N+1}$: $(\Psi_k^\Gamma|\tilde{H}_{N+1}|\Psi_{k'}^\Gamma) = E_k\delta_{kk'}$;
- Calculate the R-matrix for each energy: $R(E) = \frac{1}{2a}\sum_{k=1}^{\infty}\frac{w_{ik}(a)w_{jk}(a)}{E_i-E}$;
- Calculate the **K**-matrix for each energy and finally the desired eigenphase sums and cross sections.

2.4 Eigenphase sum and time-delay analysis

The main focus of this thesis is the identification and characterisation of electronic resonances, as mentioned. It was shown by Hazi in 1979 [64] that an isolated resonance in electron-molecule collisions manifests itself in the eigenphase sum as a characteristic jump of π radians, whose shape is described by the Breit-Wigner formula:

$$\delta_{sum}(E) = \delta_r(E) + \delta_{bg}(E) = -\arctan\frac{\Gamma/2}{E-E_r} + \delta_{bg}(E) \tag{2.28}$$

- E_r and Γ are the position and width of the resonance, respectively;
- δ_{bg} is the background non-resonant contribution, weakly dependent on energy.

However, the analysis of the eigenphase sums is not the only method that can be used to identify resonances. If the molecule possesses a lot of resonances, the eigenphase sums can get very complex and their analysis is not a straightforward task. It is not unusual for a resonance not to manifest as exact an jump of π, due to the contribution of non-resonant processes, that can also hidden wide resonances.

The other method employed by us is the analysis of the time-delay. It proved to be an essential tool for finding most of the resonances we report; we will now proceed to a brief description of it.

The advantages of the time-delay analysis over the more conventional analysis of the eigenphase sums have been highlighted already elsewhere [65, 66]. The most important is that the time-delay analysis allows for unambiguous identification of resonances, even in cases in which the eigenphase sum does not display the typical resonant behaviour, or when its behaviour seems to be completely "non-resonant". This is because this method allows for a better separation of resonances from the background and also from each other, as we will present in the results chapters. However, the method fails when: (i) there are strongly overlapping resonances, as we just mention; (ii) we are trying to identify very narrow resonances close to an excitation threshold; and (iii) resonances are very broad.

We use the definition of the time-delay as formulated by Smith [67]. In this formulation, the lifetime or time-delay is defined in terms of the excess number of particles (charge density) present near the scattering centre obtained after subtracting the number that would have been

present in the absence of the interaction. The time-delay is then obtained by dividing the excess number of particles by the total incoming flux through a closed surface at large distance from the scattering centre. In practice the time-delay analysis is performed using the **Q**-matrix (the time-delay matrix), which is calculated, for a given energy, directly from the **S**-matrix, using the formula below:

$$\mathbf{Q}(E) = i\hbar\mathbf{S}\frac{d\mathbf{S}}{dE} \tag{2.29}$$

The most valuable information we can take from this technique is contained in the analysis of the positive eigenvalues (or time-delays) and associated eigenvectors of the **Q**-matrix, for each scattering energy E. Time-delays much larger than $\hbar/E$ are interpreted as arising from resonant processes and have the shape of a Lorentzian function. The associated eigenvectors of these resonances give us information about their parent states: the square of the jth coefficient of the eigenvector corresponding to a resonance is equal to the branching ratio, i.e. the probability of a resonance to decay to a specific channel (its parent state). For Feshbach resonances this approach cannot be applied since its parent state is positioned higher in energy and therefore the resonance cannot decay into it.

On the other hand, and although they are not typically used, the negative eigenvalues of the **Q**-matrix mean a time-advance, and are associated to the incoming electron being either accelerated by passing through a strongly attractive interaction region or reflected by a strongly repulsive interaction.

2.5 Scattering models

The choice of the number of target states to include in the calculation and the type of the L^2 functions, define what we call the scattering model. More generally, a scattering model can be defined as including specific type(s) of electron-molecule interaction (e.g. exchange interaction, polarisation of the target molecule, etc.). However, comparing the results obtained with the same model but using different computational methods is not always comparing like with like, as the way the electron-molecule interactions are modelled can be different. Because of the way the R-matrix method evaluates these interactions, the further descriptions apply only to the R-matrix method.

The choice of the more suitable scattering model for a given collision depends greatly on the energy range of the incoming electron. In this work our focus is on electron energies below the ionization threshold of our target molecules. Therefore, the scattering models presented below describe the electron-molecule interaction accurately only below the ionization threshold of the target molecule.

2.5.1 Static-Exchange approximation

The simplest scattering method we used is the *Static-Exchange* (SE) approximation. It can be defined as one in which the scattering electron moves in the static potential of the molecule and which includes the exchange interaction between the scattering electron and the electrons of the target molecule. In this model, only the ground state of the target molecule is included in the calculation, and is described at Hartree-Fock level. Polarisation effects are not included in this approximation, that is the molecule is not allowed to be polarised by the incoming electron. The L^2 functions to be used in expansion 2.4 in this approximation can be written as:

$$\chi_i^{SE} : (\text{ground state})^N (\text{virtual})^1 \tag{2.30}$$

- N is the number of electrons in the target molecule;
- *Ground state* stands for the doubly occupied orbitals that describe the ground state of the target;
- *Virtual* stands for the set of unoccupied orbitals.

The SE approximation is capable of describing only shape electron resonances, but these normally appear too high in energy due to an incomplete modelling of the interaction between the target and the scattering electron. Since a shape resonance can be understood as the scattering electron being captured in a specific virtual orbital, inclusion of this virtual orbital in the SE model is essential for its description.

2.5.2 Static-Exchange plus polarisation approximation

In the Static Exchange plus polarisation (SEP) approximation only the ground state wavefunction is included in expansion 2.4, but the molecule is now allowed to be polarised by the incoming electron, which is manifested in the choice of the L^2 configurations. In addition to those described by equation 2.30, we also include configurations of the type:

$$\chi_i^{SEP} : (\text{core})^{N_d} (\text{valence})^{N-N_d-1} (\text{virtual})^2 \tag{2.31}$$

- N_d is the number of electrons frozen in doubly occupied target orbitals;
- *Core* orbitals of the molecule are always doubly occupied by N_d electrons and do not participate in the excitation process;
- *Valence* are the set of orbitals from where it is possible to promote one electron to a selected number of virtual orbitals, which are also available for the scattering electron, and allow the molecule to be polarised.

The presence of the frozen core in the model can be avoided depending on the size (i.e. number of electrons) of the target molecule. In few electrons systems it might be possible to allow excitations from all orbitals.

The SEP is our preferred method to describe shape resonances, and is also capable of modelling core-excited resonances associated with single excitations of the target molecule, which is the reason why sometimes we observe signatures of core-excited resonances in a SEP calculation. However, it has the disadvantage of suffering from the appearance of pseudoresonances, due to the way the polarisation is modelled: this is done by performing single-excitations of the target molecule from the valence to the virtual space. Some of these configurations are associated with the main configuration of a particular excited state, and therefore can couple with the ground state. As a result, the outgoing probability flux should be allowed to flow also to the channels corresponding to these electronic states that are being described. However, as these channels are not included in the SEP calculations, the pseudoresonances appear usually at higher energies (at least above the first excitation threshold). These pseudoresonances are visible in the eigenphase sums, time-delays and cross sections and their behaviour is the same as that of physical resonances. Despite possessing all the features of a physical resonance, the pseudoresonances are unphysical.

The pseudoresonances, however, are not the biggest issue we have to deal with in our calculations. When setting up the models, there is no way to choose the optimal number of the virtual orbitals (VOs) to include in order to accurately describe the polarisation effects. If we use just a few of them, the quality of the calculation is poor; on the other hand, if we include too many we will have overcorrelation effects (the description of the scattering wavefunctions is better than the target one). To overcome this problem, our approach is to gradually increase the number of VOs in our scattering calculations, in energy order, until a good agreement between the position of the first resonance with the experiments is reached.

2.5.3 Close-coupling approximation

The most sophisticated model we use is the Close-Coupling approximation (CC) in which the eigenfunctions Ψ_k^Γ have the full form of equation 2.4 with a number of target electronic excited states included. One of the most important aspects of scattering calculations based on the CC expansion is that of balance: the description of the N-electron target electronic states Φ_i should be of the same quality (or at least, as close as possible) as the description of the $N+1$ electronic basis functions of the electron-molecule collision problem.

In our calculations, we choose to base our target models around the CAS representation of the target wavefunction. This model has been found to produce satisfactory balanced results for small targets, when a simple set of L^2 functions is used. These L^2 configurations have the form of the target CAS configurations, but with the extra incoming electron in the active space:

$$\chi_i^{CC} = (\text{core})^{N_d}(\text{CAS})^{N-N_d+1} \tag{2.32}$$

- CAS represents the orbitals of the active space.
- *Core* and *virtual* have the same meaning as described before.

In some cases, particularly when the polarisability of the target is big, the following configurations are also included:

$$\chi_i^{CC} = (\text{core})^{N_d}(\text{CAS})^{N-N_d}(\text{virtual})^1 \tag{2.33}$$

Similarly to the case of the SEP L^2 functions 2.31, the frozen core is optional (for sufficiently small molecules it might be possible to allow excitations from these orbitals). The uncertainty regarding the number of VOs to include is also present in this model, when configurations of the type 2.33 are used. Our approach is the same as at SEP level, although in this case we have less control over the polarisation we are including, as the excitations into the virtual space are done from a reduced space. Also, the inclusion of the electronically excited states of the target also describes, in part, the polarisation effects.

The CAS orbitals are selected according to the computer resources: for small molecules, it is possible to include all the orbitals in the active space; for medium and large molecules, however, it is common to select the valence ones (usually the higher-energy occupied molecular orbitals (HOMOs) and lower unoccupied molecular orbitals (LUMOs)), keeping the calculation within the computational limits.

2.6 Computational tools

In this section we briefly describe both software suites used to perform our calculations: UKRmol and UKRmol+ (more information can be found in reference [43] for the former, the first one to be developed, and in [44] for the latter- these suites can be downloaded from Zenodo [68, 69]). Both of them are divided into two subsets of programs that perform the calculations for the inner and the outer region. Many of the programs are common in both suites, as we shall present in the following subsections, where we summarise the main characteristics of each suite.

2.6.1 UKRmol

The UKRmol suite [43] is an implementation of the R-matrix method for electron and positron molecule collisions, as mentioned before, and was used to perform the majority of the scattering calculations presented in this work.

A full scattering calculation using UKRmol comprises three steps:

- Target calculation;
- Inner region calculation;
- Outer region calculation.

In the target calculation (flowchart presented in figure 2.2), the geometry of the molecule and the GTO target basis set are required as an input for the *swmol3* program that calculates the atomic integrals. The calculated integrals are then ordered by *sword*. As we use *molpro* to generate the target orbitals (*molpro* is a quantum chemistry software to calculate wavefunctions and molecular properties [70]), the *mpoutrd* interface (developed by Z. Mašin) ensures the MOLPRO output is in the right format to be read by the following programs. However, UKRmol is capable of generating its own HF orbitals or pseudo-natural orbitals if required. *Sword* generates the input (ordered integrals) for *swedmos*, responsible for the orbital orthogonalization. After *swedmos*, *swtrmo* transforms the integrals over the atomic GTOs into integrals over the target molecular orbitals. Then, the configurations (CSFs) are generated by *congen*, and used together with the transformed integrals as input for the *scatci* program, which builds and diagonalizes the target molecule's Hamiltonian to obtain the target states and their energies. The last step in the calculation is performed by *denprop*, which uses the outputs from the *scatci* and *gausprop* (that produces the property integrals) to generate the target properties file containing dipole and quadruple permanent and transition moments, which are necessary to perform the outer region calculations.

The inner region calculation uses many of the same programs as the target calculation. Its flowchart is presented in figure 2.3. The first program to run is once again *swmol3*, this time including the extra continuum GTO basis set describing the scattering electron. The *gaustail* program calculates the integrals between the R-matrix boundary and infinity (also called integral "tails"), involving the continuum GTOs in order to obtain integrals over the inner region only. These tail integrals are then subtracted from the molecular integrals in *sword*, that again orders all the resulting integrals. The continuum orbitals are obtained in *swedmos* using the following procedure: first, the continuum GTOs are Schmidt orthogonalized to the selected (orthogonal) subset of target molecular orbitals and then symmetrically orthogonalized among themselves. This final set of continuum orbitals is obtained by deleting the orbitals with eigenvalues of the overlap matrix smaller than a selected deletion threshold. The following program is *swtrmo*, which transforms the integrals over the primitive GTOs into integrals over the target and continuum orbitals. *Congen* is again used to generate the basis of the CSFs for the R-matrix basis functions and *scatci* builds and diagonalizes the $N+1$ Hamiltonian to obtain the coefficients a_{ijk}, b_{ik} in equation 2.4 and the energies E_k of the R-matrix basis functions.

In the outer region calculation, unlike the inner region part, not every program needs to be invoked. We can specify which programs to run depending on the data we are interested in generating, although *swinterf* and *rsolve* must always be run.

The first program to run in the outer region calculation is *swinterf*. This program requires

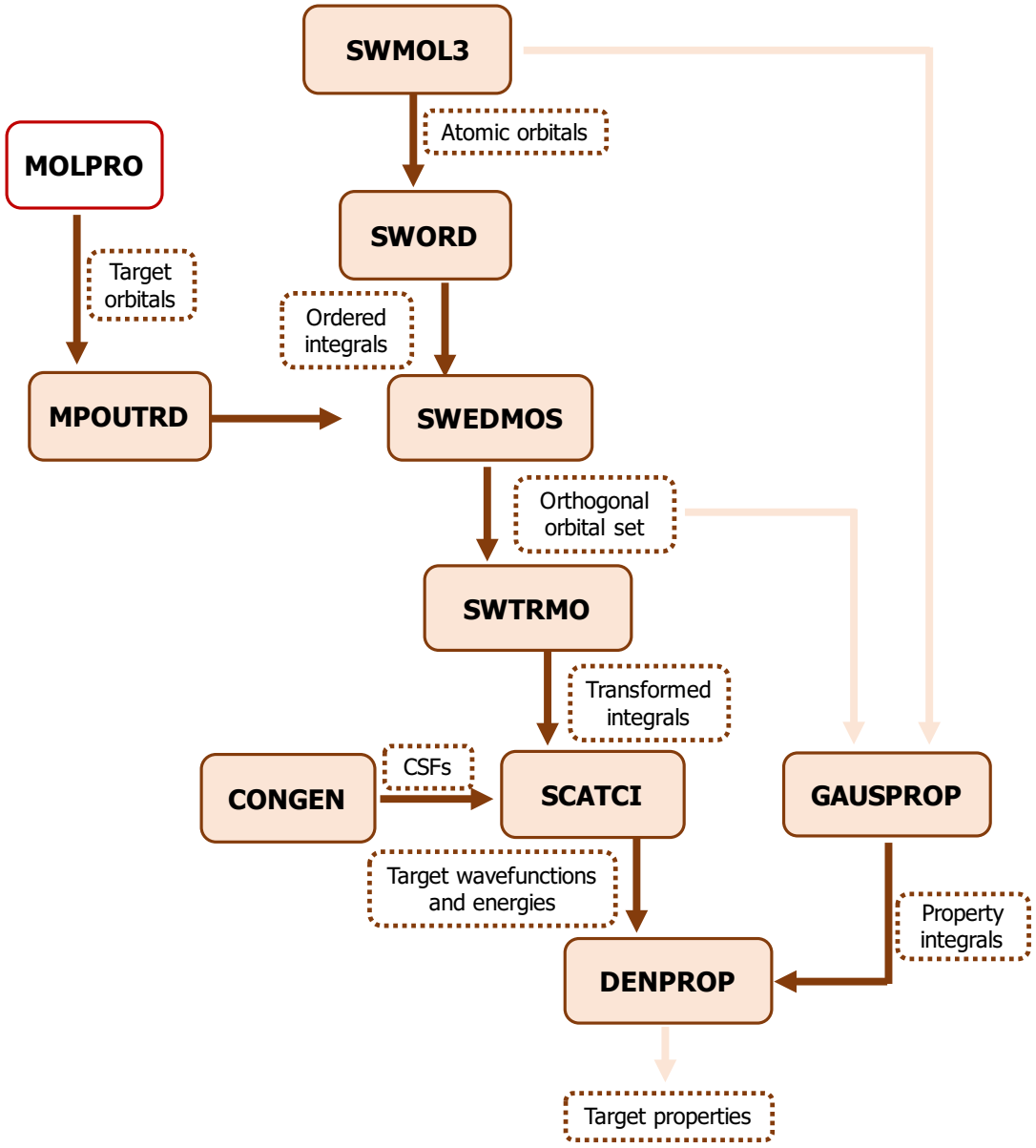

Figure 2.2: Flowchart for the target calculation using the UKRmol suite. The light beige filled boxes represent the programs called during the calculation; the boxes with the dashed brown border correspond to the data that are output from one program and serve as input to the following ones or are final results; the box with a red border corresponds to the programs that is not part of the UKRmol suite.

data both from the target and inner region calculations (target properties, raw boundary amplitudes, eigenfunctions and eigenvalues) and generates channel data and that needed to build the R-matrix (the boundary amplitudes, and also the coefficients of the interaction potential). *Rsolve* generates the K-matrices (by solving the set of differential equations 2.21 using the propagation method and matching to the asymptotic expression to obtain the K-matrices from equation 2.24), *eigenp* calculates eigenphases sums by diagonalizing the K-matrix, *tmatrx* builds T-matrices and *ixsec* produces the integral elastic and inelastic cross section. *Reson* uses the

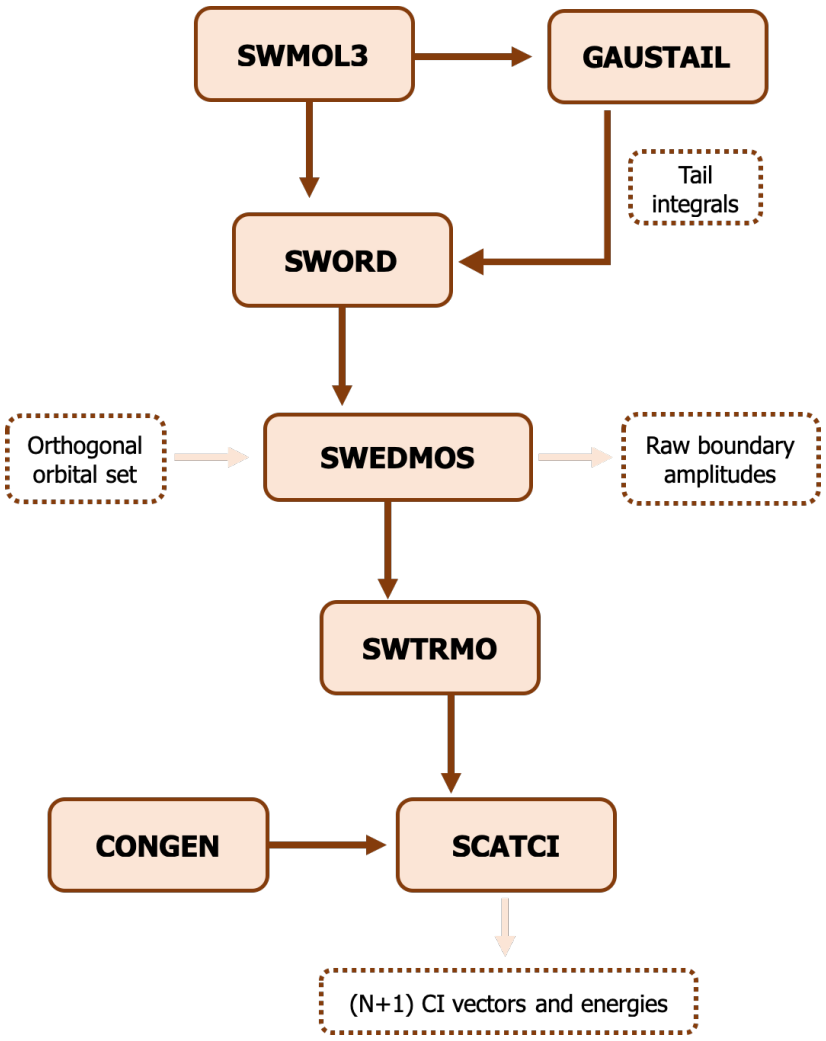

Figure 2.3: Flowchart for the inner region calculation using the UKRmol suite. The light beige filled boxes represent the programs called during the calculation; the boxes with the dashed brown border correspond to the data that are output from one program and serve as input to the following ones or are final results. The "target orbitals"come from the target calculation, and the "raw boundary amplitudes"and "(N+1) CI vectors and energies"will be used as input in the outer region.

K-matrices data to determine the positions and widths of the resonances, by using an automated fitting procedure. *Time-delay* (see section 2.4) was created by Z. Mašin on the basis of another program with the same purpose called *timedel*. Time-delay is easier to run and its performance is much better, although the resonance fitting has to be made manually. *Polydcs* (created by N. Sanna and F. Gianturco [71]) is used to obtain elastic differential cross sections (DCS) for a chosen range of energies. The program uses the K- or the T-matrices (we used the T-matrices during this thesis) as input and calculates Born-corrected (when the target has a dipole moment) elastic DCS and integral cross sections (the correction accounts for the partial waves not included in the *ab initio* calculation). Rotationally elastic, state-to-state rotationally inelastic cross section and excitation functions for a specific angle, are calculated using the DCS

program, created by Z. Mašin.

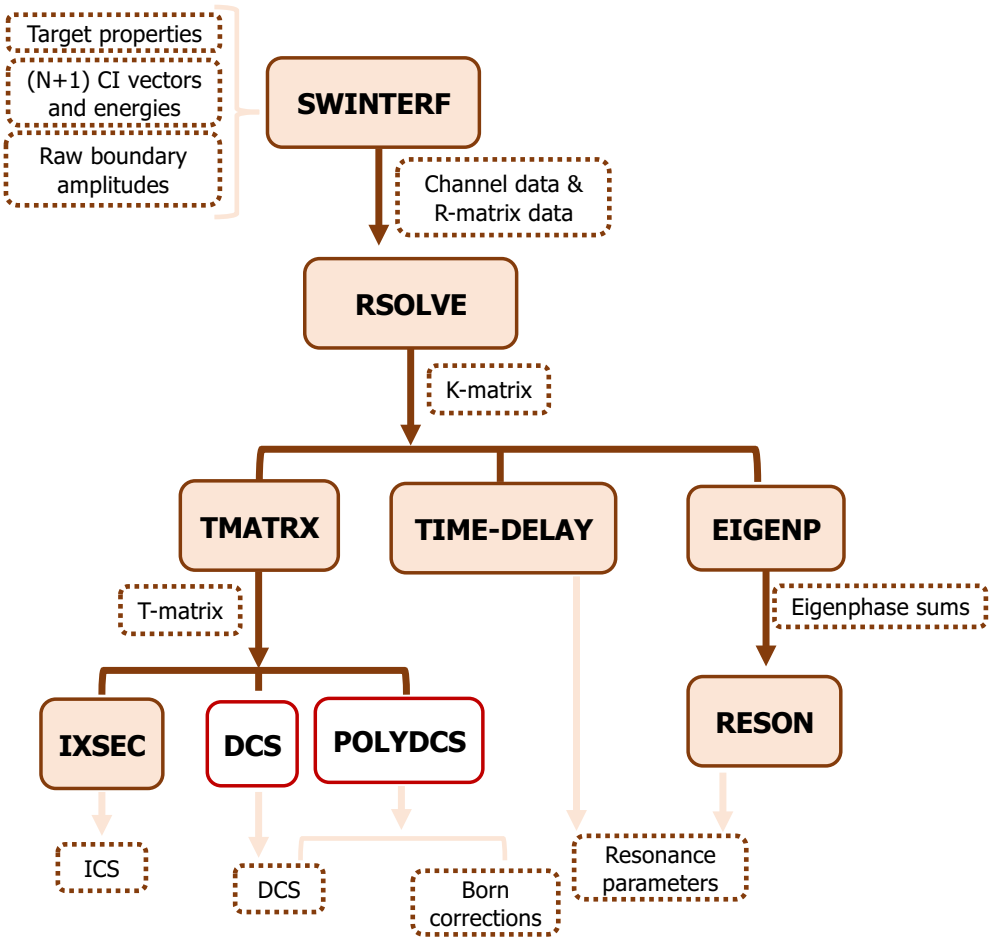

Figure 2.4: Flowchart for the outer region calculation using the UKRmol suite. The light beige filled boxes represent the programs called during the calculation; the boxes with the dashed brown border correspond to the data that are output from one program and serve as input to the following ones or are final results; the boxes with a red border corresponds to the programs that is not part of the UKRmol suite.

There are other programs that are not in the flowcharts (because they were only used occasionally) but belong to the suite, as *radden* and *hamdiag*. *Radden*, created by Z. Mašin, calculates the radial charge densities of the target orbitals, allowing the user to select an R-matrix radius for which the charge density is negligible small (usually around 10^{-7} at a particular radius). *Hamdiag* can be used to diagonalize the Hamiltonian in parallel, after *scatci* has built it.

2.6.2 UKRmol+

The novelty of this suite is that all the programs dealing with integrals and orbitals in the UKRmol suite (*swmol3, sword, swedmos, swtrmo, gausprop* and *gaustail*) have been replaced with

one program called *scatci-integrals*, implemented by Z. Mašin and others. Therefore, all the integral evaluation is different from UKRmol, and more accurate.

The main advantages of this suite, despite being more compact, are the possibility to use more partial waves and compile in double or quadruple precision (which improves the quality of the orthogonalization), serially or in parallel (which reduces the computational time). The use of B-splines to describe the continuum is another great advantage, although it was not used throughout this thesis. The disadvantage is the fact that needs the *molden* file as an input for *scatci-integrals* program, and this file can only be obtained by external commercial software like *molpro*. This file contains the target GTO basis set, the molecular geometry and the target orbitals.

To perform the target calculation we use the programs indicated in figure 2.5.

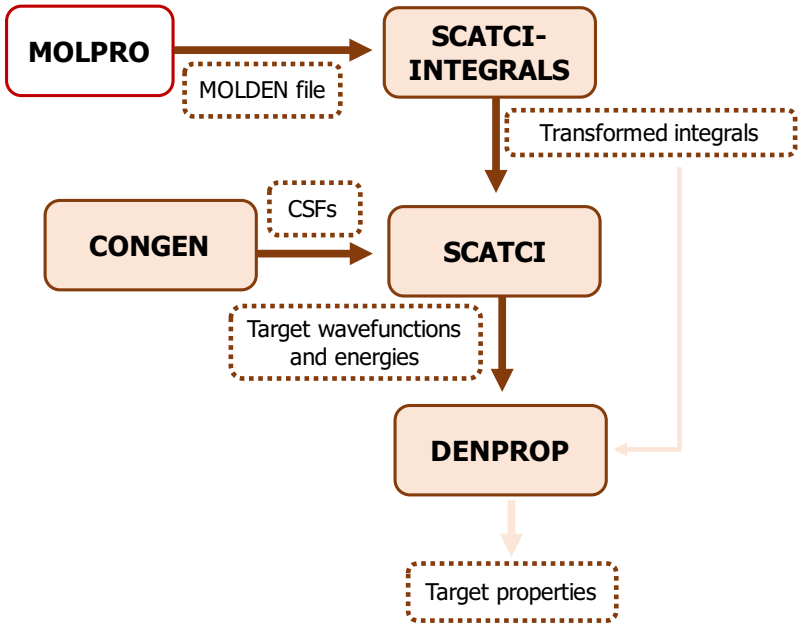

Figure 2.5: Flowchart for the target calculation within the UKRmol+ suite. The light beige filled boxes represent the programs called during the calculation; the boxes with the dashed brown border correspond to the data that are output from one program and serve as input to the following ones or are final results; the box with a red border corresponds to the programs that is not part of the UKRmol+ suite.

In this suite, the basis set, molecular geometry and target orbitals are read from MOLPRO output. *Scatci-integrals* calculates the atomic integrals and then transforms them to obtain the target molecular orbitals. After that, it performs the orthogonalization of the orbital and computes the property integrals. As mentioned before, *congen* generates the configuration state functions (CSFs), used in the CI description of the target and *scatci* builds and diagonalizes the Hamiltonian. Finally, and similarly to UKRmol, *denprop* generates the target properties file containing dipole and quadruple permanent and transition moments.

In the inner region calculation, we use the output from *scatci-integrals* from the target calculation (because we evaluate the integrals for both bound and continuum orbitals at the same

time), from where we already obtained the transformed integrals and the boundary amplitudes. Therefore, *congen* and *scatci* are the only programs to run here. Once again, *congen* generates the CSFs for the basis functions (see equation 2.4) and *scatci* builds and diagonalizes the Hamiltonian to obtain the coefficients a_{ijk} and b_{ik}, and therefore, $N+1$ wavefunctions and energies (E_k).

The outer region codes are the same as in the UKRmol suite.

2.6.3 Running UKRmol and UKRmol+ suite

Running the suites used to be a complicated task. As each of the programs (for each suite) needs an input file (plus some generated before), preparing them manually was very time consuming and the user would easily make mistakes (especially the input for *congen* and *swinterf*).

In order to become more user friendly, a perl script is now used (no previous knowledge of the perl language is needed) to run the calculations. The script was written by K. Houfek and developed and adapted by A. Asieradzka, and can be used for both UKRmol and UKRmol+ suite.

With this script, the user specifies the parameters with which the calculation must be performed: the basis set (provided in separated files; when needed, the data to build these files can be found online, although just for the target - see reference [72]), geometry, scattering model, radius (a file with the continuum for each specific radius is provided; if not, those can also be built by the user using the procedure described in reference [59]), point group of the target molecule, etc. Then, the script generates the inputs itself, invoking the programs in the right order. In the same way, it produces outputs that can be easily read and plotted.

Another big advantage of these scripts is that we do not need to run all the programs in each calculation: we can run only the ones we are interested in, in the same way we can change the inputs manually if needed. For example, if we need to test a different number of VOs, there is no need to run the target part of the calculation, and we can start from the inner region.

The version of the script used in this thesis is divided into a few files, only one of them containing the user settings. So far there are no manual or documentation available, but the script itself has comments on every variable, which makes it very clear and user friendly. The scripts are currently available on Gitlab.

CHAPTER 3

ELECTRON COLLISIONS WITH *para*-BENZOQUINONE

The focus of this chapter is *para*-benzoquinone (*p*-BQ, 1,4-benzoquinone or $C_6H_4O_2$, see chemical structure in figure 3.1).

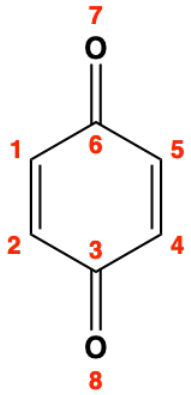

Figure 3.1: Chemical structure of *para*-benzoquinone.

p-BQ is the prototypical member of the quinone's family. Quinones are commonly found in nature and are known to play a crucial role in electron transfer reactions in chemistry and biology [73, 74]. An example of these reactions is photosynthesis [22]: ubiquinones (see general structure on the left side of figure 3.2), for example, are the final electron acceptors in photosynthesis and respiration [75]. The underlying processes of these photon induced reactions are photoionisation or photodetachment, depending on whether the photon interacts with a neutral or an anion target molecule, respectively.

From the biochemical point of view, several natural and synthetic quinones are recognised due to their antitumoral activity [76, 77], whilst others are involved as redox cofactors in quinoenzymes [78, 79] (e.g. pyrroloquinoline quinone (PQQ), commonly known as methoxatin, see right side structure in figure 3.2).

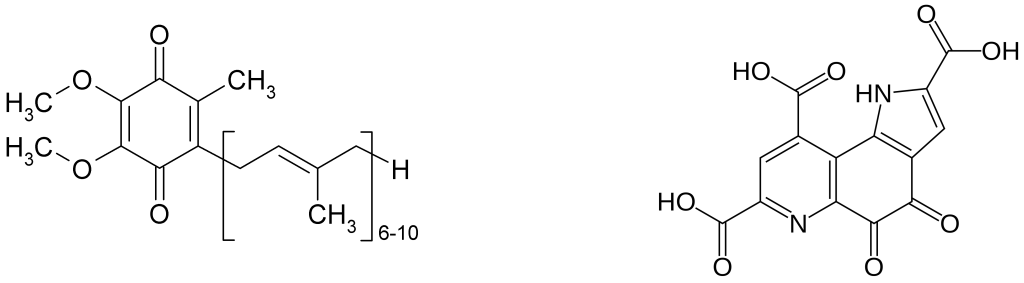

Figure 3.2: General chemical structure of ubiquinones (left) and pyrroloquinoline (right).

To understand the reactions involving quinones, it is crucial to obtain fundamental insights into the mechanism of resonance formation (as they behave as electron acceptors) for this family of molecules. This process has been vastly studied through the years, both at theoretical and experimental levels (predominantly from a non-scattering perspective), as we will present here, especially due to its importance in the photodetachment phenomena. Our interest in *p*-BQ was mainly triggered by the work performed before by other groups on the photodetachment process [80, 81, 82, 83]. In order to fully comprehend this process, one must understand *p*-BQ anion resonances. Our preliminary photodetachment studies and available results from literature are presented in chapter 6, and briefly mentioned later on in this chapter.

Another reason that lead us to study *p*-BQ was the lack of agreement in the literature about its resonant spectrum, specially theoretically. As presented in the following sections, we believe that, in this case, the significant reason behind this disagreement (despite the use of different methods) is the differences in the geometry used to perform the calculations.

This chapter is divided into two main parts: calculations for the ground state geometry of neutral *p*-BQ; and calculations using the ground state geometry of the anionic *p*-BQ. However, it is important to keep in mind that, in both cases, the scattering calculations were performed for the neutral molecule (not $p\text{-BQ}^-$). The reason we have studied both geometries is the following: for comparison with electron scattering experiments, similarly to what we have done in the following chapters, the target molecule is in its ground state neutral geometry, as it is in the experiments. In the particular case of *p*-BQ, however, as we are also interested in the photodetachment process, using the anion geometry to perform the calculations is more appropriate.

We will, in the following sections, start by revising the literature on the electronic structure of *p*-BQ and respective electron collisions studies. Then we provide our calculated resonant spectrum within the 0-8 eV energy range, as well as integral and differential cross sections (for both geometries). The link between our results and the DEA data is also presented. From our studies with the neutral geometry of *p*-BQ, one paper emerged [46]. Many, but not all the results included in this chapter were presented in the paper.

3.1 Literature on the electronic structure of *p*-BQ

p-BQ has 56 electrons and belongs to the D_{2h} point group, so it possesses no dipole moment. The experimentally determined ionisation energy is 9.9 eV [84] and its experimental polarisability is 11.23 Å^3 [85]. The first electronic excitation threshold of *p*-BQ is ≈2.3 eV [86, 87]. *p*-BQ is solid at room temperature and its crystal has a bright-yellow colour, with a characteristic irritating odour.

Over the last couple of years, several groups have dedicated their efforts to the identification and characterization of the electronically excited states of *p*-BQ, both theoretically and experimentally, as we will briefly review in this chapter.

Regarding the visible absorption spectrum of *p*-BQ, Koyanagi *et al.* [86, 87] scrutinised the lowest triplet n,π^* state of *p*-BQ, and obtained evidence that an orbital and spin forbidden transition is a possible phosphorescence process.

Trommsdorff [88] provided a complete assignment of the electronic transitions involved in the visible and near ultraviolet spectra of *p*-BQ. He also provided results for CNDO type calculations that are in a good agreement with the experimental data.

Horst *et al.* [89] studied the fluorescence excitation spectra of the singlet $n-\pi^*$ transitions of *p*-BQ (both hydrogenated and deuterated) in a supersonic jet, identifying the origin of some particular transitions. No differences were observed for the deuterated molecule.

Pou-Amérigo *et al.* [90] calculated the electronically excited states of *p*-BQ using multiconfigurational second-order perturbation theory (CASPT2) and CASSCF methods, and extended atomic natural orbital (ANO) basis sets. Their computed vertical excitation energies are in a good agreement with the experiments from Cooper *et al.* [91].

Schreiber *et al.* [92] calculated vertical excitation energies, for several small organic molecules, for the valence states using both CASPT2 and a hierarchy of coupled cluster methods (CC2, CCSD and CC3). The CC3 method produced the closest results to the CASPT2 ones.

More recently, Jones *et al.* [93] reported a high-resolution synchrotron investigation (in the energy range of 4.0-10.8 eV) into the excited electronic structure of *p*-BQ, as well as detailed quantum chemical computations. Last year, the same group [94] recorded the angle resolved electron energy loss spectra for incident electron energies of 20, 30 and 40 eV.

Nowadays, there is a satisfactory consensus regarding the electronic spectra of *p*-BQ (at least for the lower energies).

3.2 Available work on electron collisions with *p*-BQ

Christophorou *et al.* [95] looked at the electron capture processes (using the swarm-beam technique) and the lifetime of the negative ions. They identified a resonance at 2.1 eV. These authors studied a relatively small energy range - only up to 2.5 eV. Collins *et al.* [96] reported the energy dependence of the nondissoactive electron attachment cross sections of *p*-BQ.

Cooper *et al.* [91] performed electron and cesium scattering measurements (the latter to determine the electron affinity of *p*-BQ) and found three resonances up to 2 eV. A fourth peak

at 4.35 eV was also reported by these authors but its origin could not be definitely assigned to an anion state. The authors claim it could also arise from an electronically excited state of the molecule (so a core-excited resonance).

Allan [97, 98] used time-resolved electron energy loss spectra (EEL) to study the long-lifetime of *p*-BQ anion. He identified three resonances up to 2.2 eV, and also investigated vibrational and electronic excitation through electron impact.

Modelli and Burrow [99] performed electron transmission spectroscopy (ETS) measurements to locate shape resonances in gas-phase *p*-BQ in the 0-6 eV energy range. The only two resonances they found are in good agreement with the ones reported before by the other groups (that generally found more than those).

Jones *et al.* [100] measured absolute integral cross sections for electron impact excitation of 6 bands of unresolved electronic-states in *p*-BQ for incident electron energies between 20 and 40 eV. The group also used the IAM-SCAR and the SMC-PP methods to calculate integral cross sections; the agreement found with the measurements is acceptable.

Lozano *et al.* [101] obtained the total elastic scattering cross sections for impact energies from 1 to 200 eV by measuring the attenuation of a linear electron beam under magnetic confinement conditions. This group collaborated with the aforementioned group of Jones *et al.*, and in this work they compiled and complemented the previous data with new elastic and inelastic cross sections.

Beside the work on electron scattering, there have been several theoretical studies focused on the identification of the temporary anions of *p*-BQ. These studies are based either on conventional (bound-state) quantum chemistry techniques or use approaches specifically developed to treat transient anions (i.e. stabilisation techniques or use of a complex absorbing potential). The latter are expected to produce reasonable results for the position and width of the resonances. On the other hand, standard bound variational techniques are always at risk of collapse to the continuum and should be interpreted in this light.

The majority of the aforementioned studies provide resonance information for the ground state geometry of neutral *p*-BQ. There were others, however, that looked at other geometries of interest, particularly the (bound) ground state anion equilibrium geometry (as we also did; the results are presented in section 3.5).

Pou-Amérigo *et al.* [102] used standard quantum chemistry approaches (CASSCF/CASPT2 and extended atomic natural orbital (ANO) basis sets) to investigate resonances found in previous experiments. They provide vertical excitation energies at the optimized geometries of the anion and the neutral molecule and link their theoretical results with the data provided by different spectroscopic techniques, such as UV/vis absorption, excitation, fluorescence, electron photodetachment, and electron scattering.

Honda *et al.*[103] used the symmetry adapted cluster configuration interaction (SAC-CI) method to investigate the excited and ionised states of *p*-BQ, and the ground and excited states of its anion radical. They identified 6 experimentally observed resonances of shape and Feshbach character below 5 eV.

Cheng *et al.* [104] studied shape and core-excited resonances using the stabilization method (SM): for shape resonances, the stabilized Koopmans theorem is adopted in the framework of long range corrected density functional theory (LC-DFT), and for core-excited resonances, the SM coupled with long range corrected time-dependent density functional theory (LC-TDDFT). They report the energies and widths of ~20 resonances - of shape and core-excited character - in the range of 0-6 eV. Our results will be mainly compared with theirs.

West *et al.* [105] reported results from anion frequency-resolved photoelectron imaging and from some standard (bound state) quantum chemical calculations for the energy of six resonances in the range 0-2.4 eV, for the geometry of both neutral and anion *p*-BQ. In their studies and regardless of the geometry, they only used *p*-BQ in its anionic form.

Finally, Kunitsa and Bravaya [106, 107] performed complex-absorbing potential equation-of-motion coupled-cluster calculations for the ^2A_u resonance [106] and used the multi-state multireference second order perturbation approach to investigate the bound and seven resonant states for the neutral and anion geometries of *p*-BQ. The group have also investigated the direct and resonant photodetachment channels of *p*-BQ anion, as well as its electronic relaxation pathways in the 2.4-3.1 eV energy range. The latter results will be presented and discussed in chapter 6.

The energy order of the low-lying resonances at the equilibrium geometry of the neutral molecule varies between publications, as does the character of some of the resonances. The results and main conclusions from these studies are presented in sections 3.6 and 5.5, and discussed along with ours.

3.3 Calculation details and stability tests

The results presented in this chapter were obtained using the UKRmol suite described in chapter 2.

3.3.1 Target description

The ground state configuration of *p*-BQ is $1a_g^2\ 1b_{1u}^2\ 2a_g^2\ 2b_{1u}^2\ 3a_g^2\ 1b_{2u}^2\ 3b_{1u}^2\ 1b_{3g}^2\ 4a_g^2\ 4b_{1u}^2\ 5a_g^2\ 2b_{2u}^2\ 5b_{1u}^2\ 2b_{3g}^2\ 6a_g^2\ 7a_g^2\ 6b_{1u}^2\ 3b_{2u}^2\ 4b_{2u}^2\ 7b_{1u}^2\ 8a_g^2\ 1b_{3u}^2\ 1b_{2g}^2\ 3b_{3g}^2\ 5b_{2u}^2\ 4b_{3g}^2\ 2b_{3u}^2\ 1b_{1g}^2$. In our calculations we have used the geometry described on the NIST website calculated at MP2 level using the cc-pVDZ basis set [108].

We used the HF and the SA-CASSCF methods to generate the target orbitals. These calculations were performed using the commercial software MOLPRO [70]. In order to obtain optimal target orbitals for the description of the scattering process, three basis sets were tested: 6-311G** ("less diffuse"), 6-311++G** ("more diffuse") and cc-pVDZ ("compact"). After a series of tests (presented throughout this section) we choose the compact basis set to perform our scattering calculations, as it provided better agreement between our calculated excitation thresholds and the literature.

As explained in chapter 2, the description of core-excited resonances requires the inclusion of the electronic excited states in expansion 2.32. These excited states have been extensively studied in *p*-BQ using both theoretical and experimental methods, as we summarised in section 3.1. For the energy range we are interested in (0-8 eV) most of the states are reported to have valence character. To obtain their best description, several CASSCF models were tested. Table 3.1 lists the energies (in eV) for the first ten electronically excited states of *p*-BQ using different CAS models, and averaging different states, as well as the absolute energy (E, in Hartree) of the ground state for each of the sets. Experimental data is also presented for comparison. We used the work of Pou-Amérigo *et al.* [90] as a starting point to determine the best (within our computational resources) active space.

From the analysis of table 3.1[1] and comparing our results with the literature, we choose the compact basis set and an active space of (12,10) (12 electrons distributed among 10 orbitals) that includes the 4π and $4\pi^*$ orbitals corresponding to double bonds, plus two non-bonding orbitals of the oxygen atoms ($1b_{3u}$ (π), $1b_{2g}$ (π), $5b_{2u}$ (n), $4b_{3g}$ (n), $2b_{3u}$ (π), $1b_{1g}$ (π), $2b_{2g}$ (π^*), $1a_u$ (π^*), $3b_{3u}$ (π^*) and $3b_{2g}$ (π^*)); we used the state averaging labelled X: the 8 states included were - 1^1A_g, 1^1B_{3u}, 1^1B_{1g}, $1-2^1B_{1u}$, $1-2^1B_{3g}$ and 1^1A_u. The choice of the best model is a tricky step in our calculations, as at least three points need to be taken into account: the number of configurations generated (it cannot be too big, otherwise we easily get out of the computational limits), and the agreement of the ground state energy and the electronic excitation thresholds with the more accurate values. The use of an active space of (12,8) (12 electrons distributed among 8 orbitals, that includes the 4π and $4\pi^*$ orbitals corresponding to double bonds) was also tested, but produced poorer results, as seen in table 3.1.

The comparison between our selected model and other calculations is provided in table 3.2, where we present the 48 vertical excitation (VE) energies of the states included in our CC calculations (although our scattering calculations are focused only on energies up to 8 eV). Agreement is, in general, better with the results obtained by Pou-Amérigo *et al.* [90] at CASSCF than CASPT2 level, though our excitation energies tend to be between the two values, and occasionally closer to the CASPT2 ones (note that Pou-Amérigo *et al.* used a slightly different geometry which is, in part, the reason behind the differences observed). The energies obtained by Schreiber *et al.* [92] calculated at CASPT2 level are lower than Pou-Amérigo *et al.*'s using the same method. Agreement with experimental data is reasonable.

[1] We have also tested active spaces of (10,8) and (10,10) but the excitation thresholds obtained were too high and in poor agreement with the literature. For simplicity, those results were omitted from table 3.1.

A.S.					(12,10)					
Conf.					2610					Exp
B.S.		6-311G**			6-311++G**			cc-pVDZ		
S.A.	X	Y	Z	X	Y	Z	X	Y	Z	
1^3B_{1u}	2.947	2.970	2.940	2.956	2.982	2.951	**2.958**	2.980	2.951	-
1^3A_u	3.167	3.173	3.102	3.193	3.201	3.124	**3.158**	3.165	3.095	2.32 [86, 109], 2.35 [87]
1^3B_{1g}	3.171	3.179	3.106	3.194	3.206	3.126	**3.163**	3.174	3.102	2.28 [86], 2.31 [87]
1^1A_u	3.317	3.322	3.252	3.341	3.349	3.272	**3.309**	3.316	3.247	2.48 [89]
1^1B_{1g}	3.332	3.339	3.267	3.354	3.365	3.286	**3.326**	3.336	3.265	2.48 [109], 2.49 [89]
1^3B_{3g}	3.650	3.682	3.704	3.631	3.664	3.690	**3.666**	3.696	3.719	-
1^3B_{1u}	5.154	5.167	5.027	5.205	5.224	5.070	**5.135**	5.151	5.013	-
1^1A_g	5.139	5.143	5.201	5.141	5.211	5.198	**5.135**	5.154	5.219	-
1^3A_g	5.260	5.273	5.209	5.276	5.292	5.220	**5.282**	5.296	5.232	-
3^3B_{1u}	5.487	5.570	5.537	5.489	5.582	5.546	**5.502**	5.583	5.599	-
E	-379.316	-379.317	-379.318	-379.321	-379.322	-379.323	**-379.261**	-379.262	-379.262	-
A.S.					(12,8)					
Conf.					48					Exp
B.S.		6-311G**			6-311++G**			cc-pVDZ		
S.A.	X	Y	Z	X	Y	Z	X	Y	Z	
1^3B_{1u}	3.056	3.093	2.994	3.076	3.114	2.965	3.068	3.104	2.954	-
1^3A_u	3.495	3.567	3.249	3.528	3.613	3.288	3.487	3.555	3.239	2.32 [86, 109], 2.35 [87]
1^3B_{1g}	3.382	3.448	3.172	3.407	3.485	3.204	3.377	3.438	3.166	2.28 [86], 2.31 [87]
1^1A_u	3.558	3.630	3.308	3.591	3.675	3.346	3.551	3.619	3.299	2.48 [89]
1^1B_{1g}	3.477	3.546	3.258	3.504	3.584	3.290	3.473	3.537	3.252	2.48 [109], 2.49 [89]
1^3B_{3g}	4.228	4.159	4.318	4.188	4.105	4.270	4.251	4.188	4.342	-
1^3B_{1u}	5.390	5.524	4.966	5.458	5.616	5.040	5.372	5.497	4.945	-
1^1A_g	5.345	5.397	5.215	5.401	5.597	5.572	5.534	5.647	5.235	-
1^3A_g	6.790	6.848	6.719	6.767	6.836	6.699	6.815	6.870	6.744	-
3^3B_{1u}	6.158	6.211	6.108	6.128	6.207	6.094	6.172	6.220	6.120	-
E	-379.211	-379.211	-379.217	-379.217	-379.217	-379.223	-379.157	-379.126	-379.162	-

Table 3.1: Vertical excitation energies (in eV) obtained from CASSCF calculations using different states in the state-averaging procedure and different active spaces for the three basis sets tested. Also presented are the experimental data from Koyanagi *et al.* [86, 87], Hollas *et al.* [109] and Horst *et al.* [89]. A.S. stands for Active Space; B.S. stands for basis sets; Conf. is the highest number of configurations generated per symmetry, in this case the A_g; S.A. corresponds to the set of states averaged, and are represented the letters X, Y and Z, where X: [1,1,0,1,2,0,2,1]; Y: [1,1,0,1,1,0,1,1]; and Z: [2,1,0,1,2,0,1,1]. The order of the symmetries is: a_g, b_{3u}, b_{2u}, b_{1g}, b_{1u}, b_{2g}, b_{3g} and a_u. Note that all the states averaged are singlets. E is the absolute energy of the ground state (in Hartree) obtained at SA-CASSCF level.

Table 3.2: Vertical excitation thresholds (in eV) obtained in this work from CASSCF calculations for the compact basis set, and the chosen active space and state-averaging. ES stands for Excited State. Also listed are the theoretical results obtained by Pou-Amérigo *et al.*[90] using CASPT2 and CASSCF methods; Scheiber *et al.* also using CASPT2 [92] and Jones *et al.* using TD-DFT and MOB-SCI/5s5p2d methods [93, 94]. The experimental values were obtained by Koyanagi*et al.* [86, 87], Hollas *et al.* [109], Trommsdorff [88], Horst *et al.* [89] and Jones *et al.* [94].

	Pou-Amerigo		Schreiber	Jones	Exp.	This work
ES	CASPT2	CASSCF	CASPT2	TD-DFT/MOB-SCI	-	cc-pVDZ
1^3B_{1u}	2.91	3.41	2.99	2.43,2.96	-	2.958
1^3A_u	2.27	3.55	2.68	2.17,5.11	2.32[86, 109],2.35[87]	3.158
1^3B_{1g}	2.17	3.53	2.63	2.00,4.81	2.28[86], 2.31[87]	3.163
1^1A_u	2.50	3.84	2.80	2.68,5.58	2.48[89]	3.309
1^1B_{1g}	2.50	3.88	2.78	2.49,5.26	2.48[109],2.49[89]	3.326
1^3B_{3g}	3.19	3.82	3.31	2.76,3.29	-	3.666
2^3B_{1u}	-	-	-	4.88,6.49	-	5.135
1^1A_g	4.41	6.17	-	-	-	5.135
1^3A_g	-	-	-	4.95,6.74	-	5.282
3^3B_{1u}	-	-	-	6.42,9.02	-	5.502
1^1B_{3g}	4.19	6.11	4.25	3.80,5.85	4.07[88]	5.907
1^3B_{3u}	-	-	-	5.16,8.61	-	6.153
1^3B_{2g}	-	-	-	5.44,9.13	-	6.158
2^1A_g	5.90	7.04	-	-	-	6.178
1^1B_{3u}	5.15	6.92	5.60	5.38,9.03	-	6.211
1^1B_{2g}	4.80	6.87	-	-	-	6.215
2^3A_u	-	-	-	5.92,10.1	-	6.550
2^3B_{1g}	-	-	-	5.60,9.00	-	6.551
2^1A_u	5.79	7.22	-	-	-	6.700
2^1B_{1g}	5.76	7.22	-	-	-	6.702
1^3B_{2u}	-	-	-	6.76,8.78		6.938
1^1B_{2u}	6.89	8.30	-	6.90,10.1		7.462
1^1B_{1u}	5.15	7.81	5.29	4.88,7.41	5.12[88]	7.783
3^3B_{1g}	-	-	-	6.29,8.09	-	7.854
3^3A_u	-	-	-	-	7.875	8.686
2^1B_{1u}	6.86	9.11	7.91	7.05	7.1[110]	7.950
4^3B_{1u}	-	-	-	6.42	-	7.955
3^1A_g	5.90	7.04	-	-	-	8.229
4^3B_{1g}	-	-	-	6.29	-	8.284
4^3A_u	-	-	-	-	-	8.292
3^1B_{1g}	7.33	8.44	-	-	-	8.336
5^1A_u	7.39	8.97	-	-	-	8.355
2^3B_{3g}	-	-	-	6.64,9.68	-	8.380
2^1B_{3g}	6.53	8.32	-	-	-	8.400
5^3B_{1u}	-	-	-	-	-	8.448
2^3A_g	-	-	-	-	-	8.605
3^3A_g	-	-	-	-	-	8.737
4^1A_g	7.08	9.12	-	-	-	8.766
2^3B_{3u}	-	-	-	6.53,10.4	-	8.845
2^3B_{2g}	-	-	-	6.14,10.6	-	8.849
2^1B_{2g}	5.49	9.37	-	-	-	8.931
2^1B_{3u}	8.01	8.11	-	7.15	-	8.942
3^3B_{3g}	-	-	-	-	-	8.956
3^3B_{3u}	-	-	-	-	-	9.069
3^3B_{2g}	-	-	-	-	-	9.078
2^3B_{2u}	-	-	-	-	6.76	9.079
3^3B_{2u}	-	-	-	-	-	9.377

3.3.2 Scattering model

For the chosen basis set, an R-matrix radius of $a = 13a_0$ was selected as the most appropriate by analysing the radial charge density of the target molecule obtained with the program RADDEN. To be contained within the R-matrix sphere, we estimate that the charge densities should be smaller than $1x10^{-6}$. Figure 3.3 presents the charge densities for eight of the most diffuse orbitals of *p*-BQ, calculated at HF and CASSCF levels.

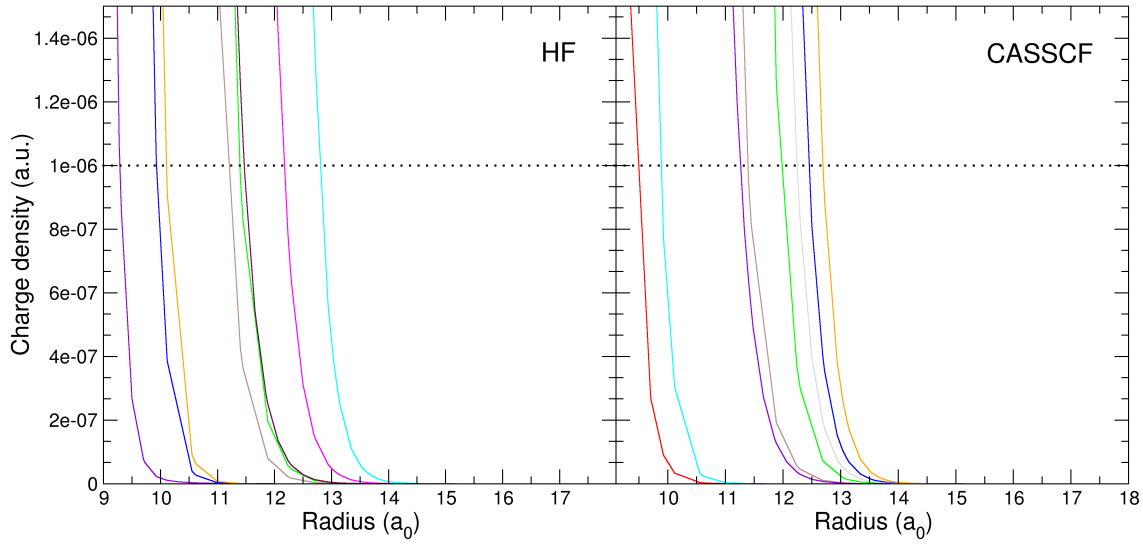

Figure 3.3: Charge densities of the eight most diffuse orbitals calculated at HF and CASSCF levels, using the cc-pVDZ basis set. The black dashed line represents the threshold of $1x10^{-6}$.

The effect of including an extra partial wave ($l_{max} = 5$) in the continuum basis set made a significant difference at higher energies, compared to $l_{max} = 4$, as seen in the cross sections calculated at SE level, plotted in figure 3.4. What would seem to be two broad resonances (when $l_{max} = 4$ is used) become one after adding another partial wave. Therefore, checking the convergence of the partial wave expansion at SE level allowed us to identify nonphysical resonances.

However, using $l_{max} = 5$ is very computational demanding; as the most significant differences are in an energy range we were not interested in (above 8 eV), we choose to use partial waves up to $l_{max} = 4$ in the calculations presented in this chapter.

The number of VOs were chosen in order to provide the best agreement with the literature for the position of the lowest-lying π^*, as described in chapter 2. Figure 3.5 presents the SEP cross sections obtained using different number of VOs (selected in energy order), as we attempt to find the optimal number to use. The effect of increasing the VOs number on the resonances positions and width are clearly visible. The same procedure was performed at CC level, where we had to include all the VOs available (100) to get the best possible description. The influence

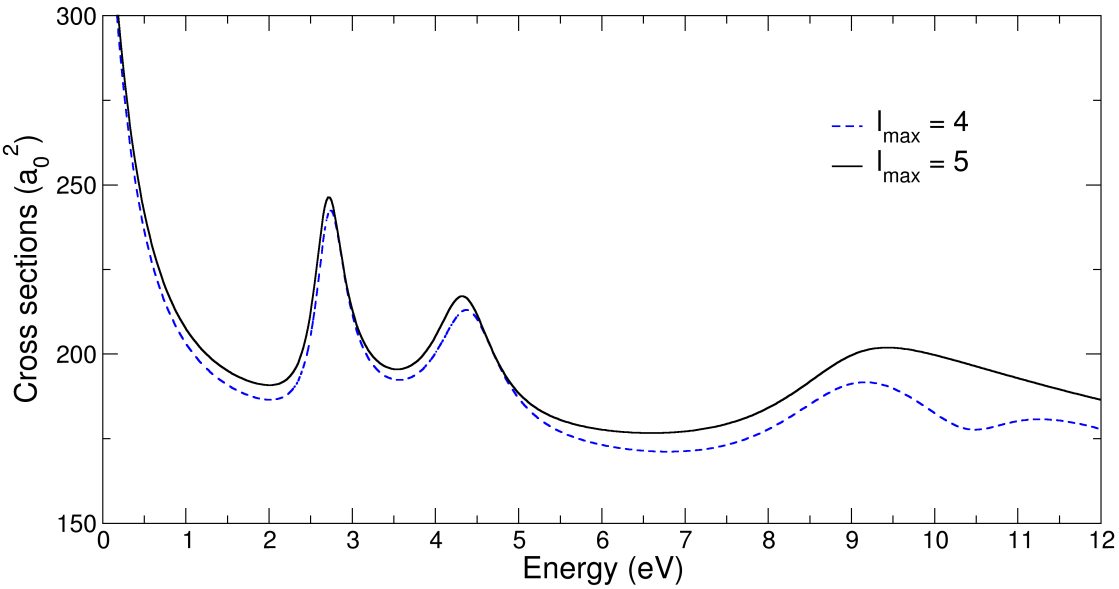

Figure 3.4: Cross sections as a function of electron energy. Both curves were obtained with the same parameters at SE level (cc-pVDZ basis set, 10 VOs, deletion threshold of 10^{-7} and $a = 13a_0$). The dashed blue curve corresponds to the inclusion of partial waves up to $l_{max} = 4$, whereas the solid black line correspond to $l_{max} = 5$.

of the inclusion of more VOs was not so strong in the latter as we observed at SEP level, where the best agreement was found when 35 VOs were included.

We performed our scattering calculations using three models: SE, SEP and CC (introduced in chapter 2, section 2.5). The parameters used in each of these models are listed in table 3.3, as well as the number of orbitals that were kept frozen in each models.

Table 3.3: Parameters used for the SE, SEP and CC calculations presented in the remainder of the chapter.

Approximation	**SE**	**SEP**	**CC**
Basis set		cc-pVDZ	
Radius (a_0)		13	
Highest partial wave (l_{max})		4	
Del.Tresh.		10^{-7}	
No. Target states	1	1	48
No. VOs	10	35	100
Core electrons (N_d)	-	8	22

As we were running *p*-BQ calculations in double precision, no attempt was made to decrease the deletion threshold, and the typical (for a smaller radius) value of 10^{-7} was used. However, in the future, a smaller deletion threshold should be tested to verify the convergence of the results.

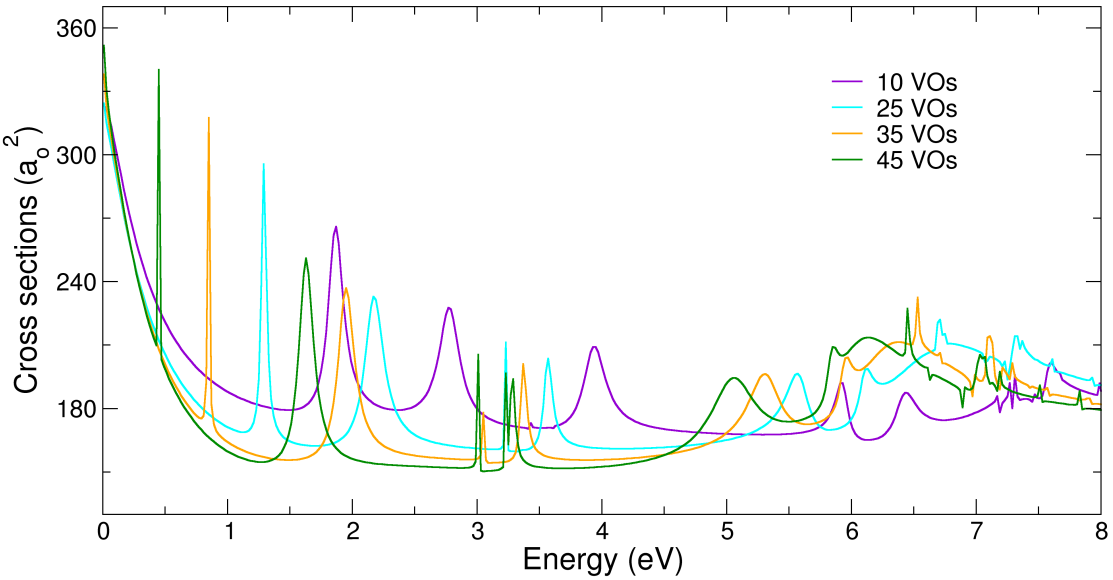

Figure 3.5: Cross sections as a function of electron energy calculated at SEP level, using the same parameters (cc-pVDZ basis set, deletion threshold of 10^{-7} and $a = 13a_0$), except for the number of VOs that is indicated the figure .

As we will demonstrate in chapter 5, changes in the deletion threshold can provide significantly different results, although it does not necessarily mean this would be the case for *p*-BQ.

In the following sections we present and discuss the shape and core-excited resonance we identified for *p*-BQ, as well as our calculated cross sections for both neutral and anion geometries.

3.4 Resonances

As explained in chapter 2, we use the investigation of the eigenphase sums, the cross sections and time-delay analysis to identify resonances. In this chapter we focus mainly on the last two, resorting to the eigenphase sums occasionally.

We will present our results in two main groups: low- and higher-lying resonances. The main reason for this is that the low-lying resonances have been extensively studied in the literature, so a detailed comparison of results can be performed. On the other hand, there is significantly less information available regarding the high-lying resonances.

3.4.1 Low-lying resonances

As just mentioned, the six lowest-lying resonances of *p*-BQ are well known from the literature, especially due to their contribution to the photodetachment process (discussed in detail in

chapter 6) and are the focus of this section. Although the resonances located below the first excitation threshold tend to be of shape character, *p*-BQ reveals the presence of two resonances identified as Feshbach, and two of mixed character.

Figure 3.6 and 3.7 present the time-delays for each of the eight irreducible representations of *p*-BQ, calculated at SE/SEP and CC level, respectively, using the parameters summarized in table 3.3. For these resonance-rich systems, the SE model can be extremely helpful, as it allows the identification of the pure shape resonances, that could be easily confused with the mixed character or shape core-excited ones.

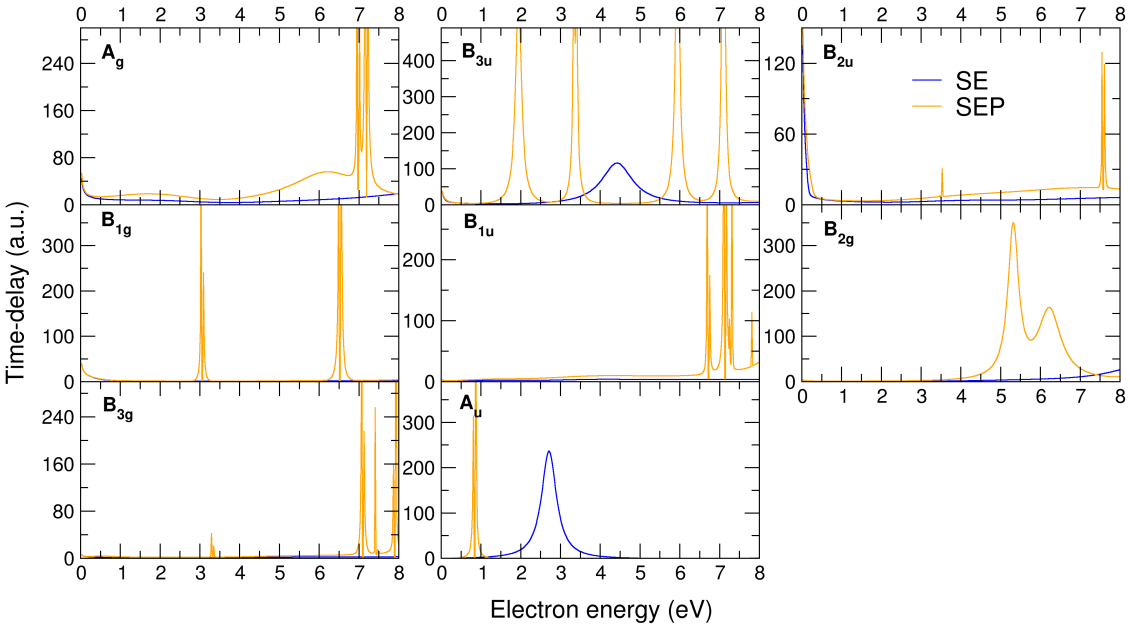

Figure 3.6: Largest eigenvalues of the time-delay matrix for the scattering symmetries indicated in the panels, at SE (solid blue line) and SEP (solid orange line) levels.

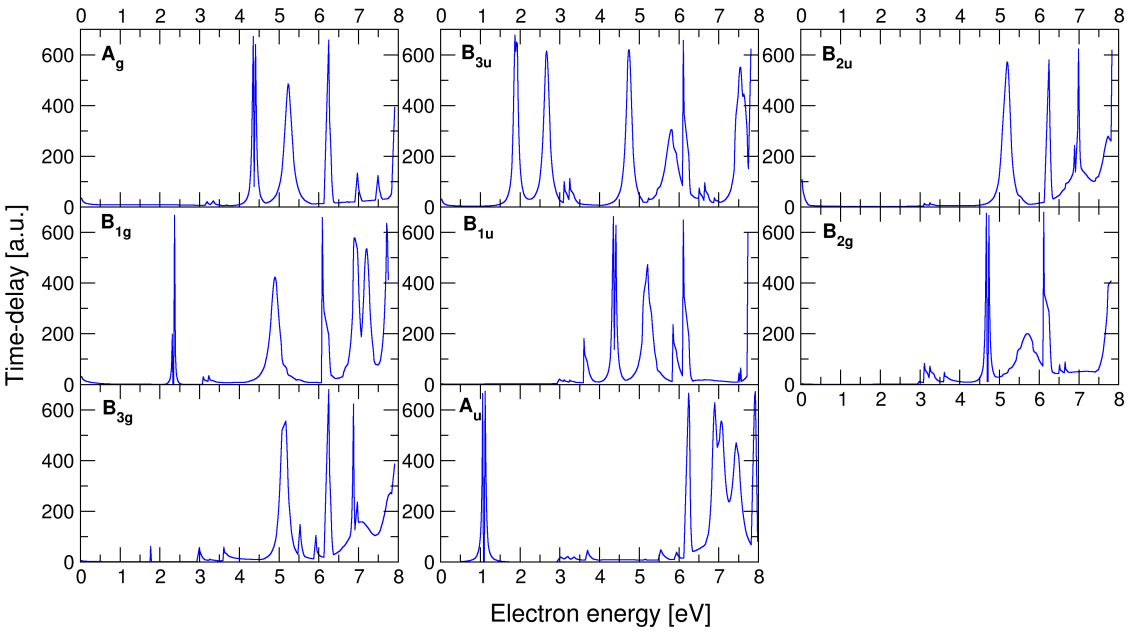

Figure 3.7: Largest eigenvalue of the time-delay matrix for the scattering symmetries indicated in the panels, calculated at CC level. Note that most sharp peaks (that normally appear in more than one symmetry) correspond to excitation thresholds.

Due to the large amount of structure present in the time-delay, we used the cross sections to help to identify (and characterise) the resonances in *p*-BQ. These cross sections calculated at SEP and CC level, are plotted in figure 3.8.

Besides helping in their identification, the analysis of the cross sections can also provide reliable information about the character of the resonances: whether a particular resonance manifests itself in the elastic or inelastic (or both) cross sections is a good indicator of its shape or core-excited character (or mixed), respectively. Later on this chapter, we will present a detailed discussion of the character of all the resonances we have identified.

Looking at the relative resonance positions for each of the models (either in the time-delay or in the cross sections) is also a good "recipe"to infer the resonance character: if a particular resonance shifts to lower energies at SEP level (compared to its position calculated at CC level), we can conclude its description has improved and therefore it has shape character (we know that the SEP model is more appropriate to describe shape resonances than the CC one). On the other hand, when a resonance shifts to lower energies at CC level, then we conclude it possesses some core-excited character, as the inclusion of the electronically excited states in the close-coupling expansion improves its description. These effects have been shown in prior work [111].

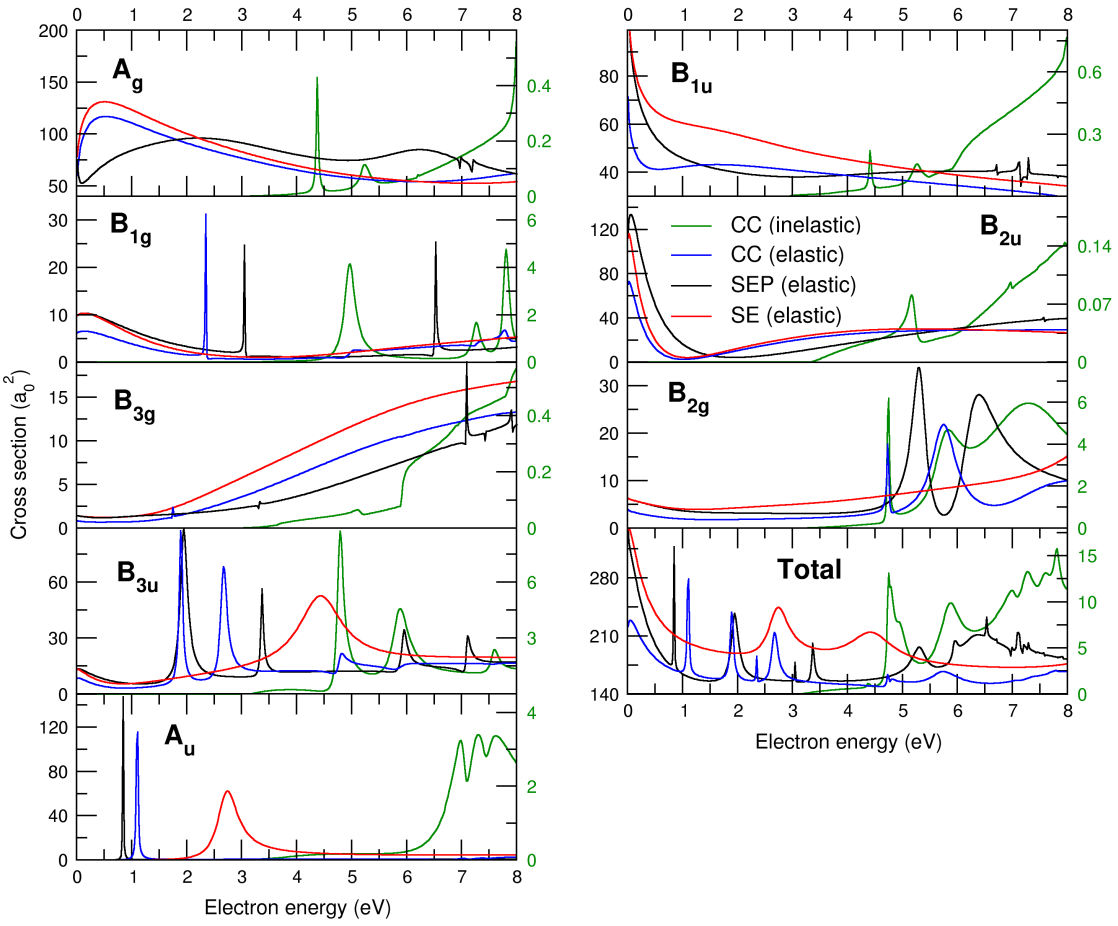

Figure 3.8: Cross sections as a function of electron energy, calculated at SEP and CC level, using the parameters described in table 3.3, for each of the irreducible representations indicated in the panels. The total cross section is shown in the right bottom panel. Note the *y*-axis is scaled for the elastic cross sections on the left, whereas the green labels on the right side of the plots correspond to the inelastic cross sections.

Using the aforementioned methodology, we present in table 3.4 our values for the positions and widths of the six low-lying resonances of *p*-BQ, together with the available theoretical and experimental data.

Table 3.4: Positions and widths (in brackets) in eV of the low-lying resonances of *p*-BQ calculated at SEP and CC levels. Sym: below the former, the symmetry of the resonance ; C: Character. The capital letters mean: S: shape; M: mixed and F: Feshbach. We also list theoretical (Cheng *et al.*[104], West *et al.*[105], Kunitsa and Bravaya [107], Pou-Amérigo *et al.*[102], Honda *et al.*[103]) and experimental (Cooper *et al.*[91], Modelli and Burrow[99] and Allan[97, 98]) data available. The character of the resonances in the corresponding paper is indicated in brackets.

Sym.	E_R (Width) SEP	E_R (Width) CC	C	[104]	[105]	[107]	[102]	[103]	Experiments
1^2A_u	0.85 (0.012)	1.10 (0.030)	S	0.910(S) (0.346)	1.01(S)	0.56 (S)	0.91 (S)	0.83(S)	1.35[91] 1.43[97](S) 1.60[98](S) 1.41[99]
1^2B_{2u}	-	1.70 (8E-4)	F	1.136 (F) (0.014)	1.03 (F)	0.68 (F)	0.96 (F)	1.22 (F)	
1^2B_{3g}	-	1.75 (0.001)	F	0.956 (F) (0.042)	~0.9	0.7 (F)	0.87 (F)	1.09 (F)	
1^2B_{3u}	1.96 (0.159)	1.90 (0.138)	S	1.587 (M) (0.351)	0.68 (S)	1.43 (M)	1.31 (M)	1.79 (S)	0.70[91] 0.72[97](S) 0.77[98](S) 0.69[99]
1^2B_{1g}	3.05 (0.007)	2.35 (0.007)	M	2.099 (F) (0.058)	-	1.73 (F)	1.99 (F)	2.66 (F)	
2^2B_{3u}	3.36 (0.058)	2.67 (0.071)	M	2.332 (M) (0.139)	1.86 (F)	2.14 (F)	1.87 (M)	2.44 (F)	1.90[91] 2.15[97](S) 2.0[98](S)

A general look at table 3.4 points to a very good agreement among the experimental data (the energy spread is ≈0.25 eV) whereas the spread of theoretical results is much broader (up to 1.26 eV). These differences among calculations are due to two main factors that we will discuss within the next paragraphs. According to existing calculations, it seems clear that the symmetry assignation of the first two resonances in the experiments is swapped: the lowest-lying resonance (positioned at ≈ 0.7 eV) has A_u symmetry, and the second (at ≈ 1.4 eV) has B_{3u} symmetry.

The SEP and CC models produce the same resonance order (the Feshbach resonances are, of course, not seen in the SEP calculation). The pure shape resonances tend to appear lower in energy in the SEP calculation (not seen in the first B_{3u} resonance), whereas the mixed shape core-excited resonances are better described by the CC model where the excited parent states of the resonances are included. Therefore, we consider our 'best results' to be a combination of the SEP positions and widths for the shape resonances and the CC ones for the others. The first pure shape resonance (the 1^2A_u) is significantly narrower than shape resonances tend to be, but wider than those identified as pure Feshbach by us in this target. Our calculated width corresponds to a lifetime of around 55 fs, in excellent agreement with the value calculated by Kunitsa and Bravaya [106] of 51 fs. The mixed character resonances (usually the other authors do not identified them as such) have widths of the same order of magnitude as the shape resonances, the 1^2B_{1g} being the narrower.

Our positions for the two pure shape resonances calculated at SEP level are in good agreement with experiments, whereas the mixed character 2^2B_{3u} resonance appears more than 0.5 eV

higher (at CC level) than the highest experimental position. This is not unexpected for two reasons: (i) the potential parent states of this resonance, listed in the next section, are 0.3-0.7 eV higher in our calculations. Consequently, we expect the resonance to be shifted to higher energies by a similar energy factor; and (ii) since this resonance has partly shape character the poorer description of polarisation effects in the CC calculation would also lead to a overestimation of the resonance energy.

The agreement with the theoretical results is harder to rationalise, due to the spread of values. We note that the order of our resonances is consistent with Kunitsa and Bravaya[107] but not with that of West *et al.*[105], Pou-Amérigo *et al.*[102], Honda *et al.*[103] or Cheng *et al.*[104]. For the last three cases, our order corresponds to swapping the Feshbach resonances. We note that when analysing the results of Cheng *et al.* we have chosen, for consistency, to compare with the resonance positions obtained with the LC-TDDFT method (listed at the bottom of their table 3), instead of the ones obtained using the LC-DFT method, that was used to identify only shape resonances. The position of the A_u shape resonance is in good agreement with the majority of the calculations (except the position calculated by Kunitsa and Bravaya [106]), but the width is not (except, again, for Kunitsa and Bravaya [107]): both our SEP and CC calculations produced a much narrower width for this resonance than the one obtained by Cheng's *et al.* [104]. The same tendency is observable for all other resonances, as seen in table 3.4.

This discrepancy between the theoretical results can be attributed to two main reasons: (i) the methods used to perform the calculations - the majority of the calculations were performed using standard quantum chemistry methods, except for the ones of Kunitsa and Bravaya [106, 107] (who used adapted methods to describe the A_u resonance only) and Cheng *et al.* [104] (who used a stabilization method); and (ii) the neutral equilibrium geometry of *p*-BQ used in the calculations. Some of the resonance energies are very sensitive to small changes in the geometry: CC calculations with a geometry optimised at HF level lead to the two shape resonances being 0.21 and 0.48 eV higher whereas the Feshbach ones were 0.61 and 0.71 eV higher; this changes the order of the resonances, locating the second shape and Feshbach resonances at almost the same energy and below the first Feshbach resonance in table 3.4. This might also help explain the differences in the character assignation of the resonances: Kunitsa and Bravaya [107] assign a mixed shape-Feshbach character to the 1^2B_{3u} resonance in the equilibrium geometry of the neutral, but Feshbach character at the anion equilibrium geometry. In our calculations, we find it to have pure shape character. This indicates that the geometries differences can not affect only resonance positions but also their character. Similarly, those resonance we find to have mixed character could become pure shape resonances, for a slightly different geometry. This sensitivity of the resonance spectrum to small changes in geometry has already been highlighted by other authors [105, 107, 112], and is confirmed by our calculations using the equilibrium geometry of the anion molecule, presented in section 3.5.

The two Feshbach resonances we found are below the peaks described in 1999 by Schiedt *et al.* [83]. Six peaks were identified in the energy range of 2.213-2.430 eV that they postulate were likely to correspond to vibrational features of two Feshbach resonances. The parent state of the first Feshbach resonance (1^2B_{2u}) has been easily identified as the lowest excited state, the 1^3A_u,

by looking at the R-matrix poles. This is done by finding the pole energetically closest to the resonance position, and searching for the biggest coefficient of the wavefunction associated to that pole. That coefficient is associated to a specific configuration allowing us to identify the parent state. One should be careful with this method as it implies two rough approximations: the closest pole might be far from resonance, and not describe it particularly well and, in choosing just the main configuration, we are neglecting the contribution of all the other configurations for that state, even though their contribution is smaller). In the case of the second Feshbach resonance, 1^2B_{3g}, the identification of the parent state(s) was not possible. Both our Feshbach resonances are positioned more than 1 eV below the first excitation threshold, which is unusual.

Finding the excited parent state(s) of the mixed character resonances was not a success either: these resonances should have at least two parent states, the ground state and an excited one. However, the identification of potential excited parent states from the configurations of the closest poles was inconsistent with the behaviour of the resonances for calculations with different amount of polarization; and the branching ratios are of no help in this cases either, as Feshbach resonances do not decay to their parent state (since they are energetically below).

3.4.2 High-lying resonances

We now proceed to the discussion of the remaining resonances identified for *p*-BQ.

The SEP calculation revealed the presence of twelve resonances of shape, mixed shape core-excited and core-excited character, identified through the cross section and time-delay analysis (figures 3.8 and 3.6, respectively). Although, as mentioned before, this calculation does not include the excited states of the target molecule, it does include in the $N+1$ wavefunctions some of the configurations required to describe them. Therefore, it is not unusual that we observe signatures of core-excited shape resonances at SEP level. Nonetheless, as described in chapter 2, core-excited resonances are more accurately described when the CC method is used, and some of them are more clearly visible in the inelastic cross section (figure 3.8). The CC time-delay, plotted in figure 3.7, presents, in every symmetry, some structure within the energy range of 3 to 4 eV. Although the presence of Feshbach resonances in this region cannot be excluded, the majority of the structure is due to the five excitation thresholds present in this range (see table 3.2).

Table 3.5 summarizes the resonances positions and widths we have determined, as well as their respective parent state(s). The little available theoretical and experimental data for these resonances is also listed. Not included in the table are the resonances that were detected experimentally, but for which no symmetry assignation has been attempted. For example, Modelli and Burrow identify a core-excited resonance at 2.11 eV, but do not assign it a symmetry. Similarly, they see a band at 5.8 eV that is very likely a resonance. Allan [98] sees a very broad feature around 4.2 eV that he describes as of σ^* character and another one at 5.45 eV. Cooper *et al.*[91] report a broad energy loss peak at 4.35 eV that they state could correspond to electronic excitation of the neutral molecule.

Table 3.5: Positions and widths (in eV), and character of the resonances found in our CC calculations as well as their most likely parent state(s) (P.S.). The capital letters mean: M: mixed shape core-excited; CE: core-excited shape. Earlier theoretical data: Cheng *et al.* [104] (most results quoted are those from their non-averaged calculation; for the 1^2B_{2g} and 2^2B_{2g} resonances we also quote the positions and widths from their table 3. Also shown are their identified parent states.) and data from West *et al.* [105]. Experimental position of first $^2B_{2g}$ resonance: Modelli and Burrow [99] and Allan [98].

Symm.	E_R (Width)	Char.	Most likely P.S.	Cheng *et al.*/other	P.S. (Cheng's)
1^2A_g	4.37 (0.041)	CE	1^1A_u, 1^3A_u, 1^1B_{1g}	3.69	A_u, B_{2g}, B_{2u}
1^2B_{1u}	4.41 (0.043)	CE	1^1B_{1g}, 1^3B_{1g}, 1^1A_u	3.37	B_{3u}, B_{1g}, B_{2u}
1^2B_{2g}	4.74 (0.032)	M	g.s., 1^3B_{3g}	4.24/4.410 (0.397) 4.37[99],4.24[98]	g.s., A_g, B_{1u}
3^2B_{3u}	4.81 (0.133)	M	g.s., 1^3A_u, 1^3B_{3g}	3.58, 2.4[105]	g.s., B_{3g}, B_{2u}, B_{1u}
2^2B_{1g}	4.97 (0.238)	M	g.s., 2^3B_{1u}	4.14	g.s., B_{2u}, B_{1u}, B_{3g}
2^2B_{3g}	5.10 (0.147)	CE	1^1A_u, 1^3A_u, 1^1B_{1g}	4.30	A_u, B_{1u}, B_{1g}
2^2B_{2u}	5.16 (0.169)	CE	1^3B_{1g}, 1^1B_{1g}, 2^3B_{1u}	3.97	A_u, B_{1u}, B_{1g}
2^2A_g	5.24 (0.189)	CE	1^1A_u, 1^3A_u, 1^3B_{1g}	4.06	A_u, B_{2u}, B_{2g}
2^2B_{1u}	5.27 (0.137)	CE	1^3B_{1g}, 1^1B_{1g}	3.82	B_{2u}, B_{3u}, B_{1g}
2^2B_{2g}	5.76 (0.526)	M	g.s., 2^3B_{1u}	5.92/5.910 (0.375)	g.s., B_{1u}
4^2B_{3u}	5.95 (0.316)	M	g.s., 1^3B_{3g}	5.46	g.s., B_{2u}, B_{1u}, B_{3g}
3^2B_{2u}	6.96 (0.039)	CE	1^1A_u, 1^3B_{1g}, 2^1B_{1g}	4.88	A_u, B_{1g}, B_{1u}
2^2A_u	6.99 (0.142)	CE	2^3B_{1u}, 3^3B_{1u}	5.41	B_{2u}, B_{3g}, B_{1u}
3^2B_{3g}	7.08 (0.71)	CE	1^3B_{1g}, 1^1B_{1g}	4.64	g.s., B_{1g}
3^2B_{1g}	7.29 (0.186)	CE	1^3B_{3u}	5.12	B_{2u}, B_{1u}, B_{3g}
3^2A_u	7.31 (0.249)	CE	2^3B_{1u}, 3^3B_{1u}	-	-
5^2B_{3u}	7.62 (0.172)	CE	1^3B_{3g}, 1^1B_{3g}, 2^1A_g	5.87	g.s., B_{2u}, B_{1u}, B_{3g}
4^2A_u	7.62 (0.300)	CE	2^3B_{1u}, 3^3B_{1u}, 1^A_u	-	-
4^2B_{1g}	7.79 (0.096)	M	g.s., 1^3B_{1u}	-	-

Looking at the panel for the A_g symmetry in figure 3.8 we observe in the SEP cross section an extremely broad peak centered slightly above 6 eV, that could correspond to a wide resonance: the corresponding feature is visible in the time-delay (figure 3.6). However, the CC results do not show a structure that could correspond to this one. There is some structure above 6.5 eV in the SEP cross sections, again consistent with some peaks in the time-delay that might be attributed to pseudoresonances. If we look at the inelastic A_g cross section presented in figure 3.8, two clear peaks are visible (and they are also present in the time-delay, figure 3.7) that, since they are absent from the SEP results, we identify as core-excited resonances. These two resonances are then considered physical and therefore are included in table 3.5.

At the SEP level, the B_{3u} symmetry presents four resonances clearly visible in the time-delay. The lowest two are the pure shape and mixed-character resonances already reported in table 3.4 and discussed in the previous section. The higher two resonances appear at lower energies in the CC calculation and the inelastic cross section shows the presence of a fifth resonance. This indicates three resonances that have partial (or whole) core-excited character. The analysis of the branching ratios indicates that the resonance at 4.81 eV is of mixed shape core-excited character. Modelli and Burrow found a resonance of this symmetry at 4.37 eV that possibly corresponds to our third resonance or to the wider one present at 5.95 eV. The calculations presented by West *et al.* [105] locate the third B_{3u} resonance at much lower energy; all of these

resonances are also listed by Cheng *et al.* [104] at lower energies.

The Feshbach resonance of B_{2u} symmetry listed in table 3.4 is neither visible in the CC cross section nor the time-delay with the grid we have used in figures 3.7 and 3.8. An additional calculation with a grid four times finer was necessary to identify and characterize it (the same happens for the $^2B_{3g}$ Feshbach resonance). The cross sections obtained from that calculation are presented in figure 3.9. At higher energies, the SEP calculation only shows the presence of pseudoresonances. The CC calculation shows two resonances at 5.16 eV and 6.96 eV, confirmed by the time-delay, that have pure core-excited character.

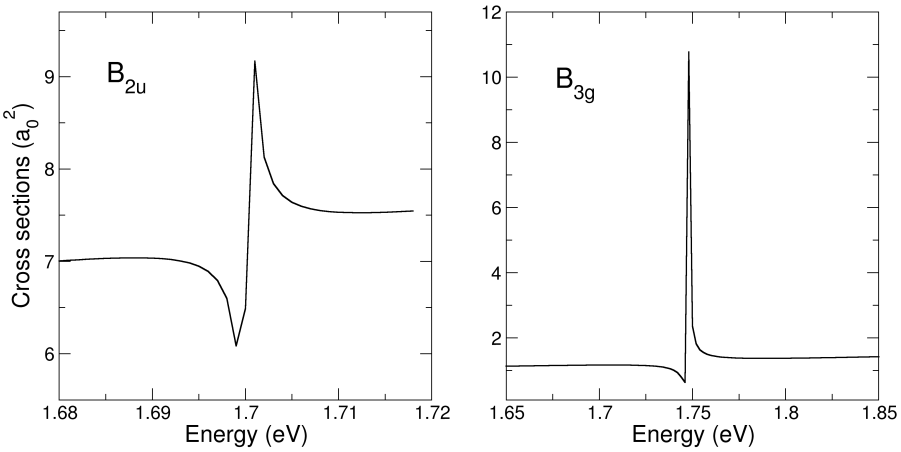

Figure 3.9: Inelastic cross sections as a function of electron energy, calculated at CC level, for the irreducible representations presented in the panels. The energy grid used was of 0.002 eV.

The B_{1g} symmetry has one resonance reported in table 3.4, visible in the elastic cross section and time-delay for both methods. As explained above, the relative positions in both methods points to a mixed character. Taking into account its width, one could argue this should be a Feshbach resonance; the fact that it appears at the SEP level makes us discard that option. The higher peak in the SEP results is most likely a pseudoresonance than a physical resonance. The elastic CC cross section shows a kink at 4.97 eV, more visible as a clear peak in the inelastic cross section, and confirmed by time-delay as a resonance. There are two other resonances at higher energies - 7.29 and 7.79 eV, that could also be identified in the time-delay analysis. These 3 resonances are of pure core-excited character and the last one has not been identified before.

The SEP cross sections for the B_{1u} symmetry show some structure above 6.5 eV that we identified as pseudoresonances. Even though there are no peaks in the elastic CC cross section, the inelastic one presents two peaks at 4.41 and 5.27 eV with the corresponding peaks visible in the time-delay. These resonances are assigned as pure core-excited and are also observed by Cheng *et al.* [104].

The B_{2g} symmetry presents two clear resonances in the elastic cross section of mixed shape core-excited character, as evidenced by the shifting of their positions observed between models.

In the inelastic cross section, it is possible to observe a third broad feature centred slightly above 7 eV that we cannot conclusively identify as a physical resonance: the corresponding feature in the time-delay would be very wide and low and is possibly hidden by the presence of other features. Three resonances of this symmetry are identified by Cheng *et al.*: a shape one at 5.5 eV and two core-excited ones at 4.410 and 5.910 eV. The widths of these resonances are very different to ours (see table 3.5). Since the authors used two different methods to identify shape and core-excited resonances, we think it is possible they observed the same (mixed character) resonance at two different energies. One would tend to assume the resonances identified at 5.5 eV and 5.910 eV correspond to the same resonance due to their energy proximity.

It is important to highlight that *p*-BQ has a bound state of B_{2g} symmetry. For the neutral geometry, West *et al.* positioned the bound state 1.48 eV below the neutral ground state, whereas Kunitsa and Bravaya locate it 1.75 eV below. In our calculations, the lowest pole for the corresponding symmetry, which gives a reasonable estimate of the bound state energy, is 1.57 eV below the ground state. The resonance positions calculated using the anion geometry are presented in section 3.5.

The B_{3g} symmetry presents no pure shape resonances. The barely visible structure at 1.75 eV in the elastic CC cross section, also visible in the time-delay for this calculation, corresponds to the resonance reported in table 3.4 and clearly visible in the right hand panel of figure 3.9. Its narrow width indicates that it is likely to be a Feshbach resonance. The other peak in the SEP cross section (at around 7 eV) is almost certainly a pseudoresonance. The CC time-delay shows two clear resonances at 5.12 eV and 7.05 eV (the other structure corresponds to thresholds) and those can be seen as very small bumps in the inelastic cross section. We then identified these as physical resonances.

The last symmetry is the A_u, the symmetry of the lowest energy resonance for *p*-BQ, that has pure shape character and is reported in table 3.4. This resonance is the most extensively described in the literature. Our CC calculations also reveal the presence of three core-excited resonances at 6.99, 7.31 and 7.62 eV, clearly visible in both inelastic cross section and time-delay.

Table 3.5 lists the resonance positions obtained by Cheng's *et al.* (three resonances identified by them are not included in this table as they do not correspond to any of ours). The link between theirs and our resonances has been done on symmetry and energy order. The disagreement is significant, both in terms of the absolute and relative position of the resonances, which is not unexpected: we expect our calculations to overestimate the position of the resonances and, indeed, most of the ones reported by Cheng *et al.* appear at lower energies. In addition, and as we already mentioned, it is possible that we may have missed some Feshbach resonances that, being very narrow and close to an excitation threshold, are very hard to identify, either in the cross section or the time-delay.

As stated before, the parent states of the resonances were determined using the branching ratios obtained from the time-delay analysis. This procedure was adopted for all the resonances that are not of Feshbach character. Our character assignation is consistent with that of Cheng's *et al.*, except for one resonance that appears in our calculation at 7.08 eV and that we characterise as shape core-excited, whereas they identify it as of mixed character. In terms of the parent

states of the resonances, we found a good agreement for some of the resonances, but not others, as can be seen from table 3.5.

3.4.3 Link to DEA results

Understanding the way our calculated resonances link with the DEA spectra is one of the most challenging and important parts of our work, especially in this case, due to the biological relevance of *p*-BQ derivatives. Pshenichnyuk *et al.* [113] and Khvostenko *et al.* [114] performed DEA studies on *p*-BQ (the former looked at the temperature dependence of this process). Table 3.6 presents their *mass/charge* ratios, as well as the position of the maximum of the ion yield peaks and relative intensities. An attempt to link their results with ours is also made, up to 5 eV. Due to the large amount of peaks/resonances identified above that region, it becomes impossible to make any conclusive links.

Table 3.6: DEA peaks and respective *m/z* ratios and intensities from Pshenichnyuk *et al.* [113] and Khvostenko *et al.* [114], together with the resonances in our calculations most likely to lead to each of the DEA peaks, calculated at CC level.

Khvostenko [114]			Pshenichnyuk [113]		This work	
m/z	Max.(eV)	Int.(%)	Max.(eV)	Int.(%)	Resonance	Position (eV)
108	1.36	≈50	1.4	100	1^2A_u	1.10
	1.56	100			1^2B_{2u},1^2B_{3g}	1.70,1.75
107	1.70	0.066			1^2B_{3u}	1.90
	4.86	0.067			2^2B_{1g},2^2B_{3g},2^2B_{2u}	4.97,5.10,5.16
					2^2A_g,2^2B_{1u}	5.24,5.27
94	1.26	0.14			1^2A_u	1.10
93	1.78	0.006			1^2B_{3u}	1.90
82	4.96	0.126	4.7	0.15	2^2B_{3g},2^2B_{2u},2^2A_g	5.10,5.16,5.24
					2^2B_{1u},2^2B_{2g}	5.27,5.76
81	2.38	0.012			1^2B_{1g}, 2^2B_{3u}	2.35, 2.67
80	2.34	0.217	2.0	0.12	1^2B_{1g},2^2B_{3u}	2.35, 2.67
79	5.04	0.630	4.8	0.65	2^2A_g,2^2B_{1u}	5.24,5.27
					2^2B_{2g},4^2B_{3u}	5.76,5.95
72	1.42	0.052			1^2B_{2u},1^2B_{3g}	1.70,1.75
70	1.42	0.065			1^2B_{2u},1^2B_{3g}	1.70,1.75
50	1.70	0.025			1^2B_{3u}	1.90

As seen from table 3.6, some resonances are more easy to relate to the DEA peaks than others, due to their energy proximity. This is the case for the ^2A_u and 1^2B_{3u}, whose positions are more separated than the ones observed, for example, for the $1B_{2g}$ and $3B_{3u}$ resonances. We believe the DEA peaks observed at 4.7 and 4.8 eV arise from the same resonance, and therefore, we believe they are linked to either of the 1^2B_{2g} or 3^2B_{3u} resonances (found at 4.74 and 4.81 eV at CC level, respectively). However, as energy increases, the more complicated this task becomes, due to the large number of resonances *p*-BQ has, and because they are very close in energy. As a consequence, we could not link the DEA data with ours.

As mentioned, our calculations tend to overestimate resonance positions; therefore, although it is possible that the DEA peaks located at 1.26 and 1.36 eV correspond to the A_u resonance calculated at 1.10 eV, they could also be linked to some vibrational resonances.

In fact, we made the links shown in table 3.6 taking into account the energy proximity between our resonance positions and the peaks obtained in the DEA experiment.

As a first attempt to understand whether our resonances are dissociative with respect to hydrogen loss, (m/z=107), we performed SEP calculations stretching a single C-H bond (this reduced the molecule symmetry to the C_s point group). We have chosen to study this specific bond cleavage because it is the only one where the molecule remains in a planar geometry, and therefore, the calculations are more easily performed. Since the loss of symmetry increased the computational cost, the calculations could only be performed at SEP level.

We analysed the eight lowest-lying resonances ($1A_u$, $1B_{3u}$, $1B_{1g}$, $2B_{3u}$, $1B_{2g}$, $3B_{3u}$ and $2B_{2g}$) described at SEP level for two basis sets (compact and more diffuse): the resonance positions as a function of one of the C-H distance are presented in figure 3.10.

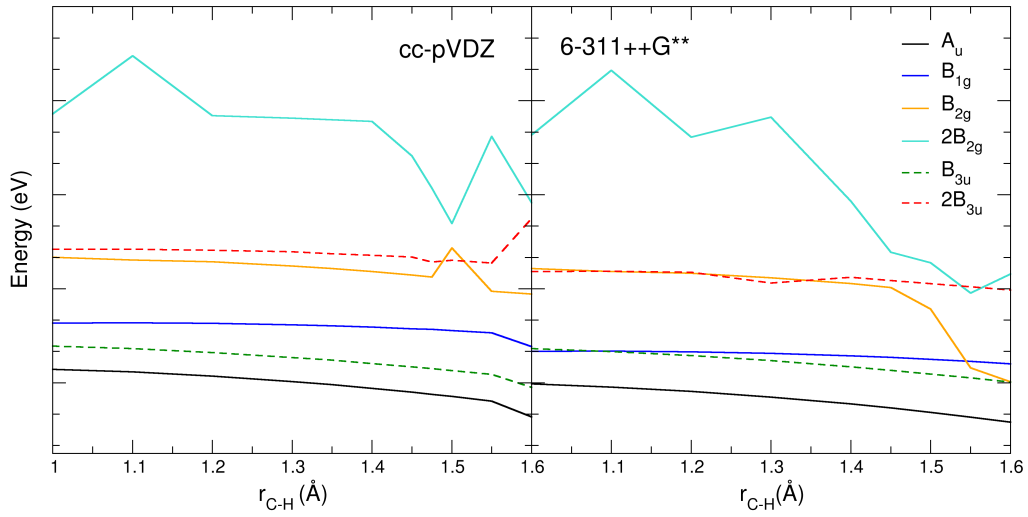

Figure 3.10: Resonance energy as a function of C-H distance (in angstroms) for two basis sets, calculated at SEP level. The C-H bond length in the equilibrium geometry is 1.095 Å. Please note the y-axis is not to scale: as the variation of the resonance positions with r_{C-H} is very small, we shifted some curves down to provide a better overview. The curve corresponding to the A_u resonance remained unaltered; the remaining curves were shifted down as follows: B_{3u} 1 eV, B_{1g} 2 eV, B_{2g} 3 eV, $2B_{3u}$ 2 eV and $2B_{2g}$ 3 eV. For simplicity, and because the $1B_{2g}$ and $3B_{3u}$ behaved completely non-dissociative (as the $1A_u$, $1B_{3u}$, $1B_{1g}$ and $2B_{3u}$ do) we decided to omit their respective curves.

The most noticeable fact in figure 3.10 is the behaviour of both resonances of B_{2g} character, that suggest the presence of an avoided crossing at 1.5 Å for the compact basis set; more points would be needed to provide any conclusions. In the absence of a more defined curve, we

can present two possibilities of which resonance would lead to dissociation, depending on the "width"of the avoided crossing: if it is sufficiently wide, the electron on the lower curve (corresponding to the B_{2g} resonance) would have a smaller probability to "jump"to the upper curve corresponding to the $2B_{2g}$ resonance; on the other hand, if the avoided crossing is narrow enough, the electron would easily move to the $2B_{2g}$ resonance, that would be the responsible for the dissociation process. Although we cannot provide a conclusive picture on this dissociation mechanism, we hypothesize that the the $2B_{2g}$ resonance is the one that leads to the hydrogen-loss, as it is in agreement with the DEA peak reported by Khvostenko *et al.* [114] at 4.86 eV, as shown in table 3.6 (taking into account the overestimation of our resonance positions). Using the more sophisticated CC method to run these calculations could be helpful, but the loss of symmetry makes the calculations very computationally demanding.

3.5 Low energy electron collisions with *p*-BQ in its anion equilibrium geometry

As mentioned in the introduction to this chapter, we have also performed electron scattering calculations using the anion geometry of *p*-BQ, as we are particularly interested in the photodetachment process from *p*-BQ - therefore, starting with the anion geometry is the most sensible choice. These results are presented and discussed in this section. We reiterate that the calculations have been performed for electron scattering from the neutral *p*-BQ.

The role of *p*-BQ in electron transfer reactions is well established, as stated in the beginning of this chapter. Therefore, studying the properties of *p*-BQ anion has received the attention of many scientists in the last few years, as a way to obtain insights into these reactions. In this section, as we have done in the previous, we will briefly review prior studies regarding the *p*-BQ anion.

Horke *et al.* [112] used time-resolved photoelectron spectroscopy and *ab initio* calculations to show the ability of *p*-BQ to retain an electron instead of autodetach. The authors excited the *p*-BQ anion using a laser and showed these excited states decay on a sub-40 fs timescale through a series of conical intersections with lower-lying excited states (that are, actually, resonances). Ultimately, these resonances decay to the ground anionic state, avoiding autodetachment. These studies confirmed once more the ability of *p*-BQ to capture and retain electrons. Their work served as a starting point to our photodetachment studies presented in chapter 6.

3.5.1 Calculation details

In our calculations we have used the anion geometry described by Kunitsa and Bravaya [107]. The bond lengths for both neutral and anionic equilibrium geometries are shown in table 3.7, the differences are very small between geometries. The anion has also a planar structure and therefore belongs to the D_{2h} point group. The internal angles remain unchanged.

Table 3.7: Bond lengths (in Å) of *p*-BQ and *p*-BQ$^-$ in their respective equilibrium geometries.

Bonds	^1A_g	$^2B_{2g}$
C=O	1.2332	1.2633
C=C	1.3579	1.3790
C-C	1.4889	1.4497

In the same way we did for the neutral geometry of *p*-BQ, we used the HF and the SA-CASSCF methods to generate the target orbitals, using the same CAS model: an active space of (12,10) and 8 states averaged (the same used before for the neutral geometry of *p-BQ*, refer to section 5.3.1). The scattering models used were also the same (see table 3.3), in order to provide a like-with-like comparison. We did not test the effect of other basis sets and CAS models for this geometry.

The comparison of the vertical excitation thresholds between the neutral and anion geometries is presented in table 3.8. As far as we know, there are no calculations of the electronically excited states for the neutral system using its anion geometry.

Table 3.8: Vertical excitation thresholds obtained in this work from CASSCF calculations. The active space ((12,10)) and state-averaging (8 states: 1^1A_g, 1^1B_{3u}, 1^1B_{1g}, $1-2^1B_{1u}$, $1-2^1B_{3g}$ and 1^1A_u) were the same for both geometries, and was described before. ES stands for Excited State, whose energies are presented in eV.

ES	Neutral Geom.	Anion Geom.	ES	Neutral Geom.	Anion Geom.
1^3B_{1u}	2.958	2.391	2^1B_{1u}	7.950	7.493
1^3A_u	3.158	2.599	4^3B_{1u}	7.955	7.366
1^3B_{1g}	3.163	2.648	3^1A_g	8.229	7.649
1^1A_u	3.309	2.714	4^3B_{1g}	8.284	7.561
1^1B_{1g}	3.326	2.764	3^3A_u	8.292	7.595
1^3B_{3g}	3.666	3.337	3^1B_{1g}	8.336	7.631
2^3B_{1u}	5.135	4.112	4^1A_u	8.355	7.680
1^1A_g	5.135	4.111	2^3B_{3g}	8.380	7.945
1^3A_g	5.282	4.852	2^1B_{3g}	8.400	7.959
3^3B_{1u}	5.502	5.137	5^3B_{1u}	8.448	7.838
1^1B_{3g}	5.907	5.174	2^3A_g	8.605	7.906
1^3B_{3u}	6.153	5.492	3^3A_g	8.737	7.968
1^3B_{2g}	6.158	5.524	4^1A_g	8.766	8.097
2^1A_g	6.178	5.298	2^3B_{3u}	8.845	8.301
1^1B_{3u}	6.211	5.492	2^3B_{2g}	8.849	8.289
1^1B_{2g}	6.215	5.572	2^1B_{2g}	8.931	8.360
1^3A_u	6.550	5.910	2^1B_{3u}	8.942	8.386
2^3B_{1g}	6.551	5.890	3^3B_{3g}	8.956	8.422
2^1A_u	6.700	6.052	3^3B_{3u}	9.069	8.518
2^1B_{1g}	6.702	6.043	3^3B_{2g}	9.078	8.537
1^3B_{2u}	6.938	6.217	2^3B_{2u}	9.079	8.610
1^1B_{2u}	7.462	6.671	3^3B_{2u}	9.377	8.642
1^1B_{1u}	7.783	7.240			
3^3B_{1g}	7.854	7.024			
2^3A_u	7.875	7.071			

As seen in table 3.8, the electronically excited states for the anion geometry are all lower than for the neutral geometry, and, especially as energy increases, their order changes too. This is the

reason why the core-excited or mixed character resonances are also shifted to lower energies, in general, and some of them are even swapped, as we shall see later on this chapter.

For this geometry, we have also performed SEP and CC calculations, using the parameters summarized in table 3.3 for each of the methods. Our results are presented next.

3.5.2 Resonances for the *p*-BQ anion equilibrium geometry and comparison with the neutral geometry

The time-delay analysis and the comparison between the SEP and CC cross sections were also used here as the tools to identify and characterise resonances. The eigenphase sums were used occasionally.

Figures 3.11 and 3.12 show the time-delay calculated at SEP and CC level, respectively. The similarities with the ones obtained for the neutral geometry are evident, as expected from the analysis of the electronically excited states. However, we can spot the presence of more resonances at higher energies than the ones listed in table 3.5; we can hypothesize this observation is due to the shifting the resonances present: if we increased our energy window for the neutral geometry, we would probably see these "new"resonances we are describing here for this geometry.

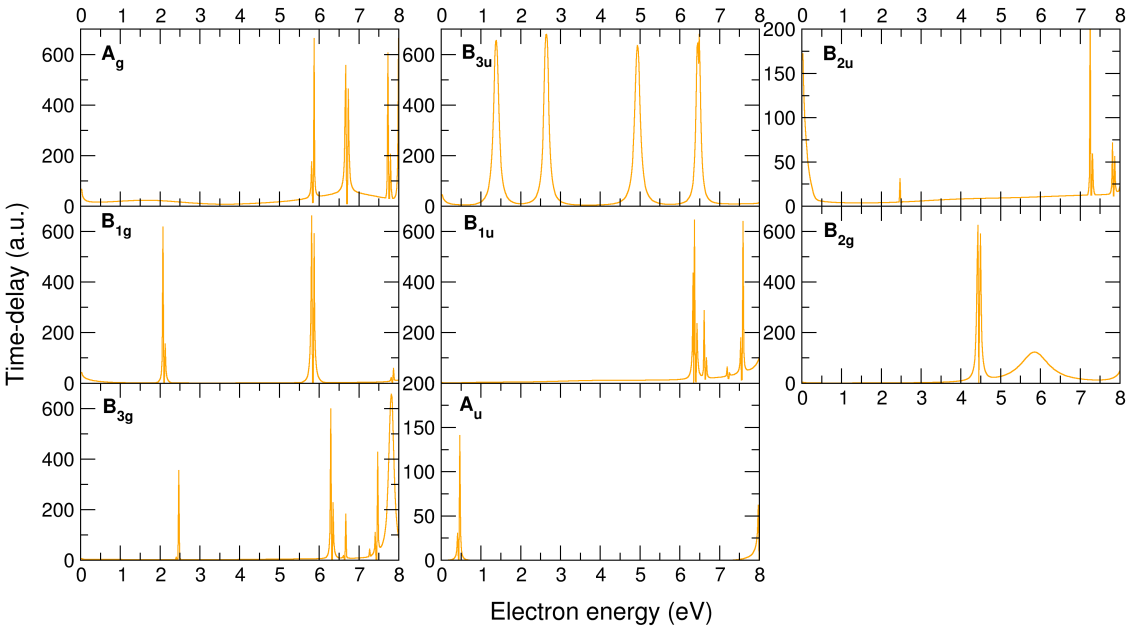

Figure 3.11: Eigenvalues of the time-delay matrix for the scattering symmetries indicated in the panels calculated at SEP level for the anion geometry.

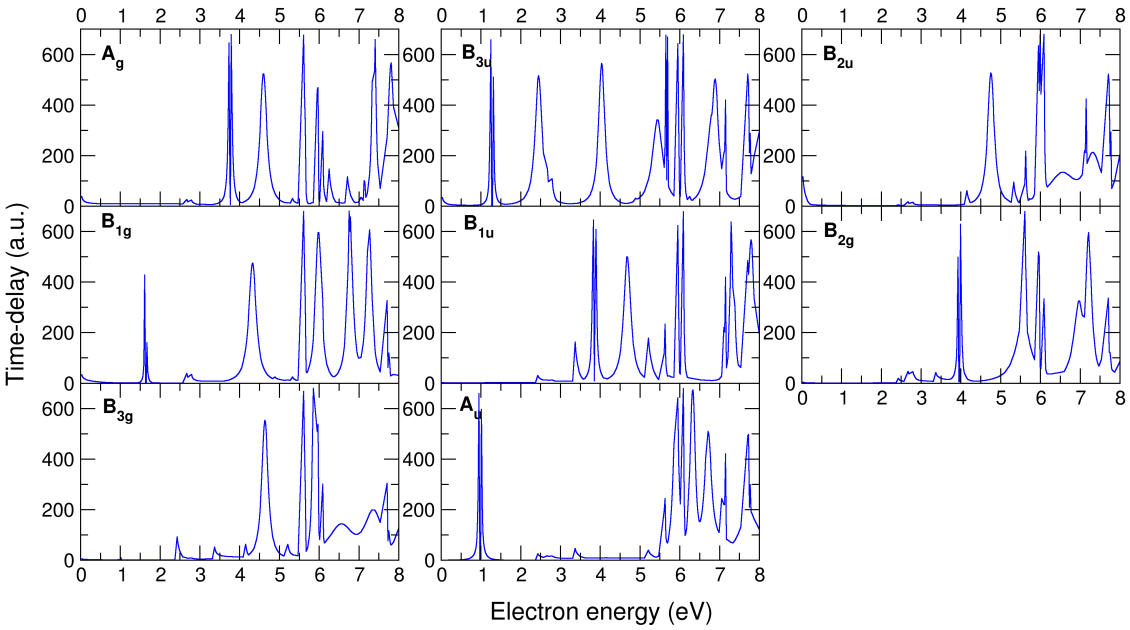

Figure 3.12: Eigenvalues of the time-delay matrix for the scattering symmetries indicated in the panels calculated at CC level for the anion geometry. Note that most sharp peaks (and the truncated ones) correspond to thresholds.

From the analysis of the time-delays and the comparison with the previous data for the neutral geometry, we identified below 8 eV a total of 31 resonances of different character, more than for the neutral geometry.

Table 3.9 lists resonance positions and widths of the well known six low-lying resonances for both geometries, at SEP and CC level. Also presented are the corresponding theoretical results found in the literature.

Table 3.9: Positions and widths (in brackets, below the former), both in eV, of the six low-lying resonances of *p*-BQ, calculated using its neutral (^1A_g) and anion ($^2B_{2g}$) geometries, at SEP and CC levels. The results presented for the neutral geometry were already shown (table 3.4) and discussed in the previous section. "Sym."indicates the symmetry of the resonance; and "Char."the respective character. The capital letters mean: S: shape; M: mixed shape core-excited and F: Feshbach. We also list theoretical work of: Kunitsa and Bravaya [107], Horke *et al.* [112], West *et al.* [105], Honda *et al.* [103] and Pou-Amérigo *et al.* [102]. The resonance positions presented by these authors were calculated using the ground state anion geometry.

Sym.	^1A_g			$^2B_{2g}$			Theory ($^2B_{2g}$ geometry)
	SEP	CC	Char.	SEP	CC	Char.	
1^2A_u	0.85	1.10	S	0.45	0.97	S	0.38 [107],0.25 [112],0.75 [103],0.86 [102]
	(0.012)	(0.030)		(0.001)	(0.020)		
1^2B_{2u}	-	1.70	F	2.46	0.85	M	0.4 [105],-0.03 [107],0.19 [112],0.32 [103],0.27 [102]
		($8E^{-4}$)			($6.5E^{-4}$)		
1^2B_{3g}	-	1.75	F	2.45	0.99	M	0.4 [105],0.06 [107],0.42 [103],0.29 [102]
		(0.001)			($7.9E^{-4}$)		
1^2B_{3u}	1.96	1.90	S	1.38	1.27	S	1.0 [105],0.76 [107],0.15 [112],0.43 [103],0.84 [102]
	(0.159)	(0.138)		(0.116)	(0.138)		
1^2B_{1g}	3.05	2.35	M	2.09	1.62	M	0.90 [107],0.54 [103],1.29 [102]
	(0.007)	(0.007)		(0.005)	(0.005)		
2^2B_{3u}	3.36	2.67	M	2.64	2.46	M	1.2 [105], 2.08 [107],1.54 [103],1.6 [102]
	(0.058)	(0.071)		(0.096)	(0.022)		

From the analysis of table 3.9, we observe that the resonances appear in general lower in energy for the anion geometry: the differences can go from 0.2 eV to almost 1 eV (comparing the same models for both geometries). As expected when a resonance goes down in energy, their widths are also affected and get narrower. What is very interesting, however, is the presence of the two (previously identified as Feshbach) resonances of B_{2u} and B_{3g} symmetry in the SEP calculations for the anion geometry, that were absent when the neutral geometry was used. Although they appear significantly above than in the CC calculations, the fact that they are seen at SEP level denotes an increase of their shape character, and therefore can no longer be classified as Feshbach.

Interestingly, Kunitsa and Bravaya [107] and West *et al.* [105] report that the B_{2u} Feshbach resonance in the anion equilibrium geometry becomes bound by 0.03 and 0.52 eV, respectively.

Figure 3.13 schematises the resonance positions listed in table 3.9 for both geometries. This figure gives us a better perspective of how much the resonant spectrum is influenced by the geometry used in the calculations, even if those changes are of the order of 10^{-2}Å , as can be seen in table 3.7. We believe this observation explains the lack of a consistent resonant spectrum for *p*-BQ in the literature, as different bondlengths were used in different calculations. Although it is not shown in figure 3.13. we have just discussed the changes in the character of some resonances, depending on the geometry.

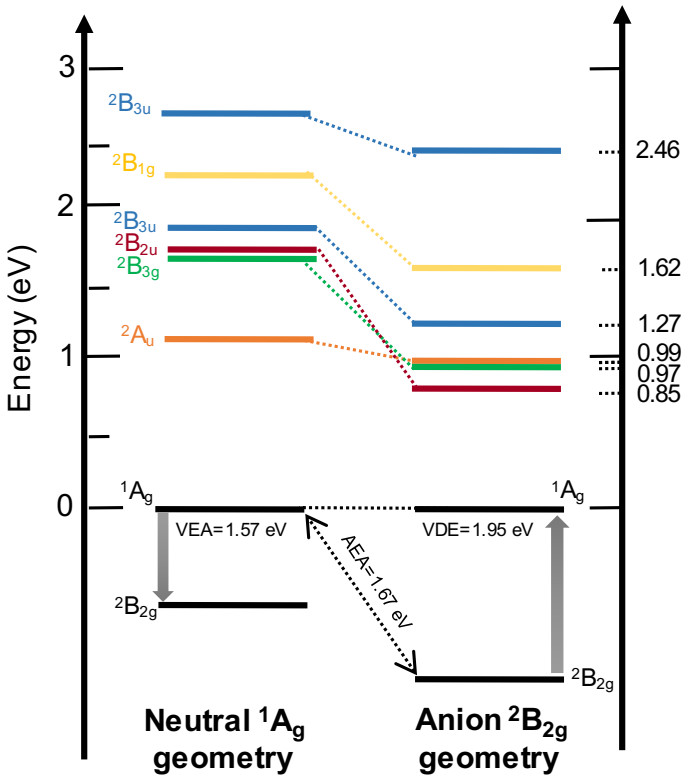

Figure 3.13: Resonance positions (in eV) for the neutral (left side) and anion geometry (right side), calculated at CC level. Also presented are the vertical detachment energy (VDE), the vertical electron attachment (VEA) and the adiabatic electron attachment (AEA), estimated by us. The coloured horizontal lines correspond to resonances, with the energies for the anion geometry in the *y*-axis.

To calculate the absolute energy of the $^2B_{2g}$ state (in both geometries), we have used MOLPRO [70]: the calculations included an extra electron (in a total of 57) and were performed at CASSCF level using the same model as for the ^1A_g state (basis set, active space and state-averaging). As the model was not optimized for this state, one would expect that our calculated energies might be overestimated.

The VDE and AEA of *p*-BQ have been reported by several groups, and we present these values in table 3.10 (for completeness), along with ours. The VDE is defined as the smaller transition energy from the anionic ground state to the neutral, retaining its geometry; the VAE is the inverse process - corresponds to the energy of the vertical transition from the neutral ground state to the anion; and the AEA is the adiabatic electron affinity, that is basically the energy difference between both ground states in their equilibrium geometries.

Table 3.10: VDE and AEA (both in eV) for the *p*-BQ anion. Also presented are the calculated values from Kunitsa and Bravaya [107], Horke *et al.* [112], Honda *et al.* [103] (computed at CASPT2 level) and Pou-Amérigo *et al.* [102].

	CASSCF	[107]	[112]	[103]	[102]
VDE	1.95	2.17	1.98	1.86	1.96
AEA	1.67	1.97	2.04	2.01	-

From table 3.10, we can observe a better agreement between the literature for the AEA energies, whereas for the VDE the energy spread is bigger. On the other hand, our calculated VDE is in excellent agreement with the literature, whereas the AEA is lower by, at least, 0.3 eV.

As mentioned, our calculations were optimized for neutral *p*-BQ in the equilibrium neutral geometry (A_g), and no attempt of optimization was performed for the states in the anion geometry or the anion bound state ($^2B_{2g}$) in the neutral geometry. It is then expected that the description of these states is poor, and therefore, the respective energies are overestimated. This unbalanced description of states makes our calculated VDE to be in agreement with the literature (as both ^1A_g and $^2B_{2g}$ in the anion geometry are overestimated), whereas the AEA is smaller than the literature (as the ^1A_g state for the neutral geometry is well described and its energy is accurate, but the $^2B_{2g}$ for the anion one is overestimated).

For completeness (and because there is no information in the literature to compare with), we present the comparison between the high-lying resonances found with the anion and neutral geometries.

Table 3.11: Positions and widths (in eV), and character of the resonances found in our CC calculations for the neutral and anion equilibrium geometries of *p*-BQ. The capital letters mean: M, mixed shape core-excited; CE, core-excited shape. The resonances labelled with ^{T} are only visible in the time-delay and therefore had their width determined by fitting those curves with the Breit-Wigner formula. The remaining resonances were fitted by an automated procedure in the RESON program (see chapter 2, section 2.6.1), that fits the eigenphase sums.

Symm.	Neutral Geom.		Anion Geom.	
	E_R (Width)	Char.	E_R (Width)	Char.
1^2A_g	4.37 (0.041)	CE	3.77 (0.035)	CE
1^2B_{1u}	4.41 (0.043)	CE	3.85 (0.188)	M
1^2B_{2g}	4.74 (0.032)	M	3.97 (0.022)	M
3^2B_{3u}	4.81 (0.133)	M	4.06 (0.159)	M
2^2B_{1g}	4.97 (0.238)	M	4.35 (0.203)	M
2^2B_{3g}	5.10 (0.147)	CE	4.62 (0.163)	CE
2^2B_{2u}	5.16 (0.169)	CE	4.71 (0.176)	CE
2^2A_g	5.24 (0.189)	CE	4.60 (0.177)	CE
2^2B_{1u}	5.27 (0.137)	CE	4.68 (0.188)	CE
2^2B_{2g}	5.76 (0.526)	M	5.61 ($\approx$ 0.5)^T	M
4^2B_{3u}	5.95 (0.316)	M	5.44 (0.315)^T	M
5^2B_{3u}	-	-	5.66 ($\approx$ 0.05)^T	CE
3^2B_{2u}	6.96 (0.039)	CE	-	-
2^2A_u	6.99 (0.142)	CE	6.30 (0.109)	CE
3^2B_{3g}	7.08 (0.71)	CE	6.56 (0.780)^T	CE
3^2B_{1g}	7.29 (0.186)	CE	6.80 ($\approx$ 0.19)^T	M
3^2A_u	7.31 (0.249)	CE	6.71 (0.225)^T	CE
6^2B_{3u}	7.62 (0.172)	CE	6.91 (0.164)	CE
3^2B_{2g}	-	-	6.97 (0.331)^T	CE
4^2B_{2g}	-	-	7.21 (0.185)	CE
4^2B_{1g}	7.79 (0.096)	M	7.25 (0.191)^T	M
3^2B_{1u}	-	-	7.33 ($\approx$ 0.12)^T	CE
3^2A_g	-	-	7.38 (0.105)	CE
4^2B_{3g}	-	-	7.36 (0.630)^T	CE
4^2A_u	7.62 (0.300)	CE	7.72 ($\approx$ 0.45)^T	CE

Once again, the resonances found for the anion geometry are shifted to lower energies compared with those for the neutral one, which is expected given what we had observed in table 3.8. It is interesting, however, that the resonances do not shift by the same amount for the same irreducible representation. A very clear example is seen in the B_{2g} symmetry, where the first resonance moves around 0.8 eV, whereas the second one only shifts 0.15 eV. This is suggesting the second resonance is linked to a bond of similar size in both geometries, whereas the first one clearly is being more affected by the geometry used.

These calculations revealed the presence of more resonances than for the neutral geometry (mainly above 7 eV), in the same energy range (0-8 eV). This might be due to two reasons: (i) the fact that, as the resonances are shifted to lower positions for the anion geometry, they will appear above 8 eV for the neutral one and we are not seeing them; or (ii) they are actually not present for the neutral geometries. We believe the latter is highly unlikely, as the appearance of new resonances should not be linked with bond stretching/shrinking (unless it changes the orbitals

significantly). Further calculations with a broader energy range would be recommended to clarify this point.

Similarly to what we have observed for the low-lying resonances, some of these resonances changed their character between geometries, whereas their widths are consistent.

3.6 Cross sections

In this section, we present integral and differential elastic, electronically inelastic and total cross sections in the 0 to 8 eV energy range, for both *p*-BQ geometries studied in this work. The cross sections for the neutral ground state geometry are experimentally measurable, whereas the cross sections for the anion geometry are presented mainly for comparison. When available, we compare with other studies.

As *p*-BQ has no dipole moment, no Born correction is included in these cross sections.

3.6.1 Integral cross sections

Figure 3.14 presents the integral elastic cross sections, calculated at SEP and CC level, for each scattering symmetry, and for the sum of them.

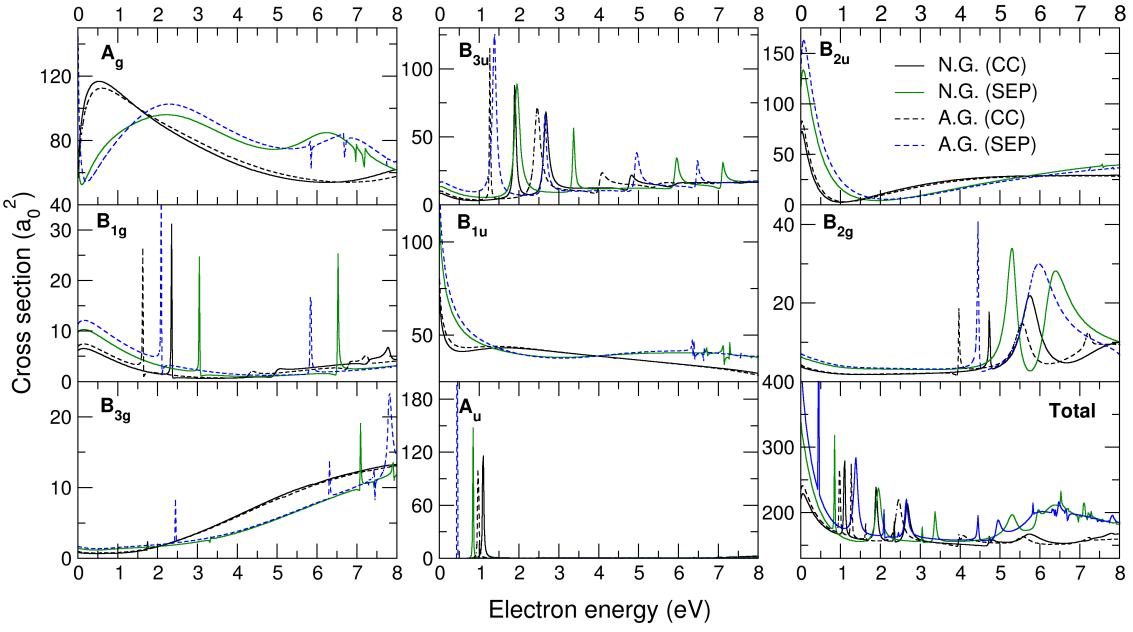

Figure 3.14: Contributions to the integral elastic cross section from the scattering symmetries indicated in the panels for the anion (dashed lines, black at CC and blue at SEP level) and neutral equilibrium geometries (solid lines, black at CC and green at SEP level): N.G. stands for neutral geometry and A.G. for anion geometry. The bottom right hand panel shows the total elastic cross sections(sum of all contributions shown in the other panels).

Except for the A_g symmetry, the cross sections are extremely similar between the SEP and CC methods (when resonance effects are excluded) and also between geometries. The more significant differences are seen in the SEP cross sections for the A_g symmetry: careful investigation of the two wide features, centered just above 2 and 6 eV, proved they do not derive from resonant processes, despite their suggestive shape. The cross sections calculated for the remaining symmetries are very similar both in size and shape, if one ignores the new peaks that appear at higher energies for the anion geometry, as discussed.

The cross sections reported in the literature [100, 101] were obtained at higher energies than ours. Therefore, no comparison is possible so they are not presented here.

We present in figure 3.15 our total (summed over all excited states included in the calculation) inelastic cross sections calculated at CC level for the anion geometry, and compare them with the already presented results for the neutral geometry.

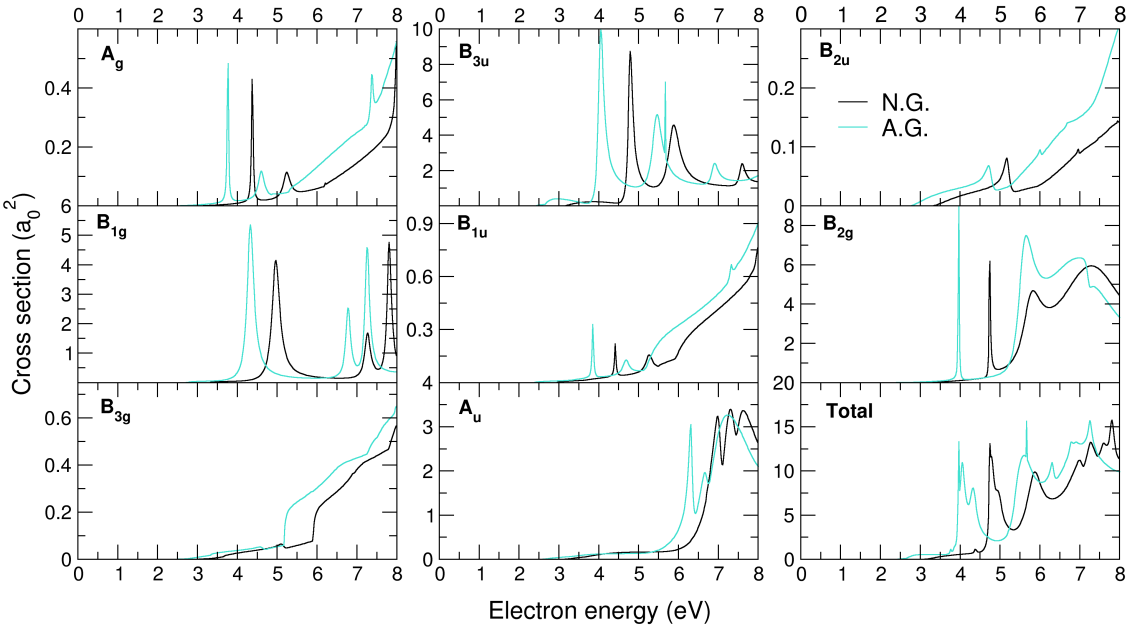

Figure 3.15: Contributions to the total integral inelastic cross section from the scattering symmetries indicated in the panels for the anion (light blue line) and neutral equilibrium geometries (black line). The bottom right hand panel shows the total integral inelastic cross sections (sum of all contributions shown in the other panels).

The analysis of both these sets of cross sections were of the most use in identifying and characterising resonances, as they have proven to be in the previous section for the neutral geometry. The peaks identified as resonances were already presented and discussed in the previous section.

Although we can easily obtain state-to-state excitation cross sections, we do not present any results for *p*-BQ for two main reasons: (i) as far as we know, there are no calculations or experiments below 15 eV that would allow a comparison; and (ii) the electronic low-lying states

of *p*-BQ are very close in energy and therefore, state-to-state measurements would be very tricky to perform. The experimental results would correspond to bands (as in reference [94]), i.e., as excitations into several states, sufficiently close in energy not to be differentiated.

3.6.2 Differential Cross Sections

Recently, new publications have emerged providing differential elastic cross section for *p*-BQ using two other theoretical methods: the IAM-SCAR and the SMC-PP (more details about these methods can be found in references [115] and [116], respectively). These DCS together with those calculated by us for the neutral equilibrium geometry are plotted in figure 3.16. Although the IAM-SCAR method is not accurate at these energies, it is still an interesting comparison to make, as seen in figure 3.16. As expected, at 1 eV the agreement is poor between methods, and also between our models, mainly due to the different description of the polarisation effects. This discrepancy, found especially at smaller angles, was also observed for pyrimidine **??** and thiophene (see chapter 4), although these targets have a non-zero dipole moment. At higher energies, convergence between our SEP and CC models is achieved, and the agreement with the SMC method improves, although the IAM-SCAR results are still fairly different, as expected. At 4 eV, we obtain the best agreement between the four curves, especially between our results and the SMC ones. The IAM-SCAR results are missing for 6 eV.

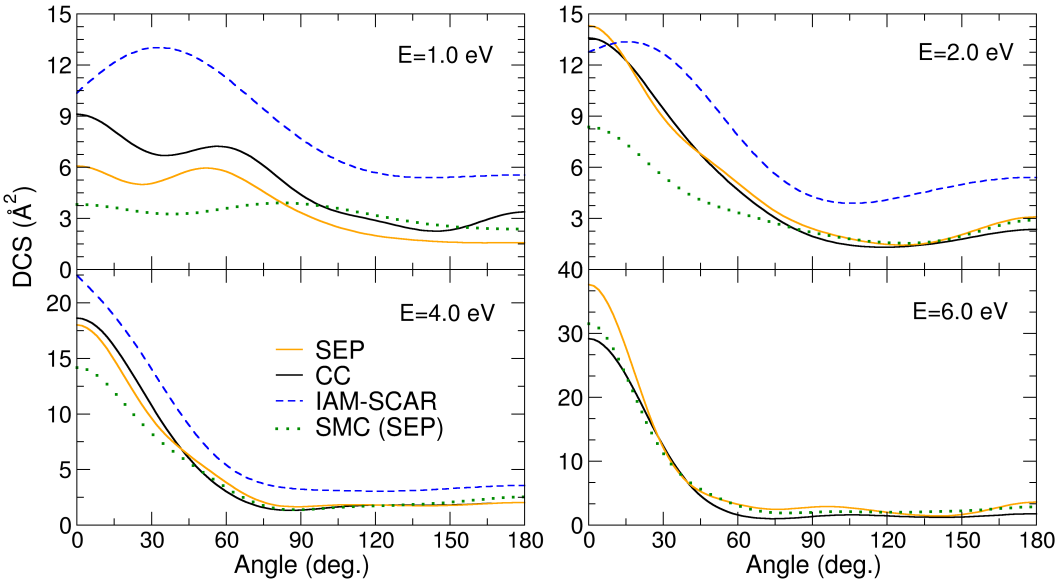

Figure 3.16: Differential cross sections as a function of electron energy, calculated at SEP and CC levels. Also presented are the IAM-SCAR and the SMC results from Lozano *et al.* [101].

3.7 Chapter remarks

In this chapter we presented our scattering calculations for *p*-BQ using two geometries of interest: the equilibrium ground state geometry of the neutral and of the anionic systems. Target

calculations with three basis sets - 6-311G**, 6-311++G** and cc-pVDZ - were performed and compared, and our final scattering calculations used the compact one, as it provided a better agreement with the literature, with a smaller computational cost. This system possesses a lot of electronically excited states very close in energy that are not easily described.

The best (qualitative) agreement was obtained between our results and those of Kunitsa and Bravaya [107]. For the core-excited resonances we discussed their position and widths and made, as far as we could, a link to the available literature: both with calculated resonance parameters, and with DEA results. The link with the latter, however, needs to be analysed skeptically, due to the complexity of this target's resonant spectrum.

We have also presented our calculated integral and differential cross sections. The former were used along with the time-delay analysis to identify and characterise the aforementioned resonances. Studying both geometries allowed us to demonstrate the sensitivity of the resonances parameters to the molecular geometry. The cross sections, however, do not seem to be as affected by the geometry.

As future plans, we would recommend performing the calculations using a smaller deletion threshold, that could not be tested during this work, and using UKRmol+ to run in quadruple precision. This would serve to confirm the accuracy of the results presented here. To close this chapter, it is important to state that *p*-BQ is a very interesting molecule to study, and we believe that there is a lot more to investigate, particularly related to Feshbach resonances. Even though a lot of effort has been put in through the years, the *p*-BQ resonant spectrum is still to be accurately describe. Further scattering calculations would be useful, as well as experiments, in particular EEL or Velocity Slice Imaging ones. The latter would be of great interest, as it is able to identify the symmetry of some resonances. The EEL technique enables the accurate description of resonance positions, providing the best like-with-like comparison with our results.

CHAPTER 4

ELECTRON COLLISIONS WITH THIOPHENE

Studying low energy electron collisions with thiophene (C_4H_4S) is the focus of this chapter. Thiophene is a prototypical, aromatic, five-membered heretocyclic ring (see chemical structure in figure 4.1). It is a colourless liquid with a benzene-like odour, and an active participant in substitution reactions, due to the presence of the relatively heavy and highly polarizable sulphur atom. Theoretical calculations suggest that its degree of aromaticity is less than that of benzene, as the lone pair of electrons of sulphur are significantly delocalised in the π electron system. Compounds analogous to thiophene include furan (C_4H_4O), selenophene (C_4H_4Se) and pyrrole (C_4H_4N), which differ in the heteroatom in the ring.

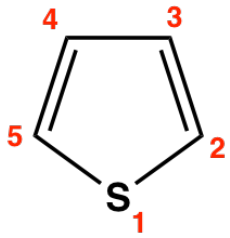

Figure 4.1: Chemical structure of thiophene.

Thiophene is one of the most used building blocks of anti-inflammatory drugs [42] - see two examples in figure 4.2. Tiaprofenic acid (1) is a non-steroidal anti-inflammatory drug of the arylpropionic acid (profen) class, used to treat pain, especially arthritic pain; and Tenidap (2) is a member of indoles, ureas, thiophenes and an organochlorine compound. It has a role as a non-steroidal anti-inflammatory drug and as a prostaglandin-endoperoxide synthase inhibitor [117].

Thiophene is also the main unit of several types of materials, like polythiophene. When properly doped, polythiophene is conductive and has several applications in electrochromic displays, electro-optic devices, protection against photocorrosion and energy storage [118, 119]. In other materials, thiophene's presence confers various important properties, making

them promising as photochromic molecular switches [120], organic semiconductors [121], solar cells [122], light-emitting diodes and field-effect transistors [123]. All of these applications involve electron transfer reactions. Therefore, understanding thiophene's electronic structure and electron induced processes is fundamental to comprehend these phenomena.

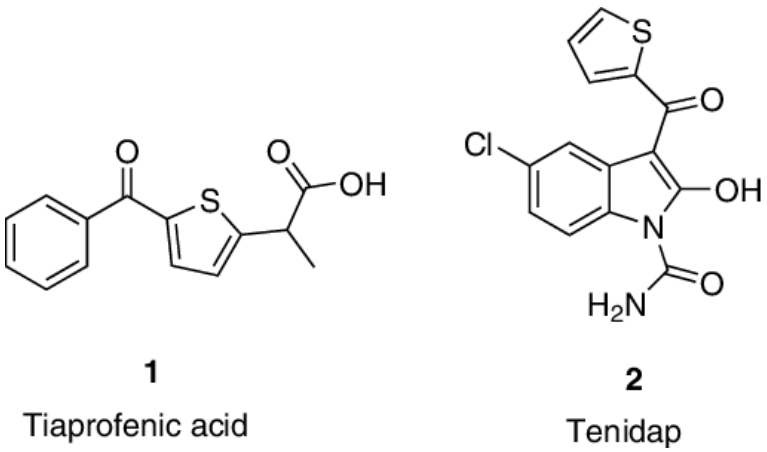

Figure 4.2: Chemical structure of tiaprofenic acid (1) and tenidap (2), two thiophene based non-steroidal anti-inflammatory drugs [124].

Similarly to what we have done in the previous chapter, we performed calculations using the R-matrix method as implemented in the UKRmol suite, at different levels of complexity. Our goal was to investigate resonance formation in thiophene, as well as calculate integral and differential cross sections, and a few excitation functions. Combining our results with another theoretical method (IAM-SCAR) and experimental technique (EEL[1]), three publications emerged [48, 49, 125]. In this chapter we include both IAM-SCAR and EEL results for comparison with our calculations. We also compare with da Costa *et al.* [126], who used the theoretical SMC-PP method. It is important to note that, unlike other targets (e.g. *p*-BQ), thiophene represented a very good opportunity to study state-to-state excitation cross sections: its first two electronically excited states are energetically distant, as we show in section 4.3.1.

Comparison with other type of experiments (DEA [127]) is also presented.

4.1 Electronic spectrum of thiophene

Thiophene is a planar molecule that belongs to the C_{2v} point group. It contains 44 electrons and has a dipole moment of 0.52 Debye [128]. Its experimentally determined polarizability [129] is 60.8 a_0^3 and its ionization energy is 8.86 eV[130]. Thiophene is an asymmetric top, with rotational constants of 3.297×10^{-5}, 2.197×10^{-5} and 1.319×10^{-5} eV. Its first electronic excitation threshold is around 3.7 eV [131, 132, 133, 134].

The electronic excited states of thiophene have been studied both experimentally and theoretically, as we briefly review in the following paragraphs.

[1] A summary of the EEL can be found here: http://homeweb.unifr.ch/allanm/pub/ma/dir_allan/thiophene_EELS.PDF

Jones and Moodie [135] synthesized and measured the absorption spectra of isomeric dithienyl sulphides and thiophene itself and found two bands at 5.28 and 5.77 eV.

Lonardo *et al.* [136] measured the electronic absorption spectra of thiophene and some deuterated derivatives. In the energy range of interest (4.9 to 8.9 eV), they found three electronic transitions at 5.16, 5.99 and 6.60 eV, and two Rydberg series. The broadness of the band prevented the identification of the symmetry of the upper states.

Flicker *et al.* [134] performed electron impact experiments with furan, thiophene and pyrrole, at scattering angles from 0° to 80° and impact energies of 30 and 50 eV. The group identified two low-lying features at 3.75 and 4.62 eV in thiophene, and assigned them to singlet-triplet transitions. The locations and the energy splitting of these excitations suggested that they are analogous to the ones found in benzene.

Nyulászi and Veszprémi [137] investigated the vapour and condensed phase spectra of 18 thiophene derivatives and of the parent molecule, in the near ultraviolet region. To interpret the spectra, CNDO/S calculations were carried out, and they conclude that although two bands were observed in the vapour phase spectra of thiophene and most of its derivatives, the near UV spectrum contains three singlet transitions.

Merchán *et al.* [138] studied the electronic spectrum of thiophene using multiconfiguration second-order perturbation theory and an extended ANO basis set. Their results were used to assign the experimental spectrum [134, 136, 137, 139, 140] below 8 eV, with a maximum deviation of about 0.1 eV for vertical transition energies.

Palmer *et al.* [131] reinvestigated and extended the VUV and EEL spectra of thiophene, and assigned the bands by means of high level multi-reference multi-root CI studies, with several basis sets, looking at valence and Rydberg-type states.

Nakatsuji *et al.* [141] used in their calculations the symmetry-adapted cluster configuration interaction (SAC-CI) method and a basis set augmented with diffuse Rydberg functions. They computed seventy singlet and four lowest triplet electronic states in order to provide a detailed theoretical interpretation of the VUV and the EEL spectra of thiophene.

Kleinschmidt *et al.* [142] used SPOCK (a code that calculated spin-orbit matrix elements in the one-center mean-field approximation for multireference CI wave functions) and the DFT/MRCI approach to calculate excitation energies in good agreement with the experiments.

Haberkern *et al.* [133] measured high-resolution EEL spectra of thiophene (and bithiophene) in the range of the low-lying singlet-triplet excitations. In combination with *ab initio* calculations, the spectral structures were assigned and the vertical and adiabatic energies were determined.

Salzmann *et al.* [143] used the time-dependent Kohn-Sham DFT combined with a DFT/MRCI to study the ground and low-lying electronically excited states of thiophene. They managed to explain the ultrafast decay of low-lying vibrational levels of the lowest singlet state, observed by time-resolved pump-probe femtosecond multiphoton ionization spectroscopy [144], *via* a close-by conical intersection.

Holland *et al.* [145] used synchrotron radiation-based Fourier transform spectroscopy to

study the excited states of thiophene. A highly resolved photoabsorption spectrum was measured between 5 and 12.5 eV, combined with high-level *ab initio* calculations that used the second-order algebraic-diagrammatic construction polarisation propagation approach, and the equation-of-motion coupled-cluster (EOM-CC) method at the CCSD and CC3 levels, to assign the spectrum.

The results obtained by many of these groups are presented in table 4.4 in section 4.3.1, and discussed along with our calculated vertical excitation energies.

4.2 Earlier work on electron collisions with thiophene

Contrary to the large amount of information regarding thiophene's electronic spectrum, there is significant fewer studies on low energy electron collisions from it. In this section, we briefly review the literature, both experimental and theoretical.

Starting with the experiments, Asmis [132] measured EEL spectra for vibrational excitation of thiophene and found three resonances at 1.27, 2.83 and 5.5 eV. He assigned the first two resonances as 1 particle (i.e. shape) π^* resonances and the last one tentatively to a low-lying core-excited resonance.

Modelli and Burrow [146] obtained electron transmission spectra (ETS) for thiophene below $\simeq$4.5 eV. They found two intense resonances at 1.15 and 2.63 eV, associated with electron capture into the two lowest empty π^* molecular orbitals, of b_1 and a_2 symmetry. They state the signal corresponding to an expected σ^* resonance (scaled virtual orbital energies in their work put it around 2-2.1 eV) is probably masked by overlap with the high-energy tail of the lower, more intense π^* resonance appearing at around 1.8 eV.

Hedhili *et al.* [118] investigated electron stimulated desorption (ESD) of anions from multilayer thiophene condensed on a polycrystalline platinum substrate. The yield functions they obtained show that anions are desorbed both by DEA, and for higher energies, *via* dipolar dissociation.

From the theoretical point of view, three methods were applied to the study of electron scattering from thiophene. Firstly, Mozejko *et al.* [147] calculated integral elastic and ionisation cross sections at intermediate and high electron-impact energies using the additivity rule approximation and the binary-encounter-Bethe approach.

da Costa *et al.* [126] reported electron impact integral, momentum transfer and differential cross sections calculated with the Schwinger multichannel method with pseudopotentials (SMC-PP) for energies ranging from 0.5 to 6 eV. They identified two π^* and a σ^* shape-resonances, the latter with a strong d-wave character.

Vinodkumar *et al.* [148] used the R-matrix method (through the QUANTEMOL-N interface) for low energy calculations and the Spherical Complex Optical Potential (SCOP) formalism for intermediate to high energy. Their R-matrix calculations are based on the same theory as those presented in this chapter. However, their results are very different and reveal a number of clear inconsistencies, as we shall discuss later on.

A detailed discussion of the aforementioned results is presented in section 4.5.

4.3 Calculation details

4.3.1 Target description

The ground state configuration of thiophene is $1a_1^2\ 2a_1^2\ 1b_2^2\ 3a_1^2\ 2b_2^2\ 4a_1^2\ 3b_2^2\ 5a_1^2\ 1b_1^2\ 6a_1^2\ 7a_1^2\ 4b_2^2\ 8a_1^2\ 5b_2^2\ 9a_1^2\ 6b_2^2\ 10a_1^2\ 7b_2^2\ 2b_1^2\ 11a_1^2\ 3b_1^2\ 1a_2^2$.

In our calculations, we have used the ground state equilibrium geometry listed on the NIST website, calculated at MP2 level using the cc-pVDZ basis set [108]. In order to obtain the target orbitals for the description of the scattering process, we have tested two basis sets[2]: cc-pVDZ ("compact") and 6-311G** ("diffuse"). Hartree-Fock SCF (HF) and SA-CASSCF orbitals were generated using *molpro* [70] and used in the scattering calculations.

To find the best CASSCF model, several tests were performed: the results are summarized in table 4.1. These tests involved changing the active space and the number of states to be averaged in the calculation, until a good agreement with the literature was achieved (as we have done in other chapters). It is also important to take into account the number of configurations generated by each of the models, as the scattering part of the calculations might get too computationally demanding.

The active space (10,9) correspond to [10a_1,6b_2,1b_1,0a_2] frozen orbitals and [11-12a_1,7-8b_2,2-4b_1,1-2a_2] active orbitals; (6,7) correspond to [11a_1,7b_2,1b_1,0a_2] frozen orbitals and [12a_1,8b_2,2-4b_1,1-2a_2] active orbitals; and (8,8) corresponds to [10a_1,7b_2,1b_1,0a_2] frozen orbitals and [11-12a_1,8b_2,2-4b_1,1-2a_2] active orbitals. In table 4.2 we present the character of the orbitals involved in the active spaces we tested.

Table 4.2: Character of the orbitals involved in the set of tested active spaces.

Orbitals		Character
$7b_2$	HOMO-4	σ
$2b_1$	HOMO-3	σ
$11a_1$	HOMO-2	σ
$3b_1$	HOMO-1	π
$1a_2$	HOMO	π
$4b_1$	LUMO	π^*
$8b_2$	LUMO+1	σ^*
$2a_2$	LUMO+2	π^*
$12a_1$	LUMO+3	σ^*

Although the values presented in table 4.1 are fairly similar for all the three active spaces and state-averaging models (excluding Y, as the description of the higher energy states is the poorest), we chose to use the model that provided the results marked in bold. As the focus of this work is mainly the low-lying resonances, our goal was to get the best possible agreement for the low-lying electronic states. Therefore, taking this consideration into account, the model with an active space of (10,9) and 7 states averaged (1-2$^1A_1$ 1-3$^1B_1$ 1^1B_2 1^1A_2) was deemed to

[2] A third basis set was also tested - 6-311++G** - but because the radial density (calculated with *radden*) was too big, even for a radius of $a = 18a_0$, we discarded it before further calculations were performed.

produce the best set of results. Despite the fact this model produced the biggest number of configurations, it is still a reasonable number to work with.

The ground state energy and dipole moment calculated using both HF and CASSCF methods are presented in table 4.3, together with the available published results of equivalent calculations.

Table 4.3: Energies (E, in Hartree) and dipole moment (μ, in Debye) of the ground state of thiophene in its equilibrium geometry, obtained at HF and CASSCF levels, for each of the tested basis sets. Our CAS model used an active space of (10,9). The absolute state energies in brackets were calculated at HF level, using the same basis sets [108]; the dipole moment value in the last row was obtained experimentally [128].

	Level	6-311G**	cc-pVDZ
E	HF	-551.3425	-551.3184
		(-551.3471)	(-551.3217)
	CASSCF	-551.4281	-551.3184
μ	HF	0.722	0.738
	CASSCF	0.549	0.665
		0.52	

It is worth referring that our calculated ground state energy at HF level is not identical to the ones listed in the NIST website, because we have used the thiophene geometry optimised at MP2 level, as mentioned at the beginning of this section.

From table 4.3 is possible to observe that the ground state properties obtained using the diffuse basis set are significantly better. In addition, as thiophene is known to have a lot of excited states with Rydberg character [138], the diffuse basis set should provide a better description of these states, and that was our choice in our calculations.

Table 4.4 lists the vertical excitation energies of the 25 states (ground state + 24 excited states) calculated with this model and included in our CC calculation, and the theoretical and experimental results summarised in section 4.2.

Table 4.4: Calculated vertical excitation thresholds (in eV) of the electronic states included in our CC calculations. Also listed are previous results from calculations: Salzmann *et al.* [143], Kleinschmidt *et al.* [142], Holland *et al.* [145], Nakatsuji *et al.* [141], Palmer *et al.* [131] (who also presents some EELs results) and Merchán *et al.* [138] (both CASSCF and PT2 results are presented); and experiments: Jones *et al.* [135], Regeta [47], Lonardo *et al.* [136], Flicker *et al.* [134], van Veen *et al.* [140], Asmis [132], Haberkern *et al.* [133] and Nyulászi *et al.* [137]. The energies labelled with a R correspond to Rydberg states. The vertical dots indicate that several other states are present in that energy range, for the calculation listed in that column.

	Ours	[143]	[142]	[145]	[141]	[138]		[131]	Exp.
						CASSCF	CASPT2		
$1\,^3B_2$	3.722	3.53	3.39	-	3.94	3.83	3.75	4.45	3.7[140],3.72[47, 132] 3.75[134],3.74[133] 3.8[131]
$1\,^3A_1$	4.943	4.35	4.33	-	4.86	4.90	4.50	5.03	4.6[140],4.61[47],4.7[131] 4.62[132, 133, 134]
$1\,^1A_1$	5.916	5.39	5.24	5.64	5.41	6.41	5.33	6.55	5.41[47],5.43[132, 133] 5.45[132],5.48[134]
$1\,^3B_1$	6.371	5.65_R	5.69	-	5.94_R	5.93	5.90	8.43	5.9[47]
$1\,^3A_2$	6.457	5.77_R	5.64	-	5.75_R	5.57	5.88	9.82	5.9[47]
$1\,^1B_1$	6.660	5.86_R	5.88	6.17	5.87_R	6.72	6.23	6.33_R -	
					⋮				
$2\,^3A_1$	6.816	-	5.63	-	-	-	-	6.82	-
$1\,^1A_2$	6.877	5.88	5.72	6.23	6.41_R	6.43	5.93	5.78_R	5.9[134],6.0[136, 137]
$2\,^3B_2$	6.906	-	5.99	-	-	-	-	5.85	-
$1\,^1B_2$	6.952	5.54	5.42	5.97	5.72	8.10	5.72	6.61	5.61[132, 133] 5.65[139],5.77[135]
					⋮				5.6[131]
$2\,^1A_1$	8.060	-	7.03	7.38	6.73	8.85	6.69	7.12_R	6.6[140],6.7[136]
					⋮				7.05[131]
$2\,^1B_2$	9.411	-	-	6.97	6.41_R	6.79	6.56	7.1_R	7.1[134]
$3\,^3A_1$	9.563	-	-	-	-	-	-	8.76	-
$2\,^3A_2$	9.731	5.80_R	-	-	-	-	-	10.41	-
$2\,^1A_2$	10.055	6.10_R	6.33	-	6.73_R	7.50	6.97	7.03_R	-
$3\,^3B_2$	10.116	-	-	-	-	-	-	11.98	-
$4\,^3B_2$	10.139	-	-	-	-	-	-	-	-
$5\,^3B_2$	10.368	-	-	-	-	-	-	-	-
$3\,^1B_2$	10.630	-	-	7.69	7.12_R	7.44	7.28	7.94_R	-
$3\,^1A_1$	10.749	-	-	7.65	7.32	7.46	7.23	7.72_R	-
$2\,^3B_1$	10.827	-	6.18	-	-	-	-	9.67	-
$3\,^3A_2$	11.046	-	6.11	-	-	-	-	10.41	-
$6\,^3B_2$	11.247	-	-	-	-	-	-	-	-
$4\,^3A_1$	11.422	-	-	-	-	-	-	-	-

We observe that the agreement between our results and both theory and experiment gets worse as the energy increases, as seen before for other targets. The agreement is reasonably good for the first few states (except for Palmer's *et al.* [131] calculations, which provided results considerably higher than their measurements, and than ours and other calculations) but differences of several eV occur for the higher states. The calculations of Nakatsuji's *et al.* [141] produce a large number of Rydberg states (most of them are not listed, with those omitted

being represented by the vertical dots), that we were not able to describe, as an even more diffuse basis set would be needed, and therefore, the use of a much larger R-matrix radius in the scattering calculation. Unfortunately, as already mentioned, with the UKRmol suite this would lead to either serious linear dependence problems, or a significant decrease in the quality of the continuum description [24]. It is important to note that this poor and incomplete description of the Rydberg states in our calculations means that any resonances associated to them will be poorly described or not described at all.

4.3.2 Scattering model

For the chosen 6-311G** basis set, an R-matrix radius of $a = 15a_0$ was selected as the most appropriate by analysing the radial charge density of the target orbitals obtained with the program *radden*.

The effect of including an extra partial wave ($l_{max} = 5$) in the continuum basis set made a significant difference at higher energies, as seen in the cross sections calculated at SE level presented in figure 4.3. Therefore, we have chosen to use partial waves up to $l_{max} = 5$ in the calculations presented here (in the previous chapter, for *p*-BQ, we decided not to use partial waves up to $l_{max} = 5$ because the calculation would get even more computational demanding. In this case, the use of a higher number of partial waves still leads to a calculation of a reasonable size). A higher number of partial waves was not tested.

As explained in the previous chapter, our scattering calculations do not exhibit convergence of the resonance positions with respect to the number of VOs used to generate the L^2 configurations. Therefore, the optimal number was chosen in order to provide the best agreement between the position of the first two π^* resonances and the experiments. We start with a small number of VOs (usually 10) and increase it gradually (the orbitals are selected in energy order) until we obtain a good position for the lowest-lying resonance. The results of this procedure are presented in figure 4.4 at SEP level. We have concluded that, for thiophene, the inclusion of the lowest 35 and 70 VOs, at SEP and CC level respectively, produce the best description of the first two resonances. The analysis of the position of a feature in the time-delay as a function of the number of VOs included is a very good way to identify (in CC calculations) whether it is a resonance (as it is polarisation dependent, and therefore it shifts according to the amount of polarisation we are including) or an excitation threshold (that is not polarisation dependent).

We used a deletion threshold of $1\text{x}10^{-7}$, which is relatively high for a radius of $a = 15a_0$. However, due to computational limitations, we did not test the effect of a smaller deletion threshold.

The set of parameters that we believe is the best (within our computational limitations) to describe the scattering process for thiophene is listed in table 4.5 for each of the three models (SE, SEP, CC) used to carry out our calculations.

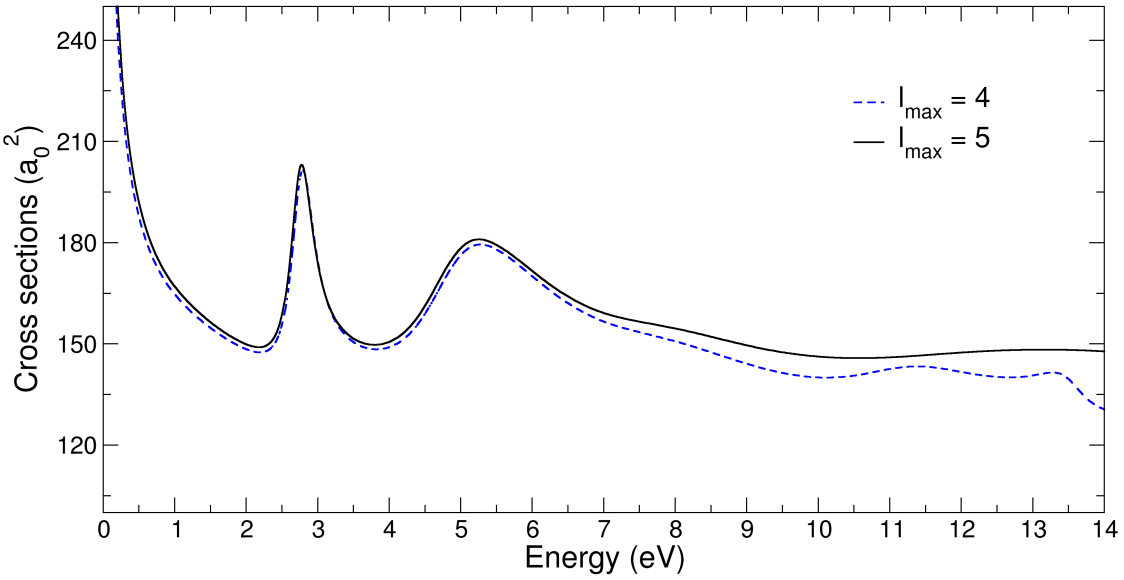

Figure 4.3: Cross sections as a function of electron energy for two SE calculations using the same parameters (6-311G** basis set, deletion threshold of 10^{-7} and $a = 15a_0$), and the partial waves indicated. The dashed blue line correspond to the inclusion of partial waves up to $l_{max} = 4$, whereas the solid black line correspond to $l_{max} = 5$. Both were calculated using the UKRmol suite.

Table 4.5: Parameters used in the SE, SEP and CC calculations.

Approximation	**SE**	**SEP**	**CC**
Basis set		6-311G**	
Radius (a_0)		15	
No. Partial waves (l_{max})		5	
Del.Tresh.		10^{-7}	
No. Target states	1	1	25
No. VOs	10	35	70

4.4 Cross sections

In this section, we present integral and differential elastic and inelastic cross sections, as well as excitation functions, for electron scattering from thiophene calculated in the energy range of 0-10 eV. Unlike the cross sections presented in the other chapters, some of those presented here include a Born correction and were calculated using POLYDCS, briefly described in chapter 2, section 2.6.1. The POLYDCS calculations assume the molecule is initially in its ground rotational state and, in this case, sum over all possible final states with $J < 9$.

For simplicity, we have treated thiophene as a symmetric top (for which the rotational energies, needed in POLYDCS, can be calculated analytically) using the rotational constants

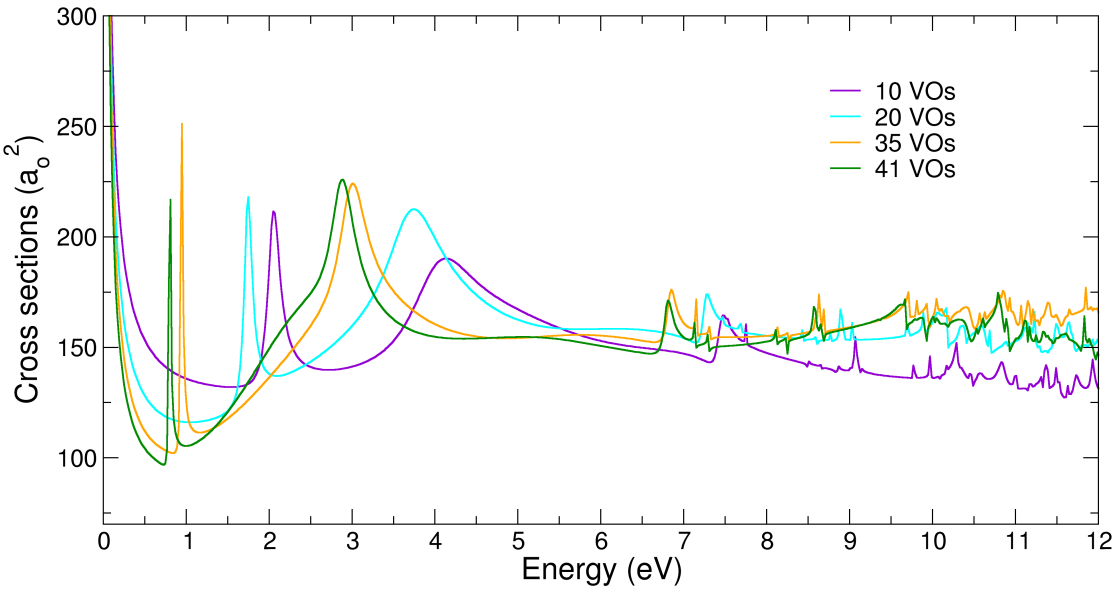

Figure 4.4: Cross section as a function of electron energy, calculated at SEP level using the same parameters (6-311G** basis set, deletion threshold of 10^{-7} and $a = 15a_0$), and the number of VOs indicated in the figure.

3.297×10^{-5} and 1.758×10^{-5} eV. This corresponds to the first accurate one (see section 4.1) and the average of the second and third ones to perform the calculation. Tests using other values for the rotational constants led to very similar integral and differential elastic cross sections.

Whenever possible, we also present a comparison between our calculated cross sections and other calculations and measurements.

4.4.1 Integral cross sections

We start by focusing on the integral cross sections. Figure 4.5 shows our R-matrix results and the SMC-PP ones from da Costa *et al.* [126]. Both CC and SEP approximations produce cross sections with similar profiles, particularly when the Born correction is included. This correction is bigger at lower energies, where the influence of the dipole moment on the collision process is stronger. Above the second visible resonance, the size and shape of our R-matrix cross sections are almost identical, except for the presence of non-physical pseudoresonances, appearing as spikes in the cross section at SEP level.

Below the second visible resonance, the difference between our SEP and CC results is noticeable, and we attribute it to a different description of the polarisation effect (this difference also leads to slightly different resonance positions, as expected). The results from da Costa *et al.* [126] plotted in the figure correspond to their SEP cross section and do not include any correction to incorporate the effect of those partial waves not included in the SMC-PP calculation.

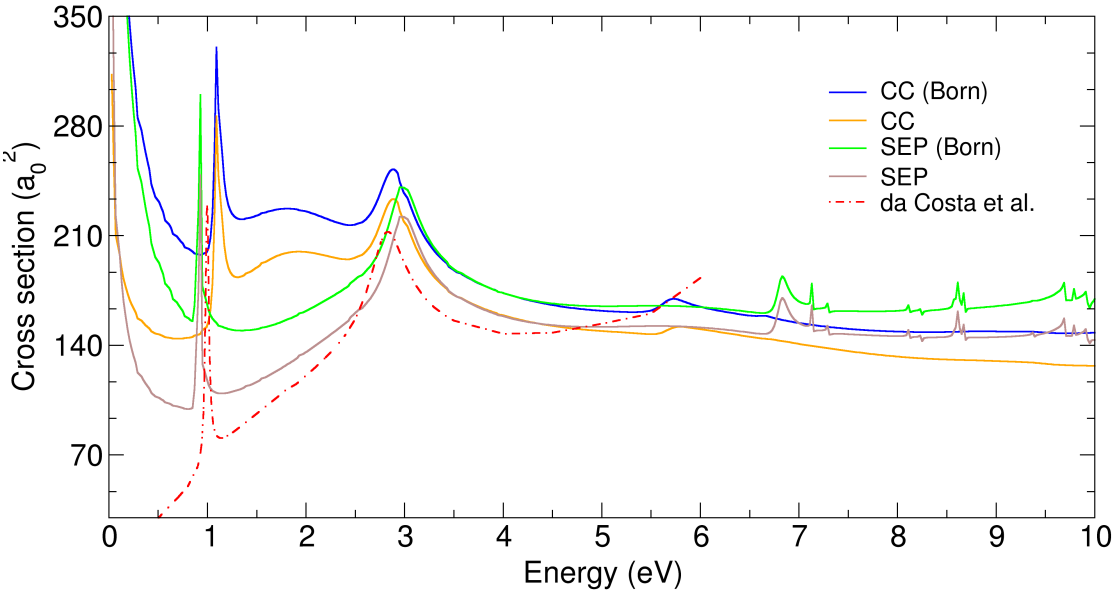

Figure 4.5: Integral elastic cross section for electron scattering from thiophene for energies up to 10 eV calculated with the R-matrix approach at SEP and CC levels, with and without the Born correction (labeled Born in the former case). Also plotted are the SEP results from da Costa *et al.*[126].

Agreement with our uncorrected SEP cross sections is excellent, except below 1 eV where our calculation accounts for more of the dipole effect.

In figure 4.6 we present the total electronically inelastic cross sections and compare them with those calculated for higher energies using the IAM-SCAR method [48]. Note that the IAM-SCAR method incorporates the rotational contribution and a correction term known as "interference term". This corrected version of the IAM-SCAR method is the one that provided the better agreement [48], and therefore is the one we present here (and also in section 4.4.2). For a more detailed description of the IAM-SCAR method and respective correction terms, please consult references [48, 115].

Our inelastic cross sections were obtained summing over all the 25 states included in the calculation (ground state + 24 electronically excited states). No inclusion of a Born-type correction for the dipole-allowed excitation processes was included, but the effect is not expected to be significant [48]. Figure 4.6 presents our CC results using partial waves up to $l_{max} = 4$ and $l_{max} = 5$ to show that the additional partial wave increases the size of the cross section by, at most, 10%. Note that for the IAM-SCAR method, the cross section is zero below 7 eV, because the states lying below this threshold are neglected. The first experimental excitation threshold is below 4 eV so the R-matrix cross section is non-zero between 4 and 7 eV. The agreement between our calculated cross sections and the ones calculated with the IAM-SCAR method at 15 eV is, however, good and an interpolation between the R-matrix and the IAM-SCAR results

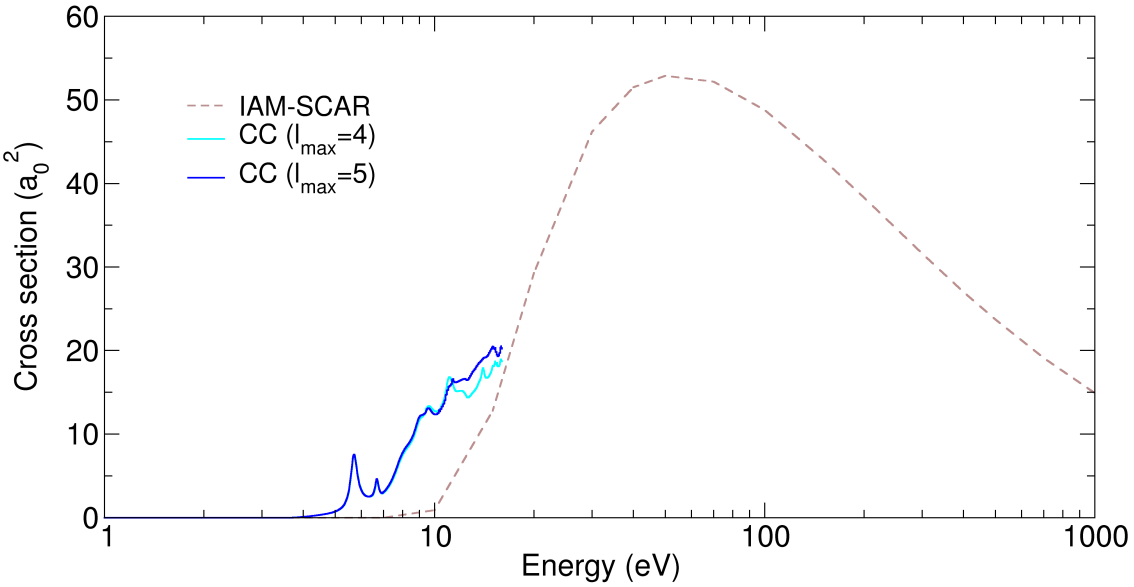

Figure 4.6: Integral electronically inelastic cross section for electron scattering from thiophene calculated using the R-matrix and IAM-SCAR methods [48]. R-matrix cross sections from calculations including partial waves up to $l_{max} = 4$ and $l_{max} = 5$ are plotted.

could be easily done.

4.4.2 Differential cross sections

The DCS presented in this chapter were obtained using the POLYDCS program described in chapter 2, section 2.6.1.

Figure 4.7 presents our calculated DCS at SEP and CC level (both including the Born correction). Also presented are DCS calculated with the IAM-SCAR and SMC-PP methods (more data and details in reference [48]).

Generally, the shape and size of our DCS calculated at both levels of approximation are very similar. Agreement of these results with da Costa *et al.* is very good at 3 and 5 eV (this was also the case, for example, for pyridine [149]). For 1 eV, however, both the shape and size of the DCS are very different. This discrepancy at low energies was also observed for pyrimidine when compared with SMC results from Winstead and McKoy [150], but in that case it was the R-matrix method that produced bigger cross sections for the higher angles, in poorer agreement with the experiments. For these angles, our DCS at 1 eV seems to be more similar in shape to the SE results from da Costa *et al.* [126] (not included in the figure), a sign that perhaps our calculations somewhat underestimate the polarisation effects.

As expected, the IAM-SCAR DCS are very different from our results at lower energies, where the former method fails. However, above 10 eV both methods seem to provide DCS of a similar size, reaching the best agreement at 15 eV, where the shape of the DCS is also very similar.

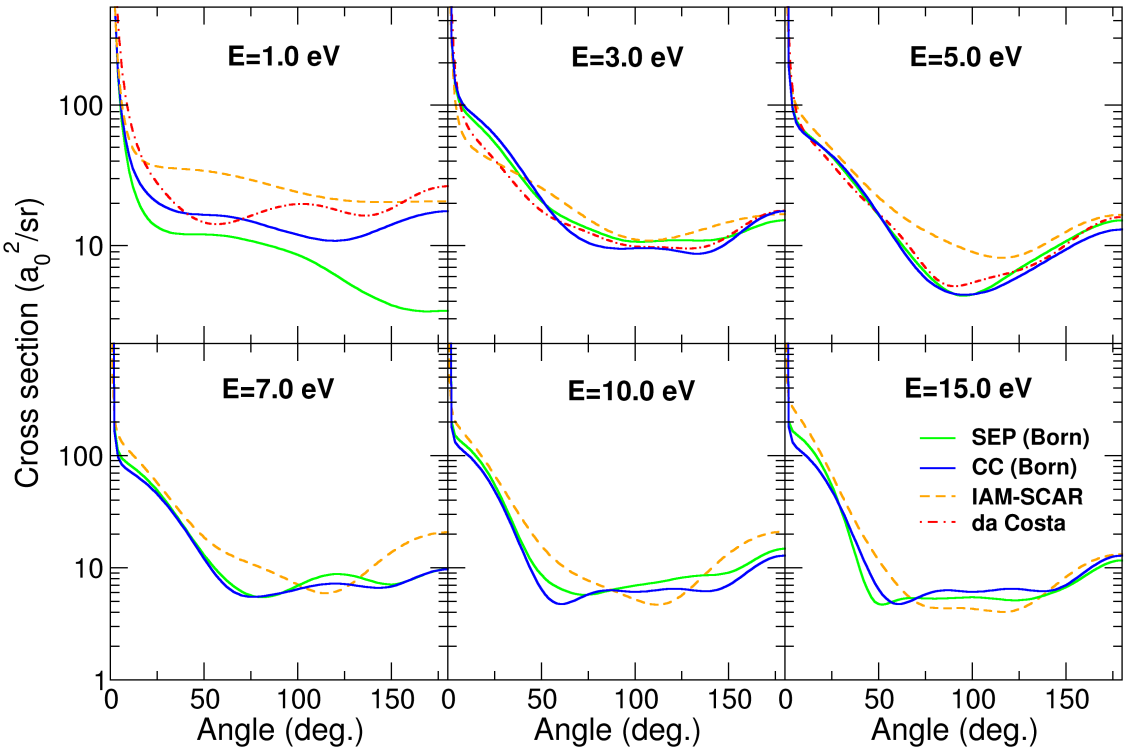

Figure 4.7: Elastic differential cross sections for electron scattering from thiophene for the energies indicated in the panels. The R-matrix DCS are Born corrected (labeled "Born"). The SMC-PP were calculated at SEP level and incorporate a Born based correction [126].

4.4.3 Excitation functions

The experimental results presented in this section were measured by Regeta [47] using electron energy loss spectroscopy (EELs). In this technique, a sample is exposed to a beam of electrons of a known range of kinetic energies, that is usually very narrow. As explained in chapter 1, those electrons can interact elastically with the sample, and keep their kinetic energy; or interact inelastically, and lose some of their kinetic energy, having their paths randomly deflected. These scattered electrons are counted (usually using an electron spectrometer) with respect to their energy loss (ΔE). Either the incident or the residual energy is kept fixed. The peak locations in an EELs spectrum correspond to the energy levels of the target molecule, and the intensities are related to the excitation cross sections [47, 132].

More than cross sections data, the excitation functions provide valuable information about resonances and respective parent state(s). The more separated in energy the electronically excited states of the target molecule are, the more likely is the excitation into a specific state. Unlike the other targets studied in this thesis, this was the case for thiophene, specially for the first two triplet states. For the third state, corresponding to the first singlet, the presence of more states closer in energy turned this task more difficult, as more states can be excited simultaneously, as we will discuss later on.

To calculate the excitation functions for thiophene, we used a program called DCS, developed by Z. Mašin. Functionally, it is similar to *polydcs*, with the advantage of calculating inelastic cross sections, or excitation functions. However, the version of DCS used to perform these calculations did not take into account the dipole contribution to the cross sections. This contribution is zero for singlet-triplet transitions, but can have a noticeable effect in the excitation function for the singlet S1 state.

Figure 4.8 presents our calculated excitation functions for two different electron scattering angles, 90° and 135°, as well as K. Regeta's EELs measurements [47, 48]. The measurements were also done for these two angles [47].

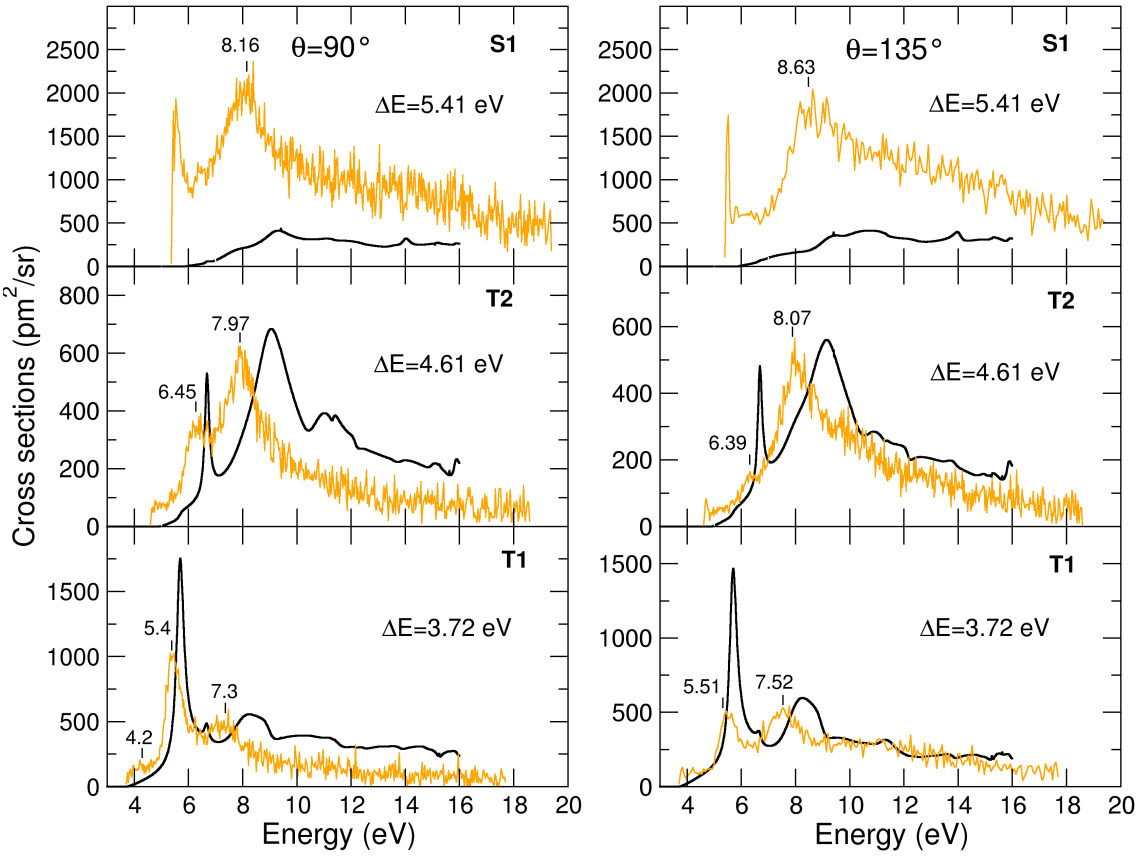

Figure 4.8: Calculated (full black lines) and measured (full orange line) excitation functions for the energy losses indicated in the panels: left panels, scattering angle of 90°; right panels scattering angle of 135°. The peaks of the measured excitation functions are also indicated in the panels. The ΔE correspond to the energy losses measured by Regeta [47] and T1, T2 and S1 indicate the first and second triplet states, and the first singlet state, respectively.

The measured EELs spectra [47] place the first triplet state (1^3B_2, T1) at 3.72 eV, the second (1^3A_1, T2) at 4.61 eV and the first singlet state (1^1A_1, S1) at 5.41 eV. For this reason, the excitation functions were measured by Regeta [47, 48] for energy losses, ΔE, of 3.72 eV, 4.61 eV and 5.41 eV.

The size[3] and shape of the measured and calculated excitation functions for ΔE=3.72 and 4.61 eV agree extremely well (considering our resonances positions are shifted to slightly higher

[3]Note that the measured excitation functions in *y*-axis in figure 4.8 are absolute.

energies). This agreement is similar to that obtained before for pyrimidine [151], but for bands instead of state-to-state. In that case the quantity compared was integral excitation cross sections (obtained from the integration over all angles of the excitation functions). Here, we show the agreement to be excellent for specific angles.

For ΔE=5.41 eV, the agreement between our calculations and the experiments is not as good: our cross sections are significantly smaller, although the peaks are still in their expected position. As the S1 state has a lot of other states close in energy, it is possible that the excitation is not into this state only, but to a group of states in its vicinity. To verify this hypothesis, we summed our state-to-state cross sections for the S1 state to those of other states closer in energy, as shown in figure 4.9.

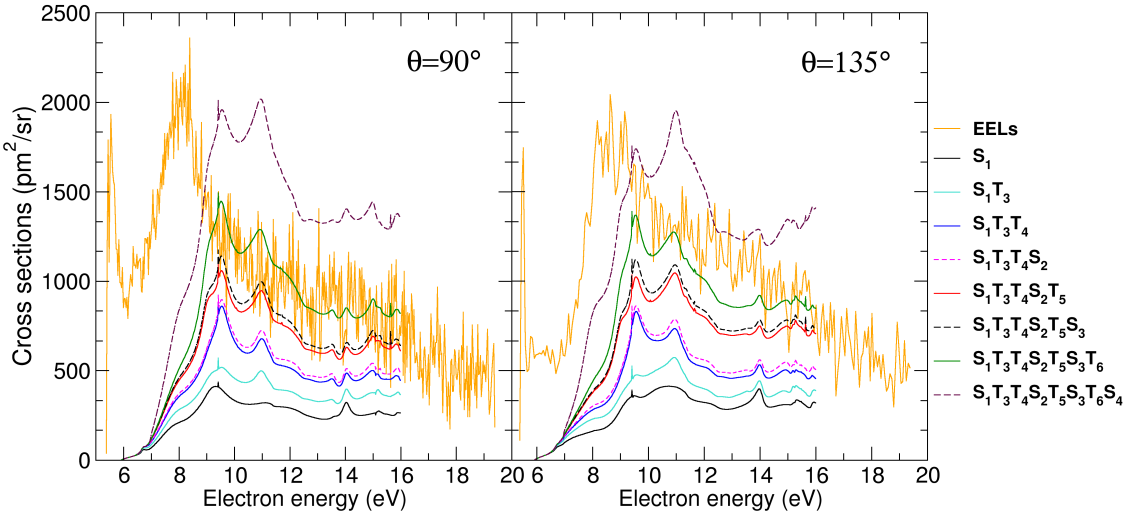

Figure 4.9: Calculated and measured (full orange line) excitation functions for ΔE=5.41 eV energy loss, for the two angles indicated in the panels. The calculated curves correspond to increasing the number of states that are added. The labels on the right side of the panels indicate which states these are; T_3 corresponds to the third triplet state (recall table 4.4), T_4 to the fourth, and so on.

It is clear from figure 4.9 that only the inclusion of 7 or more states in our calculation produces an excitation function of similar size to the experimental one. This does not necessarily mean that all these states actually contribute to this excitation function.

There are two possible sources for this discrepancy for the S1 state: (i) the quality of description of the electronic states of thiophene in our calculations gets worse as their energy increases, in part, but not only, because some of these states have Rydberg character. Therefore, our calculations will clearly provide a less accurate description of electronic excitation into higher-lying states; and (ii) the DCS code does not take into account the contribution of the dipole moment to the cross section, and therefore, neglecting this effect will decrease the size of the cross section.

As mentioned, the peaks in the experimental curves correspond to resonances. From figure 4.8, it is possible to observe that the agreement between the calculated and measured resonance positions is excellent, if ones takes into account the shift of our results to higher energies. Two effects might be responsible for this shifting: (i) the energies of the parent states are overestimated in our calculations; and/or (ii) it is expected that the polarisation effects are not fully described in a CC calculation. The latter is likely to be a smaller effect for thiophene, as the shape resonances are in fairly good agreement with experiments, as we will show in the next section. A similar comparison for pyrimidine [151] produced very similar agreement (including the absence of some calculated resonances in the EELs cross sections): the shifts are somewhat smaller in this case but, as for pyrimidine, increase as the resonance energy increases.

4.5 Resonances

As we have explained in chapter 2, we use the investigation of the eigenphase sums, the cross sections and time-delay analysis to identify and characterise resonances. In this chapter we used mainly the last two tools, looking at the eigenphase sums only occasionally.

Below we describe in detail the resonances we have identified, splitting their discussion according to the energy range they appear in: low- and higher energy resonances. The low-energy resonances are well described in the literature, both at theoretical and experimental level, whereas for the higher-energy resonances there is significantly less information available. The agreement between our results and the literature is also discussed. Please note that we present elastic and inelastic cross sections in this section for the purpose of helping in resonance identification. For this reason, these are not Born corrected (more accurate cross section calculations were presented in the previous section).

4.5.1 Low energy resonances

Our calculations revealed the presence of two low-lying π^* resonances, which are characteristic of molecules with double bonds, and that were already identified in earlier experimental and theoretical work [126, 132, 146, 148]. The third well known resonance for thiophene, of σ^* character, was only identified in previous calculations [126].

Figure 4.10 presents the time-delay for the four C_{2v} irreducible representations calculated at SEP level. As it is possible to observe, every irreducible representation presents resonant-like features, but in this section we will only focus on the aforementioned three resonances. The remainder will be discussed in the next subsection.

Figure 4.11 presents the elastic cross sections as a function of electron energy for each irreducible representation, and the total (sum over all the four symmetries) cross sections, calculated at SE and SEP level. The SE results provided us some guidance about the character of the resonances: we have explained in chapter 2 that the resonances that are described at this level of approximation possess pure shape character, and therefore, the ones that are visible at

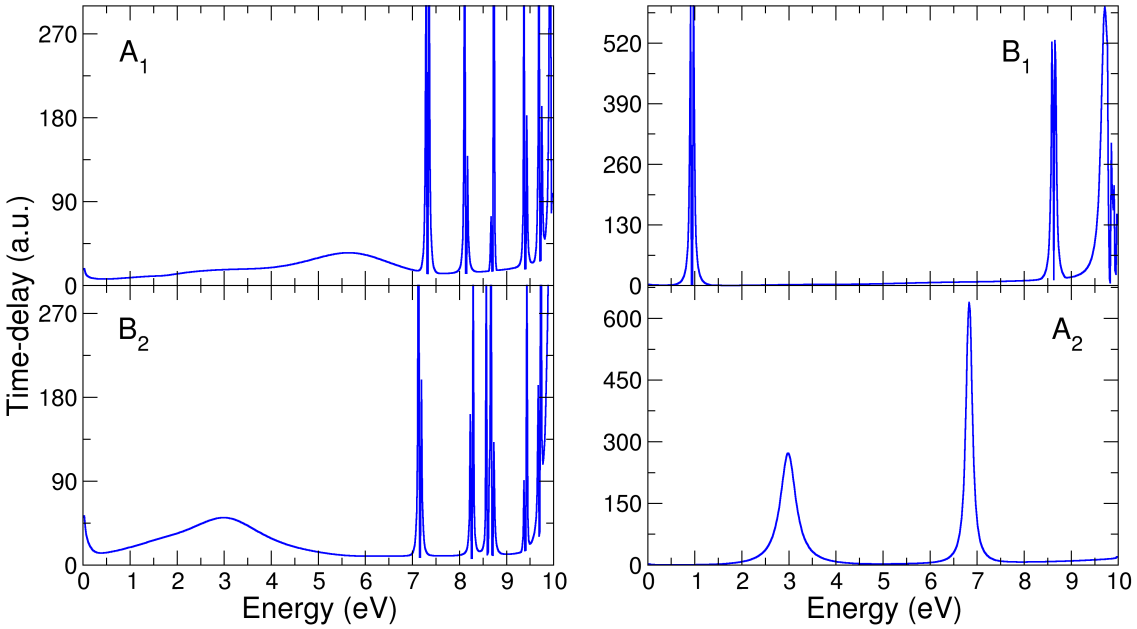

Figure 4.10: The largest eigenvalue of the **Q**-matrix (time-delay) as a function of electron energy for the four irreducible representations that constitute the C_{2v} point group. The calculations were performed at SEP level with UKRmol suite, using a deletion threshold of 10^{-7}, $l_{max} = 5$, the 6-311G** basis set and $a = 15a_0$.

SEP but not at SE level must have some core-excited character. Note that, as usual, due to the lack of polarisation description, the resonances appear at much higher energies at SE level.

Taking into account these two sets of data, we were able to identify the three low-lying resonances mentioned at the beginning of this section (two π^* and one σ^*), and their positions are listed in table 4.6 with their respective widths. This table also shows the positions and widths of these resonances calculated at CC level, for which the time-delay and cross sections are presented in the next subsection (figures 4.12 and 4.13, respectively), and values available in the literature.

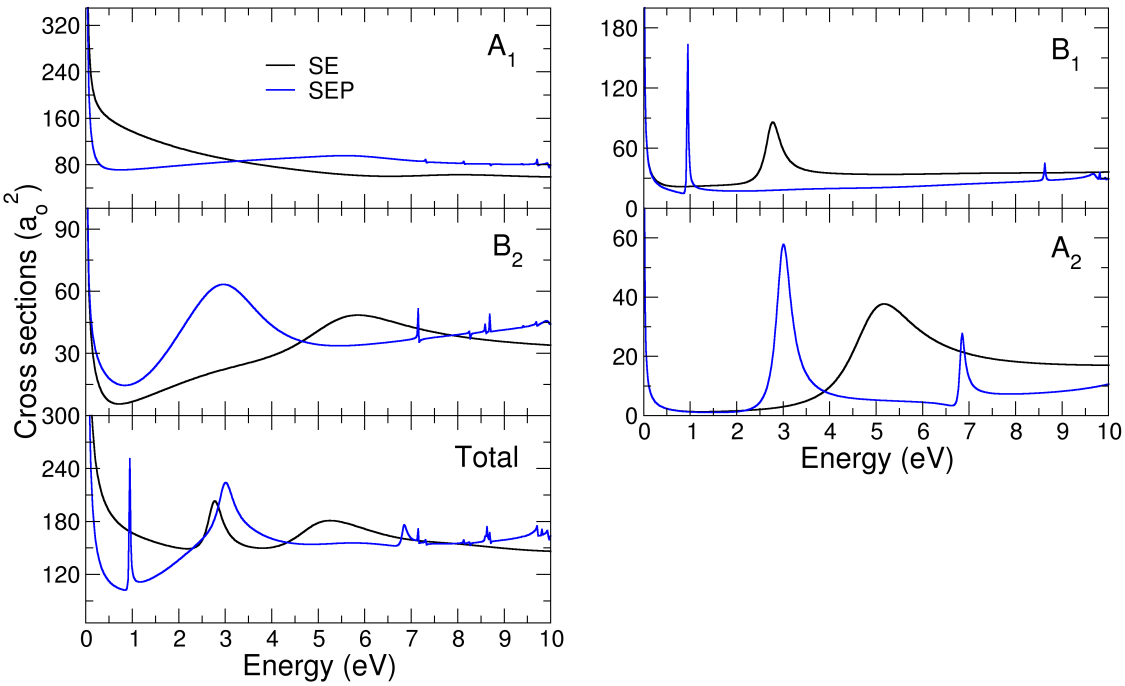

Figure 4.11: Cross sections as a function of electron energy, calculated at SE (full black line) and SEP (full blue line) level, using the parameters listed in table 4.5 for the irreducible representations indicated in the panels. The total cross section is shown in the bottom panel.

Table 4.6: Positions and widths (in brackets) in eV of the low-lying shape resonances in thiophene taken from our time-delay analysis. The SEP results were calculated for 35 and 41 VO, whereas the CC calculation used 70 VOs. We list the calculated results from da Costa *et al.*[126] obtained using the SCM-PP method, Vinodkumar *et al.* [148] (R-matrix method) and the VAE obtained by Regeta [47] through the scaled Koopman's theorem; the experimental resonance positions were obtained by Asmis [132] and Modelli and Burrow [146].

	Present results			Other calc.			Exp.	
Resonances	SEP		CC	VAE [47]	[126]	[148]	[132]	[146]
	35 VO	41 VO	70 VO					
π_1^* (B_1)	0.949	0.80	1.114	0.95	1.00	2.51	1.27	1.15
	(0.035)	(0.020)	(0.05)	-	(0.33)			
σ^* (B_2)	2.990	2.51	~1.5	2.11	2.78	18.69	-	-
	(2.35)	(2.107)	(2.26)	-	(1.10)	-	-	
π_2^* (A_2)	2.993	2.87	2.909	3.10	2.82	4.35	2.83	2.63
	(0.438)	(0.43)	(0.48)	-	(1.28)			

The positions of the resonances calculated at SEP level agree well with those of da Costa *et al.* [126] calculated at the same level. The geometry they used was slightly different to ours (the average difference in the bond lengths is ≈0.02Å), so we performed SE tests that showed this leads to shifts smaller than 0.1 eV in the resonance positions. These observations allowed us to prove that, unlike *p*-BQ studied in the previous chapter, the resonance positions in thiophene are much less geometry dependent. The positions of the π^* resonances also agree reasonably

well with the vertical attachment energies (VAE) determined from the application of the scaled Koopman's theorem using Hartree-Fock orbitals obtained with the 6-31G* basis set [47]. The position of the σ^* resonance determined from the VAE is significantly lower than that obtained from SEP scattering calculations. The results of Vinodkumar *et al.* [148], however, overestimate the majority of resonance positions. This is also the case for the core-excited ones, most of which appear at energies above thiophene's ionization threshold. This can have two reasons: (i) their calculations are describing the polarisation effects poorly; and/or (ii) their excitation energies for the parent states are much higher than in experiments. As we believe their results are incorrect, they will not be presented and/or discussed throughout the remaining of this chapter.

The positions of the π^* resonances determined experimentally are in good agreement among themselves and with the theoretical results. For reasons explained below, we present our calculations at SEP level using two different numbers of VOs. The effect of increasing the number of VOs by only 6 is negligible in the A_2 π^* resonance, as shown in table 4.6, but lowers the B_1 π^* one by around 0.15 eV and the σ^* resonance by around 0.4 eV.

Prior experience of describing π^* shape resonances in molecules containing a carbon ring [46, 152] (see also chapter 3) indicates that these resonances are better described in SEP calculations where sufficient L^2 configurations can be included to describe polarization accurately. Therefore, it is commonly seen in our calculations that the positions of pure π^* shape resonances determined using the CC method are higher than those determined in SEP calculations, as is the case here for the first π^* resonance. When this is not the case, the fact is used to identify the resonances as mixed core-excited shape because it is understood that it is the inclusion of excited states in the close-coupling expansion that improves the description of the resonance, lowering its position. The σ^* resonance appears at significantly lower energy in our CC calculation. This behaviour would be interpreted as an indication that the σ^* resonance has mixed character. This is unlikely for two reasons: (i) the lowest excited states is at 3.7 eV in our calculation, more than 2 eV above this resonance; and (ii) being below its excited parent state the resonance could only decay to the ground state. This tends to make resonances longer lived and therefore narrow, which is not the case here - the σ^* resonance is more than 2 eV wide. One could argue that this behaviour may simply be due to the wrong number of VOs being used in the calculations. However, as shown, our choices lead to π^* resonances with positions in very good agreement with the experiments. As table 4.6 shows, increasing the number of VOs in the SEP calculation lowers the π^* resonances below their experimental positions. Inclusion of fewer VOs in the CC calculation leads either to fairly small changes (we tested 50 VOs and the upwards shift for all three resonances is of the order of 0.2 eV); or a shift that makes agreement for the π^* resonances much worse (when 30 VOs are used, the σ^* resonance is centred, in the time-delay, around 2.3 eV. However the π^* resonances appear at approximately 1.5 and 3.3 eV).

Taking into consideration the previous observations, we believe that our usual procedure of determining the best number of VOs to include in the calculations (including VOs until a reasonable agreement with experiment is reached for the lowest π^* resonance) cannot be applied here. This may happen for two reasons: (i) unlike our earlier molecules, this target has a

mix of σ^* and π^* resonances; (ii) a more subtle effect related to the polarization description is at play. Careful investigation of our SE/SEP and CC calculations indicated that the improvement of polarisation description has a bigger effect on the σ^* resonance at all levels. However, whereas when polarisation is included in an SE calculation (when 35 VOs are used in the SEP model), the shift is of around 2.4 eV for the σ^* resonance and around 1.8-1.9 eV for the π^* ones, in the CC case (comparing a calculation where no VOs are used with the one using 70 VOs[4]) the shift for the σ^* resonance is around 2.5 eV, but for the π^* ones is of 1.2-1.4 eV. Therefore, we conclude that it is possible that our CC calculation with 70 VOs overestimates the polarisation effect in the B_2 symmetry, placing the σ^* resonance too low in energy. As a result from these observations, we cannot conclude confidently where the σ^* resonance should appear in experiments: Modelli and Burrow's comment [146] would put it closer to the 1.5 eV of our CC calculations, but the calculations of da Costa *et al.* and VEA indicate a position above 2 eV.

It is worth noticing that the peak associated to the σ^* resonance in the total cross section calculated at CC level appears around 0.5 eV higher than in the time-delay, as presented in figures 4.13 and 4.12, respectively. However, this is not the case for the SEP calculations, where the difference in position is around 0.1 eV. We believe this indicates the CC calculations are modelling a strong contribution of non-resonant scattering for the B_2 symmetry that shifts the resonance peak in the cross sections.

4.5.2 High energy resonances

The time-delay obtained at CC level is presented in figure 4.12. From a general observation, we rapidly identify the two π^* resonances described in the previous subsection, as well as the broad σ^* resonance of B_2 symmetry. A prominent peak at 6.95 eV is also easily identifiable in every symmetry in figure 4.12, corresponding to one of our excitation thresholds (that are very often visible as narrow peaks/spikes in the time-delay).

The first panel in figure 4.12 presents the results for symmetry A_1. We observe two broad peaks corresponding to physical resonances, at 7.9 and 9.5 eV. It is hard to tell whether there are corresponding peaks at SEP level (figure 4.10), but since no higher energy resonances appear in our SE calculation, we believe these are pure core-excited resonances, as confirmed by the peaks in the inelastic cross sections seen in the upper left panel in figure 4.13. In addition, a wide structure is visible in the SEP time-delay centred around 5.7 eV. The feature is less obvious in the CC time-delay and both elastic and inelastic cross sections, but the analysis of the second largest eigenvalue of the **Q**-matrix does indicate a peak centered around a similar energy. Investigation of the orbitals that contribute to its description indicate that they have some contribution of CH bond character. The measured excitation function for the first triplet states (see figure 4.8 in section 4.1) displays a small band at 4.2 eV to which experimental considerations would assign B_1 symmetry and shape character, although no corresponding structure was found by Asmis. It

[4]Note that even when no VOs are used in the CC calculation, the inclusion of excited states, and some L^2 functions already describe some polarization.

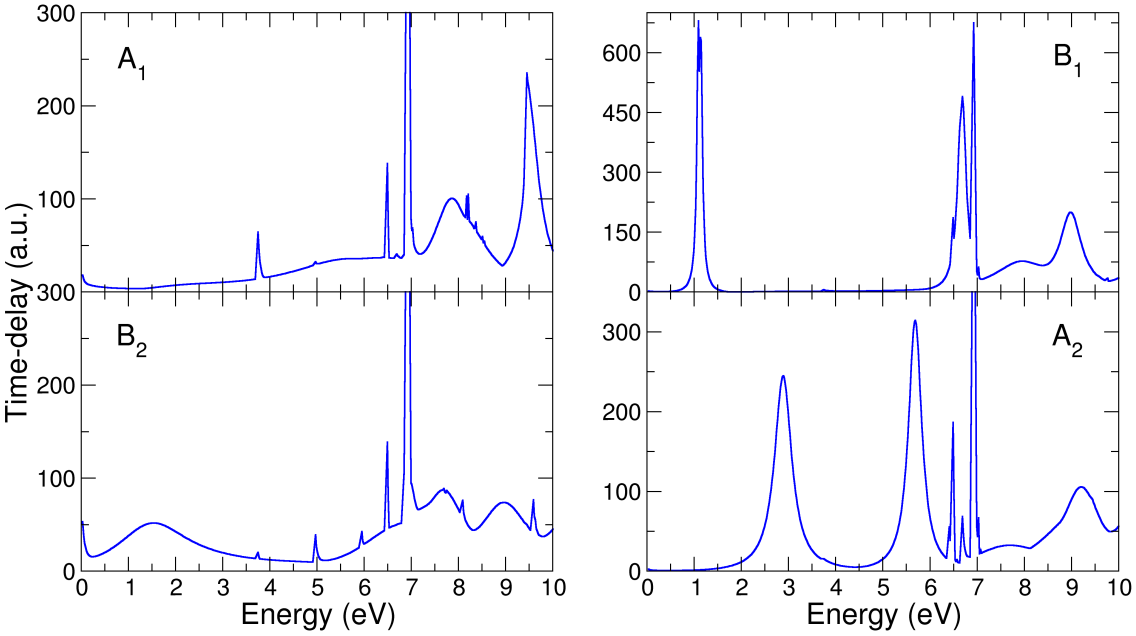

Figure 4.12: The largest eigenvalue of the **Q**-matrix (time-delay) as a function of electron energy for the four irreducible representations of the C_{2v} point group. The calculations were performed at CC level with the UKRmol suite, using a deletion threshold of 10^{-7}, $l_{max} = 5$, the 6-311G** basis set and $a = 15a_0$.

is possible that this experimental peak corresponds to this resonance, despite the inconsistency in the symmetry.

As for the B_2 symmetry, besides the already discussed σ^* resonance, two other peaks appear in the CC time-delay at around 7.7 and 9 eV. These correspond to core-excited resonances. In addition, there is a feature at ~6.9 eV that is hidden in figure 4.12 as it overlaps with the peak corresponding to the 7.7 eV resonance, but corresponds to a resonance too. This is confirmed by the analysis of the eigenphase sum. No resonances appear in the SE calculation above the σ^* shape resonances, so all the B_2 resonances (except the σ^* one) are of core-excited character. The inelastic cross sections (see figure 4.13) is not very clear, but two features can be seen at ≈8 and 9 eV, which is in agreement with the two resonances seen in the time-delay.

The upper right panel in figure 4.12 corresponds to the B_1 symmetry. This is where the lowest-energy π^* resonance appears. At higher energies, three more resonances are observed in the time-delay analysis: at 6.7 eV, near a threshold, there is a very well defined peak corresponding to a core-excited resonance; a broader feature appears at almost 8 eV with core-excited character; and finally, at 9 eV it is possible to observe a well defined peak. Interestingly, a peak is visible slightly above at SEP level; this peak is much wider than the ones we identify as pseudoresonances, so we believe it is likely to be physical. The analysis of the branching ratios indicates that all of these resonances possess mixed shape core-excited character, although they are not visible in the elastic cross section (see figure 4.13).

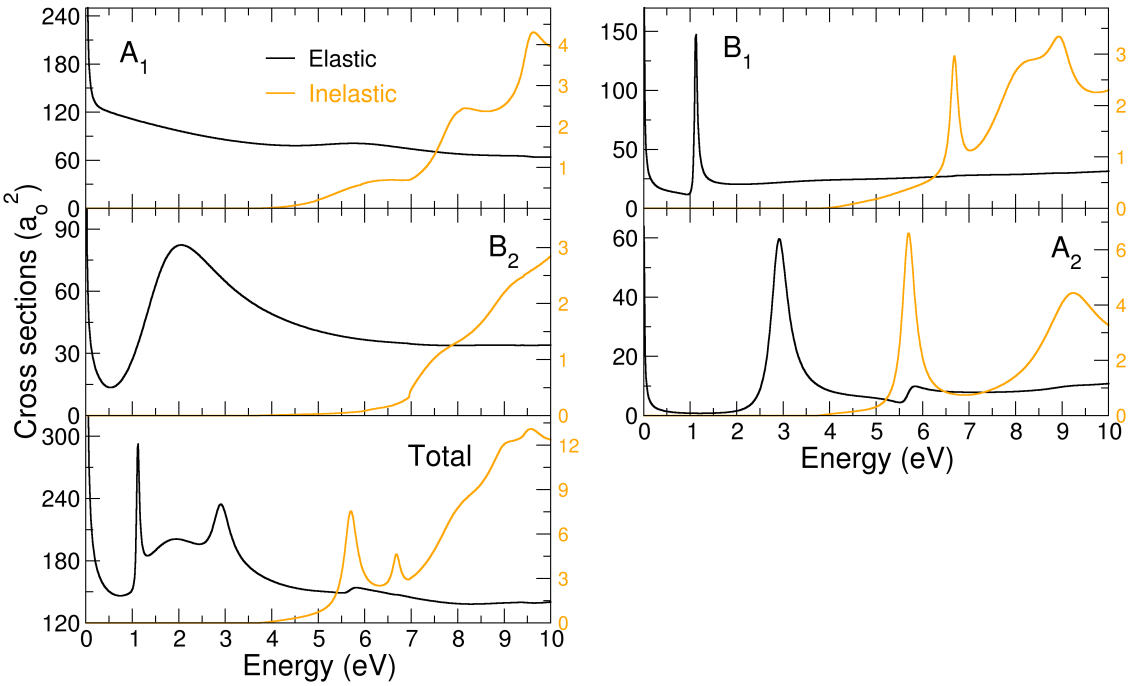

Figure 4.13: Cross sections as a function of electron energy, calculated at CC level using the parameters listed in table 4.5. The full black line corresponds to the elastic cross section and the full orange line corresponds to the inelastic one. The total cross section is shown in the bottom panel. Note that the left side *y*-axis scale (in black) corresponds to the elastic cross section, whereas the right side one (in orange) corresponds to the inelastic cross section.

Finally, the A_2 symmetry shows the second shape π^* resonance discussed earlier and a second resonance present around 5.7 eV in the CC calculation that has its corresponding peak at SEP level appearing at almost 1 eV higher. This resonance possesses mixed shape-core-excited character, as confirmed by its presence in the elastic and inelastic cross section (see figure 4.13). Another resonance, of core-excited character, is located at 9.2 eV. The structure between 6 and 7 eV is hard to discern: it may just correspond to the thresholds or be linked to Feshbach resonances.

Table 4.7 summarizes the resonance positions and widths calculated at CC level, as well as the experimental positions obtained from EELs spectra, presented in section 4.4.3. It is not surprising that the majority of the resonances identified in our calculations cannot be seen in the EELs experiments: not all core-excited resonances have a strong effect in the electronic excitation cross sections. Also, our calculated resonances that are also visible in the EELs spectra appear, as expected, in the excitation function of their parent states (see figure 4.8). The 1^2A_2 one appears in the T1, the 1^2B_1 appears both in T1 and T2, the 2^2B_1 appears again in both T1 and T2 and the 2^2A_2 appears in all three. Of the resonances that are not seen in the experimental excitation functions, only the 3^2B_1 (at around 9 eV in our calculations) has either the T1, T2 or S1 as the main parent state (specifically, the T1).

Our results are also in good agreement with the ones obtained by Asmis [132] using the same experimental method.

Table 4.7: Positions and widths in brackets (in eV) of the higher energy resonances in thiophene. Also listed are the experimental positions from the EELs measurements presented in section 4.4.3, and those obtained by Asmis [132]. These results are presented in ranges, determined from the positions of the peaks in the excitation functions for two angles (see figure 4.8). CE stands for pure core-excited resonances, MCES for mixed core-excited shape resonances and gs for ground state. The most likely parent states (PS) have been obtained from the branching ratios (when possible).

Res.	E_R (width)	Character	PS	EELs	[132]
2^2A_2	5.695 (0.329)	MCES	1^3B_2, gs	5.4-5.5	5.38
2^2B_1	6.70 (0.172)	CE	1^3A_1,1^3B_2	6.4-6.45	6.22
2^2B_2	6.9 (1.85)	CE	-	-	-
3^2B_2	7.72 (1.15)	CE	1^3A_2	-	-
1^2A_1	7.87 (1.00)	CE	1^1B_2,1^1B_1	-	-
3^2B_1	7.96 (1.20)	MCES	1^3B_2,1^3A_1, gs	7.3-7.5	7.39
4^2B_2	8.98 (1.35)	CE	1^1B_2,1^1A_1	-	-
4^2B_1	9.01 (0.58)	MCES	1^3B_2,1^1B_2, gs	-	-
3^2A_2	9.22 (0.95)	CE	1^3A_1,2^3A_1,1^3B_2	8.0-8.1	7.93
2^2A_1	9.48 (0.2)	CE	1^3A_2,1^1A_2	-	-

We could not confidently identify any Feshbach resonances in thiophene, although their presence cannot be completely discarded.

4.5.3 Link with DEA results

As far as we know, the only DEA study for thiophene was performed by Muftakhov *et al.* [127] who recorded mass spectra in the gas phase in the energy range of 0-12 eV. They interpreted the peaks in these spectra as corresponding to 7 resonant states mainly of Feshbach character, a couple of which lie above the ionisation threshold and therefore, are expected to correspond to core-excited resonances in which the electron is excited from a deeply bound orbital.

The results from their experiments are difficult to correlate to the resonances we identified, as we have experienced for other targets (see, for example, chapter 3). However, some links can be made, as shown in table 4.8: the ion yields for hydrogen-loss and the formation of a fragment with mass 32 have a peak around 3.4-3.5 eV. This peak can only be linked to the higher lying pure shape π^* resonance located around 2.9 eV. Another possibility is that this peak would correspond to a narrow Feshbach resonance that we have failed to identify, and whose parent

is the lowest excited state (the 1^3B_2). The ion yields for several fragments (among them the one coming from single hydrogen-loss) present peaks at around 5.3, 5.5 and 5.8 eV. In our calculations, the only resonance that could be linked to these peaks is the 1^2A_2 at ~5.7 eV, seen by the EELs closer to 5.4-5.5 eV. Peaks in the mass spectra in the range 6.15-6.4 eV could be linked to the 1^2B_1 resonance that we observe at 6.7 eV and that the EELs shows at 6.4-6.45 eV (the 1^2B_2 resonance around 6.9 eV is much shorter lived, so it is less likely to lead to dissociation). Finally, the peaks in the 8.5-8.9 eV range can be linked to one (or several) of the resonances we describe in the 8.98-9.45 eV range. Muftakhov *et al.* do not report peaks below 3.3 eV.

Table 4.8: DEA peaks [127] (or energy range where peaks were identified) and corresponding resonances identified in our calculations. Please note that above a certain energy, it is impossible for us to confidently link a DEA peak with a specific resonance and therefore, we assigned them to any of the resonances in the corresponding energy range.

DEA peaks	This work	
	Position (eV)	Symm.
1.5-1.8	1.114	1^2B_1
3.1	2.909	1^2A_2
5.1-5.85	5.695	2^2A_2
6.0-6.4	6.7	2^2B_1
8.5-8.9	8.98-9.45	-

4.6 Chapter remarks

We have performed SE/SEP and CC calculations for thiophene, providing a detailed resonance spectrum within the energy range of 0-10 eV, as well as integral and differential elastic, inelastic and excitation functions cross sections for the same energy range. Our results were then compared with those obtained with other theoretical (SMC-PP and IAM-SCAR) and experimental (EELs) methods, and the agreement was found to be, in general, very good.

From section 4.4.1, we observed that our integral elastic cross sections are in good agreement with the ones from da Costa *et al.* [126], specially in shape. The biggest difference is observed at very low energies, where their cross sections are lower than ours. Although we have not presented those results in this thesis, we have complemented and compared our integral cross sections with several variations of the IAM-SCAR method, as can be seen elsewhere [49].

Our calculated positions of the pure shape resonances agree well with previous calculations and experiments, although some uncertainty persists about the accurate position of the σ^* resonance. The comparison with the EELs measurements corroborate our calculated core-excited resonances. Comparison of the measured and calculated excitation functions for two different scattering angles and two different energy losses show an excellent agreement: both their size and shape agree very well, where it is clear which states are being excited, due to their energy separation; for the third one, the agreement is not so good. This indicates that the calculations are modelling the physics of the collision process accurately, despite the fact that our usual strategy for determining how to model the polarisation effects does not seem to

work particularly well for this system. It also demonstrates that it is now possible to provide quantitatively accurate cross sections for low energy electronic excitation of low-lying states of biologically relevant molecules.

Four core-excited and mixed core-excited resonances described by our calculations are visible in the excitation functions, although, as expected, our results appear higher in energy. These are the longer lived (and consequently narrower) resonances we identified. A feature is visible at around 4.2 eV in the excitation function, that we believe could correspond to a poorly described resonance of A_1 symmetry.

To finalize, we were also able to link some of the core-excited resonances to the DEA spectra of Muftakhov *et al.* [127], but for the higher-lying resonances this assignment is not straightforward, as our calculated resonances are very close in energy.

It is important to note that, contrary to what was observed for *p*-BQ in the previous chapter, there are targets where the agreement between our calculated data (both resonances positions and cross sections) and experiments is very good, as demonstrated here for thiophene (a similar agreement has been seen before for other molecules [149, 153, 154, 155]).

Table 4.1: Vertical excitation energies (in eV) for the eight low-lying excited states of thiophene obtained including different states in the state-averaging procedure and using different active spaces, for the diffuse basis set. Also listed are the respective ground state energies and dipole moments. A.S. stands for Active Space; Conf. corresponds to the number of configurations generated for the A_1 symmetry; and S.A. indicates the choice of states we averaged. X: $[2A_1,3B_2,1B_1,1A_2]$, Y: $[2A_1,1B_2,0B_1,0A_2]$ and Z: $[2A_1,2B_2,1B_1,1A_2]$. Note that all the states averaged are singlets. As the state averaging Y provided the biggest disagreement with the experiments for the higher energy excitation thresholds, we did not test it with any other active spaces. The numbers in bold are the ones for the SA-CASSCF model we chose as the best set to perform our calculations. The ground states energies labelled $^{6-311G**}$ and $^{cc-pVDZ}$ were calculated at MP2 level using the respective basis sets [108].

A.S.	(10,9)			(6,7)		(8,8)		
Conf.	1368			139		468		Exp
S.A.	X	Y	Z	X	Z	X	Z	
1^3B_2	**3.722**	3.728	3.690	3.609	3.506	3.718	3.729	3.7-3.75
1^3A_1	**4.943**	5.008	5.022	4.901	4.974	4.937	4.965	4.6-4.62
1^1A_1	**5.916**	5.950	5.999	5.999	6.052	5.980	5.987	5.41-5.48
1^3B_1	**6.371**	9.606	6.205	6.290	6.172	6.093	6.094	5.9
1^3A_2	**6.457**	9.772	6.342	6.181	6.182	6.132	6.152	5.9
1^1B_1	**6.660**	10.049	6.488	6.557	6.431	6.399	6.415	-
1^3A_1	**6.816**	9.696	7.094	6.983	7.340	6.843	6.855	-
1^1A_2	**6.877**	10.233	6.733	6.554	6.561	6.519	6.538	5.9-6.0
E	-551.4281	-551.4371	-551.4289	-551.3927	-551.3953	-551.4050	-551.4059	$-552.0372^{6-311G**}$ $-551.9841^{cc-pVDZ}$
μ	0.549	0.607	0.546	0.911	0.788	0.659	0.653	0.55 [128]

CHAPTER 5

ELECTRON COLLISIONS WITH ALANINE

This chapter is focused on electron collisions with α-alanine (Ala, CH_3CHNH_2COOH), the smallest chiral aminoacid and the second smallest from the 20 natural aminoacids, after glycine that has already been extensively studied [156, 157, 158, 159].

The growing interest in the shape and spectra of conformationally flexible aminoacids comes from several reasons: the search for the origin and signs of life in interstellar space [160], the desire to establish the intrinsic tautomeric and conformational energies and the underlying potential energy surfaces and hypersurfaces of these species, with the aim of providing some insights into peptides and proteins; and finally, to stimulate and provide vital data for the development of better, more efficient and more reliable computational methods.

Compared to the other molecules studied in this thesis, alanine represented a challenge specially due its lack of symmetry and its size. The comparison between our results and experimental data was also a challenging task, as alanine presents a large number of conformers energetically close - we have focused our studies on the more stable one, that we will refer to as *I*, with the chemical structure represented in figure 5.1.

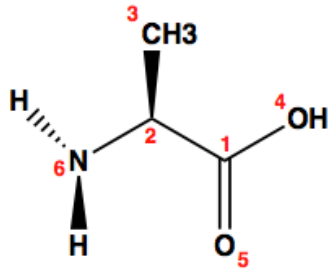

Figure 5.1: Chemical structure of conformer *I* of alanine. Note the stereochemistry.

The results presented were obtained using the UKRmol+ suite, described in chapter 2, as opposed to the UKRmol one we used in other chapters, and we will explain why in the next

pages. None of the cross sections presented here are Born corrected, as our main focus was resonance identification.

5.1 Geometry and electronic structure of alanine

Alanine has 48 electrons and belongs to the C_1 point group. The conformer we are interested in has a vertical ionisation energy of 8.8 eV [108], a first electronic excitation threshold of 5.4 eV [161] and its spherical polarisability is around 45 a_0^3 [162]. Its dipole moment is 1.4 Debye [163]. Alanine is solid at room temperature and its crystal has a zwitterionic form, vaporizing at temperatures near 120C [164].

The electronic structure of gas phase alanine has been the subject of a large number of both experimental and theoretical works, that highlighted the importance of taking into account several low-lying structural conformers of this floppy molecule [163, 165, 166, 167, 168, 169, 170, 171, 172, 173, 174, 175], even in jet-cooled conditions, as studied by Blanco *et al.* in 2004 [176]. The general observation was that conformer *I* is the most stable (and consequently more abundant) compared to the other conformers and, therefore, the most sensible choice for our study.

From all of the studies regarding alanine's conformers, we based our work on the coupled-clusters single double (perturbative triples) CCSD(T) calculations (the so-called "gold standard") by Átila Császár in 1996 [163]. Through the potential energy surfaces analysis for neutral α-alanine, Császár found thirteen conformers, and determined several properties for them: accurate geometry, relative energies, rotational and quartic centrifugal distortion constants, dipole moments, harmonic vibrational frequencies and infrared intensities. His calculations involve zero-point vibrational energy corrections and were confirmed by the more recent *ab initio* calculations of Jarger *et al.* [177], although they are significantly different from the ones provided by Godfrey *et al.* in 1993 [166].

An earlier description of the electronic excited states of alanine was performed by Osted *et al.* in 2005 [178], who paid special attention to the valence excitation from the nonbonding lone-pair on the carboxylic oxygen atom to the antibonding π-orbital ($n_O \rightarrow \pi^*_{CO}$) and the first Rydberg excitation from the nonbonding lone-pair on the nitrogen atom ($n_N \rightarrow 3s$). They used a set of coupled-cluster methods, combined with augmented correlation consistent basis sets, and were able to describe nine electronic excited states within the 5.9-8.3 eV energy range.

After Osted's calculations, Kumar *et al.* [179] studied the infrared, Raman and electronic spectra of alanine, comparing their measurements with *ab initio* calculations. Their experiments locate the electronic thresholds around 2 eV below their calculations. Those calculations involved several methods (AM1, RHF and DFT) and basis sets (6-31G, 6-31+G* and 6-311++G**) and identified four singlet states within the energy range of 6.6-9.8 eV. Their calculations are in a good agreement with Osted's.

Abouaf [161] investigated the excitation of electronic states below the ionisation threshold of alanine and resonant vibrational excitation around 2 eV using the EEL technique. The five

singlet states he found between 5 and 10 eV were in good agreement with calculations from Osted *et al.*[178] and Kumar *et al.*[179].

All these results are presented in table 5.3 in section 5.3.1 along with our calculated vertical excitation energies.

In a side matter and taking into account the chirality of alanine (most relevant from the biological point of view), Tia *et al.* [180] recorded alanine's UV/VUV gas phase ion photochemistry and discussed it within a prebiotic context. The photostability of this aminoacid against fragmentation is important in terms of survival during the journey from the interstellar medium, where aminoacids have probably been formed, toward Earth.

5.2 Earlier work on electron collisions with alanine

Contrary to the large amount of studies concerning its conformers, there is significantly less information on electron collisions with alanine and on its resonances.

An early attempt to identify the temporary negative ions of alanine was made by Aflatooni *et al.* [181], who used ETS to measure vertical attachment energies for the formation of low-lying temporary anion states in the gas phase. The resonance they identified at 1.8 eV is linked to the electron attaching to the empty π^* orbital of the carboxylic group. The same resonance was identified later by several other groups.

The first cross section measurements were performed by Marinković *et al.* [182], in the energy range of 40-80 eV and scattering angles from 10 to 150C. These authors measured directly the DCS using a crossed beam system, and derived the absolute cross sections by normalising to theoretical results, obtained with IAM-SCAR [183], up to 10000 eV. The agreement between their results is very good.

Panosetti *et al.* [184] were interested in radiation damage mechanisms in biomolecules, so the main focus of their study was resonance fragmentation. They reported integral elastic cross sections at the equilibrium geometry for the four smallest aminoacids. Several resonances were identified, among them a resonance centred at approximately 3 eV detected for all aminoacids, corresponding to the electron attaching to the empty π^* orbital of the carboxylic group, as reported before by Aflatooni *et al.* [181]. The authors did not find dissociative stabilisation as coming from the direct dissociation of the hydrogen atom, while indicate instead that a direct dissociative stabilisation is more likely to occur along the C-OH bond with detachment of the hydroxyl group.

Fujimoto *et al.* used the R-matrix method to calculate differential and integral elastic cross sections, as well as identify resonances in two successful works: first for the two lowest conformers [185] of alanine and two years later, for the nine lowest [186], from 1 to 10 eV. Their averaged cross sections take into account relative populations of different conformers. In order to identify resonances they used the analysis of the eigenphase sums, and an automated fitting procedure of the Breit-Wigner formula. At least two resonances were identified for all conformers (some of them revealed the presence of a third resonance). We used their scattering models as a starting point for our studies presented in this chapter (see section 5.5).

One of the most recent collision studies for alanine was performed by Nunes *et al.* [187], using the SMC-PP for both positron and electron elastic scattering. They also identified two resonances for conformer *I*, obtaining an excellent agreement in resonance positions with Fujimoto's results.

Due to the potential of this target to provide insights for more complex biosystems, some groups have looked at the DEA process in alanine: Ptasińska *et al.* [188] used a high resolution electron energy monochromator to study the DEA spectra by means of the mass spectrometric detection of the product anions. The group identified a signal related to the low-energy π^* shape resonance observed before, and two other peaks that the authors claim to be related with core-excited resonances.

Scheer *et al.* [189] measured total DEA cross sections for alanine and other aminoacids at energies below the first ionization threshold. The magnitudes of their cross sections were determined by observation of positive ion production and normalisation to ionization cross sections calculated with the binary-encounter-Bethe method. The group observed the same fragmentation pattern as Ptasińska *et al.*.

Finally, Vasil'ev *et al.*[190] studied the resonant electron capture mass spectra of aliphatic and aromatic aminoacids, particularly the anion fragmentation of alanine. They observed a tendency of alanine to form the dehydrogenated parent anion at low energies.

The main conclusions of these studies are discussed and compared to ours in section 5.5.

5.3 Calculation details

5.3.1 Target description

To perform our calculations, we have used the ground state equilibrium geometry of conformer *I* described by Császár, optimized at MP2 level of theory, with 6-311++G** basis set [163]. In order to obtain optimal target orbitals for the description of the scattering process three basis sets were tested: 6-311G** ("less diffuse"), 6-311++G** ("more diffuse") and cc-pVDZ ("compact"). We also performed some tests using the 6-31G* basis set. We used the HF and the SA-CASSCF methods to generate the target orbitals - these calculations were performed using MOLPRO [70].

Table 5.1 presents the ground state energies obtained at HF and CASSCF level for all basis sets, as well as the dipole moments, and the comparison with the most accurate results from literature. As it is possible to observe, our energies are higher than the most accurate value, especially for the 6-31G* and cc-pVDZ basis sets. This is a very good indicator that some polarised and diffuse functions are needed to accurately describe our target molecule, as confirmed when the more diffuse basis set is used. On the other hand, our calculated dipole moments are all smaller than the value measured by Godfrey *et al.* [166], with the best agreement found for the more diffuse basis set, when CASSCF orbitals were used. This is also the case for the ground state energy, and it is somehow expected if we analyse alanine's structure: it possesses intramolecular interactions, like hydrogen bonding, as well as steric effects, which can only be described accurately whenever we include both diffuse and polarised functions.

Table 5.1: Energies (E, in Hartree) and dipole moment (μ, in Debye) of the ground state of alanine in its equilibrium geometry, obtained at HF and CASSCF levels, for each of the tested basis sets. Our CAS model used an active space of (8,6). Also presented are the more accurate results of Császár [163] (using 6-311++G**MP2/cc-pVTZ RHF model) for the ground state energy and the experimental dipole moment from Godfrey *et al.* [166]. The calculation with the smallest basis set, 6-31G*, was performed in order to replicate Fujimoto's results [186], and therefore was performed only at HF level.

	Level	6-31G*	6-311G**	6-311++G**	cc-pVDZ	Best value
E	HF	-321.83406	-321.93107	-321.93869	-321.87150	-321.967 [163]
	CASSCF	-	-321.93612	-321.95061	-321.87730	
μ	HF	1.28	1.26	1.35	1.49	1.8 [166],1.4 [163]
	CASSCF	-	1.28	1.59	1.53	

The results presented in table 5.1 using the CASSCF orbitals were obtained after a series of tests to find the best CAS model. Since the more diffuse basis set provides better ground state energies, we will, for simplicity, present the results for that basis set only.

Table 5.2 lists the energies, in eV, for the lowest six electronically excited states of alanine using different CAS models, and averaging a different number of states. Experimental data is also presented for comparison.

Table 5.2: Vertical excitation energies (in eV) obtained using different states in the state-averaging procedure and different active spaces, for the 6-311++G** basis set. Also presented are ground state energy from Császár [163] and dipole moment obtained by Godfrey *et al.* [166]. The experimental excitation energies obtained by Abouaf [161] are also presented. A.S. stands for Active Space; Conf. corresponds to the number of configurations generated and S.A. represents the number of states we averaged. Note that all the states averaged are singlets.

A.S.	(8,6)			(8,8)		(10,6)		
Conf.	105			1764		21		Exp
S.A.	1	3	4	3	4	3	4	
1^3A	10.213	5.550	**5.513**	5.335	5.105	5.379	7.160	5.4
1^1A	15.696	5.835	**5.828**	5.568	5.346	5.662	7.269	6.2
2^3A	14.354	6.453	**6.456**	6.513	6.301	6.424	8.163	7.15
3^3A	21.445	6.598	**7.059**	10.363	6.699	8.791	8.675	7.85
2^1A	16.992	6.741	**7.197**	6.663	6.467	9.267	8.256	-
4^3A	25.074	10.287	**8.211**	12.459	8.642	11.642	16.282	8.35
E	-322.01	-321.95	-321.95	-321.98	-321.94	-321.95	-321.92	-321.967 [163]
μ	1.00	1.38	1.59	1.89	2.32	2.13	2.17	1.8 [166]

As shown, the differences between each model are very significant. When we averaged only the ground state using the (8,6) active space, the excitation thresholds were unphysically high, so we discarded that option for the other tests.

Since the number of configurations included in our scattering calculations scales very quickly with the size of the active space, we tried to get the best compromise between accuracy

and size. That was obtained with an active space of (8,6) - 8 valence electrons distributed among 6 orbitals, that include the π and π^* orbitals corresponding to the carboxylic double bond and 4 nonbonding orbitals of the oxygen atoms, and averaging 4 states (marked in bold in table 5.2). The number of configurations generated is small and the ground state energy and dipole moment are in a reasonable agreement with the literature. In general, for the other models, some states were in a better agreement, whereas others got worse, or the number of configurations generated was bigger.

The eighteen lowest excitation thresholds obtained with our CAS model (8,6), 4 averaged states, and several basis sets are listed in table 5.3. The first three states have very similar thresholds for all basis. As we go higher in energy, the differences start to increase and our description of the electronic excited states gets worse. Once again, it is the more diffuse basis set that provides the better agreement with earlier calculations [178, 179], and the experiments [161], proving to be the best option to perform our scattering calculations. This conclusion is expected, as alanine possesses many states with Rydberg character, and therefore, the more diffuse the basis set is, the better their description.

Table 5.3: Vertical excitation energies, in eV, for the electronic excited states of alanine used in our scattering calculations. The second, third and fourth columns correspond to our SA-CASSCF calculations using the active space (8,6) and several basis set. Also presented are the results of Osted *et al.* [178] calculated using the CCSD/aD(T) model and Kumar *et al.* [179] using the CIS/6-31G model. The experimental results were obtained by Abouaf [161]. The states labelled with $_R$ possess Rydberg character.

	CASSCF			Theory		Exp.
State	6-311++G**	6-311G**	cc-pVDZ	Osted [178]	Kumar [179]	Abouaf [161]
1^3A	5.513	5.498	5.517	5.96	-	5.4
1^1A	5.828	5.804	5.828	6.64_R	6.68	6.2
2^3A	6.456	6.665	6.685	7.26_R	-	7.15
3^3A	7.059	6.806	7.092	7.46_R	-	7.85
2^1A	7.197	7.280	7.626	7.55_R	7.97	-
4^3A	8.211	8.369	8.473	7.88_R	-	8.35
3^1A	8.291	8.673	8.783	8.05_R	8.86	-
5^3A	10.256	11.377	11.657	8.3_R	-	-
4^1A	10.445	11.494	11.889	8.79	9.77	-
5^1A	10.771	12.167	12.345	-	-	-
6^3A	12.597	12.484	12.702	-	-	-
7^3A	12.77	12.595	12.9345	-	-	-
6^1A	12.786	12.756	13.052	-	-	-
8^3A	13.023	12.756	13.087	-	-	-
7^1A	13.03	12.875	13.265	-	-	-
8^1A	13.114	12.956	13.479	-	-	-
9^3A	13.295	13.155	13.646	-	-	-
9^1A	13.439	13.229	14.022	-	-	-

In general, as seen for other targets, our calculated excitation thresholds tend to be above

those in the literature due to several factors, as explained in previous chapters. However, for alanine, this is not the case for the first five excitation thresholds: up to 8 eV all of them are lower in energy than in the literature, with an average difference of 0.49 eV. This points out to a not-so-good description of the ground state, and consequently to an overestimation of its energy. As a consequence, the energy difference between the ground state and a particular electronically excited state appears to be smaller than it is in reality.

Both the ground state and the electronic states are calculated using the variational principle [52]. The difficulty of accurately representing these states increases when the number of valence electrons involved is bigger: increasing the size of the CAS model can be a solution (although it is easier to get out the computational limits) but there are situations where other methodologies need to be applied (as the use of the perturbative theory, for example).

5.4 Scattering

For the chosen 6-311++G** basis set, an R-matrix radius of $a = 18a_0$ was selected as the most appropriate by analysing the radial charge density of the target orbitals obtained with the program RADDEN. Including an extra partial wave ($l_{max} = 5$) in the continuum basis set made a significant difference when compared to $l_{max} = 4$, as seen in the cross sections calculated at SE level, plotted in figure 5.2. The inclusion of higher partial waves is a very successful procedure to verify if the features we are observing are physical or not, as "fake"peaks might appear due to the incompleteness of the partial wave expansion, and therefore, the use of an extra partial wave is crucial.

This is very clear in figure 5.2: the peak above 4 eV is described almost identically in both calculations; on the other hand, the "kink"seen at approximately 6.5 eV when $l_{max} = 4$ is used (and that seems to have resonant character verified through the eigenphase sum and the time-delay analysis), disappears when we increase to $l_{max} = 5$, proving the feature is not physical. On the other hand, the bump above 12 eV in the dashed blue curve does not disappear when we increase the number of partial waves, but moves to lower energies which points out to an improvement of its description - it corresponds to the smooth bump in the solid black line centred below 12 eV. Both of these are seen in the eigenphase sum and the time-delay analysis. For these reasons, $l_{max} = 5$ was used throughout this chapter.

The deletion threshold turned out to be crucial to ensure the correct description of all resonances, as shown below. We started with a fairly big deletion threshold of 10^{-7}, usually used for a radius of $a = 10a_0$. Gradually, we decreased it until 10^{-17}, where all available continuum orbitals were kept in the calculation. From 10^{-7} to 10^{-12} no differences were observed in the cross section, and only the first low-energy peak was observed. With 10^{-13} a second peak is visible at higher energies (around 8.7 eV), that moves almost 2 eV when 10^{-14} is used, as presented in figure 5.3, and that we identified later as a resonance. This peak keeps moving to lower energies as we decrease the deletion threshold to 10^{-17}. Since it is approaching the experimental position of the first π^* resonance, we can state the improvement of the calculation and consequently, a better description of the physics. To this date, we do not have a final explanation as to why

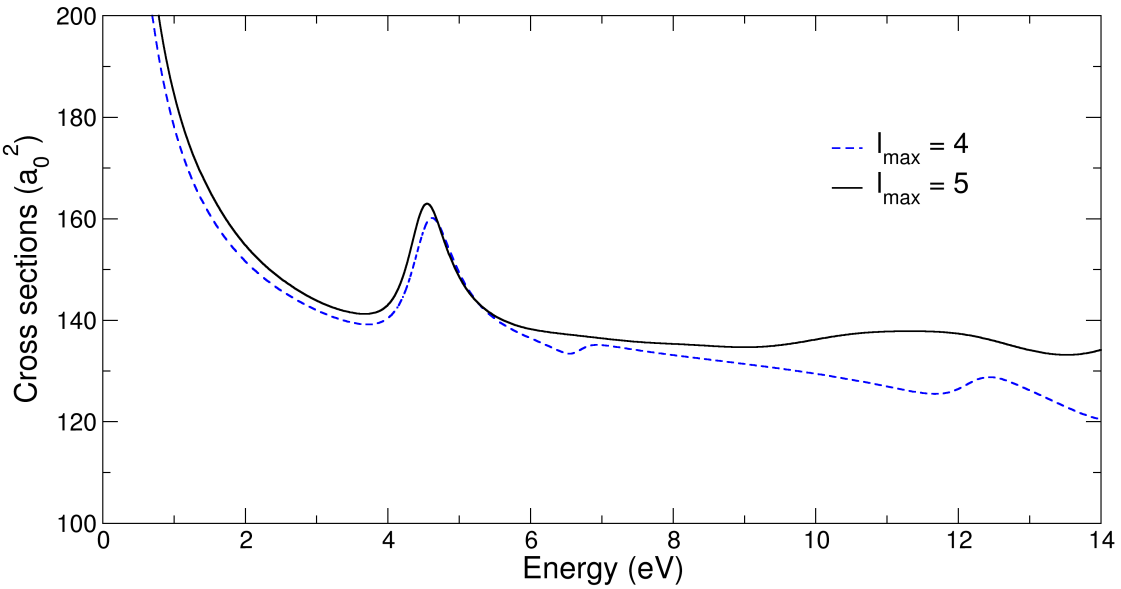

Figure 5.2: Elastic cross section as a function of electron energy for two SE calculations using the same parameters (6-311++G** basis set, deletion threshold of 10^{-17} and $a = 18a_0$), but a different number of partial waves. Both were calculated using the UKRmol+ suite. The dashed blue line correspond to the inclusion of partial waves up to $l_{max} = 4$, whereas the solid black line correspond to $l_{max} = 5$.

this particular resonance is so affected by the inclusion of continuum orbitals, but it could be related to an indirect improvement of the description of the polarisation and correlation effects, when more continuum orbitals are included in the calculation. For simplicity, we plotted in figure 5.3 only time-delays for the SEP calculations obtained using deletion thresholds of 10^{-13}, 10^{-14} and 10^{-17}. All other calculations presented in this chapter used the latter.

As mentioned earlier, all the calculations presented throughout this chapter were performed using the UKRmol+ suite. Although we had started our calculations using UKRmol, we identified later a problem in the evaluation of the integrals tails, performed by *gaustail* (see chapter 2, section **??**). This had a strong effect in the alanine calculations that was not observed for other targets, possibly due to its symmetry - whereas the other targets we have studied possess some symmetry, alanine is totally asymmetric. The results obtained using both codes are considerably different, as it can be observed for the cross section calculated at SE level plotted in figure 5.4. As UKRmol+ calculate the integral tails more accurately, we relied on it to perform the calculations presented here.

As explained previously, our scattering calculations do not exhibit convergence of the resonances positions with respect to the number of VOs included. Therefore, using the same procedure as in the previous chapter, we included in our calculations the lowest 40 and 70 VOs,

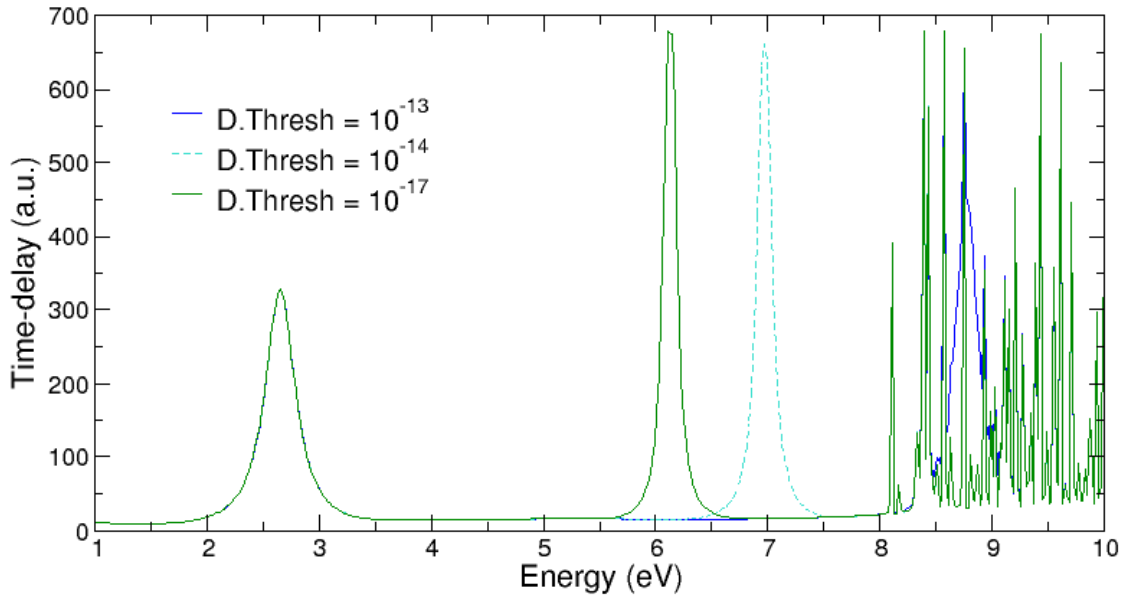

Figure 5.3: The largest eigenvalue of the **Q**-matrix (time-delay) as a function of electron energy. The calculations were performed at SEP level, using a deletion threshold of 10^{-13}, 10^{-14} and 10^{-17}. All calculations used 40 VOs, $l_{max} = 5$, the 6-311++G** basis set and $a = 18a_0$.

at SEP and CC level, respectively, as those produced the best agreement of the first resonance position with the experimental results of Aflatooni *et al.'s* [181].

Table 5.4 summarises the optimal parameters used for each one of the three models (SE, SEP, CC) to carry out the calculations presented in the remainder of this chapter.

Table 5.4: Parameters used for the SE, SEP and CC calculations presented in the remainder of the chapter.

Approximation	**SE**	**SEP**	**CC**
Basis set		6-311++G**	
Radius (a_0)		18	
Nr. Partial waves (l_{max})		5	
Del.Tresh.		10^{-17}	
Nr. Target states	1	1	19
Nr. VOs	10	40	70
Raf		50	90

Although it was not mentioned until here, *raf* is the propagation radius mentioned in chapter 2, from where the R-matrix is propagated from the outer to the asymptotic region. In our calculations we tend to use a *raf* default value of $50a_0$. However, some peculiar features as spikes and poorly defined peaks were observed at CC level when a finer energy grid was used. As we were using a very diffuse basis set and a large R-matrix radius, increasing the propagation

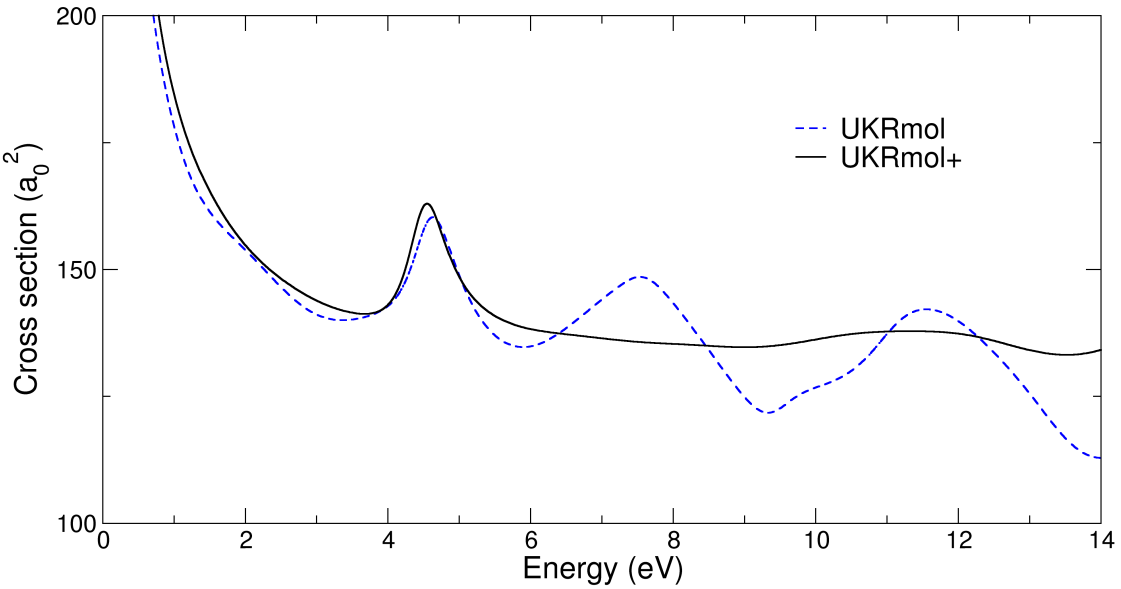

Figure 5.4: Cross sections as a function of electron energy. Both curves were obtained with the same parameters at SE level (the 6-311++G** basis set, 10 VOs, a deletion threshold of 10^{-17}, $l_{max} = 5$ and $a = 18a_0$). The full black curve was obtained using UKRmol+ suite, whereas the dashed blue curve was obtained using UKRmol.

radius enabled us to improve the quality of the calculation, as we observed.

5.5 Resonances

As we have explained in chapter 2, we generally use the investigation of the eigenphase sums, the cross sections and time-delay analysis to identify resonances. In this chapter we focus mainly on the last two, resorting the eigenphase sums in individual situations.

Below we describe in detail the shape and core-excited resonances we have identified, discussing their agreement with the literature.

5.5.1 Stability tests

Initial SEP calculations with the parameters described previously in table 5.4 produced very different cross sections from those presented by Fujimoto *et al.* [185, 186] in their recent R-matrix calculations. To understand this discrepancy, we run a calculation using Fujimoto's parameters (listed in table 5.5).

Figure 5.6 shows the results of this test: the full light blue line corresponds to the cross sections calculated by Fujimoto *et al.*; the dashed light blue line corresponds to our calculation using their parameters; and the full green line to our calculation with our parameters. Apart from the position of the first π^* resonance, that is fairly close, the differences are notorious: the

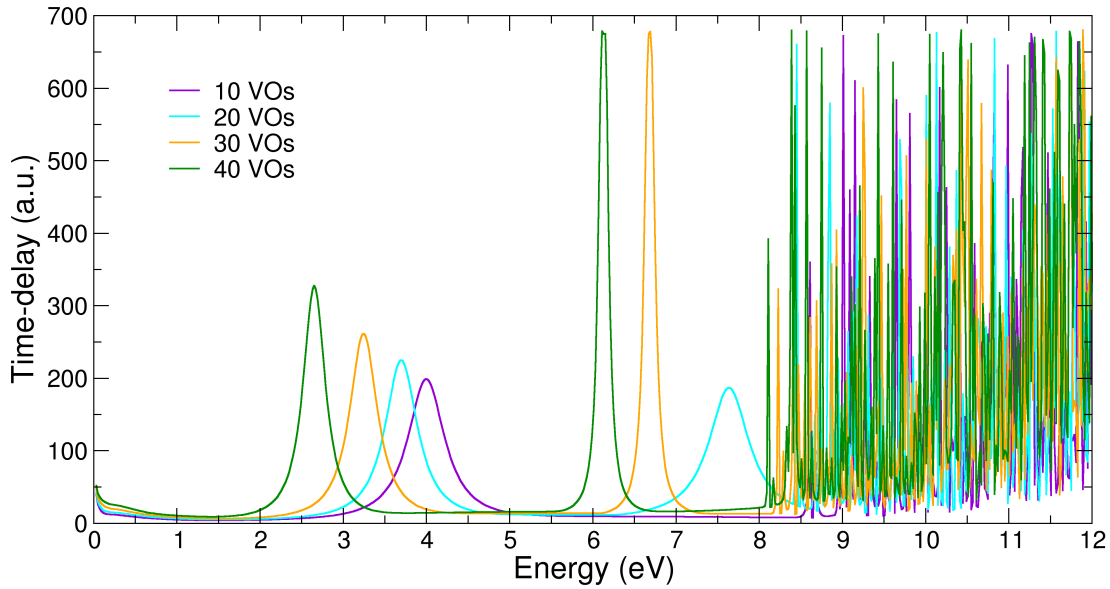

Figure 5.5: The largest eigenvalue of the **Q**-matrix (time-delay) as a function of electron energy. The calculations were performed at SEP level with UKRmol+ suite, using a deletion threshold of 10^{-17}, $l_{max} = 5$, the 6-311++G** basis set, $a = 18a_0$ and the VOs indicated in the figure.

Table 5.5: Parameters used by Fujimoto *et al.* [186]. No information was given regarding the deletion threshold, so we assumed 10^{-7} was used. The group also used the geometry provided by Császár [163].

Approximation	**SEP**
Basis set	6-31G*
Radius (a_0)	10
Nr. Partial waves (l_{max})	4
Del.Tresh.	10^{-7}
Nr. Target states	1
Nr. VO's	30

first evident discrepancy is the behaviour of the cross section at low energies, where Fujimoto *et al.* have not obtained the rapid increase typically observed in molecules with a dipole moment. Even though the researchers did not start their calculations at 0 eV, the tendency of the curve to decrease as it moves to lower energies is very clear. The absence of pseudoresonances in their calculations is also peculiar - at SEP level, the presence of these features is always expected above the first excitation threshold; these are clearly seen in our cross section above 8 eV. The third difference is the presence of a feature seen in our calculations with our parameters at approximately 6 eV, that is not seen neither in their calculations, or when their parameters are used by us.

However, although the scattering parameters might be responsible for the last two differences mentioned above, they were not the only difference between our calculations and Fujimoto's - at the time that group performed their calculations, there was a bug in the R-matrix codes: it was necessary to orient the dipole moment of the target molecule along the z-axis, otherwise it would not be taken into account properly [61, 191]. This explains the behaviour of their cross sections at low energies where the dipole moment has the bigger influence, and it is clearly not being accounted for as it should. Our calculations are not affected by this issue (as we were using UKRmol+ suite and, in any case, the bug was corrected in the UKRmol suite in 2015) and the dipole moment is fully accounted for.

Although we were using a more complete set of parameters, it does not necessarily mean the calculation is improving, as we could be pushing it to the boundaries of the implementation. However, despite none of other calculations having reported a resonance around 6 eV, there might be some experimental evidence of its existence (see section 5.5.3), suggesting that we are moving towards the right direction.

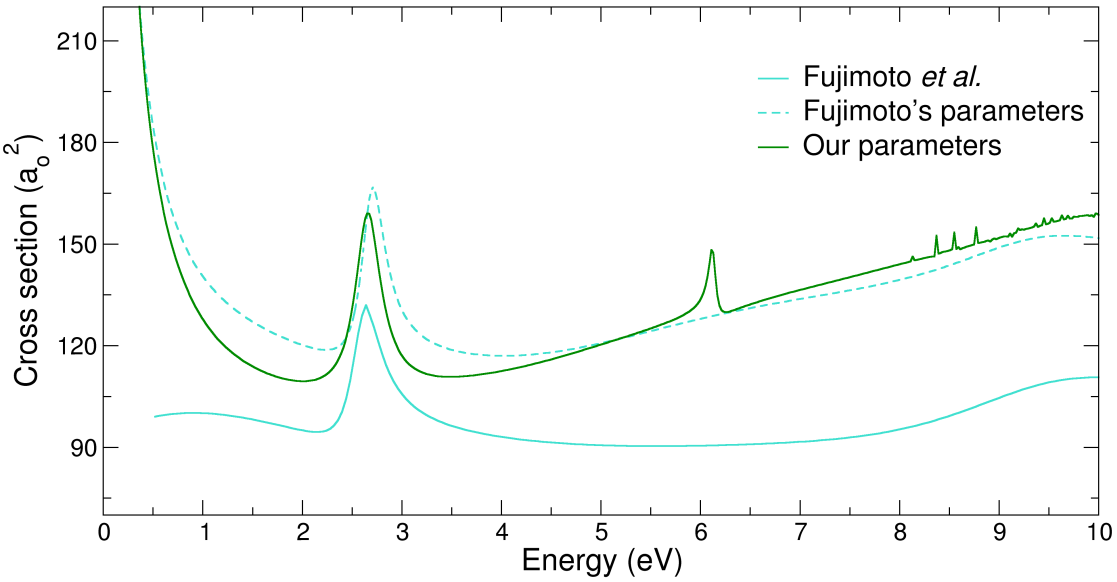

Figure 5.6: Cross sections as a function of electron energy, for calculations at SEP level. The full light blue line represents Fujimoto's *et al.* [186] results obtained with UKRmol, and using the 6-311+G* basis set, $a = 10a_0^3$, $l_{max} = 4$, a deletion threshold of 10^{-7} and 30 VOs; the dashed light blue line represents our attempt to reproduce Fujimoto's results, using his parameters and the UKRmol suite; finally, the solid green line represents the results using our parameters and UKRmol+.

As an additional test to confirm the resonant character of this feature, we performed calculations with other alanine conformers. Although some of the intramolecular interactions might

Table 5.6: Resonance positions (in eV) for alanine conformers ('Conf.') I, II-B and III-A calculated at SEP level: the time-delay analysis was used to locate the fist two resonances while the position of the third resonance was estimated from the cross section. The values marked with ^{F} were obtained by us using the parameters of Fujimoto's *et al.* [185]. The dipole moment (in Debye), μ, of the conformers determined in the R-matrix calculations is listed in the last column.

Conf.		1^2A	2^2A	3^2A	μ
I	Ours	2.65	6.14	≈10.4	1.49
		2.75^F	-	$\approx 9.5^F$	1.42^F
	Fujimoto *et al.*	2.59	-	≈9.70	1.35
II-B	Ours	3.64	5.58	≈9.43	5.1
	Fujimoto *et al.*	3.14	8.03	≈9.77	6.15
III-A	Ours	3.24	6.58	≈10.5	1.8
	Fujimoto *et al.*	2.59	-	≈9.32	1.77

influence the appearance of new resonances, all conformers are likely to have a similar resonant spectrum (even if those resonances are slightly shifted). Thus, we picked the conformers assigned by Császár as *II-B* and *III-A* (Fujimoto *et al.* used the same nomenclature) and used the geometries described in his work (chemical structures are shown in figure 5.7). Conformer *II-B* was picked due the presence of a third resonance (see figure 5.6) in between the well known two they describe; conformer *III-A* has the first π^* shape resonance in the same position as conformer *I*. Following the same strategy as for conformer *I*, we performed scattering calculations at SEP level for these two conformers, first using the Fujimoto *et al.*'s parameters (see table 5.5), and then using ours (table 5.4).

Table 5.6 lists resonance positions and widths, as well as the dipole moment, both from Fujimoto *et al.* and our calculations with our parameters.

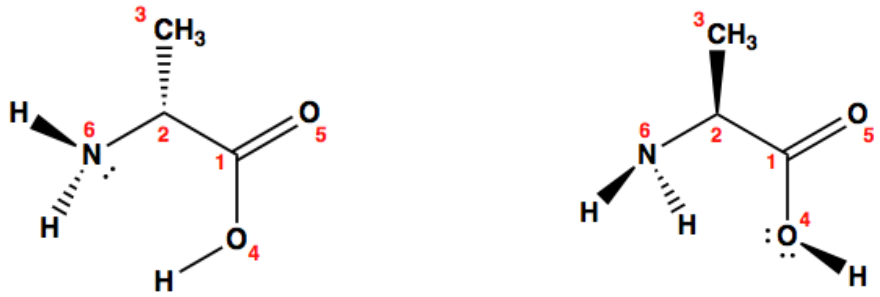

Figure 5.7: Chemical structure of conformers *II-B* (left) and *III-A* (right) described by Császár [163], and used by Fujimoto *et al.* [186].

The corresponding calculated cross sections are presented in figure 5.8. The dipole moment effect is very prominent at low energies, especially for conformer *II-B* in both calculations. The first π^* resonance is visible in all curves, although in our calculations (dashed lines) they are slightly above Fujimoto's. Even though we have used a bigger number of VOs, the scattering

model is different and so is the description of the polarisation effects. This phenomena has been observed before for pyrazine [153].

As for conformer *I*, we describe a peak for both conformers *II-B* and *III-A* in the energy range of 5-7 eV, when our parameters are used, which is not observed in Fujimoto *et al.*'s results. The fact that this feature is present in all three conformers gives us confidence that it corresponds to a physical resonance. The corrected codes and the choice of a better set of parameters to perform the calculation allowed us to describe this new resonance, which links to the DEA spectra, as we will discuss later.

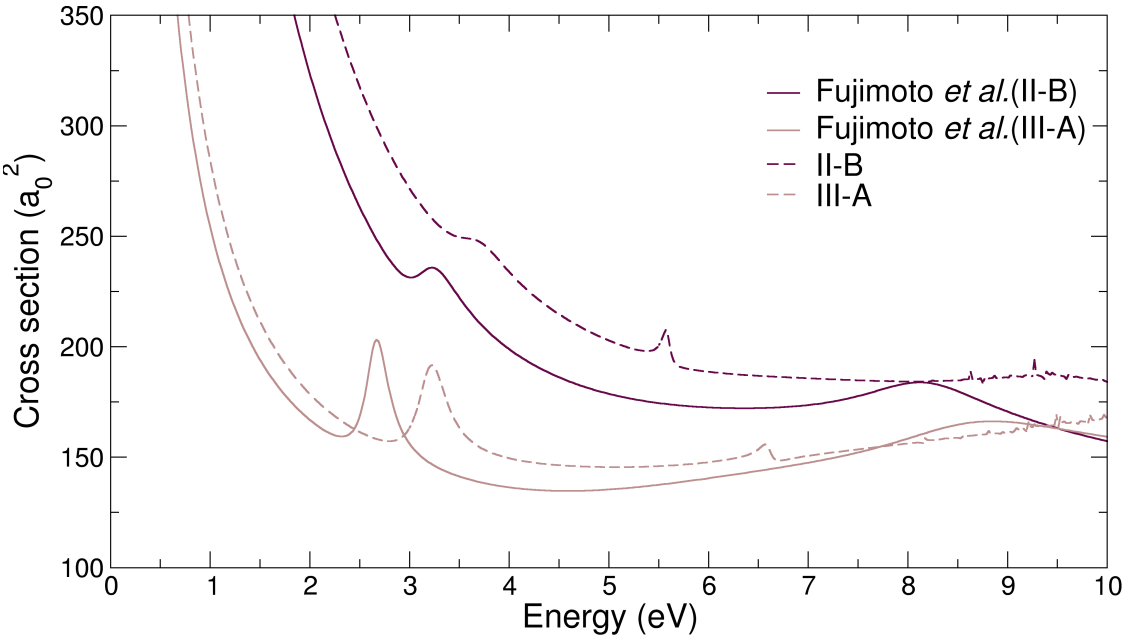

Figure 5.8: Cross sections as a function of electron energy for the conformers described by Császár [163] as II-B and III-A. The full lines represent SEP calculations using the scattering parameters described by Fujimoto *et al.* [186], whereas the dashed lines used ours.

As mentioned before, Fujimoto *et al.* found a wide resonance for conformer *II-B* at 8.03 eV, that might (or might not) be linked to our calculated 6.15 eV resonance. Both resonances Fujimoto *et al.* identified above 9 eV are not seen in this energy range (they might appear at higher energies). The same picture is seen for conformer *III-A*: the resonance Fujimoto *et al.* identified above 9 eV appears shifted to 10.5 eV in our calculations, and no sign of the intermediate resonance was found.

After these tests, and given the consistent presence of this resonance for the conformers we studied, we are confident about the resonant character of the feature observed in our SEP calculations just above 6 eV.

5.5.2 Shape resonances

In this subsection, we will describe the shape resonances found in our calculations for conformer *I*. Figure 5.9 presents the largest eigenvalue of the **Q**-matrix as a function of electron energy, at SE and SEP levels, using 10 and 40 VOs, respectively.

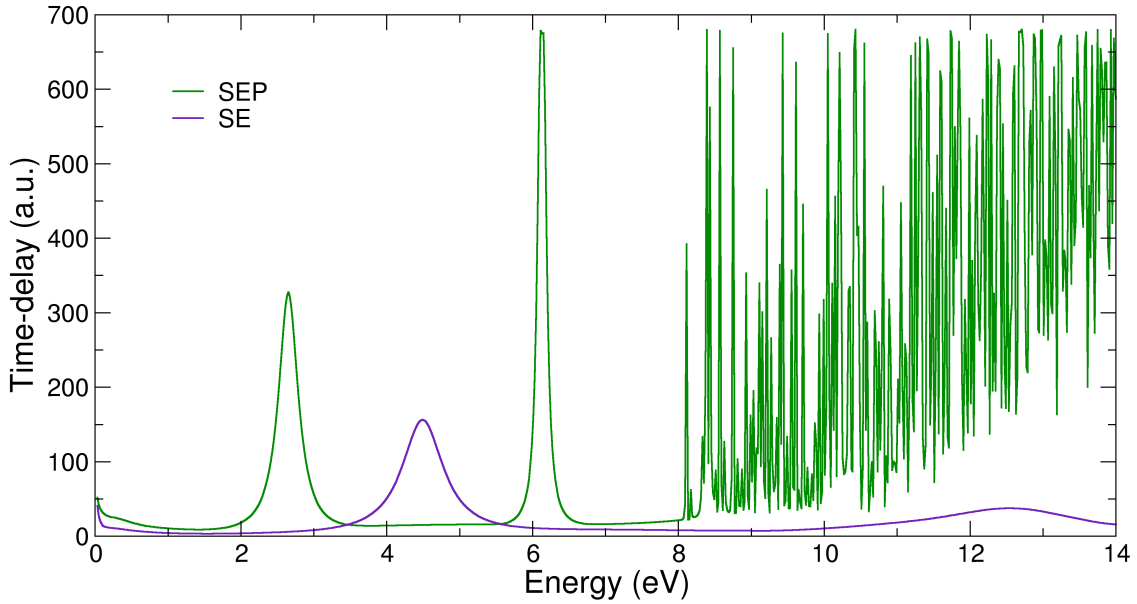

Figure 5.9: The largest eigenvalue of the **Q**-matrix (time-delay) as a function of electron energy. The full green line correspond to our SEP calculation using 40 VOs and the full purple line correspond to the SE calculation using 10 VOs. The number of VOs is the only parameter that is different between these two calculations.

At SE level, the first π^* resonance appears above 4 eV (more than 2 eV above the experimental position), whereas a second one appears as a bump centred at 12.5 eV. Note that this resonance appears at slightly lower energies in the cross sections due to the contribution of the non-resonant processes (see figure 5.4). Using the shift of the first π^* as a guide, we would assume this resonance will appear at around 10 eV when polarization is included, which would be in a very good agreement with the literature, as shown in table 5.7. There is no evidence of the $\approx$ 6 eV resonance. On the other hand, at SEP level we can clearly identify two peaks: one at 2.65 eV that corresponds to the well known π^* resonance we have been discussing, and the second at 6.14 eV that corresponds to the new resonance we have identified, and which we assigned later as having mixed character (as it does not appear at SE level but it does at SEP, and is also visible in both elastic and inelastic cross sections calculated at CC level; this resonance will be discussed in the next section). Due the presence of the pseudoresonances, it is impossible to identify any resonant feature above 8 eV in the SEP results, and consequently, to confirm the presence of higher energy resonance. However, the analysis of the cross sections profile and the eigenphase sums allowed us to identify an extremely wide resonant feature centred at 10.4 eV.

At CC level, looking at the time-delay presented in the next section (figure 5.10), we can identify the three expected resonant features, at 3.16, 6.50 and 10.47 eV, among others with different characters. The position of the highest shape resonance at CC level is in a good agreement with the SE results when we account for the polarisation effects.

Table 5.7 summarizes the pure shape resonances we have found in our calculations and the data available in the literature. Both position and width of the first resonance are in a very good agreement with other calculated values, whereas the second one is slightly shifted to higher energies, as expected. Its width calculated at CC level is much smaller than the literature, whereas at SE level the agreement with other calculated data is better. It is unclear what the origin of this discrepancy between the SE and CC widths is, but it is not impossible that the CC resonance is actually core-excited and has no link to the wide shape resonance seen at SE level (that could well be hidden by others in the CC calculation). The formation mechanism for this higher energy resonance is still not well-established: it has been suggested that it is associated with the σ^* unoccupied orbital of the hydroxyl group [189].

Table 5.7: Position and widths (in brackets), in eV, of the shape resonances identified in our SE/SEP/CC calculations, as well as theoretical and experimental results from literature. The results from Ptasińska *et al.* [188] and Scheer *et al.* [189] were obtained in DEA experiments, so the values correspond to peaks in the ion yield; Aflatooni *et al.'s* [181] results come from ETS experiments; and Vasil'ev*et al.* [190] recorded resonant electron capture mass spectra.

		1^2A	2^2A
Ours	SE	4.49 (0.64)	12.5 (3.05)
	SEP	2.65 (0.28)	10.4 (≈7)(?)
	CC	3.16 (0.36)	10.47 (0.12)
Theory	Panosetti [184]	2.78 (0.14)	9-10*
	Fujimoto [186]	2.59 (0.35)	9.70 (2.19)
	Nunes [187]	2.5	9.50
Exp.	Ptasinska [188]	1.27	-
	Scheer [189]	1.27	-
	Aflatooni [181]	1.8	-
	Vasil'ev [190]	1.2	-

To summarize, in this section we have identified two pure shape resonances of alanine, combining SE, SEP and CC methods. Whilst the π^* resonance is well described at every level of approximation and in very good agreement with the literature, the second resonance is still not well characterised. Our CC calculation provides the best agreement with earlier calculations for this resonance, despite it being of shape character, since pseudoresonances make it impossible to identify it in our SEP calculations. The SE calculation, lacking any description of polarisation, only provides a qualitative description of resonances.

5.5.3 Core-excited resonances

The CC calculations were performed including the 18 excited states listed in table 5.3 and using the parameters listed in table 5.4.

Similarly to what we have done for the SE/SEP results, in order to identify resonances we analysed the largest eigenvalue of the **Q**-matrix, plotted in figure 5.10, for 70 VOs. The first π^* resonance is clearly visible at 3.16 eV. Due to the presence of excitation thresholds, resonance identification was not straightforward above the first resonance. However, it is still possible to clearly identify the features at 7.41, 8.47 (the peak is split into two peaks - this effect has been observed before), 11.10 and 11.37 eV. To help, we looked at the elastic and inelastic cross sections calculated at the same level; these results are presented in figure 5.11. The upper panel shows the elastic (full orange line) and the inelastic cross sections (dashed black line). The lower panel presents the total cross sections (sum of elastic and inelastic cross sections for completeness).

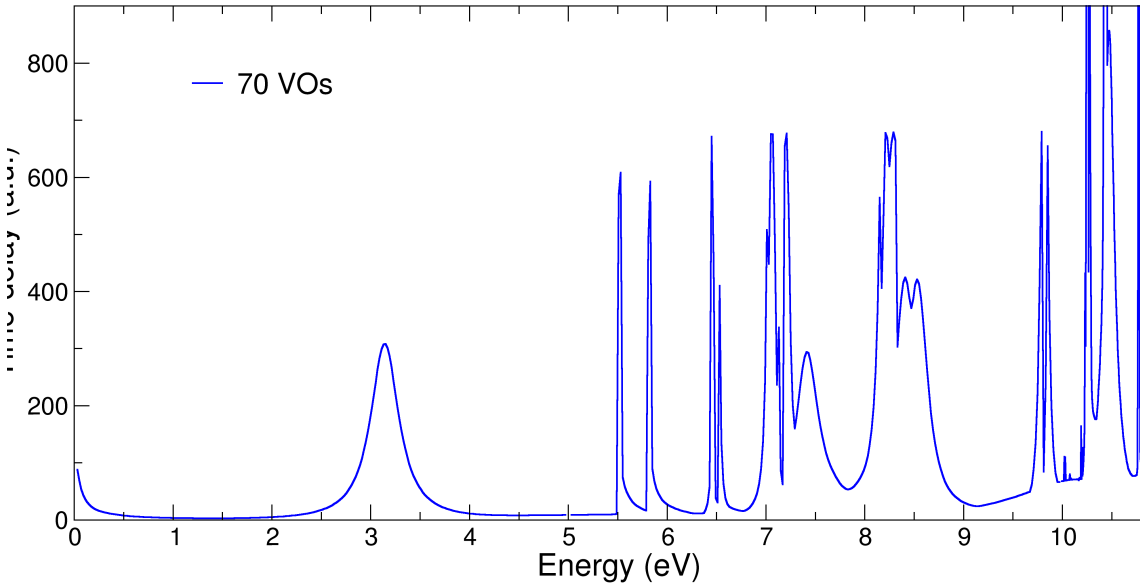

Figure 5.10: The largest eigenvalue of the **Q**-matrix (time-delay) as a function of electron energy, at CC level using 70 VOs. The narrow spikes correspond to excitation thresholds.

As observed in the time-delay, the excitation thresholds are also visible as spikes in the inelastic cross sections. Therefore, we used the gradual inclusion of VOs to help identify what is a resonance and what is a threshold, in the same way we have done in previous chapters. If a peak moves when the number of VOs changes, then it should correspond to a resonance, as the thresholds are not polarisation dependent, as can be seen in figure 5.12. This figure shows the inelastic cross sections for 0, 50 and 70 VOs: despite the large amount of structure, the effect of improving the polarisation description on the resonance positions is very obvious in some energy ranges.

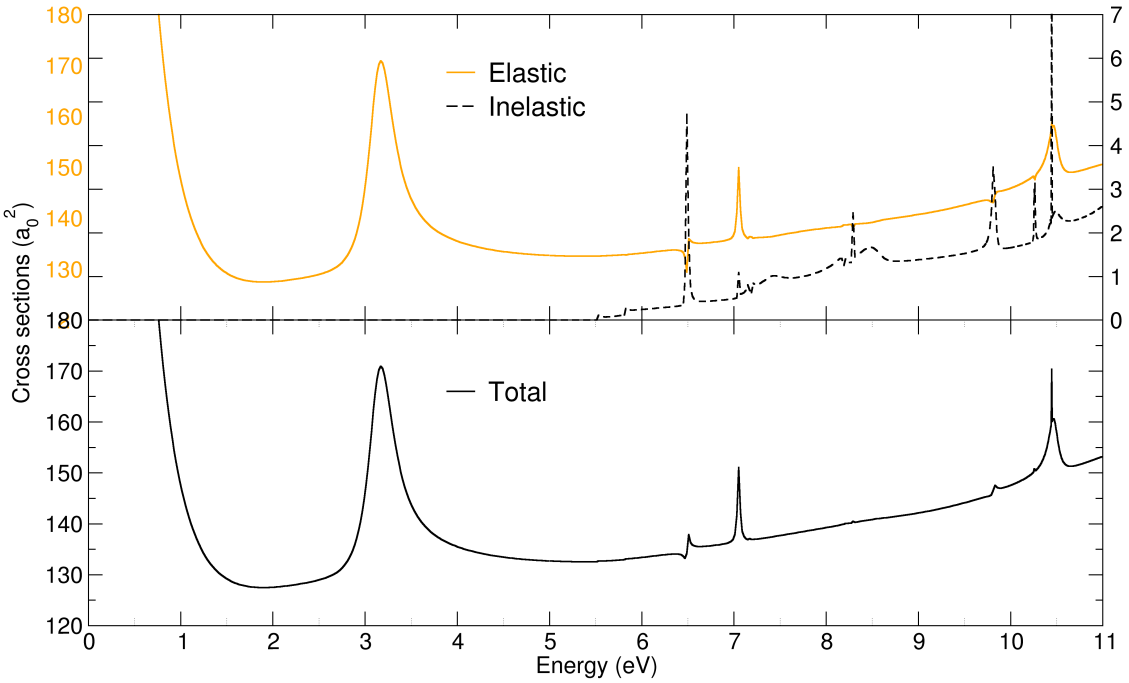

Figure 5.11: Cross sections as a function of electron energy, calculated at CC level. In the upper panel, the orange full line represents elastic cross sections, and the dashed black line the inelastic cross sections. The total cross section is shown in the lower panel. Note that the scale for the inelastic cross section in the upper panel is indicated on the right side.

Table 5.8 summarises all the resonances we have identified. The positions and widths were obtained by fitting the resonances in the time-delay using the formula presented in chapter 2. Despite our efforts, we cannot guarantee that all resonances above 6 eV were identified: some of them might overlap with wider resonances, or be hidden by the excitation thresholds. The latter could be the case particularly for Feshbach resonances that tend to be very narrow. This table does not include all the DEA peaks listed in the literature, because it is impossible to assign which resonance to link them to. We have decided to correlate the ones that are energetically close to our calculated resonances, which is easier for lower energies.

Despite neither Scheer *et al.* [189] or Ptasińska *et al.* [192] mentioning it, the feature both found at 1.27 eV might be linked to some vibrational Feshbach resonance, as none of the calculations report a resonance at those low energies. Vasil'ev *et al.* [190] also report a few peaks close to 1 eV that we believe to be related to the ones reported by Scheer and Ptasińka at 1.27 eV. These values are around 0.5 eV below the position of π^* resonance determined in Aflatooni *et al.'s* ETS experiments, and below all calculated positions for this resonance. Therefore, DEA at this energy seems unlikely to correspond to a direct attachment to this resonance. A more likely explanation is provided by Abouaf [161]: hydrogen detachment from the hydroxyl group at this low energies probably occurs via direct electron attachment to the tail of an extremely wide σ^* resonance located at higher energies. However, we were unable to detect evidence of this resonance in our calculations, although it is well known that these extremely wide resonances

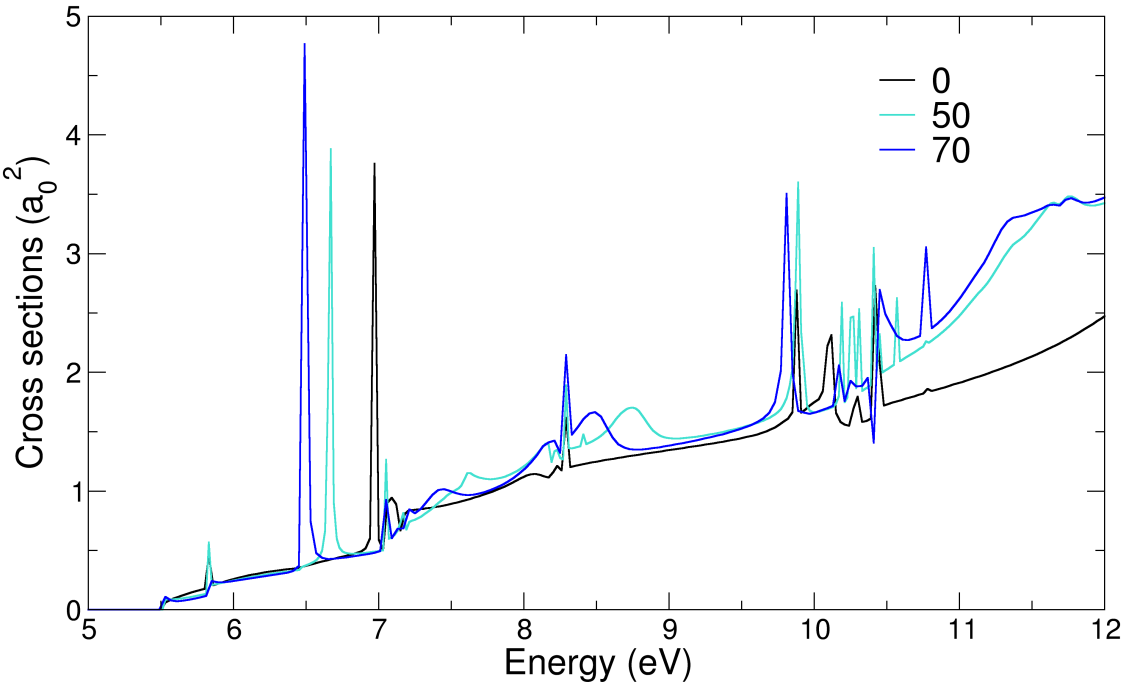

Figure 5.12: Inelastic cross sections as a function of electron energy calculated at CC level for the number of VOs indicated in the figure. The remaining parameters are listed in table 5.4.

are hard to model.

The second peak in their DEA spectra is located at 1.42 eV, and we also think this is unlikely to be related to the direct attachment to the first π^* resonance. On the other hand, the ion yield fragment with m/z=72 (corresponding to the anion produced by abstraction of OH or NH_3) has a peak centered at 1.72 eV, that is much closer to the position of the π^* resonance obtained by Aflatooni *et al.* at 1.8 eV, and consistent with Panosetti *et al.* observations that the first π^* resonance has a nodal plane across the C-OH bond.

The DEA experiments from Vasil'ev *et al.* and Ptasińska *et al.* presents peaks in some anion yields at energies between 2.3 and 3.2 eV, that are energetically close to the π^* resonance. However, we can only suggest those are related to this resonance.

Skipping the π^* shape resonance, already discussed in the previous subsection, we shall now focus on resonance number 2, the first of mixed character, and discuss the agreement between our calculations and the literature. Although none of the earlier calculations have identified a resonance around these energies, it has been observed experimentally: Scheer *et al.* [189] and Ptasińka *et al.* [188] identified a peak at 5.60 eV and 5.5 eV respectively, that they both claim to have core-excited character. We believe these peaks they report are linked to our second resonance at 6.50 eV calculated at CC level, although we disagree on its character.

Scheer *et al.* [189] and Ptasińska *et al.* [188] also identified a third peak they attributed to another core-excited resonance at 7.63 eV and 9 eV, respectively. Due the overestimation of

Table 5.8: Resonance positions (in eV) and widths (in eV, in brackets) for all resonances identified using the time-delay and cross sections analysis, from our SEP and CC calculations. "Ch"stands for character, "S": shape; "M": mixed shape-core-excited; "CE": core-excited. Also presented are the theoretical results obtained by Panosetti *et al.* [184]; the R-matrix SEP results of Fujimoto *et al.* [186] and the SMC results of Nunes *et al.* [187]. As for the experiments, the ETS results of Aflatooni *et al.* [181], some of the DEA results obtained by Ptasińska *et al.* [188] and Scheer *et al.* [189], and the Vasil'ev *et al.* [190] results obtained via resonant electron capture are also listed.

	This work			Theory			Experiments			
No.	SEP	CC	Ch.	[184]	[186]	[187]	[181]	[188]	[189]	[190]
1^2A	2.65 (0.28)	3.16 (0.355)	S	2.78 (0.14)	2.59 (0.35)	2.5	1.8	1.27	1.27	1.2
2^2A	6.14 (0.11)	6.50 (0.07)	M	-	-	-	-	5.5	5.60	6
3^2A	-	7.05-7.15	M	-	-	-	-	-	-	-
4^2A	-	7.41 (0.27)	CE	-	-	-	-	-	7.63	-
5^2A	-	8.18	CE	-	-	-	-	-	-	-
6^2A	-	8.42	CE	-	-	-	-	-	-	-
7^2A	-	8.53	CE	-	-	-	-	-	-	-
8^2A	-	9.82 (0.09)	M	-	-	-	-	-	-	-
9^2A	-	10.47 (0.12)	S	9.89 (1.48) 9.90 (0.94) 10.91 (1.94)	9.70	9.5	-	9.0	-	-

resonance positions in our method, we can only hypothesise this higher energy resonance is related to the resonance we found at 10.47 eV, although we believe it is of shape character.

Within the energy range of 7.05 and 7.15, due to the presence of many excitation thresholds, resonance identification is more complicated, and we cannot confirm the existence of one or two resonances. Above those, we have identified four core-excited shape resonances and one of mixed character. As mentioned before, due to the complexity of the time-delay, the fitting was not possible.

At 10.47 eV we found the shape resonance discussed in the previous section. As already stated, this resonance is not visible at SEP level due to the presence of the pseudoresonances, and appears at 12.5 eV at SE level. Above this energy, due to the complexity of the resonant spectra of alanine, we will not attempt to identify any resonances, although there is strong evidence of a resonance around 11.8 eV.

The shape resonances found by Panosetti *et al.* [184] are significantly more difficult to correlate with ours or with the experiments: they described five shape resonances for alanine (respective widths in brackets) at 2.78 (0.14), 9.89 (1.48), 9.90 (0.94), 10.91 (1.94) and 14.37 (1.12)

eV. They related the first resonance at 2.78 eV to the DEA signal observed by Ptasińksa *et al.* [188], due to a nodal surface they observe in the C-OH bond in the wavefunction map, although the discrepancy in the position is fairly big. Once again, we tried to link their results with ours according to the energy proximity and the resonances character.

5.6 Chapter remarks

In this chapter we established a new scattering model for calculations with alanine, improving the previous R-matrix calculations performed by Fujimoto *et al.* [186]. Target calculations with three basis sets - 6-311G**, 6-311++G** and cc-pVDZ - were performed and compared, and our choice was the more diffuse basis (6-311++G**), as it provided better results. We compared the position of the low-lying π^* shape resonance with other calculations and experiments, finding a reasonably good agreement, and discussed the position of the second shape resonance. For the core-excited resonances we discussed their position and widths and made, as far as we could, a link to the available literature. We also discussed the link between our resonances and the DEA experiments.

The time-delay analysis and the elastic and inelastic cross sections were used to identify and characterise these resonances. In electron rich systems, the electronic excited states are very close in energy, and therefore their identification and that of associated resonances is more complicated.

To close this chapter, it is important to note that alanine is a very complex target: we believe that it has more resonances than the ones we have described. Further studies would be fundamental both to verify the resonant features we found, and hopefully, to provide some insights into alanine fragmentation.

CHAPTER 6

ADDITIONAL STUDIES ON *para*-BENZOQUINONE

This chapter deals with two different types of studies involving *p*-BQ: its photodetachment process, the importance of which was highlighted in chapter 3 and will be discussed in more detail here; and low-energy electron collisions with the complex *p*-BQ-H_2O. There was a need to separate these two studies from the one presented in chapter 3, as the results presented here are preliminary and require further investigation. It was also the first time we applied the R-matrix method to perform photodetachment calculations, and therefore, these results in particular should be carefully interpreted.

The photodetachment study is presented in the first section: it starts with a brief introduction, where the importance of quinones in photo induced processes, like photosynthesis, is explained. As the photodetachment calculations are fairly different from the scattering ones, new programs were used and will be described in detail in this section. Finally, we will present our results and the comparison with the literature [83], as far as possible.

Section 6.2 presents our preliminary scattering calculations with the complex *p*-BQ-H_2O. The main interest in these types of complexes comes from the fact that quinones are present in biological environments, and therefore, surrounded by water molecules. The calculations were performed at a very basic level (SE), so resonances with core-excited character are not described. Comparison between our results and Stockett and Nielsen's [50] is also presented.

6.1 Photoinduced reactions of benzoquinones

The more important characteristic of quinones is their redox chemistry coupled with acid-base properties: they can accept two electrons in two separate steps and a double protonation is associated to the reduction. Therefore, these molecules are the ideal intermediates for electron transfer reactions [193].

One of most famous examples of this family of compounds is plastoquinone (PQ): it is an

isoprenoid quinone molecule involved in the electron transport chain in the light-dependent reactions of photosynthesis. The most common form of plastoquinone is a 2,3-dimethyl-1,4-benzoquinone molecule with a side chain of nine isoprenyl units. There are other plastoquinone derivatives which differ in their side chains. The benzoquinone and isoprenyl units are both nonpolar, anchoring the molecule within the inner section of a lipid bilayer, where the hydrophobic tails are usually found. Like ubiquinone, PQ can appear in several redox forms: "simple"plastoquinone, plastosemiquinone (unstable) and plastoquinol, where both carbonyl groups were reduced to two hydroxyl groups instead of two carbonyl groups. Plastoquinol also functions as an antioxidant by reducing reactive oxygen species, some produced from the photosynthetic reactions, that could harm the cell membrane. One example of how it does this is by reacting with superoxides to form hydrogen peroxide and plastosemiquinone [194].

The role that plastoquinone plays in photosynthesis is that of a mobile electron carrier through the membrane of the thylakoid (membrane-bound compartment inside chloroplasts and cyanobacteria; they are the site of the light-dependent reactions of photosynthesis.) [195].

The first chemical step in photosynthesis is the reduction of a quinone (plastoquinone) to a hydroquinone with a free-radical semiquinone as an intermediate. This is catalysed by light-driven electron transfer reactions in photosystem II: a light-harvesting complex funnels the excitation energy from antenna chlorophylls to a reaction-center chlorophyll where charge separation occurs as the chlorophyll transfers an electron to pheophytin (i.e., a chlorophyll that lacks magnesium). The latter donates the electron to protein- bound quinone. After two electron and proton transfers, hydroquinone is formed and released into the hydrophobic membrane region where it further participates in electron-transfer processes linking photosystem I and II together. [50]

From all that has been said, it is crucial to understand the behaviour of these negatively charged species (p-BQ$^-$ in our case), as it can have a great influence in the upcoming chain of reactions.

6.1.1 The photodetachment process from *p*-BQ anion

The photodetachment process from p-BQ has attracted much attention over the last couple of decades [80, 81, 82, 83].

Holroyd [82] reported electron attachment to p-BQ and photodetachment from p-BQ anion spectrum in nonpolar solvents, using the laser photodetachment technique. They observed a photodetachment threshold from 2.32 to 2.58 eV, depending on the solvent.

Strode and Grimsrud [80] studied the simultaneous interaction of low-energy electrons and light with p-BQ using an atmospheric pressure ionization mass spectrometer (APIMS) and a photodetachment-modulated electron capture detector (PDM-ECD). They provided for the first time photodetachment cross sections within the energy range of 2-6.2 eV, and obtained a photodetachment threshold of 2.43 eV.

Schiedt and Weinkauf [83] reported the photodetachment spectra of p-BQ anion in a photon energy range from 2 to 2.6 eV. Sharp and broad resonances were observed, interpreted as

corresponding to one shape and six Feshbach resonances. Their experiments were performed with cold and mass-selected anions to exclude contributions of fragment anions and internally excited molecules. The major goal of this work was detection and spectroscopy of anionic states of p-benzoquinone situated above photodetachment threshold and investigation of their autodetachment behavior.

Asfandiarov *et al.* [81] measured the temperature dependence of the autodetachment lifetime in the gas phase of the *p*-BQ anion using electron capture negative ion mass spectrometry (ECNI-MS). They observed that the energy of the anion formation shifts to lower energies (from 1.35 to 1.16 eV) as the temperature increases (from 348 to 568K), and the autodetachment lifetime decreases (from 41 to 24 μs). These results are in a good agreement with the position of the first resonance, at roughly, 1.4 eV reported by Cooper *et al.* [91] and the autodetachment lifetime reported earlier by Christophorou *et al.* [95].

Our photodetachment studies were mainly inspired by Horke *et al.*'s [112] work that aimed to provide a fundamental understanding of the processes involved after electron capture, observing the relaxation dynamics in real time. This was achieved by using time-resolved photoelectron (PE) spectroscopy on photoexcited *p*-BQ. Although photoexcitation is not the same as electron attachment, the initial photoexcited state may be expected to resemble closely the initially populated resonance after electron impact and the subsequent relaxation dynamics can be reasonably compared for both processes. Hence, time-resolved PE spectroscopy is well suited to observe the electronic dynamics in such systems. The authors also used *ab initio* electronic structure calculations to support their results. A range of molecular geometries were taken into account: the energy provided by the photon can take the system into one of the temporary anionic states of *p*-BQ which will decay, through conical intersections, to the ground anionic state. As seen in chapter 3, there is a strong dependence of the anionic states positions on the molecular geometry. Their studies provided a detailed picture of the mechanism by which internal conversion proceeds.

The main conclusions of their study is that the excited states provide an alternative reaction pathway that bypasses the free-energy barrier connecting the reactants to the products. Once these excited states are populated, extremely fast internal conversion drives the system towards the ground anionic state, which prevents back-electron transfer from occurring and quenching the highly reactive excited states. This alternative pathway preserves the overall driving force of the reaction and avoids the free-energy barrier. In a condensed-phase environment, any excess vibrational energy can be lost to the surroundings. In their work, they consider only the energies and structures of the five lowest states (the ones that play an important role in the photodetachment process, as demonstrated by West *et al.* [105]) with excitation energies below 3.2 eV at the equilibrium geometry of the $^2B_{2g}$ ground state. Experimentally, they excited *p*-BQ$^-$ at 2.58 eV (480 nm) and 3.10 eV (400 nm), which are close to the resonances at 0.7 eV and 1.35 eV above the thresholds.

6.1.2 Theory and additional programs

The UKRmol suite has been used in the past for photoionization calculations (e.g. [196, 197]); in this thesis we adapted those codes to perform our photodetachment studies. The main difference between the photoionization and photodetachment processes is the initial and final states. In the former, the initial state is the neutral target, whereas the final states are cations. In the photodetachment case, the initial state is an anion, and the final states are neutral, as schematised by equations 6.1 and 6.2, respectively.

$$\text{Target} \xrightarrow{\text{light}} \text{Target}^+ + e^- \tag{6.1}$$

$$\text{Target}^- \xrightarrow{\text{light}} \text{Target} + e^- \tag{6.2}$$

To calculate the photoionization observables and the transition dipoles required for this purpose, we need the expansion coefficients for the initial and final states in the inner region, and the target transition dipoles between the inner region states. In contrast, to obtain scattering observables only the expansion coefficients in terms of the asymptotic solutions are required.

The molecular-frame photoelectron angular distribution is given by:

$$\frac{d\sigma_{fi}}{d\mathbf{k}_f} = 4\pi^2 \alpha a_0^2 \omega | < \Psi_f^{(-)N+1}(\mathbf{k}_f | \mathbf{d} | \Phi_i^{N+1} > |^2 \tag{6.3}$$

where α is the fine structure constant, N is the number of electrons in the molecule, a_0 is the Bohr radius, ω is the photon energy in atomic units, $\mathbf{d}$ is the dipole operator in the length gauge, f labels the state of the residual neutral states, and $\mathbf{k}_f$ is the momentum of the ejected electron. $\Psi_f^{(-)N+1}(\mathbf{k}_f)$ are the continuum wavefunctions satisfying incoming wave boundary conditions and Φ_i^{N+1} is the initial bound wavefunction.

Both the bound and the continuum wavefunctions in equation 6.3 are obtained from an R-matrix calculation and explicitly expanded in terms of the basis functions ψ_k^{N+1}:

$$\Psi_f^{(-)N+1}(\mathbf{k}_f) = \sum_k A_{fk}^{(-)}(\mathbf{k}_f) \psi_k^{N+1}(\mathbf{x}_1, ..., \mathbf{x}_{N+1}) \tag{6.4}$$

$$\Phi_i^{N+1} = \sum_k B_{ik} \psi_k^{N+1}(\mathbf{x}_1, ..., \mathbf{x}_{N+1}) \tag{6.5}$$

where $A_{fk}^{(-)}$ and B_{ik} are energy dependent expansion coefficients determined from matching the wavefunctions 6.4 and 6.5 to the asymptotic solutions of the system (remember chapter 2), and $\mathbf{x}_i$ stands for the space-spin coordinates of the ith electron.

The mathematical procedure to get the expansion coefficients of the scattering states, the bound states and the dipole between the inner region eigenfunctions for calculating the photodetachment observables, is outside the scope of this thesis, but can be consulted in detail in reference [196].

THE PROGRAMS

As mentioned previously, we used two new codes to perform the calculations described in this section. The first one is ***cdenprop***, used to calculate the inner region dipoles [196, 198], and therefore, resides primarily in the inner region stage. *Cdenprop* takes as input the target states and transition dipoles from the target calculation, dipole integrals between both bound and continuum orbitals restricted to the inner region, inner regions wavefunctions (the $N+1$ CI vectors) and, optionally, bound states produced by the outer region code *bound*. The outputs are the inner region dipoles and Dyson orbitals [1]. *Cdenprop* is also capable of calculating permanent transition dipoles between the target states.

Figure 6.1 presents the flowchart of the inner region calculations with the UKRmol suite, including *cdenprop*.

The other module we used is ***dipelm***. It reads the partial wave dipoles from the adapted *rsolve*, and creates the angular grid for defining the real spherical harmonics and the Wigner rotation matrices. Subsequently, *dipelm* performs the necessary frame transformations and calculates the photoelectron angular distributions in the laboratory frame, in an angular grid. The output is not only oriented observables, but also orientationally averaged partial photoionization cross section and asymmetry parameters. An extra feature in *dipelm*, is the possibility of smoothing the partial wave dipoles, in order to remove narrow peaked auto-ionizing resonances: this makes the comparison of the calculations to experimental data easier, if the latter does not have enough energy resolution to observe the auto-ionizing resonances [196]; this has not been used in this work.

The library used by *dipelm* is *compak*[2]. This support library is a set of routines that needs to be added to the outer region suite, so that its execution of *rsolve* calculates also the partial wave dipole moments needed by *dipelm*. Besides that functionality, it also produces scattering/wavefunction coefficients A_k (equation 6.4).

6.1.3 Characteristics of the calculation

Our calculations were performed at HF level and only single-excitations were allowed from the ground state. We included the 6 lowest excited states of the neutral *p*-BQ, and the ground state: 1^1A_g, 1^3B_{1u}, 1^3A_u, 1^3B_{1g}, 1^1A_u, 1^1B_{1g} and 1^3B_{3g}. The respective configurations are presented in table 6.1.

The calculated energy of the states listed in table 6.1 is significantly higher than the accurate values, obtained with a more sophisticated calculation (see chapter 3), as expected. However, it is encouraging that their relative positions are the same, with the exception of the third and fourth states, which are swapped.

From symmetry considerations, the dipole moment couples the B_{2g} ground state with states of the following symmetries: A_u, B_{1u} and B_{3u} (please consult tables in reference [199]).

[1] A Dyson orbital is defined as the overlap between the ground state wavefunction of a N-electrons system and the wavefunction of an ionic state ($N-1$ electrons state). This overlap between wave functions differing by one electron thus give a one electron function, which is a so-called Dyson orbital. These are not used in our calculations.

[2] Created by A. Harvey and Z. Mašin.

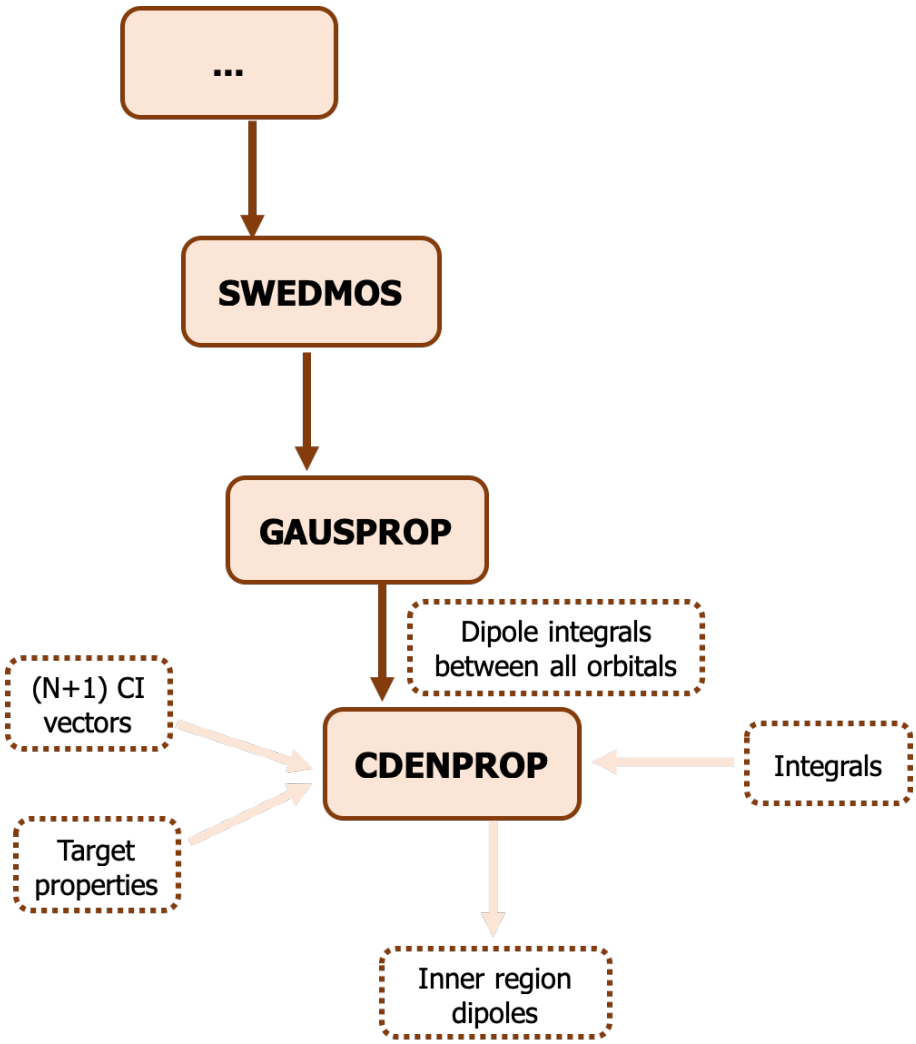

Figure 6.1: Flowchart for the inner region calculation using the UKRmol suite. The light beige filled boxes represent the programs called during the calculation; the boxes with the dashed brown border correspond to the data that are output from one program and serve as input to the following ones or are final results; the ellipsis represent all the programs that run before and after *swedmos*, and that were already presented in chapter 2, figure 2.3.

Table 6.1: States, and respective energies (in H, with respect to the ground state 1^1A_g), included in the photodetachment calculation and described as single excitations from the ground state configuration. Also presented are the energy of the states obtained in a more accurate calculation (see chapter 3).

States	Configuration	Energy	Acc. Calc.
1^1A_g	$(1\text{-}8a_g)^2(1\text{-}2b_{3u})^2(1\text{-}5b_{2u})^2(1b_{1g})^2(1\text{-}7b_{1u})^2(1b_{2g})^2(1\text{-}4b_{3g})^2$	0	0
1^3B_{1u}	$(1\text{-}8a_g)^2(1b_{3u})^2(1\text{-}2b_{3u})^1(1\text{-}5b_{2u})^2(1b_{1g})^2(1\text{-}7b_{1u})^2(1b_{2g})^2(1\text{-}2B^1_{2g})(1\text{-}4b_{3g})^2$	4.423	2.391
1^3A_u	$(1\text{-}8a_g)^2(1\text{-}2b_{3u})^2(1\text{-}4b_{2u})^2(1\text{-}5b_{2u})^1(1b_{1g})^2(1\text{-}7b_{1u})^2(1b_{2g})^2(1\text{-}2b_{2g})^1)(1\text{-}4b_{3g})^2$	5.608	2.599
1^3B_{1g}	$(1\text{-}8a_g)^2(1\text{-}2b_{3u})^2(1\text{-}5b_{2u})^2(1b_{1g})^2(1\text{-}7b_{1u})^2(1b_{2g})^2(1\text{-}2b_{2g})^1(1\text{-}4b_{3g})^1$	5.867	2.648
1^1A_u	$(1\text{-}8a_g)^2(1\text{-}2b_{3u})^2(1\text{-}5b_{2u})^1(1b_{1g})^2(1\text{-}7b_{1u})^2(1b_{2g})^2(1\text{-}2b_{2g})^1(1\text{-}4b_{3g})^2$	5.739	2.713
1^1B_{1g}	$(1\text{-}8a_g)^2(1\text{-}2b_{3u})^2(1\text{-}5b_{2u})^2(1b_{1g})^2(1\text{-}7b_{1u})^2(1b_{2g})^2(1\text{-}2b_{2g})^1(1\text{-}4b_{3g})^1$	5.813	2.764
1^3B_{3g}	$(1\text{-}8a_g)^2(1\text{-}2b_{3u})^2(1\text{-}5b_{2u})^2(1b_{1g})^1(1\text{-}7b_{1u})^2(1b_{2g})^2(1\text{-}2b_{2g})^1(1\text{-}4b_{3g})^2$	6.166	3.337

For the scattering part of the calculation, we used the same parameters listed in table 6.2. Due to time limitations, no other parameters were tested.

Table 6.2: Scattering parameters used in the photodetachment calculation.

Approximation	**SE**
Basis set	cc-pVDZ
Radius (a_0)	13
Highest partial wave (l_{max})	4
Del.Tresh.	10^{-7}
No. Target states	1
No. VOs	10

6.1.4 Preliminary results

To calculate the total photodetachment cross sections of p-BQ$^-$, we have used only the geometry of the anionic bound state (of B_{2g} symmetry).

We have compared, as far as we could, our results with Schiedt and Weinkauf's [83], presented in figure 6.2. They identified six peaks between 2.213 and 2.430 eV (see table 6.3) that they postulated are likely to correspond to vibrational features of two Feshbach resonances, and a broad peak that correspond to a shape resonance. As reported in chapter 3, we also found two Feshbach resonances in p-BQ$^-$: the first one of 1^2B_{2u} symmetry, whose parent state has been easily identified as the lowest excited state, the 1^3A_u, by looking at the R-matrix poles. In the case of the second Feshbach resonance, of 1^2B_{3g} symmetry, the identification of its parent state(s) has not been possible. Both resonances are positioned more than 1 eV below the first excitation threshold, which is unusual.

Figure 6.2 shows three prominent features: (i) at threshold, the photodetachment cross section is extremely low, first increases slowly and then steeply with photon energy; (ii) sharp resonances are observed in the energy range of 2.2-2.4 eV photon energy; and (iii) at energies above 2.48 eV, the photodetachment cross section exhibits a broad peak before rising steeply.

Table 6.3 lists the positions and widths of the peaks identified by Schiedt and Weinkauf [83].

Table 6.3: Position and widths (in eV) and lifetimes (in ps, except the last one) of the autodetaching states as observed in the photodetachment spectrum (see figure 6.2, taken from reference [83]).

Peak label	**Position (eV)**	**Width (eV)**	**Lifetime (ps)**
F1	2.213	$5.2\text{x}10^{-4}$	>1.2±0.1
F2	2.228	$6.6\text{x}10^{-4}$	>1.0±0.1
F3	2.270	$7.1\text{x}10^{-4}$	>0.9±0.1
F4	2.396	$3.0\text{x}10^{-3}$	0.21±0.03
F5	2.406	$2.1\text{x}10^{-3}$	0.30±0.03
F6	2.429	$1.4\text{x}10^{-3}$	0.46±0.03
S	2.504	$2.5\text{x}10^{-2}$	25 fs

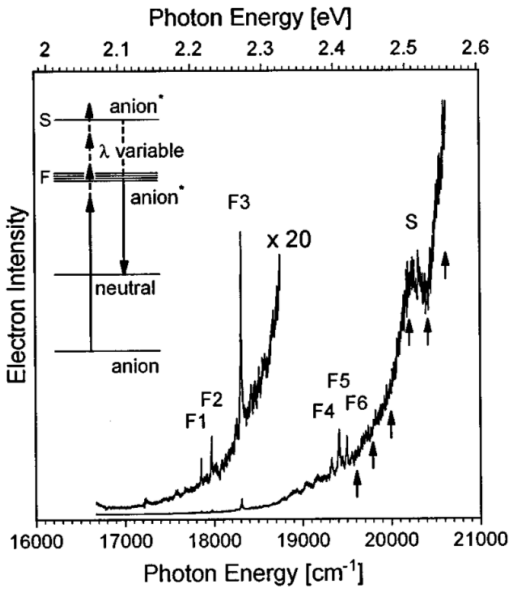

Figure 6.2: Photodetachment spectrum of *p*-BQ$^-$. The sharp features (labelled with F correspond to features linked to Feshbach resonances, whereas the broad resonance (S) is of shape character. Taken from [83]. Please see reference for more information on the experimental procedure.

The widths of the first three features (F1-F3) are very similar; they present an asymmetric line shape, which cannot be simulated by a Fano profile. Therefore, Schiedt and Weinkauf [83] interpret these widths as the rotational band contour of the transitions. The F4-F6 resonances have bigger widths, which are clearly not given by the rotational band contour. At 2.5 eV, a broad resonance is visible, that they attributed to a shape resonance. This difference in the lifetimes and intensities of both Feshbach and shape resonances indicates that these features correspond to photoexcitation to states of very much different character.

Our photodetachment results are presented in figure 6.3.

The broad feature centred around 4.7 eV corresponds to the shape resonance observed by Schiedt and Weinkauf [83] at 2.5 eV. The position of this resonance is overestimated by more than 2 eV with respect to the experiment, as expected, due to the absence of polarization in the calculation. This resonance has a width of 0.32 eV which is an order of magnitude bigger than the literature.

Three possibilities are open for the peaks observed above the shape resonance: (i) they can correspond to some of the Feshbach resonances identified by Schiedt and Weinkauf [83] (as long as they possess some shape character); (ii) they can be pseudoresonances; or (iii) are simply appearing due to numerical problems. In any case, no attempt is made to rationalize them.

We did not calculate the photodetachment spectrum of *p*-BQ at higher energies, as the data available in the literature do not exceed 2.6 eV, and therefore, no comparison can be made.

The fact that we could model the shape resonance using such a simple model, gives us

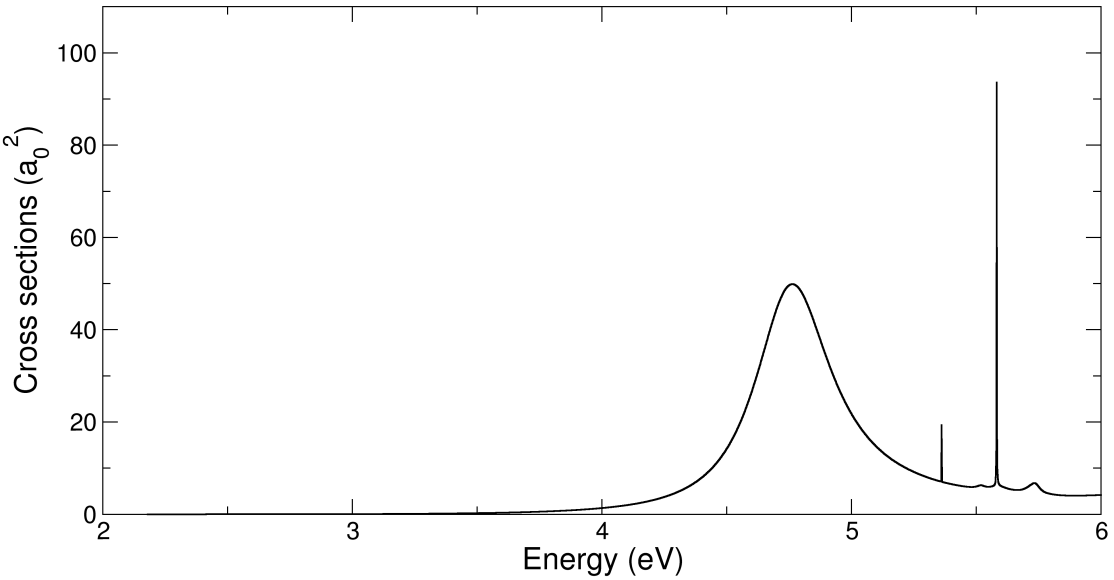

Figure 6.3: Photodetachment cross sections (in a_0^2) as a function of the photon energy (in eV).

confidence about the way we are performing the calculations. Further work is still required to model other types of resonances.

6.1.5 Section remarks

This section reports the first attempt to perform photodetachment calculations using the R-matrix method and the UKRmol suite.

The order of the shape/Feshbach resonances is the wrong way round in our calculations. The closeness of the shape resonance to the photodetachment threshold in our calculations prevents us from assessing wither the cross section has the right shape near threshold; at higher energies our cross section is flat, unlike the experiment. So our results are a proof of principle: we obtain cross sections that look physically possible, but that clearly show more sophisticated calculations are needed.

However, the consistency found in the position of the shape resonance is promising, and more efforts should be made in order to model other types of resonances, for example: performing multiconfiguration calculations and include nuclear motion. Other convergence tests should also be performed, as presented in other chapters.

Unfortunately, the calculations are too basic to provide a meaningful comparison with the experiment. Since the measured cross section is not given in absolute values, we cannot say if our results are of the same order of magnitude.

6.2 Low energy electron collisions with *p*-BQ-H_2O

The importance of studying low-energy electron collisions with the complex *p*-BQ-H_2O was already mentioned at the beginning of this chapter: the need to model the biological environment, where targets, as *p*-BQ in this case, are surrounded mainly by water molecules. These complexes formed by biologically relevant molecules and water have received attention from our group for some years (clusters with one or several water molecules) e.g. [18, 149]. Also, we aim to understand if the energetics of the anion states remained unchanged upon hydrogen bonding with a single water molecule, as the interpretation of the experiments indicates.

Similar studies with water clusters have been performed using the SMC-PP method, with several types of targets: from formic acid [200], to glycine [157]) or phenol [201]. Structurally, the latter is the more similar to *p*-BQ.

Recently, Stockett and Nielsen [50] studied experimentally the effect of a single water molecule in the transition energies of the *p*-BQ anion. Their work represented the starting point for the study we present here.

The group looked at the photo-induced dissociation mass spectrum of the *p*-BQ^--H_2O complex measured at 445 nm and the only dissociation channel they observed corresponds to the separation of the complex yielding *p*-BQ^- at *m*/*z*=108 (and H_2O). They also performed laser power dependence measurements, and showed that the dissociation of the complex occurs after absorption of a single photon. Quantum chemical calculations performed at DFT level (using the B3LYP/6-311++G* model) also showed that water-loss is much more favorable than formation of the hydroxyl anion, with dissociation energies of 0.62 eV and 4.61 eV, respectively.

Their measurements showed that the beam depletion action spectra of *p*-BQ^-, *p*-BQ^--H_2O and H_2O-loss from the complex present very similar profiles (see figure 6.4), in both visible and UV regions, indicating that the electronic transition energies of isolated *p*-BQ anions are unaffected by a single water molecule over the energy ranges of 2.1-2.75 eV and 3.65-4.43 eV. This implies that *p*-BQ^--H_2O is still highly capable of accepting electrons, as the rate of electron transfer is governed by the matching of energy levels between the donor and acceptor species. This is particularly important in the electron transport chain in photosynthesis, as we explained in section 6.1.

They concluded that any fluctuations of the local environment of the quinone (such as water attachment or detachment) are unlikely to have an effect on the electron transfer rate, as the excited state energies of the *p*-BQ^- remain unaltered. This robustness against environmental perturbations makes *p*-BQ a perfect electron acceptor.

In the next pages we will present our calculated cross sections for the isolated *p*-BQ and its respective complex with water, *p*-BQ-H_2O, in both neutral and anion equilibrium geometries. Resonance positions are discussed, looking at the direct effect of the water molecule, and the indirect effect of the change to the *p*-BQ geometry in the dimer. A comparison with the experimental results from Stockett and Nielsen [50] is presented lastly.

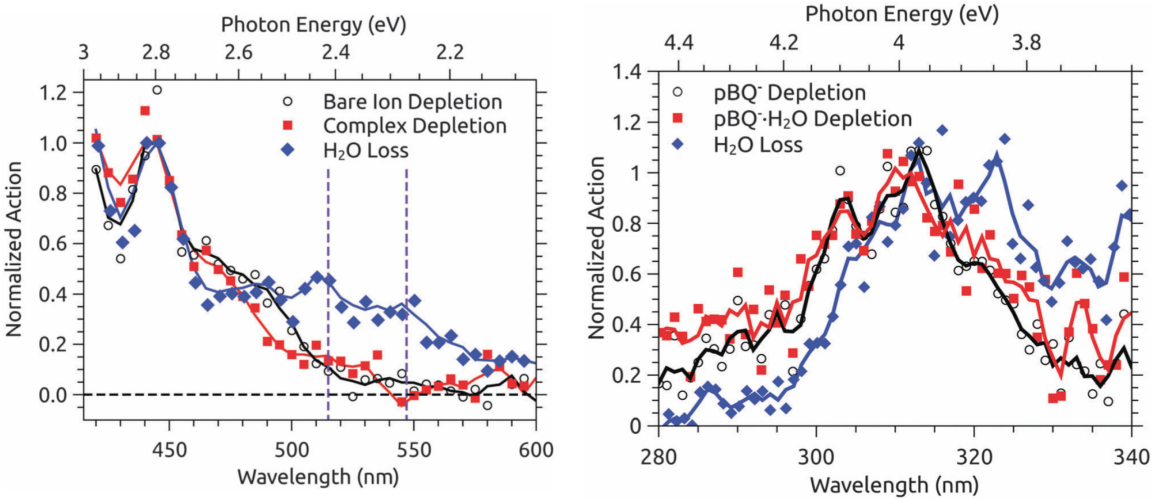

Figure 6.4: Action spectra for *p*-BQ^- and *p*-BQ^--H_2O depletion and H_2O-loss from the complex. The symbols correspond to raw data and the lines are 3-point moving averages. The dashed vertical lines correspond to the resonance positions obtained from Schiedt *et al.* [83] from their photodetachment studies. The pictures were taken directly from Stockett and Nielsen's paper [50].

6.2.1 Characteristics of the calculation

We have performed simple SE calculations for the complex *p*-BQ-H_2O, schematically presented in figure 6.5, using the cc-pVDZ basis set. Due to the symmetry loss (it belongs to the C_1 point group, whereas the isolated *p*-BQ is highly symmetric, with D_{2h} symmetry), SEP and CC calculations would be very computational demanding so could not be performed. Moreover, CC calculations presented an insurmountable difficulty: the choice of the electronically excited states of the target (in this case, the complex) that should be included in the calculation in order to have a similar calculation for the isolated system. Determining which of these states actually correspond to *p*-BQ or to the water molecule is not always straightforward. An even bigger problem would be the choice and size of the active space needed to accurately describe the physics, as it would easily exceed our computational limits, due to the large amount of electrons involved. In addition, no data is available in the literature on the excited states of the complex, or whether they are bound.

In our calculations we have used the geometries for the complex described in Stockett and Nielsen's [50] work: the bond lengths are presented in table 6.4[3]. For completeness, we have also performed scattering calculations with the isolated *p*-BQ using the geometry it acquires in the complexes (both neutral and anion), and compared our calculated resonance positions (and widths) with the equilibrium ground state geometries of both the neutral and anion molecules, presented in chapter 3.

[3]The bond lengths are the only quantity that is presented, as it provides the reader a better feel for the geometry differences. The complete geometry can be found in reference [50].

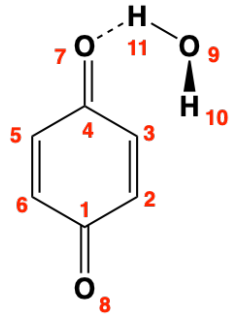

Figure 6.5: Chemical structure of the *p*-BQ-H_2O complex used in out calculations: the hydroxyl group from the water is in the same plane as the *p*-BQ ring, whereas the other hydrogen is perpendicular to that plane.

Table 6.4: Bond lengths (in Å) for the *p*-BQ-H_2O cluster in the ground state equilibrium geometry, as optimised by Stockett and Nielsen [50]. Also presented are the bond-lengths of the equilibrium geometry of the neutral (calculated at MP2/cc-pVDZ level [108]) and anion (optimised by Kunitsa and Bravaya [107] and used in our calculations in chapter 3) ground state of *p*-BQ.

Bond-lengths (Å)	*p*-BQ-H_2O	*p*-BQ-H_2O^-	*p*-BQ	*p*-BQ^-
C_1-C_2	1.483	1.450	1.489	1.450
C_2-C_3	1.336	1.366	1.358	1.379
C_3-C_4	1.481	1.444	1.489	1.450
C_4-C_5	1.480	1.443	1.489	1.450
C_5-C_6	1.335	1.366	1.358	1.379
C_1-O_8	1.273	1.259	1.233	1.263
C_4-O_7	1.224	1.273	1.233	1.263
C_2-H_2	1.083	1.087	1.095	1.087
C_3-H_3	1.084	1.087	1.095	1.087
C_5-H_5	1.084	1.087	1.095	1.087
C_6-H_6	1.084	1.086	1.095	1.087
O_7-H_{11}	1.742	2.008	-	-
O_9-H_{10}	0.963	0.963	-	-
O_9-H_{11}	0.992	0.971	-	-

From table 6.4 we can observe that, for the neutral systems, the bond-lengths in the isolated *p*-BQ are bigger than in the complex, except for the carboxylic bond C_1-O_8, that is 0.04 Å smaller. The same is observed for the anion, except for the aforementioned carboxylic bond, that in this case, is 0.04 Å smaller in the complex.

The effect of including partial waves up to $l_{max} = 5$ in the continuum basis set made a significant difference when compared to $l_{max} = 4$, even at lower energies, as can be seen in the cross sections calculated at SE level presented in figure 6.6 for isolated *p*-BQ in the complex anion geometry. These significant differences suggest that a higher number of partial waves would perhaps be needed to describe the continuum. However, inclusion of another partial wave (up to $l_{max} = 6$) makes no difference in this energy range, as figure 6.6 shows. Therefore, we have chosen to include partial waves up to $l_{max} = 5$ in the calculations presented in this chapter.

The differences observed between using $l_{max} = 4$ and $l_{max} = 5$ for the other geometries studied throughout this chapter were similar.

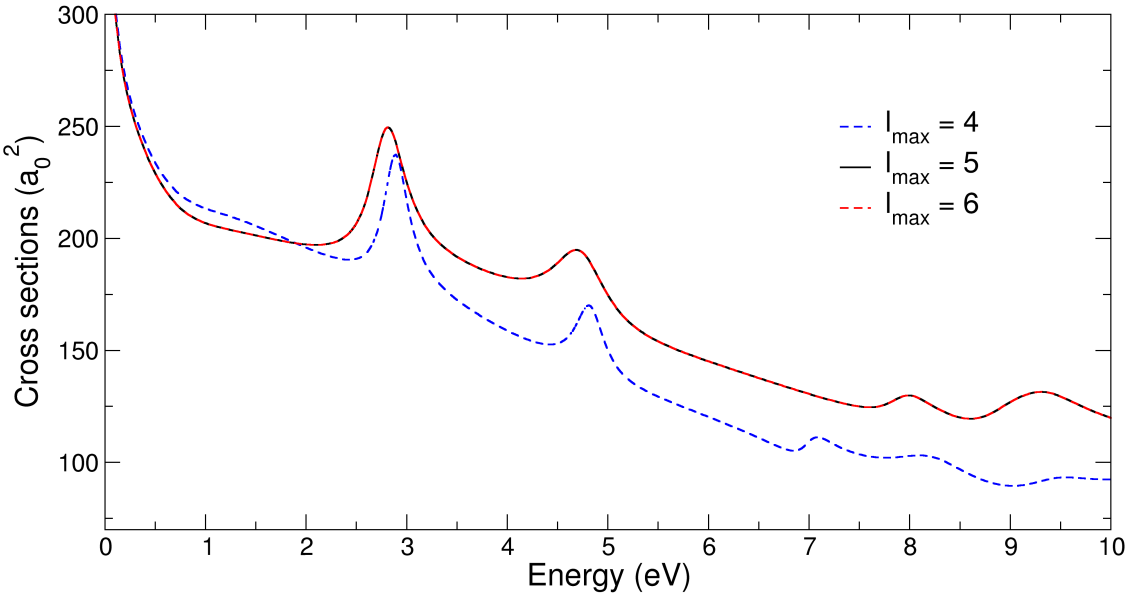

Figure 6.6: Cross sections as a function of electron energy for SE calculations using the same parameters (cc-pVDZ basis set, deletion threshold of 10^{-7} and $a = 16a_0$), and the partial waves indicated for isolated *p*-BQ in the cluster geometry. The dashed blue line correspond to the inclusion of partial waves up to $l_{max} = 4$, the solid black line corresponds to $l_{max} = 5$, and the dashed red line corresponds to $l_{max} = 6$. All of them were calculated using the UKRmol suite.

In order to have a closer comparison with the results shown in chapter 3, we have used the same basis set and deletion threshold to perform the calculations. The radius, however, had to be larger due to the charge density of the complex orbitals. Table 6.5 summarizes the parameters used to perform the calculations presented throughout this chapter.

Table 6.5: Parameters used in our SE calculations.

Basis set	cc-pVDZ
Radius (a_0)	16
No. Partial waves (l_{max})	5
Del.Tresh.	10^{-7}
No. Target states	1
No. VOs	10

The absolute energies obtained for both the complex and isolated target are presented in table 6.6, as well as Stockett and Nielsen's [50], together with our calculated dipole moments.

Table 6.6: Absolute energies (in Hatree) and dipole moment (μ) of the ground state of the complex *p*-BQ-H_2O (in neutral and anion geometries) and isolated *p*-BQ. *NC* stands for the geometry *p*-BQ possesses in the neutral complex; *AC* stands for its geometry in the anion complex; *NG* corresponds to the equilibrium ground state geometry of the neutral target; and *AG* to the equilibrium ground state geometry of the anion target. The energies in brackets were calculated by Stockett and Nielsen [50] at B3LYP/6-311++G* level.

	p-BQ-H_2O		Isolated *p*-BQ			
			Complex geom.		Ground state geom.	
	NG	*AG*	*NC*	*AC*	*NG*	*AG*
Energy	-455.300	-455.272	-379.254	-379.241	-379.258	-379.238
	(-458.025)	(-458.012)	-	-	(-381.563)	(-381.553)
μ (Debye)	0.676	2.018	0.020	0.091	0	0

Our calculated absolute energies are all higher than the ones calculated by Stockett and Nielsen - however, from a qualitative point of view, we also obtain lower energies for the neutral geometries (both in the complex and isolated) than the anion ones, as expected.

6.2.2 Preliminary results

In this subsection we present the preliminary results obtained for this study. Following the work of Sieredzka [202], we looked at the direct and indirect effects of the water molecule, as mentioned before: the former is related to the presence of the water molecule itself, whereas the latter is related to the change in the geometry of *p*-BQ, due to the hydrogen bonding (comparing the equilibrium ground state and its geometry in the cluster). Both of these effects were studied in the neutral and anion geometries of the complex and isolated *p*-BQ, for comparison. It is important to mention that, as the equilibrium geometry (both neutral and anion) of *p*-BQ possesses D_{2h} symmetry, we could easily identify the irreducible representation corresponding to each of the resonances visible in figure 6.7. However, as we mentioned in the beginning of this section, the complex does not have any symmetry, which prevents us from providing any direct information about the symmetry of the resonances. It is possible, though, to link the observed resonances (identified using the cross sections and the time-delay analysis) to the ones previously identified for the isolated ground state geometry. Unfortunately, the geometry *p*-BQ assumes in the complex does not have any symmetry either.

We start by comparing the effect of hydrogen bonding of water molecule on the resonance positions for the neutral system. Figures 6.7 and 6.8 presents the cross sections and time-delay, respectively, calculated for *p*-BQ in its equilibrium ground state geometry, its geometry in the complex (that is different from the equilibrium geometry, as we showed in table 3.7) and for the complex itself.

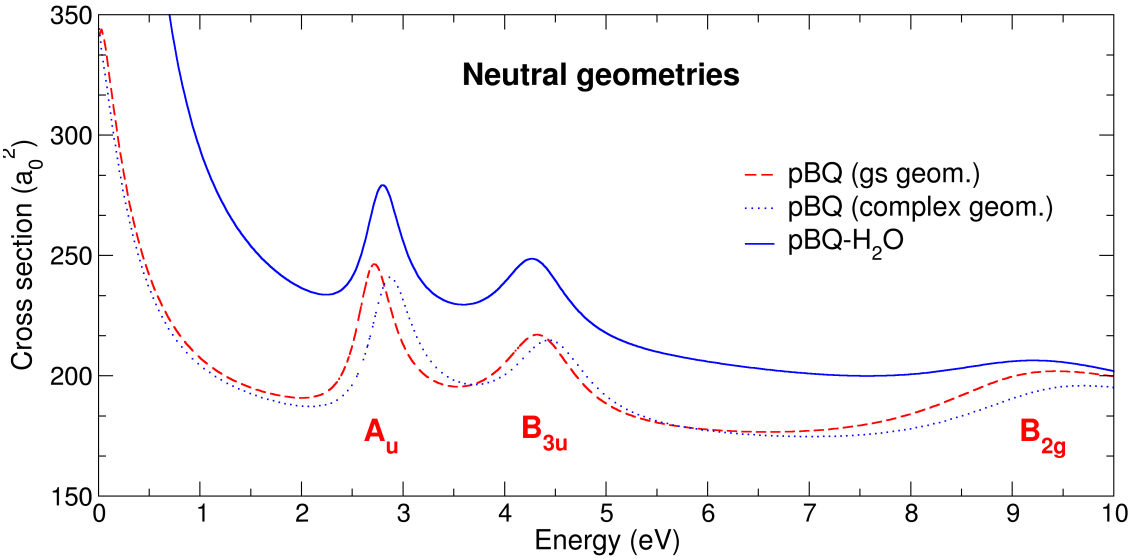

Figure 6.7: Cross section as a function of electron energy, calculated at SE level using the parameters listed in table 6.5. The dashed red line corresponds to the calculation performed using the ground state equilibrium geometry of *p*-BQ; the dotted blue line to the isolated *p*-BQ in the geometry it acquires in the complex; and the solid blue line to *p*-BQ-H_2O in its ground state equilibrium geometry.

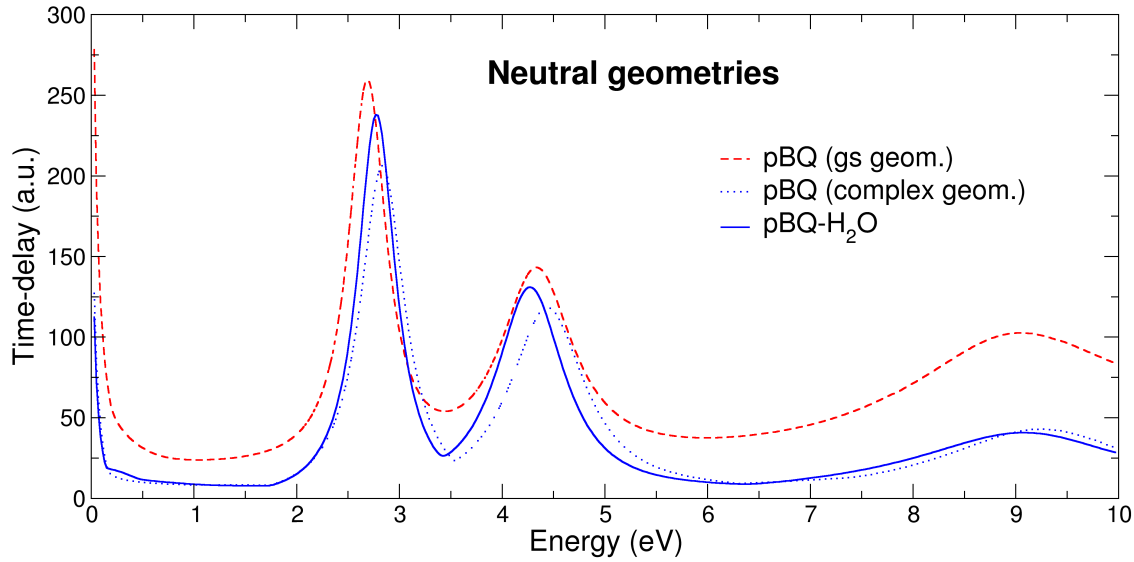

Figure 6.8: The largest eigenvalue of the **Q**-matrix (time-delay) as a function of electron energy, calculated at SE level, with the parameters listed in table 6.5. The dashed red line corresponds to the calculation performed using the ground state equilibrium geometry of *p*-BQ; the dotted blue line to the isolated *p*-BQ in the geometry it acquires in the complex; and the solid blue line to *p*-BQ-H_2O in its ground state equilibrium geometry.

From figures 6.7 and 6.8 we observe that the presence of the water has a stabilization effect on the position of all resonances, compared to the resonance positions of the isolated *p*-BQ in the cluster geometry (direct effect). This stabilisation is negligible for the first resonance (see table 6.10), but gets stronger as we go higher in energies. This is expected if we analyse the orbitals participating in these resonances, shown in table 6.7: the orbitals corresponding to the first resonance remain unaltered, whereas in the orbitals corresponding to the second and third resonances are distorted/changed by the presence of water. These three resonances are the shape ones we found for *p*-BQ in chapter 3 (two of shape, and one of mixed character).

Resonances	***p*-BQ-H_2O**	***p*-BQ^{NC}**
1 ($\approx A_u$)	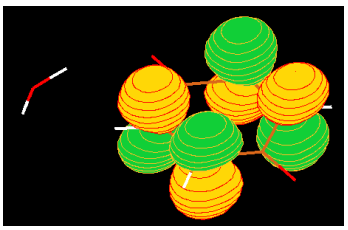	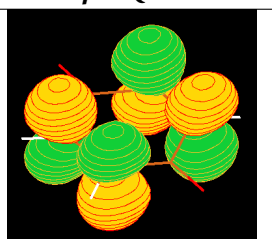
2 ($\approx B_{3u}$)	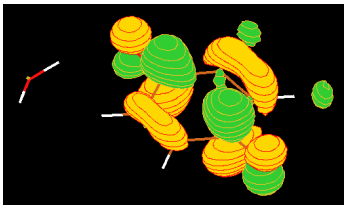	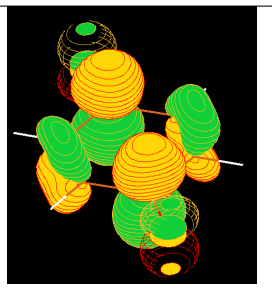
3 ($\approx B_{2g}$)	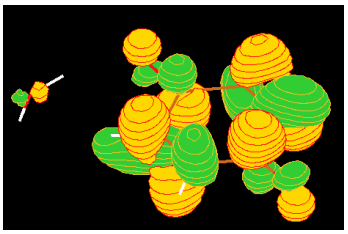	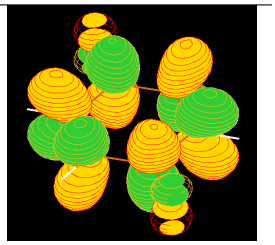

Table 6.7: Orbitals involved in the three resonances identified in the SE cross sections and time-delay analysis for the neutral complex and isolated *p*-BQ (in the equilibrium ground state geometry). Resonance number 1 corresponds to electron attachment to the LUMO+1 orbital; number 2 to the LUMO+3 and number 3 to LUMO+5. *NC* means we are using the isolated *p*-BQ in the geometry it acquires in the neutral complex.

Contrary to the direct effects, the change of geometry of *p*-BQ in the cluster geometry leads to a destabilisation of the resonances when compared to isolated *p*-BQ in the equilibrium ground state geometry - indirect effect. Taking into account both direct and indirect effects, the total effects leads to differences in the resonance positions are smaller than 0.14 eV (see table 6.11).

The stabilizing effect of the water is also observed for the first two π^* shape resonances, when we compare the complex and the isolated molecule in the anion geometries, as can be

seen in the cross sections presented in figure 6.9, and respective time-delays shown in figure 6.10.

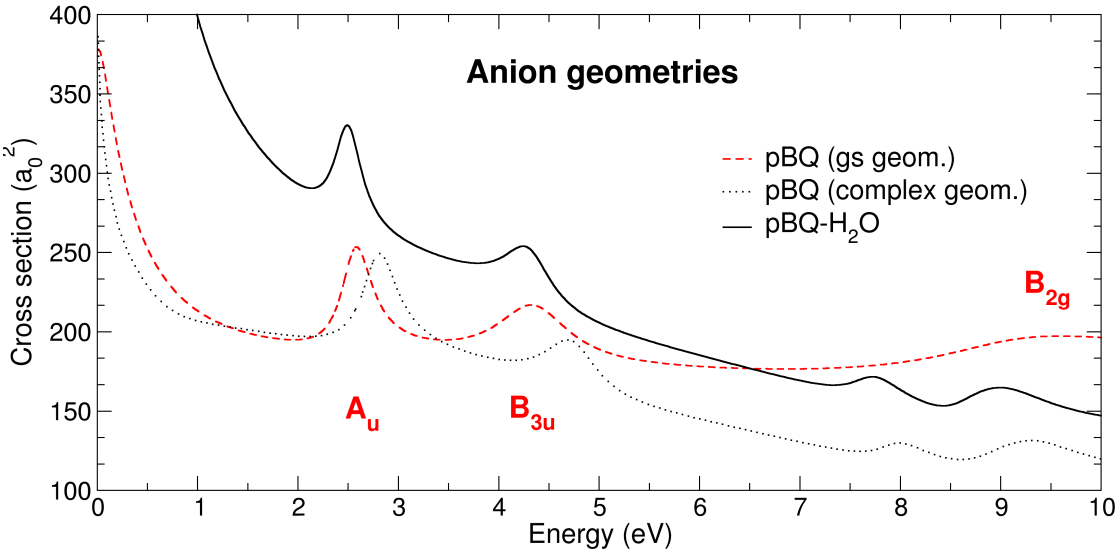

Figure 6.9: Cross section as a function of electron energy, calculated at SE level using the parameters listed in table 6.5. The dashed red line corresponds to the calculation performed using the anion ground state equilibrium geometry of *p*-BQ; the dotted black line to the isolated *p*-BQ in the geometry it acquires in the anion complex; and the solid black line to to *p*-BQ-H_2O^- in its ground state equilibrium geometry.

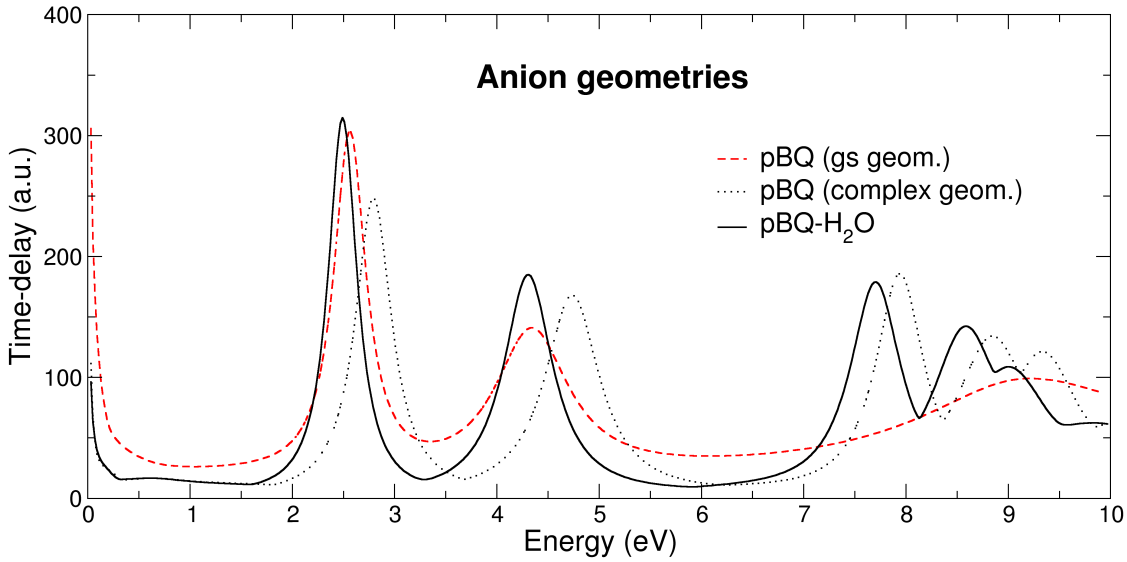

Figure 6.10: The largest eigenvalue of the **Q**-matrix (time-delay) as a function of electron energy, calculated at SE level, with the parameters listed in table 6.5. The dashed red line corresponds to the calculation performed using the anion ground state (gs) equilibrium geometry of *p*-BQ; the dotted black line to the isolated *p*-BQ in the geometry it acquires in the anion complex; and the solid black line to *p*-BQ-H_2O^- in its ground state equilibrium geometry.

However, the most obvious differences lay above 7 eV. Both isolated *p*-BQ in the cluster anion geometry and the complex in the anion geometry lead to the presence of more peaks than those observed before for the neutral geometry (and also for the equilibrium anion geometry of the isolated molecule), as seen in figures 6.9 and 6.10. We investigated whether these two (in the case of the cross sections, but three in the case of time-delay) "resonance-like"peaks were physical, as they have not been observed before. Several tests were performed:

- The inclusion of higher partial waves up to $l_{max} = 6$ retained the two peaks in the cross sections;
- The calculations for the isolated *p*-BQ were run using two different point groups - in C_s and C_1 - as, numerically, the integral calculations could be affected and affect the results. However, identical cross sections were obtained;
- To exclude any linear dependence problems, we run the calculations using a deletion threshold of $1x10^{-5}$. Negligible differences in the results were obtained;
- We also tested the effect of using the UKRmol+ suite in this calculation: it was mentioned in chapter 5 that, for alanine, significant differences were observed when comparing the results obtained with UKRmol and UKRmol+, due to the integrals evaluation being more accurate in the latter. However, in this case and as it was seen for *p*-BQ itself, no differences were observed between the calculations with the two codes.

We also looked carefully at the VOs energy in each calculation, in order to identify any differences that would justify the appearance of these features, but our analysis was unfruitful. None of our tests indicated the peaks visible above 7.5 eV are not physical. On the other hand, however, nothing that we looked at justifies how the change in geometry and reduction in symmetry leads to the appearance of the additional peaks, since this happens for one less symmetric geometry (anion) but not the neutral one, as seen in figures 6.7 and 6.8.

To identify the origin of these two additional features, and confirm their physical nature, further investigations are needed that would include running the calculations with a different basis set and the investigation the poles linked to the peaks to assess which orbitals play a role in the resonance formation. In the absence of these (due to lack of time), from now on, we will only focus on the first two π^* resonances for *p*-BQ-H_2O in the anion geometry and the isolated *p*-BQ in the cluster anion geometry.

The shape of the orbitals for the anion geometry is identical to the ones presented before (see table 6.7) for the neutral geometry, as is the distortion effect from the water molecule. Therefore, these orbitals are not plotted. Looking at the differences in the resonance positions, one would expect a more significant distortion of the orbitals in this case. However, that was not observed, and a more subtle effect might be taking place.

As presented in chapter 3, the resonances in *p*-BQ are very geometry dependent. Similarly to what was observed for the ground state geometry of the neutral and anion molecules, the resonances for the complex are shifted to lower energies (although by a smaller amount than in the *p*-BQ case) when the anion geometry is used. In figures 6.11 and 6.12 we present the cross sections and time-delay, respectively, for both geometries of the *p*-BQ-H_2O complex, where this effect is evident in the first two π^* resonances.

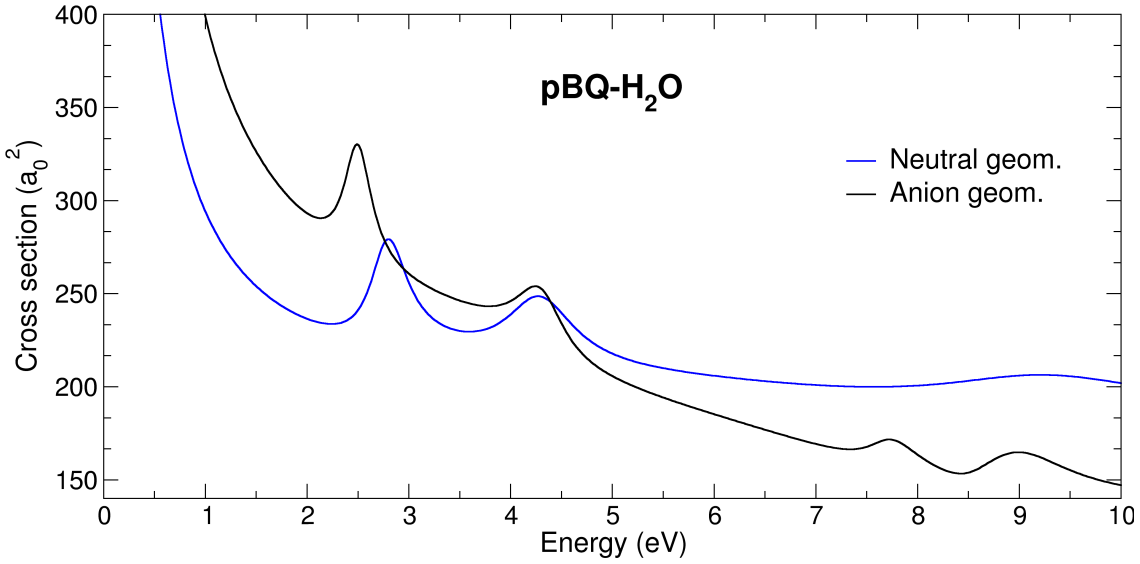

Figure 6.11: Cross section as a function of electron energy, calculated at SE level using the parameters listed in table 6.5 for the complex. The solid blue line corresponds to the calculation performed using the neutral equilibrium geometry of the complex, and the solid black line to the calculation using its anion equilibrium geometry.

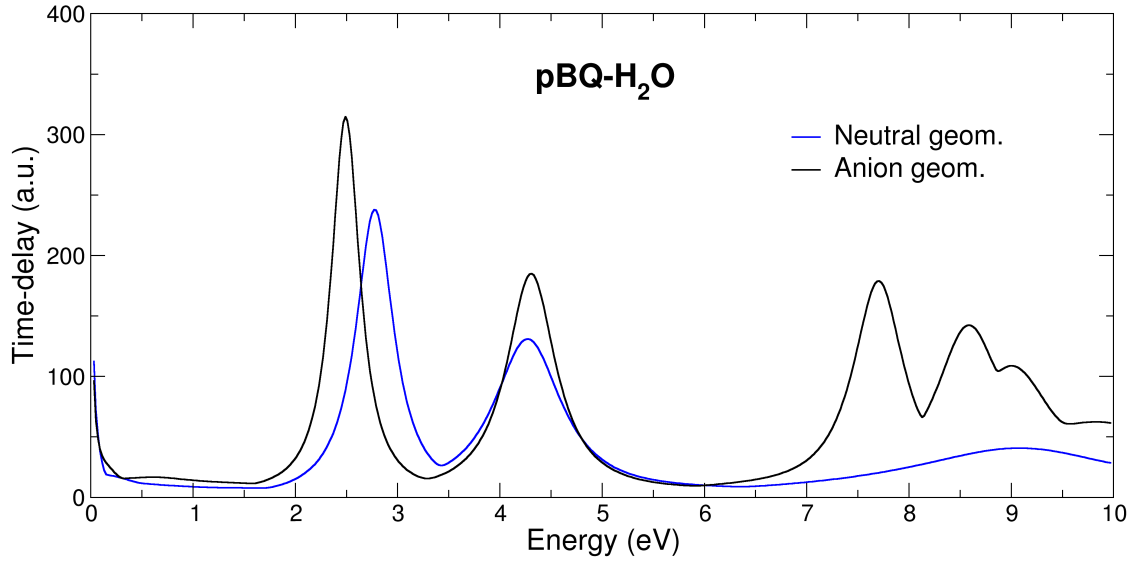

Figure 6.12: The largest eigenvalue of the **Q**-matrix (time-delay) as a function of electron energy, calculated at SE level, with the parameters listed in table 6.5. The solid blue line corresponds to the calculation performed using the neutral equilibrium geometry of the complex and the solid black line to the calculation using its anion equilibrium geometry.

A summary of the resonance positions and widths are presented in table 6.8.

Table 6.8: Positions and widths (in brackets) in eV for the resonances calculated at SE level for the complex *p*-BQ-H_2O and for the isolated *p*-BQ in the equilibrium ground state and in the complex geometries. The labels are the following: ^{NC} stands for the geometry *p*-BQ possesses in the neutral complex; ^{AC} stands for its geometry in the anion complex; ^{NG} corresponds to the equilibrium ground state geometry of the neutral target; and ^{AG} to the equilibrium ground state geometry of the anion target. The widths were obtained with RESON (see chapter 2), except the ones that are approximated values (preceded by ≈): those were obtained by a manual fit of the time-delay.

	p-BQ-H_2O		*p*-BQ			
			Complex geom.		Ground state geom.	
Res.	*NG*	*AG*	*NC*	*AC*	*NG*	*AG*
1	2.82	2.49	2.85	2.82	2.69	2.56
	(0.403)	(0.332)	(0.521)	(0.488)	(0.439)	(0.369)
2	4.27	4.25	4.43	4.69	4.39	4.35
	(0.976)	(0.897)	(1.019)	(0.921)	(0.875)	(0.879)
3	≈9.3	-	9.68	-	9.25	9.14
	(≈2.5)		(≈2.5)		(2.350)	(2.303)

From a general look at table 6.8, we observe that the resonance widths are fairly consistent between geometries, with a tendency to be narrower when the anion geometry is used (compared with the respective neutral target and geometry). We can also observe that the calculations performed for the isolated *p*-BQ in the geometry it possesses in the complex (both in the neutral and anion geometry) give resonance positions higher than those obtained using the ground state equilibrium geometry or the complex one.

To fully understand the water effect on the resonance positions of *p*-BQ, we should look at the indirect and direct effects separately.

INDIRECT EFFECTS

As mentioned before, the indirect effects are linked to the differences in the geometry of *p*-BQ, namely between its equilibrium ground state geometry when isolated, and the geometry it has in the cluster.

Unsurprisingly, the use of the ground state equilibrium geometry has a stabilisation effect over all the resonances, compared to the ones obtained using the geometry in the cluster (see figure 6.8 and 6.10 for time-delays using the neutral and anion geometries, respectively). As observed before by Sieradzka *et al.* [149], this stabilisation effect is observed when the bond-lengths are bigger.

The resonance shifts are presented in table 6.9. Although the shifts are not very significant, it is worth noticing the resonances are not all destabilized by the same amount.

Table 6.9: Shifts (in eV) in resonance positions of isolated *p*-BQ in the complex geometry, with respect to isolated *p*-BQ in its ground state equilibrium geometry, for both neutral and anion geometries.

Resonance	1	2	3
Neutral geom.	0.16	0.04	0.43
Anion geom.	0.26	0.34	-

DIRECT EFFECTS

In figures 6.8 and 6.10 we could also observe the behaviour of the resonances corresponding to the isolated *p*-BQ in the cluster geometry, and the cluster itself. This allow us to look at the direct effect of the water molecule. What we can easily conclude, for both neutral and anion geometries, is that the water has a stabilisation effect in all resonances, as expected in cases where the water behaves as a hydrogen donor in the hydrogen bond, as seen before for other targets [18, 149, 200].

Table 6.10 presents the shifts calculated for the all the resonances identified in the complex, with respect to the ones for isolated *p*-BQ in the complex geometry.

Table 6.10: Shifts (in eV) in resonance positions of the complex, with respect to isolated *p*-BQ in the complex geometry, for both neutral and anion geometries.

Resonance	1	2	3
Neutral geom.	-0.03	-0.16	-0.38
Anion geom.	-0.33	-0.44	-

In this case, it is clear that the stabilization effect tends to be bigger as we go higher in energy. Similarly to what we observed before in the indirect effects, the resonances in the anion geometries are more affected by changes in the environment than in the neutral geometries.

TOTAL EFFECTS

The total effects of micro-hydration are given by the sum of the direct and indirect effects. As reported before by Sieradzka *et al.* [153] for pyrazine, the change in the geometry induced by the water molecule has an opposite effect on the resonance positions to the presence of the water itself, and the latter is, in general, more significant - the direct effects are stronger than the indirect ones. The total effects are summarized in table 6.11.

Table 6.11: Shifts in resonance positions of isolated *p*-BQ in its equilibrium geometries with respect to the complex in its equilibrium geometries.

Resonance	1	2	3
Neutral geom.	0.13	-0.12	0.05
Anion geom.	-0.07	-0.10	-

In summary, the indirect effect (caused by the geometry changes) has a bigger influence for the neutral geometries than the anion ones, except for the second resonance. On the other

hand, the direct effects (caused by the water presence) seem to be more prominent when the anion geometries are used, although none of these values are particularly significant.When the total effects (sum of the indirect and direct effects) are taken into account, shifts on the resonance positions (either stabilisation or destabilisation) of less than 0.15 eV are found.

From a qualitative point of view, our results agree with those obtained by Sieradzka *et al.* [149] for pyridine and thymine [203], and Freitas *et al.* [200] for formic acid.

These calculations *per* themselves do not provide us a conclusive picture of the effect of a single water molecule in the electron collision process with *p*-BQ, as they were performed at a very basic level, and important effects (like polarization/correlation) need to be considered for more accurate results.

6.2.3 Comparison with experiments

As explained in section 6.2, we have used the work of Stockett and Nielsen [50] as the starting point for our studies with *p*-BQ-H_2O.

Any comparison with the experiments has to be made using the anion geometry of *p*-BQ and respective cluster, as Stockett and Nielsen studied the *p*-BQ anion. As our resonance positions are typically calculated with respect to the ground state of the neutral molecule, the VDE needs to be taken into account (to provide the transition energies from the anion ground state). As discussed in chapter 3, our calculated VDE (1.95 eV) for the anion geometry is in good agreement with the literature due to a compensation of errors. Therefore, and because our calculated VDE for the complex at HF level is clearly wrong (1.57 eV: the fact that is smaller than the VDE for the isolated molecule indicates that there is a destabilisation of the (bound) anion ground state), we have chosen to use the VDE reported by Stockett and Nielsen [50] for the isolated *p*-BQ anion and the *p*-BQ-H_2O cluster in the anion geometry. These values are presented in table 6.12, for the anion geometry of the cluster, and the ground state equilibrium geometry of isolated *p*-BQ.

Table 6.12: Resonance positions (in eV) calculated for the equilibrium geometries of *p*-BQ^- and *p*-BQ-H_2O^-. ΔE corresponds to the energy difference between the resonance positions for *AG* geometries.

	p-BQ-H_2O		*p*-BQ		ΔE
VDE [50]	2.52		2.06		
1 ($\approx A_u$)	2.49	5.01	2.56	4.62	0.39
2 ($\approx B_{3u}$)	4.25	6.77	4.35	6.41	0.36

As expected, these resonance positions are significantly overestimated compared to their real position (see chapter 3 for more accurate results for the isolated *p*-BQ in its equilibrium ground state geometry), due to the absence of polarisation in our calculations. The ΔE, however, is slightly different for both resonances, and seems to indicate that the water has a stronger effect on the second resonance. This effect, however, is not bigger than 0.4 eV. Taking into account that these results are only preliminary, these values are considered small enough to be

in agreement with Stockett and Nielsen's results [50]: the water effect in the transition energies of the p-BQ$^-$ is very small.

6.2.4 Section remarks

In this section we were mainly focused on the effect of a single water molecule on the resonance positions of p-BQ, in its neutral and anion equilibrium ground state geometries. To better understand this effect, four geometries were studied. Our general observation is that the water molecule does not affect significantly the resonance spectrum - however, a potential resonance was observed at higher energies for the isolated p-BQ in the anion cluster geometry, and for the cluster itself in the anion geometry. Although none of our tests seem to refute the physical character of this resonance, its appearance due to the geometric changes are still to be explained.

As reported by Stockett and Nielsen [50], for efficient electron transport, a certain robustness of the electron acceptor to the micro-environment and to any fluctuations is needed. Ideally, the excited-state energies of p-BQ$^-$ should be unaffected by any local changes. Their results imply that the stabilisation of the resonances and the bound state of p-BQ$^-$ due to the presence of a water molecule are quantitatively similar. In other words, the shift of the energy of the anion is similar to those of the resonances. Our results at SE level show that the total effect of the water molecule on the resonances is indeed small, and quite similar in size: around 0.1 eV, as shown in table 6.11.

The 0.46 eV shift in the VDE reported by Stockett and Nielsen, calculated at DFT level, is clearly much larger than the one we find for the resonances. If this value is correct, this indicates that a more accurate calculation of the resonance shifts should produce a value 3 or 4 times higher than that obtained at SE level: prior experience from SMC calculations points at the SE and SEP approximation producing shifts of a similar size [200, 204], although this could not be confirmed with earlier R-matrix calculations [202]. We note that, in any case, all prior studies involved polar molecules.

Two additional things to note: firstly, our VDE shift calculated at HF level indicate a destabilisation of the (bound) anion ground state. This is clearly incorrect and shows that either the HF calculation is very poor at describing this system or that the geometries we are using (optimised at DFT level) are inconsistent with a HF calculation (or perhaps both). Also, both direct and indirect effects on the resonances are much larger than for the neutral geometries: if one of these effects is overestimated for the anion geometries (for example, because of a not very appropriate choice of ground state (isolated or cluster) geometry), a more accurate calculation would lead to bigger shifts for the resonances, more consistent with the VDE shift calculated at DFT level.

In conclusion: our simple SE calculations do seem to provide a picture that is consistent with the experimental results of Stockett and Nielsen [50]. More accurate calculations are required to confirm them.

CHAPTER 7

CONCLUSIONS

This work was focused on low-energy electron collisions with medium-sized biologically relevant molecules: *p*-BQ (in its neutral and anion equilibrium geometries), thiophene and alanine. For all of these targets, we provided elastic and inelastic integral cross sections and elastic differential cross sections (and also inelastic ones for thiophene), as well as resonance positions and other characteristics. We also briefly studied the effect of one water molecule on the shape resonance positions of *p*-BQ and the transition energies of the *p*-BQ^-, motivated by the experimental work of Stockett and Nielsen [50], as well as photodetachment of *p*-BQ^-. To perform our calculations we used the *ab initio* R-matrix method, and three levels of approximation: SE, SEP and CC (see chapter 2). The combination of these three methods allowed us to identify and characterize a large number of resonances for all three targets, most of which had not been identified before.

We started by studying *p*-BQ, chosen due to its centrality in some biological processes, as presented in chapter 3. Although it has been studied extensively, especially over the last years, a consistent resonance spectrum is yet to be revealed. The fact that the resonance positions in *p*-BQ are very geometry dependent, combined with the large number of resonances it possesses, makes it an extremely interesting target to study - as demonstrated by the increasing number of publications that have emerged recently. Due to the relevance of *p*-BQ in electron transfer reactions, its photodetachment process has been widely studied, and motivated most of the work to clarify its resonant spectrum. Therefore, and with the aim of looking at its photodetachment spectra, we also performed scattering calculations for the ground state equilibrium geometry of the anion *p*-BQ.

We provided a detailed resonant spectrum of *p*-BQ in the energy range of 0-8 eV, and compared our resonance positions and characteristics (widths and character) with data provided by other groups, who used different theoretical methods, and also with experiments. The agreement was, in general, satisfactory for the low-lying resonances. Quantitatively, our results agree

best with those of Kunitsa and Bravaya [107]. As we go higher in energy the agreement gets worse and there is significantly less information available in the literature. Our results revealed a strong sensitivity of resonance positions to the geometric changes. The character of some resonances was different from the ones obtained previously for the ground state equilibrium geometry of the neutral *p*-BQ, and also geometry dependent.

A link between our resonances and the DEA peaks obtained experimentally by Khvostenko *et al.* [114] and Pschenichnyuk *et al.* [113] was also attempted. Since *p*-BQ possesses a lot of resonances very close in energy, it is not straightforward to rationalize which peak(s) corresponds to a particular resonance. Our approach was to link them by energy ranges, taking into account flair energy proximity.

For this target we presented our calculated integral and differential cross sections: the former were used in combination with the time-delay analysis to identify and characterize the resonances. We were able to compare our calculated DCS with other theoretical results obtained with the IAM-SCAR and the SMC-PP methods [101]. The agreement with our results was better with the latter, as expected. State-to-state inelastic cross sections were not calculated, as there were no available experiments to compare with.

Although we have provided a detailed resonant spectrum that can help those studying the photodetachment process of *p*-BQ^-, more accurate calculations need to be performed and nuclear degrees of freedom to be included in those, which is impossible to do for all the degrees of freedom of this target. For simpler molecules, such as water, it is nowadays possible to incorporate all three degrees of freedom.

In the future, we recommend performing these calculations using a smaller deletion threshold, using UKRmol+ suite in quadruple precision, to confirm the accuracy of the results presented in chapter 3. In addition, our results could be verified if further experiments were performed, particularly EELs or Velocity Slice Imaging. The latter could provide information about the symmetry of the resonances, crucial to check the symmetry assigned the resonance in earlier experiments.

Although presented in a separated chapter, as preliminary results, we performed two additional different studies involving *p*-BQ: (i) an attempt to model the photodetachment process of its anion, adapting the actual code used to perform photoionization calculations; and (ii) study the effect of a single water molecule hydrogen-bonded to the anion in the transition energies between the anion bound state and the resonances. Due to time and computational limitations, both of these studies were performed using very simple models, and the results presented for the former should be seen as a proof of concept.

The calculations with the *p*-BQ-H_2O dimer were performed only at SE level, using the geometry of the neutral and anionic cluster. We have demonstrated that the indirect effects (caused by the changed in the geometry of *p*-BQ induced by the formation of hydrogen-bond with water, but where the water molecule is not considered) have a destabilization effect over the resonance positions when compared to the isolated *p*-BQ - this effect was observed for both neutral and anion geometries. On the other hand, the direct effect caused by the water presence (we compare the cluster itself with the isolated *p*-BQ in the cluster geometry) has a stabilizing effect

over resonance positions, stronger than the indirect one for the majority of the resonances. The total effects (sum of the indirect and direct effects) play a stabilizing role in some resonances, whereas others are destabilized. Nonetheless, these shifts on the resonance positions (either stabilization or destabilization) are of less than 0.15 eV.

Although our results are preliminary, they are fairly consistent with Stockett and Nielsen's [50] experimental observations, that a single water molecule does not have a significant affect over the transition energies of *p*-BQ anion. Although the water molecule has different effects over the resonance positions (in some cases it stabilizes the resonances, whereas in others it destabilizes), that effect seems to be small (around 0.4 eV according to our results).

Two systems revealed the presence of two higher energy resonances that we were not expecting: the isolated *p*-BQ in the cluster anion geometry, and the cluster itself in the anion geometry. We investigated these two resonances carefully, and performed several tests including the use of UKRmol+ (instead of UKRmol), different deletion thresholds to discard any linear dependency issues, and also the inclusion of more partial waves. None of our tests indicated that these two features were unphysical; on the other hand, looking at the energy of the VOs used to generate the L^2 functions, nothing seems to justify the appearance of a new resonance, so further investigations are required.

Finally, in order to fully understand the hydration effect in the biological environment, studies using more water molecules would be needed (such as those of Sieradzka [203] for thymine, where up to 5 molecules were included).

The next target we studied was thiophene. We provided a detailed resonance spectrum within the energy range of 0-10 eV, as well as elastic and inelastic integral and differential cross sections, and excitation functions for the same energy range.

For the pure shape resonances, our calculations agree well with previous calculations and experiments - however, the accurate position of the σ^* resonance is still to be determined.

As for the core-excited resonances, our results were confirmed by the EELs results, where an excellent agreement was obtained for several resonances. However, some of our calculated resonances are still to be confirmed by other methods. We were also able to link some of our core-excited resonances to the DEA spectra of Muftakhov *et al.* [127]. Unfortunately, for the higher-lying resonances, this assignment is not straightforward as there are several resonances very close in energy. Although we appreciate this is a crude approximation, we used the same approach as for *p*-BQ and linked our results with the peaks in the DEA spectra taking into account their energy proximity. In the future, it could be helpful to understand which resonances are indeed dissoactive, similarly to what we did for the six low-lying resonances of *p*-BQ.

Unlike the other targets studied in this thesis, we were able to compare all of our results with other theoretical (IAM-SCAR and SMC-PP) and experimental (EELs) data, and the comparison is, in general, very satisfactory. In particular:

- Our calculated integral cross sections were in good agreement, specially in shape, with

the ones calculated by da Costa *et al.* [126] using the SMC-PP method, at SEP level. The more significant differences were observed for lower energies, where our cross sections are higher;

- The DCS were compared to the ones obtained with the IAM-SCAR method; it is well known the later method fails for lower energies. Despite this, the agreement was reasonably good, especially at higher energies;

- Our core-excited resonance positions were compared with the EELs results obtained by Regeta [47], for two different scattering angles and three energy losses: four of our core-excited and mixed core-excited shape resonances were visible in the experimental excitation functions, and the agreement was excellent both in the size of the cross sections (we compared absolute values, specially for the first two triplet states) and in the resonance positions (although it is well known that our results are shifted to higher energies).

Although we have not presented those results in this thesis, we have complemented and compared our integral cross sections with several variations of the IAM-SCAR method, as can be seen elsewhere [49].

The general good agreement between our results and the ones obtained with different theoretical and experimental methods, indicates that our calculations are modelling the physics of the collision process accurately, as it was seen before for other target molecules (see e.g. reference [153]). This is particularly visible when comparing our calculated excitation functions with EEL results, for a specific state and angle, for which the agreement is excellent. However, it seems that our usual strategy to determine how to model the polarization effects fails in this system, as demonstrated by the uncertainty about the position of the σ^* resonance. With thiophene (particularly with the comparison between our results and the EEls ones) we have also demonstrated that it is now possible to provide quantitatively accurate cross sections for low energy electronic excitation of low-lying states of biologically relevant molecules.

The last molecule studied in this thesis was alanine. Being an aminoacid, its biological relevance is evident. This molecule revealed to be the biggest challenge compared to the other targets, not only due to its size and absence of symmetry, but also because our preliminary results were not in agreement with previous R-matrix calculations from Fujimoto *et al.* [185, 186]. We found an additional resonance in our results around 6 eV, that had not been reported before theoretically. To convince ourselves that the resonance was not an artifact of the calculation, several tests were performed with different input parameters and for different conformers. However, it was the choice of the deletion threshold that revealed to be crucial to identify this resonance.

Our efforts allowed us to establish a new scattering model for scattering calculations with alanine, improving the previous R-matrix calculations performed by Fujimoto *et al.* [186], and providing information for the core-excited resonances.

We compared the position of the low-lying π^* shape resonance with other calculations and experiments, finding a reasonably good agreement. The same was observed for the higher-lying resonance (above 8 eV). Although none of the previous calculations reported a resonance at around 6 eV, there are DEA experiments that provide evidence for a resonance within this energy range.

For the core-excited resonances we discussed their position and widths and made, as much as possible, a link to the available literature, that is scarce for these resonances. A link between our resonance positions and the DEA peaks observed by Ptasínska *et al.* [188], Vasil'ev *et al.* [190] and Scheer *et al.* [189] was also presented. As we already stated, this task is much harder due to the energy proximity of the core-excited resonances.

We believe that there are more resonances to be identified in alanine than the ones reported in this work. As it is such a complex target, further studies would be fundamental both to verify the resonant features we found, and also to provide some insights into alanine fragmentation.

To finalize, it is important to look more broadly at our results and make some general remarks:

- We have identified, for all targets, a large number of resonances, most of which had not been identified before. The simultaneous comparison between the time-delay analysis and the cross sections revealed to be a powerful combination to identify and characterize resonances, as the eigenphase sum does not always reveal the presence of all resonances, as we have explained before;

- Our calculations allowed us to model resonances accurately, specially the low-lying ones, where a general good agreement was found with the literature for the majority of the targets. However, whereas for some, as thiophene, the agreement even between our higher-lying core-excited resonances and EELs experiments is excellent, for others, as *p*-BQ, some uncertainty still remains due to the lack of experimental data;

Summarizing the conclusions for all the chapters and based on the experience gained in this thesis, we believe further efforts should be applied in the following aspects:

- Develop a more accurate methodology to find how many VOs (i.e. polarization) should be included in the calculations. As we have shown, our usual strategy works reasonably well (specially for shape resonances), but not for all types of systems: as seen in thiophene, the position of the more broad σ^* resonance is still to be described;

- Using larger CAS models to ensure a better description of the electronically excited states as well (and therefore, a more accurate description of the core-excited resonances). The issue regarding this approach is the size of the calculations, that would be huge specially for bigger molecules as the ones studied in this thesis;

- From the experimental point of view, it is crucial to obtain more information on core-excited resonances, which would require the development of higher-resolution set-ups, in experiments like ETS, for example, and more EEL experiments, that proved to be of great help identifying resonances. Velocity Slice Imaging experiments would also be very helpful, specially for the match of our calculated higher energy resonances with experiments, as symmetry information would be given.

BIBLIOGRAPHY

[1] *Nações Unidas*. URL: https://nacoesunidas.org/oms-cancer-mata-88-milhoes-de-pessoas-anualmente-no-mundo/.

[2] R. Baskar and K. Itahana. "Radiation therapy and cancer control in developing countries: Can we save more lives?" In: *Int. J. Med. Sci.* 14 (2017), pp. 13–17. DOI: 10.7150/ijms.17288.

[3] I. Baccarelli, I. Bald, F. Gianturco, E. Illenberger, and J. Kopyra. "Electron-induced damage of DNA and its components: experiments and theoretical models." In: *Phys. Rep.* 508.1-2 (2011), pp. 1–44. DOI: 10.1016/j.physrep.2011.06.004.

[4] *FDA: Food & Drug Administration*. URL: https://www.fda.gov/Radiation-EmittingProducts/RadiationEmittingProductsandProcedures/MedicalImaging/MedicalX-Rays/default.htm.

[5] *Centers for Disease Control and Prevention*. 2018. URL: https://www.cdc.gov/features/medical-imaging-procedures/index.html.

[6] T. Cunha. "Negative Ion Formation in Potassium-Purine Molecules Collisions." Doctoral dissertation. Faculdade de Ciencias e Tecnologia - Universidade Nova de Lisboa, 2018.

[7] G. García, and M. C. Fuss, eds. *Radiation Damage in Biomolecular Systems*. Springer, 2012.

[8] S. M. Plimbott and J. A. LaVerne. "Production of low-energy electrons by ionizing radiation." In: *Rad. Phys. Chem.* 76 (2007), pp. 1244–1247. DOI: 10.1016/j.radphyschem.2007.02.012.

[9] E. Alizadeh and L. Sanche. "Precursors of Solvated Electrons in Radiobiological Physics and Chemistry." In: *Chem. Rev.* 112 (2012), pp. 5578–5602. DOI: 10.1021/cr300063r.

[10] B. Boudaïffa, P. Cloutier, D. Hunting, M. A. Huels, and L. Sanche. "Resonant formation of DNA strand breaks by low-energy (3 to 20 eV) electrons." In: *Science* 287 (2000), p. 1658. DOI: 10.1126/science.287.5458.1658.

[11] G. Hanel, S. Denifl, P. Scheier, M. Probst, B. Farizon, M. Farizon, E. Illenberger, and T. D. Märk. "Electron attachment to uracil: Effective destruction at subexcitation energies." In: *Phys. Rev. Lett.* 90 (2003), pp. 188104–1–4. DOI: 10.1103/PhysRevLett.90.188104.

[12] D. Huber, M. Beikircher, S. Denifl, F. Zappa, S. Matejcik, A. Bacher, V. Grill, T. D. Märk, and P. Scheier. "High resolution dissociative electron attachment to gas phase adenine." In: *J. Chem. Phys.* 125 (2004), pp. 084304–1–7. DOI: 10.1063/1.2336775.

[13] S. Denifl, S. Ptasińska, M. Cingel, S. Matejcik, P. Scheier, and T. D. Märk. "Electron attachment to the DNA bases thymine and cytosine." In: *Chem. Phys. Lett.* 377 (2003), pp. 74–80. DOI: 10.1016/S0009-2614(03)01096-0.

[14] S. Denifl, P. Sulzer, D. Huber, F. Zappa, M. Probst, T. Märk, P. Scheier, N. Injan, J. Limtrakul, R. Abouaf, and H. Dunet. "Influence of functional groups on the site-selective dissociation of adenine upon low-energy electron attachment." In: *Angew. Chem. Int. Ed.* 46 (2007), pp. 5238–5241.

[15] M. Mucke, M. Braune, S. Barth, M. Forstel, T. Lischke, V. Ulrich, T. Arion, U. Becker, A. Bradshaw, and U. Hergenhahn. "A hitherto unrecognized source of low-energy electrons in water." In: *Nat. Phys.* 6 (2010), pp. 143–146. DOI: 10.1038/nphys1500.

[16] E. Alizadeh and L. Sanche. "Precursors of solvated electrons in radiobiological physics and chemistry." In: *Chem. Rev.* 112 (2012), pp. 5578–5602.

[17] J. D. Gorfinkiel and S. Ptasińska. "Electron scattering from molecules and molecular aggregates of biological relevance." In: *J. Phys. B: At. Mol. Opt. Phys.* 50 (2017), p. 182001. DOI: 10.1088/1361-6455/aa8572.

[18] A. Sieradzka and J. D. Gorfinkiel. "Theoretical study of resonance formation in microhydrated molecules. II. Thymine-(H2O)n, n = 1,2,3,5." In: *J. Chem. Phys.* 147 (2017), p. 034302. DOI: 10.1063/1.4993946.

[19] B. Barc, M. Ryszka, J. C. Poully, E. J. A. Maalouf, Z. el Otell, J. Tabet, R. Parajuli, P. J.M. V. der Burgt, P. Limao-Vieira, P. Cahillane, M. Dampc, N. J. Mason, and S. Eden. "Multi-photon and electron impact ionisation studies of reactivity in adenineâwater clusters." In: *Int. J. Mass Spectrom.* 176 (2014), pp. 194–199. DOI: 10.1016/j.ijms.2014.01.007.

[20] L. Sanche, A. D. Bass, P. Ayotte, and I. I. Fabrikant. "Effect of the condensed phase on dissociative electron attachment: CH3Cl condensed on a Kr surface." In: *Phys. Rev. Lett.* 75 (1995), pp. 3568–3571. DOI: 10.1103/PhysRevLett.75.3568.

[21] F. Weik, E. Illenberger, K. Nagesha, and L. Sanche. "Dissociative electron attachment to gas- and condensed-phase CF3Cl: Anion desorption and trapping." In: *J. Phys. Chem. B* 102 (1998), pp. 824–830. DOI: 10.1021/jp972535t.

[22] H. Nohl, W. Jordan, and R. J. Youngman. "Quinones in Biology: Functions in electron transfer and oxygen activation." In: *Adv. Free Radical Bio.* 2.1 (1986), pp. 211 –279. ISSN: 8755-9668. DOI: http://dx.doi.org/10.1016/S8755-9668(86)80030-8. URL: http://www.sciencedirect.com/science/article/pii/S8755966886800308.

[23] K. H. Becker. *Novel Aspects of Electron Molecule Collisions.* World Scientific, 1998.

[24] J. Tennyson. "Electron-molecule collision calculations using the R-matrix method." In: *Phys. Rep.* 491 (2010), p. 29. DOI: 10.1016/j.physrep.2010.02.001.

[25] J. R. Taylor. *Scattering Theory.* Dover publications, inc., 2013.

[26] M. N. Piancastelli. "The neverending story of shape resonances." In: *J. Electron. Spectrosc. Relat. Phenom.* 100 (1999), pp. 167–190. DOI: 10.1016/S0368-2048(99)00046-8.

[27] J. M. Herbert. *Reviews in Computational Chemistry.* New York: Wiley, 2015.

[28] P. Mozejko, A. D. Bass, A. D. Bass, L. Parenteau, and L. Sanche. "Intrinsic and extrinsic factors in anion electron-stimulated desorption: D- from deuterated hydrocarbons condensed on Kr and water ice films." In: *J. Chem. Phys.* 121 (2004), pp. 10181–10189. DOI: 10.1063/1.1807813.

[29] I. I. Fabrikant, S. Eden, N. J. Mason, and J. Fedor. "Chapter Nine - Recent Progress in Dissociative Electron Attachment: From Diatomics to Biomolecules." In: *Advances in atomic, molecular, and optical physics.* Ed. by C. C. L. Ennio Arimondo and S. F. Yelin. Vol. 66. Advances In Atomic, Molecular, and Optical Physics. Academic Press, 2017, pp. 545 –657.

[30] R. M. Thorman, T. P. R. Kumar, D. H. Fairbrother, and O. Ingolfsson. In: *Beilstein J. Nanotechnol.* 6 (2015), 1904â1926. DOI: 10.3762/bjnano.6.194.

[31] M. U. Bug, W. Y. Baek, H. Rabus, C. Villagrasa, S. Meylan, and A. B. Rosenfeld. "An electron-impact cross section data set (10 eV-1 keV) of DNA constituents based on consistent experimental data: A requisite for Monte Carlo simulations." In: *Rad. Phys. Chem.* 130 (2017), pp. 459–479. DOI: 10.1016/j.radphyschem.2016.09.027.

[32] J. van Dijk, G. M. W. Kroesen, and A. Bogaerts. "Plasma modelling and numerical simulation." In: *J. Phys. D: Appl. Phys.* 42 (2009), p. 190301. DOI: 10.1088/0022-3727/42/19/190301.

[33] R. D. White, M. J. Brunger, N. A. Garland, R. E. Robson, K. F. Ness, G. García, J. de Urquijo, S. Dujko, and Z. Petrovíc. "Electron swarm transport in THF and water mixtures." In: *Eur. Phys. J. D* 68:125 (2014). DOI: 10.1140/epjd/e2014-50085-7.

[34] S. Ronen, D. Nachtigallova, B. Schmidt, and P. Jungwirth. "Nonadiabatic chemical reaction triggered by electron photodetachment: An *ab initio* quantum dynamical study." In: *Phys. Rev. Lett.* 93 (2004), 048301(4). DOI: 10.1103/PhysRevLett.93.048301.

[35] *Encyclopedia Britannica.* URL: https://www.britannica.com/science/photochemical-reaction.

[36] W. M. Huo and F. A. Gianturco, eds. *Computational Methods for Electron Molecule Collisions.* Plenum Press, New York, 1995.

[37] P. G. Burke. *R-matrix Theory of Atomic Collisions: Application to Atomic, Molecular and Optical Processes.* Springer, 2011.

[38] C. Winstead and V. McKoy. "Parallel computational studies of electron-molecule collisions." In: *Computer Phys. Comm.* 128 (2000), pp. 386–398. DOI: 10.1016/S0010-4655(00)00066-7.

[39] R. da Costa, M. T. do N. Varella, M. H. F. Bettega, and M. A. P. Lima. "Recent advances in the application of the Schwinger multichannel method with pseudopotentials to electron-molecule collisions." In: *The Eur. Phys. J. D* 69 (2015). DOI: 10.1140/epjd/e2015-60192-6.

[40] T. B. Resigno, C. W. McCurdy, A. E. Orel, and B. H. Lengsfield. *Computational methods for electron molecule collisions.* Plenum Press, New York, 1995.

[41] W. Y. Baek, M. Bug, H. Rabus, E. Gargioni, and B. Grosswendt. "Differential elastic and total electron scattering cross sections of tetrahydrofuran." In: *Phys. Rev. A* 86 (Sept. 2012). DOI: 10.1103/PhysRevA.86.032702.

[42] D. Gramec, L. Peterlin, and M. Sollner. "Bioactivation potential of thiophene-containing drugs." In: *Chem. Res. Toxicol.* 8 (2014), pp. 1344–1358. DOI: 10.1021/tx500134g.

[43] J. M. Carr, P. G. Galiatsatos, J. D. Gorfinkiel, A. G. Harvey, M. A. Lysaght, D. Madden, Z. Mašín, M. Plummer, J. Tennyson, and H. N. Varambhia. "UKRmol: a low-energy electron- and positron-molecule scattering suite." In: *Eur. Phys. J. D* 66 (2012), p. 58. DOI: 10.1140/epjd/e2011-20653-6.

[44] Z. Mašín, J. Benda, A. Harvey, A. al Refaie, J. D. Gorfinkiel, and J. Tennyson. "in preparation." In: *Computer Phys. Comm.* ().

[45] 2019. URL: https://gitlab.com/uk-amor/ukrmol/ukrmol-in.

[46] A. Loupas and J. D. Gorfinkiel. "Resonances in low-energy electron scattering from para-benzoquinone." In: *Phys. Chem. Chem. Phys.* 19 (2017), pp. 18252–18261. DOI: 10.1039/C7CP02916K.

[47] K. Regeta. Doctoral dissertation. Université de Fribourg, Switzerland, 2015.

[48] A. Loupas, K. Regeta, M. Allan, and J. D. Gorfinkiel. "Shape and core-excited resonances in thiophene." In: *The Journal of Physical Chemistry A* 122.4 (2018), pp. 1146–1155. DOI: 10.1021/acs.jpca.7b11865. eprint: https://doi.org/10.1021/acs.jpca.7b11865.

[49] A. Loupas, A. I. Lozano, F. Blanco, J. D. Gorfinkiel, and G. García. "Cross sections for electron scattering from thiophene for a broad energy range." In: *J. Chem. Phys.* 149 (2018). DOI: 10.1063/1.5040352.

[50] M. H. Stockett and S. B. Nielsen. "Transition energies of benzoquinone anions are immune to symmetry breaking by a single water molecule." In: *Phys. Chem. Chem. Phys.* (2015). DOI: 10.1039/c5cp06095h.

[51] S. P. Khare. *Introduction to the Theory of Collisions of Electrons with Atoms and Molecules.* Springer, 2001.

[52] R. L. Dekock and H. B. Gray. *Chemical Structure and Bonding.* University Science Books, 1989.

[53] P.Atkins and R.Friedman. *Molecular Quantum Mechanics.* Oxford University Press, 2005.

[54] E. P. Wigner and L. Eisenbud. "Higher angular momenta and long range interaction in resonance reactions." In: *Phys. Rev.* 72 (1947), pp. 29–41. DOI: 10.1103/PhysRev.72.29.

[55] P. G. Burke. *R-Matrix Theory of Atomic Collisions: Application to Atomic, Molecular and Optical Processes*. Springer, 2011.

[56] P. G. Burke and K. A. Berrington. *Atomic and Molecular Processes, an R-matrix Approach*. Bristol: Institute of Physics Publishing, 1993.

[57] P. G. Burke, W. Robb, D. Bates, and B. Bederson. "The R-Matrix theory of atomic processes." In: *Adv. At. Mol. Phys.* 11 (1976), pp. 143–241.

[58] 2018. URL: https://en.wikipedia.org/wiki/Spherical_shell.

[59] A. Faure, J. D. Gorfinkiel, L. A. Morgan, and J. Tennyson. "GTOBAS: fitting continuum functions with Gaussian-type orbitals." In: *Comp. Phys. Commun.* 144 (2002), pp. 224–241. DOI: 10.1016/S0010-4655(02)00141-8.

[60] *Wolfram MathWorld*. URL: http://mathworld.wolfram.com/Gram-SchmidtOrthonormalization.html.

[61] Z. Mašín. "Resonance formation in electron collisions with pyrimidine-like targets." Doctoral dissertation. The Open University, 2012.

[62] K. L. Baluja, P. G. Burke, and L. A. Morgan. "R-matrix propagation program for solving coupled second-order differential equations." In: *Comput. Phys. Commun.* 27 (1982), pp. 299–307.

[63] M. Gailitis. "New forms of asymptotic expansions for wavefunctions of charged-particle scattering." In: *J. Phys. B: At. Mol. Opt. Phys.* 9 (1976), pp. 843–854. DOI: 10.1088/0022-3700/9/5/027.

[64] A. U. Hazi. "Behavior of the eigenphase sum near a resonance." In: *Phys. Rev. A* 19 (1979), p. 920. DOI: 10.1103/PhysRevA.19.920.

[65] I. Baccarelli, F. Sebastianelli, F. A. Gianturco, and N. Sanna. "Modelling dissociative dynamics of biosystems after metastable electron attachment: the sugar backbones." In: *Eur. Phys. J. D.* 51 (2009), pp. 131–136. DOI: 10.1140/epjd/e2008-00104-5.

[66] I. Shimamura, E. Cleanthes, A. Nicolaides, and J. Sabin. *Advances in Quantum Chemistry*. Academic, 2012.

[67] F. T. Smith. "Lifetime matrix in collision theory." In: *Phys. Rev.* 118 (1960), p. 349. DOI: 10.1103/PhysRev.118.349.

[68] *UKRMol*. Version 1.0. Apr. 2019. URL: https://doi.org/10.5281/zenodo.2630454.

[69] *UKRMol+*. Version 3.0. Apr. 2019. URL: https://doi.org/10.5281/zenodo.3371125.

[70] H.-J. Werner, P. J. Knowles, G. Knizia, F. R. Manby, M. Schütz, P. Celani, W. Györffy, D. Kats, T. Korona, R. Lindh, A. Mitrushenkov, G. Rauhut, K. R. Shamasundar, T. B. Adler, R. D. Amos, A. Bernhardsson, A. Berning, D. L. Cooper, M. J. O. Deegan, A. J. Dobbyn, F. Eckert, E. Goll, C. Hampel, A. Hesselmann, G. Hetzer, T. Hrenar, G. Jansen, C. Köppl, Y. Liu, A. W. Lloyd, R. A. Mata, A. J. May, S. J. McNicholas, W. Meyer, M. E. Mura, A. Nicklass, D. P. O'Neill, P. Palmieri, D. Peng, K. Pflüger, R. Pitzer, M. Reiher, T. Shiozaki, H. Stoll, A. J. Stone, R. Tarroni, T. Thorsteinsson, and M. Wang. *MOLPRO, version 2015.1, a package of ab initio programs.* see http://www.molpro.net. Cardiff, UK, 2015.

[71] N. Sanna and F. A. Gianturco. "Differential cross sections for electron/positron scattering for polyatomic molecules." In: *Comput. Phys. Commun.* 114 (1998), pp. 142–167.

[72] *Basis Set Exchange: v1.2.2.* URL: https://bse.pnl.gov/bse/portal.

[73] R. Doong, C. Lee, and C. Lien. "Enhanced dechlorination of carbon tetrachloride by Geobacter sulfurreducens in the presence of naturally occurring quinones and ferrihydrite." In: *Chemosphere* 97 (2014), p. 54. DOI: 10.1016/j.chemosphere.2013.11.004.

[74] B. Huskinson, M. Markshak, C. Suh, S. Er, M. Gerhardt, C. Galvin, X. Chen, A. Aspuru-Guzik, R. Gordon, and M. Aziz. "A metal-free organic-inorganic aqueous flow battery." In: *Nature* 505 (2014), p. 195. DOI: 10.1038/nature12909.

[75] D. L. Nelson and M. M. Cox. *Lehninger Principles of Biochemistry.* 2018.

[76] J. Lown. "Discovery and development of anthracycline antitumour antibiotics." In: *Chem. Soc. Rev.* 22 (1993), p. 165. DOI: 10.1039/CS9932200165.

[77] M. Colucci, G. Couch, and C. Moody. "Natural and synthetic quinones and their reduction by the quinone reductase enzyme NQO1: from synthetic organic chemistry to compounds with anticancer potential." In: *Org. Biomol. Chem.* 6 (2008), p. 637. DOI: 10.1039/b715270a.

[78] K. Klinman and D. Mu. "Quinoenzymes in biology." In: *Annu. Rev. Biochem.* 63 (1994), p. 299. DOI: 10.1146/annurev.bi.63.070194.001503.

[79] T. Stites, A. Mitchell, and R. Rucker. "Physiological importance of quinoenzymes and the O-quinone family of cofactors." In: *J. Nutr.* 130 (2000), p. 719. DOI: 10.1093/jn/130.4.719.

[80] K. S. Strode and E. P. Grimsrud. "Photon-induced electron attachment and electron detachment chemistry of p-benzoquinone and its methylated derivatives." In: *Chem. Phys. Lett.* 229 (1994), p. 551. DOI: 10.1016/0009-2614(94)01084-6s.

[81] N. Asfandiarov, S. Pschenichnyuk, A. Fokin, and E. Nafikova. "Temperature dependence of mean autodetachment lifetime of molecular negative ion of p-benzoquinone molecule." In: *Chem. Phys.* 298 (2004), p. 263. DOI: 10.1016/j.chemphys.2003.12.003.

[82] R. Holroyd. "Electron attachment to p-benzoquinone and photodetachment from benzoquinone anion in nonpolar solvents." In: *J. Phys. Chem.* 86 (1982), p. 3541. DOI: 10.1021/j100215a011.

[83] J. Schiedt and R. Weinkauf. "Resonant photodetachment via shape and Feshbach resonances: p-benzoquinone anions as a model system." In: *J. Chem. Phys.* 110 (1999), p. 304. DOI: 10.1063/1.478066.

[84] M. J. S. Dewar and S. D. Worley. "Photoelectron spectra of molecules. I. ionization potentials of some organic molecules and their interpretation." In: *J. Chem. Phys.* 60 (1969), p. 654. DOI: doi.org/10.1063/1.1671114.

[85] M. Gussoni, R. Rui, and G. Zerbi. "Electronic and relaxation contribution to linear molecular polarizability. An analysis of the experimental values." In: *J. Mol. Struct.* 447 (1998), p. 163. DOI: 10.1016/S0022-2860(97)00292-5.

[86] M. Koyanagi, Y. Kogo, and Y. Kanda. "Phosphorescence from the two triplet states of p-benzoquinone and toluquinone vapour." In: *Mol. Phys.* 20 (1971), p. 747. DOI: 10.1080/00268977100100711.

[87] M. Koyanagi, Y. Kogo, and Y. Kanda. "n, π^* electronic states of p-benzoquinone; The T-S emission spectrum in mixed crystals." In: *J. Mol. Spect.* 34 (1970), p. 450. DOI: 10.1016/0022-2852(70)90026-3.

[88] H. P. Trommsdorff. "Electronic states and spectra of p?benzoquinone." In: *J. Chem. Phys.* 56 (1972), p. 5358. DOI: 10.1063/1.1677047.

[89] G. T. Horst and J. Kommandeur. "The singlet $n\pi^*$ states of para-benzoquinone." In: *Chem. Phys.* 44 (1979), p. 287. DOI: 10.1016/0301-0104(79)80126-3Get.

[90] R. Pou-Amérigo, M. Merchán, and E. Ortí. "Theoretical study of the electronic spectrum of p-benzoquinone." In: *J. Chem. Phys.* 110 (1999), p. 9536. DOI: 10.1063/1.478918.

[91] C. Cooper, W. Naff, and R. Compton. "Negative ion properties of p?benzoquinone: Electron affinity and compound states." In: *J. Chem. Phys.* 63 (1995), p. 2752. DOI: doi.org/10.1063/1.431627.

[92] M. Schreiber, M. Silva-Junior, S. Sauer, and W. Thiel. "Benchmarks for electronically excited states: CASPT2, CC2, CCSD and CC3." In: *J. Chem. Phys.* 128 (2008), p. 134110. DOI: 10.1063/1.2889385.

[93] D. B. Jones, P. Limao-Vieira, M. Mendes, N. C. Jones, S. V. Hoffmann, R. F. da Costa, M. T. do N. Varella, M. H. F. Bettega, F. Blanco, G. García, O. Ingólsson, M. A. P. Lima, and M. J. Brunger. "An experimental and theoretical investigation into the electronically excited states of para-benzoquinone." In: *J. Chem. Phys.* 146 (2017), p. 184303. DOI: 10.1063/1.4982940.

[94] D. B. Jones, R. F. da Costa, F. Kossoski, M. T. do N. Varella, M. H. F. Bettega, F. F. da Silva, P. Limao-Vieira, G. García, M. A. P. Lima, R. D. White, and M. J. Brunger. "Electron-impact electronic-state excitation of para-benzoquinone." In: *J. Chem. Phys.* 148 (2018), p. 124312. DOI: 10.1063/1.5023494.

[95] L. Christophorou, J. Carter, and A. Christodoulides. "Long-lived parent negative ions in p-benzoquinone formed by electron capture in the field of the ground and excited states." In: *Chem. Phys. Lett.* 3 (1969), p. 237. DOI: 10.1016/0009-2614(69)80037-0.

[96] P. M. Collins, L. G. Christophorou, E. L. Chaney, and J. G. Carter. "Energy dependence of the electron attachment cross sections and the transient negative ion lifetime for p-benzoquinone and 1,4-naphtoquinone." In: *Chem. Phys. Lett.* 4 (1970), pp. 646–650. DOI: 10.1016/0009-2614(70)80108-7.

[97] M. Allan. "Time-resolved electron-energy-loss spectroscopy study of the long-lifetime p-benzoquinone negative ion." In: *Chem. Phys.* 81 (1983), p. 235. DOI: 10.1016/0301-0104(83)85317-8.

[98] M. Allan. "Vibrational and electronic excitation in p-benzoquinone by electron impact." In: *Chem. Phys.* 84 (1984), p. 311. DOI: 10.1016/0301-0104(84)85215-5.

[99] A. Modelli and P. D. Burrow. "Electron transmission study of the negative ion states of p-benzoquinone, benzaldehyde, and related molecules." In: *J. Phys. Chem.* 88 (1984), p. 3550. DOI: 10.1021/j150660a034.

[100] D. B. Jones, R. F. da Costa, F. Kossoski, M. T. do N. Varella, M. H. F. Bettega, and G. García. "Integral elastic, vibrational-excitation, electronic-state excitation, ionization, and total cross sections for electron scattering from para-benzoquinone." In: *J. Chem. Phys.* 148 (2018), p. 204305. DOI: 10.1063/1.5028298.

[101] A. I. Lozano, J. C. Oller, D. B. Jones, R. F. da Costa, M. T. do N. Varella, M. H. F. Bettega, F. F. da Silva, P. Limao-Vieira, M. A. P. Lima, R. D. White, M. J. Brunger, F. Blanco, A. Munoz, and G. García. "Total electron scattering cross sections from para-benzoquinone in the energy range 1-200 eV." In: *Phys. Chem. Chem. Phys.* 20 (2018), pp. 22368–22378. DOI: 10.1039/C8CP03297A.

[102] R. Pou-Amérigo, L. Serrano-Andrés, M. Merchán, E. Ortí, and N. Forsberg. "A theoretical determination of the low-lying electronic states of the p-benzosemiquinone radical anion." In: *J. Am. Chem. Soc.* 122 (2000), p. 6067. DOI: 10.1021/ja994402m.

[103] Y. Honda, M. Hada, M. Ehara, and H. Nakatsuji. "Excited and ionized states of p-benzoquinone and its anion radical: SAC?CI theoretical study." In: *J. Phys. Chem. A* 106 (2002), p. 3838. DOI: 10.1021/jp013166a.

[104] H. Cheng and Y. Huang. "Temporary anion states of p-benzoquinone: shape and core-excited resonances." In: *Phys. Chem. Chem. Phys.* 16 (2014), p. 26306. DOI: 10.1039/c4cp03353a.

[105] C. West, J. Bull, E. Antonkov, and J. Verlet. "Anion resonances probed by photoelectron imaging of the para-benzoquinone radical anion." In: *J. Phys. Chem. A* 118 (2014), p. 11346. DOI: doi.org/10.1021/jp509102p.

[106] A. Kunitsa and K. Bravaya. "First-principles calculations of the energy and width of the (2)A(u) shape resonance in p-benzoquinone: A gateway state for electron transfer." In: *J. Phys. Chem. Lett.* 6 (2015), p. 1053. DOI: 10.1021/acs.jpclett.5b00207.

[107] A. Kunitsa and K. Bravaya. "Electronic structure of the para-benzoquinone radical anion revisited." In: *Phys. Chem. Chem. Phys.* 18 (2016), p. 3454. DOI: 10.1039/C5CP06476G.

[108] R. D. Johnson III Editor. *NIST Standard Reference Database Number 101*. 2011.

[109] J. M. Hollas. "A high resolution investigation of the visible absorption spectrum of p-benzoquinone -H_4 and -D_4." In: *Spectrochim. acta* 20 (1964), p. 1563. DOI: 10.1016/0371-1951(64)80138-7.

[110] P. Brint, J. P. Connerade, P. Tsekeris, A. Bolovinos, and A. Baig. "Vacuum ultraviolet absorption spectrum of p-benzoquinone." In: *J. Chem. Soc., Faraday Trans 2* 82 (1986), p. 367. DOI: 10.1039/F29868200367.

[111] Z. Mašín and J. D. Gorfinkiel. "Elastic and inelastic low-energy electron collisions with pyrazine." In: *J. Chem. Phys.* 135 (2011), p. 144308. DOI: 10.1063/1.3650236.

[112] D. A. Horke, Q. Li, L. Blancafort, and J. R. R. Verlet. "Ultrafast above-threshold dynamics of the radical anion of a prototypical quinone electron-acceptor." In: *Nature Chem.* 5.8 (2013), 711–717. ISSN: 1755-4330. DOI: {10.1038/NCHEM.1705}.

[113] S. Pschenichnyuk, N. Asfandiarov, V. Fal'ko, and V. Lukin. "Temperature dependencies of negative ions formation by capture of low-energy electrons for some typical MALDI matrices." In: *Int. J. Mass Spec.* 227 (2003), p. 281. DOI: 10.1016/S1387-3806(03)00166-0.

[114] O. G. Khvostenko, P. V. Shchukin, G. M. Tuimedov, M. V. Muftakhov, E. E. Tseplin, S. N. Tseplina, and V. A. Mazunov. "Negative ion mass spectrum of the resonance electron capture by molecules of *p*-benzoquinone." In: *Int. J. Mass Spectrom.* 273 (2018), pp. 69–77. DOI: 10.1016/j.ijms.2008.03.001.

[115] F. Blanco and G. García. "A screening-corrected additivity rule for the calculation of electron scattering from macro-molecules." In: *J. Phys. B* 42 (2009), p. 145203. DOI: 10.1088/0953-4075/42/14/145203.

[116] M. T. do N. Varella, M. H. F. Bettega, A. P. P. Natalense, L. G. Ferreira, and M. A. P. Lima. "Applications of the Schwinger Multichannel Method with Pseudopotentials to Electron Scattering from Polyatomic Molecules II. Rotational Excitation Cross Sections." In: *Braz. J. Phys.* 31 (2001), pp. 21–29. DOI: 10.1590/S0103-97332001000100004.

[117] *PubChem: Open Chemistry Database*. URL: https://pubchem.ncbi.nlm.nih.gov/.

[118] M. N. Hedhili, P. Cloutier, A. D. Bass, T. E. Madey, and L. Sanche. "Electron stimulated desorption of anionic fragments from films of pure and electron-irradiated thiophene." In: *J. Chem. Phys.* 125 (2006), p. 094704. DOI: 10.1063/1.2338030.

[119] H. Fujimoto, U. Nagashima, H. Inokuchi, K. Seki, Y. Cao, H. Nakahara, J. Nakayama, M. Hoshino, and K. Fukuda. "Ultraviolet photoemission study of oligothiophenes: Ïâband evolution and geometries." In: *J. Chem. Phys.* 92 (1990), pp. 4077–4092. DOI: 10.1063/1.458561.

[120] A. Staykov, J. Areephong, W. Browne, B. Feringa, and K. Yoshizawa. "Electrochemical and photochemical cyclization and cycloreversion of diarylethenes and diarylethene-capped sexithiophene wires." In: *ACS Nano* 5 (2011), pp. 1165–1178. DOI: 10.1021/nn102806z.

[121] C. Dimitrakopolous and P. Malenfant. "Organic thin film transistors for large area electronics." In: *Adv. Mater.* 14 (2002), pp. 99–117. DOI: 10.1002/1521-4095(20020116)14.

[122] Y. Liang and L. Yu. "Development of semiconducting polymers for solar energy harvesting." In: *Polym. Rev.* 50 (2010), pp. 454–473. DOI: 10.1080/15583724.2010.515765.

[123] A. Murphy and J. Frechet. "Organic semiconducting oligomers for use in thin film transistors." In: *Chem. Rev.* 107 (2007), pp. 1066–1096. DOI: 10.1021/cr0501386.

[124] A. Mohan, G. S. V. Raghava, and S. Vidavalur. "Design and synthesis of 4,5-diaryl/heteroarylthiophene-2-carboxylic acid derivatives and evaluation of their biological activities." In: *Heteroc. Comm.* 23 (2017), pp. 9–14. DOI: 10.1515/hc-2016-0131.

[125] A. I. Lozano, A. Loupas, F. Blanco, J. D. Gorfinkiel, and G. García. "Total electron scattering cross sections from thiophene for the (1-300 eV) impact energy range." In: *J. Chem. Phys.* 149 (2018), p. 134303. DOI: 10.1063/1.5050349.

[126] R. F. da Costa, M. T. do N. Varela, M. Lima, and M. Bettega. "Low-energy electron collisions with thiophene." In: *J. Chem. Phys.* 138 (2013), p. 194306. DOI: 10.1063/1.4805107.

[127] M. V. Muftakhov, N. L. Asfandiarov, and V. I. Khvostenko. "Resonant dissociative electron attachment of electrons to molecules of five-membered heterocyclic compounds and lactams." In: *J. Electron. Spectrosc. Relat. Phenom.* 69 (1994), pp. 165–175. DOI: 10.1016/0368-2048(94)02047-4.

[128] A. McClellan. *Tables of experimental dipole moments.* W.H.Freeman, 1963.

[129] M. Gussoni, R. Rui, and G. Zerbi. "Electronic and Relaxation Contribution to Linear Molecular Polarizability. An Analysis of the Experimental Values." In: *J. Mol. Struct.* 447 (1998), pp. 163–215. DOI: https://doi.org/10.1016/S0022-2860(97)00292-5.

[130] R. D.J. I. Editor. *NIST Standard reference database.* http://http://cccbdb.nist.gov. Accessed: 2017-10-04.

[131] M. H. Palmer, I. C. Walker, and M. F. Guest. "The electronic states of thiophene studied by optical (VUV) absorption, near-threshold electron energy loss (EEL) spectroscopy and *ab initio* multi-reference configuration interaction calculations." In: *Chem. Phys.* 241 (1999), pp. 275–296. DOI: 10.1016/S0301-0104(98)00425-X.

[132] K.R.Asmis. Doctoral dissertation. Université de Fribourg, Switzerland, 1996. URL: http://homeweb.unifr.ch/allanm/pub/ma/dir_allan/thiophene_EELS.PDF.

[133] H. Haberkern, K. Asmis, M. Allan, and P. Swiderek. "Triplet states in oligomeric materials: Electron energy loss spectroscopy of thiophene and bithiophene and extrapolation to the polymer." In: *Phys. Chem. Chem. Phys.* 5 (2003), pp. 827–833. DOI: 10.1039/B210845C.

[134] W. M. Flicker, O. A. Mosher, and A. Kupperman. "Electron impact investigation of electronic excitations in furan, thiophene and pyrrole." In: *J. Chem. Phys.* 64 (1976), pp. 1315–1321. DOI: 10.1063/1.432397.

[135] E. Jones and I. M. Moodie. "The synthesis and absorption spectra of the isomeric dithienyl sulphides." In: *Tetrahedron 2* 21 (1965), pp. 2413–2420. DOI: 10.1016/S0040-4020(01)93897-9.

[136] G. D. Leonardo, G. Galloni, A. Trombetti, and C. Zauli. "Electronic spectrum of thiophene and some deuterated thiophens." In: *J. Chem. Soc. Faraday Trans* 68 (1972), pp. 2009–2016. DOI: 10.1039/F29726802009.

[137] L. Nyulászy and T. Veszprémi. "Rydberg bands in the UV spectrum of thiophene and its derivatives." In: *Chem. Scr.* 26 (1986), pp. 629–634. DOI: 10.1016/0022-2860(86)87008-9.

[138] L. Serrano-Andrés, M. Merchán, M. Fulscher, and B. O. Roos. "A theoretical study of the electronic spectrum of thiophene." In: *Chem. Phys. Lett.* 211 (1993), pp. 125–134. DOI: 10.1016/0009-2614(93)80061-S.

[139] R. Hakansoon, B. Nordén, and E. N. Thulstrup. "Magnetic circular dichroism of heterocycles: Thiophene." In: *Chem. Phys. Lett.* 50 (1977), pp. 306–308. DOI: 10.1016/0009-2614(77)80187-5.

[140] E. H. V. Veen. "Triplet $\pi - \pi^*$ transitions in thiophene, furan and pyrrole by low-energy electron impact spectroscopy." In: *Chem. Phys. Lett.* 41 (1976), pp. 535–539. DOI: 10.1016/0009-2614(76)85411-5.

[141] J. Wan, M. Hada, M. Ehara, and H. Nakatsuji. "Electronic excitation spectrum of thiophene studied by symmetry-adapted cluster configuration interaction method." In: *J. Chem. Phys.* 114 (2001), pp. 845–850. DOI: 10.1063/1.1332118.

[142] M. Kleinschmidt, J. Tatchen, and C. M. Marian. "Spin-orbit coupling of DFT/MRCI wavefunctions: method, test calculations and application to thiophene." In: *J. Comput. Chem.* 23 (2002), pp. 824–833. DOI: 10.1002/jcc.10064.

[143] S. Salzmann, M. Kleinschmidt, J. T. R. Weinkkauf, and C. M. Marian. "Excited states of thiophene: Ring opening as deactivation mechanism." In: *Phys. Chem. Chem. Phys.* 10 (2008), pp. 380–392. DOI: 10.1039/B710380H.

[144] R. Weinkauf, L. Lehr, E. W. Schlag, S. Salzmann, and C. M. Marian. "Ultrafast dynamics in thiophene investigated by femtosecond pump probe photoelectron spectroscopy and theory." In: *Phys. Chem. Chem. Phys.* 10 (2008), pp. 393–404. DOI: 10.1039/B710381F.

[145] D. M. P. Holland, A. B. Trofimov, E. A. Seddon, E. V. Gromov, T. Korona, N. de Oliveira, L. E. Archer, D. Joyeux, and L. Nahon. "Excited electronic states of thiophene: High resolution photoabsorption Fourier transform spectroscopy and *ab initio* calculations." In: *Phys. Chem. Chem. Phys.* 16 (2014), pp. 21629–21644. DOI: 10.1039/C4CP02420F.

[146] A. Modelli and P. Burrow. "Electron attachment to the aza-derivatives of furan, pyrrole and thiophene." In: *J. Chem. Phys. A* 108 (2004), pp. 5721–5726. DOI: 10.1021/jp048759a.

[147] P. Mozejko, E. Ptasinska-Denga, and C. Szmytkowski. "Cross sections for electron collision with five-membered ring heterocycles." In: *Eur. Phys. J. D* 66 (2012), pp. 20659–20666. DOI: 10.1140/epjd/e2012-20659-6.

[148] M. Vinodkumar, H. Desai, and P. C. Vinodkumar. "Electron induced chemistry of thiophene." In: *RSC Adv.* 5 (2015), pp. 24564–24574. DOI: 10.1039/C5RA01035G.

[149] A. Sieradzka, F. Blanco, M. C. Fuss, Z. Mašín, J. D. Gorfinkiel, and G. García. "Electron scattering from pyridine." In: *J. Phys. Chem. A* 118 (2014), pp. 6657–6663. DOI: 10.1021/jp503665a.

[150] K. Regeta, M. Allan, C. Winstead, V. McKoy, Z. Mašín, and J. D. Gorfinkiel. "Resonance effects in elastic cross sections for electron scattering on pyrimidine: experiment and theory." In: *J. Chem. Phys.* 144.2 (2016), p. 024301. DOI: 10.1063/1.4937790. URL: http://scitation.aip.org/content/aip/journal/jcp/144/2/10.1063/1.4937790.

[151] K. Regeta, M. Allan, Z. Mašín, and J. D. Gorfinkiel. "Absolute cross sections for electronic excitation of pyrimidine by electron impact." In: *J. Chem. Phys.* 144.2, 024302 (2016), p. 024302. DOI: 10.1063/1.4939077. URL: http://scitation.aip.org/content/aip/journal/jcp/144/2/10.1063/1.4939077.

[152] Z. Mašín, J. Gorfinkiel, D. Jones, S. Bellm, and M. Brunger. "Shape and core excited resonances in electron collisions with diazines." In: *J. Chem. Phys.* 137 (2012), p. 204312. DOI: 10.1063/1.4767345.

[153] Z. Mašín and J. D. Gorfinkiel. "Elastic and inelastic low-energy electron collisions with pyrazine." In: *The Journal of Chemical Physics* 135.14, 144308 (2011), p. 144308. DOI: 10.1063/1.3650236. URL: http://link.aip.org/link/?JCP/135/144308/1.

[154] A. Sanz, M. C. Fuss, F. Blanco, J. D. Gorfinkiel, D. Almeida, F. F. da Silva, P. Limao-Vieira, M. J. Brunger, and G. García. "An investigation into electron scattering from pyrazine at intermediate and high energies." In: *J. Chem. Phys.* 139(18) (2013), p. 184310. DOI: 10.1063/1.4829771.

[155] A. Sanz, M. Fuss, F. Blanco, Z. Mašín, J. D. Gorfinkiel, F. Carelli, F. Sebastianelli, F. Gianturco, and G. García. "Electron scattering cross section calculations for polar molecules over a broad energy range." In: *Appl. Radiat. Isot.* 83-Part B (2014), pp. 57–67. DOI: 10.1016/j.apradiso.2013.01.031.

[156] F. A. Gianturco and R. R. Lucchese. "Resonant capture of low-energy electrons by gas-phase glycine: A quantum dynamics calculation." In: *J. Phys. Chem. A* 108 (2004), pp. 7056–7062. DOI: 10.1021/jp049237y.

[157] J. S. dos Santos, R. F. da Costa, and M. T. Varella. "Low-energy electron collisions with glycine." In: *J Chem Phys.* 136 (2012), p. 084307. DOI: 10.1063/1.3687345.

[158] V. S. Vukstich, A. I. Imrez, L. G. Romanova, and A. V. Snegursky. "Fragmentation of the glycine molecule by low-energy electrons." In: *J. Phys. B: At. Mol. Opt. Phys.* 43 (2010), p. 185208. DOI: 10.1088/0953-4075/43/18/185208.

[159] M. Tashiro. In: *J. Chem. Phys.* 129 (2008), p. 164308. DOI: 10.1140/epjd/e2014-40797-y.

[160] A. C. Evans, C. Meinert, C. Giri, F. Goesmann, and U. J. Meierhenrich. "Chirality, photochemistry and the detection of amino acids in interstellar ice analogues and comets." In: *Chem. Soc. Rev.* 16 (2012), pp. 5447–5448. DOI: 10.1039/c2cs35051c.

[161] R. Abouaf. "Low energy electron impact in gas phase glycine, alanine and propanoic acid: Electronic, vibrational excitations and negative ions." In: *Chem. Phys. Lett.* 451 (2008), pp. 25–30. DOI: 10.1016/j.cplett.2007.11.083.

[162] V. P. Gupta, V. D. Gupta, and C. Mehrotra. "Study of molecular polarizabilities of some amino and polyamino acids." In: *Int. J. Quant. Chem.* 20 (1981), pp. 373–376. DOI: 10.1002/qua.560200209.

[163] A. G. Császár. "Conformers of gaseous $\alpha - alanine$." In: *J. Phys. Chem.* 100 (1996), pp. 3541–3551. DOI: 0022-3654/96/20100-3541.

[164] J. D. Dunitz and R. R. Ryan. "Refinement of the alanine crystal structure." In: *Acta Cryst.* 21 (1966), pp. 617–618. DOI: 10.1107/S0365110X66003578.

[165] K. Iijima and B. Beagley. "An electron diffraction study of gaseous Î±-alanine, NH2CHCH3CO2H." In: *J. Mol. Struct.* 248 (1991), pp. 133–142. DOI: 10.1016/0022-2860(91)85008-Q.

[166] P. D. Godfrey, S. Firth, L. D. Hatherley, R. D. Brown, and A. P. Pierlot. "Millimeter-wave spectroscopy of biomolecules: alanine." In: *J. Am. Chem. Soc.* 115 (1993), pp. 9687–9691. DOI: 10.1021/ja00074a039.

[167] M. Cao, S. Q. Newton, K. Pranata, and L. Schäefer. "Ab initio conformational analysis of alanine." In: *J. Mol. Struct. (THEOCHEM)* 332 (1995), pp. 251–267. DOI: 10.1016/0166-1280(94)03943-F.

[168] S. Gronert and R. A. J. O'Hair. "Ab initio studies of amino acid conformations." In: *J. Am. Chem. Soc.* 117 (1995), pp. 2071–2081. DOI: 10.1021/ja00112a022.

[169] R. Kaschner and D. Hohl. "Density functional theory and biomolecules: A study of glycine, alanine and their oligopeptides." In: *J. Phys. Chem. A* 102 (1998), pp. 5111–5116. DOI: 10.1021/jp980975u.

[170] A. Lesarri, S. Mata, E. J. Cocinero, S. Blanco, J. C. Lóopez, and J. L. Alonso. "The structure of neutral proline." In: *Angew. Chem. Int. Ed.* 41 (2002), pp. 4673–4676. DOI: 10.1002/anie.200290012.

[171] R. M. Balabin. "The identification of the two missing conformers of gas-phase alanine: a jet-cooled Raman spectroscopy study." In: *Phys. Chem. Chem. Phys.* 12 (2010), pp. 5980–5982. DOI: 10.1039/b924029b.

[172] V. Feyer, O. Plekan, R. Richter, M. Coreno, K. C. Prince, and V. Carravetta. "Core level study of alanine and threonine." In: *J. Phys. Chem. A* 112 (2008), pp. 7806–7815. DOI: 10.1021/jp803017y.

[173] I. Powis, E. E. Rennie, U. Hergenhahn, O. Kugeler, and R. Bussy-Socrate. "Investigation of the gas-phase amino acid alanine by synchrotron radiation photoelectron spectroscopy." In: *J. Phys. Chem. A* 107 (2003), pp. 25–34. DOI: 10.1021/jp0266345.

[174] H. Farrokhpour, F. Fathi, and D. B. A. Naves. "Theoretical and experimental study of valence photoelectron spectrum of D,L-alanine amino acid." In: *J. Phys. Chem. A* 116 (2012), pp. 7004–7015. DOI: 10.1021/jp3023716.

[175] G. Bazsó, E. E. Najbauer, G. Magyarfalvi, and G. Tarczay. "Near-infrared laser induced conformational change of alanine in low-temperature matrixes and the tunneling lifetime of its conformer VI." In: *J. Phys. Chem. A* 117 (2013), pp. 1952–1962. DOI: 10.1021/jp400196b.

[176] S. Blanco, A. Lesarri, J. C. López, and J. L. Alonso. "The Gas-Phase Structure of Alanine." In: *J. Am. Chem. Soc.* 126 (2004), pp. 11675–11683. DOI: 10.1021/ja048317c.

[177] H. M. Jaeger, H. F. I. Schaefer, J. Demaison, A. G. Császár, and W. D. Allen. "Lowest-lying conformers of alanine: Pushing theory to ascertain precise energetics and semiexperimental restructures." In: *J. Chem. Theor. Comput.* 6 (2010), pp. 3066–3078. DOI: 10.1021/ct1000236.

[178] A. Osted, J. Kongsted, and O. Christiansen. "Theoretical study of the electronic gas-phase spectrum of glycine, alanine and related amines and carboxylic acids." In: *J. Phys. Chem. A* 109 (2005), pp. 1430–1440. DOI: 10.1021/jp045697f.

[179] S. Kumar, A. K. Rai, S. B. Rai, D. K. Rai, A. N. Singh, and V. B. Singh. "Infrared, Raman and electronic spectra of alanine: A comparison with *ab initio* calculations." In: *J. Mol. Struct.* 791 (2006), pp. 23–29. DOI: 10.1016/j.molstruc.2006.01.004.

[180] M. Tia, B. C. Miranda, S. Daly, F. Gaie-Levrel, G. A. García, L. Nahon, and I. Powis. "VUV Photodynamics and chiral asymmetry in the photoionization of gas phase alanine enantiomers." In: *J. Phys. Chem. A* 118 (2014), pp. 2765–2779. DOI: 10.1021/jp5016142.

[181] K. Aflatooni, B. Hitt, G. A. Gallup, and P. D. Burrow. "Temporary anion states of selected amino acids." In: *J. Chem. Phys.* 115 (2001), p. 6489. DOI: 10.1063/1.1404147.

[182] B. P. Marinkovič, F. Blanco, D. Šević, V. Pejčeva, G. García, D. M. Filiponić, D. Pavlovič, and N. J. Mason. "Elastic scattering of electrons from alanine." In: *Int. J. Mass Spec.* 277 (2008), pp. 300–304. DOI: 10.1016/j.ijms.2008.07.016.

[183] F. Blanco and G. García. "A screening-corrected additivity rule for the calculation of electron scattering from macro-molecules." In: *J.Phys. B: At., Mol. and Opt. Phys.* 42 (2009), p. 145203.

[184] C. Panosetti, I. Baccarelli, F. Sebastianelli, and F. A. Gianturco. "Modelling fragmentations of aminoacids after resonant electron attachment: Quantum evidence of possible direct -OH detachment." In: *Eur. Phys. J. D* 60 (2010), pp. 21–30. DOI: 10.1140/epjd/e2010-00168-6.

[185] M. Fujimoto, J. Tennyson, and S. E. Michelin. "Low-energy electron collisions with the alanine molecule." In: *Eur. Phys. J. D* 68 (2014), pp. 300–304. DOI: 10.1140/epjd/e2014-40673-x.

[186] M. M. Fujimoto, E. V. R. Lima, and J. Tennyson. "Averaged electron collision cross sections for thermal mixtures of $\alpha - alanine conformers in the gas phase$." In: *J. Phys. B: At. Mol. Opt. Phys.* 49 (2016), p. 215201. DOI: 10.1088/0953-4075/49/21/215201.

[187] F. B. Nunes, M. H. F. Bettega, and S. d'Almeida Sanchez. "Positron and electron scattering by glycine and alanine: Shape resonances and methylation effect." In: *J. Chem. Phys.* 145 (2016), p. 214313. DOI: 10.1063/1.4968602.

[188] S. Ptasińska, S. Denifl, P. Candori, S. Matejcik, P. Scheier, and T. D. Märk. "Dissoactive electron attachment to gas phase alanine." In: *Chem. Phys. Lett.* 403 (2005), pp. 107–112. DOI: 10.1016/j.cplett.2004.12.115.

[189] A. M. Scheer, P. Mozejko, G. A. Gallup, and P. D. Burrow. "Total dissocitive electron attachment cross sections of selected amino acids." In: *J. Chem. Phys.* 126 (2007), p. 174301. DOI: 10.1063/1.2727460.

[190] Y. V. Vasil'ev, B. J. Figard, V. G. Voinov, D. F. Barofsky, and M. L. Deinzer. "Resonant electron capture by some amino acids and their methyl esters." In: *J. Am. Chem. Soc.* 128 (2006), pp. 5506–5515. DOI: 10.1021/ja058464q.

[191] Z. Mašín and J. D. Gorfinkiel. "Resonance formation in low energy electron scattering from uracil." In: *Eur. Phys. J. D* 68 (2014), pp. 112–120. DOI: 10.1140/epjd/e2014-40797-y.

[192] S. Ptasińska, S. Denifl, P. Candori, S. Matejcik, P. Scheier, and T. D. Märk. "Dissoactive electron attachment to gas phase alanine." In: *Chem. Phys. Lett.* 403 (2005), pp. 107–112. DOI: 10.1016/j.cplett.2004.12.115.

[193] A. Barbafina, F. Elisei, L. Latterini, F. Milano, A. Agostiano, and M. Trotta. "Photophysical properties of quinones and their interaction with the photosynthetic reaction centre." In: *Photochem. Photobiol. Sci.* 7 (2008), pp. 973–978. DOI: 10.1039/b805897k.

[194] B. Nowicka and J. Kruk. "Occurrence, biosynthesis and function of isoprenoid quinones." In: *Biochim. Biophys. Acta, Bioenerg.* 1797 (2010), pp. 1587–1605. DOI: 10.1016/j.bbabio.2010.06.007.

[195] A. N. Tikhonov. "The cytochrome b6f complex at the crossroad of photosynthetic electron transport pathways." In: *Plant Physiol. Biochem.* 81 (2014), pp. 163–183. DOI: 10.1016/j.plaphy.2013.12.011.

[196] D. S. Brambila. "R-matrix theory for attosecond spectroscopy." Doctoral dissertation. Technischen Universit ät Berlis, Germany, 2016.

[197] D. S. Brambila, A. G. Harvey, Z. Mašin1, J. D. Gorfinkiel, and O. Smirnova. "The role of multichannel effects in the photoionization of the NO2 molecule: an ab initio R- matrix study." In: *J. Phys. B: At. Mol. Opt. Phys.* 48 (2015), p. 245101. DOI: 10.1088/0953-4075/48/24/245101.

[198] A. G. Harvey, D. S. Brambila, F. Morales, and O. Smirnova. "CDENPROP: Transition matrix elements involving continuum states." In: *Comput. Phys. Commun.* (2013).

[199] A. Vincent. *Molecular Symmetry and Group Theory: A Programmed Introduction to Chemical Applications*. Wiley, 2001.

[200] T. C. Freitas, K. Coutinho, M. T. do N. Varella, M. A. P. Lima, S. Canuto, and M. H. F. Bettega. "Electron collisions with the $HCOOH(H_2O)_n$ complexes (n = 1,2) in liquid phase: The influence of microsolvation on the π^* resonance of formic acid." In: *J. Chem. Phys.* 138 (2013), p. 174307. DOI: 10.1063/1.4803119.

[201] E. M. de Oliveira, T. C. Freitas, K. Coutinho, M. T. do N. Varella, S. Canuto, M. A. P. Lima, and M. H. F. Bettega. "Communication: Transient anion states of phenol...$(H_2O)_n$ (n-1,2) complexes: Search for microsolvation signatures." In: *J. Chem. Phys.* 141 (2014), p. 051105. DOI: 10.1063/1.4892066.

[202] A. Sieradzka. "Electron Attachment to Small Molecular Clusters." Doctoral dissertation. The Open University, 2017.

[203] A. Sieradzka and J. D. Gorfinkiel. "Theoretical study of resonance formation in microhydrated molecules. II. Thymine-(H2O)n, n = 1,2,3,5." In: *J. Chem. Phys.* 147 (2017), p. 034303. DOI: 10.1063/1.4993946.

[204] T. C. Freitas, M. A. P. Lima, S. Canuto, and M. H. F. Bettega. “Electron collisions with the CH_2O-H_2O complex.” In: *Phys. Rev. A* 80 (2009), p. 062710. DOI: 10.1103/PhysRevA.80.062710.

APPENDIX A

PUBLICATIONS & CONFERENCES

A.1 Conferences attended

- POSMOL 2017 "XIX International Workshop on Low-Energy Positron and Positronium Physics, XX International Symposium on Electron-Molecule Collisions and Swarms", from 22th to 24th of July 2017, Amaroo On Mandalay Resort, Magnetic Island, Queensland, Australia - **Best poster presentation**
- ICPEAC 2017 "30th International Conference on Photonic, Electronic and Atomic Collisions", from 26th July to 1st August 2017, Cairns Convention Centre, Cairns, Australia - **Poster presentation**
- DEA club meeting 2018, from 10th to 13th of April, Vila Lana, Prague, Czech Republic - **Oral and poster presentation**
- AMIG meeting 2018 "Atomic and Molecular Interactions Group", from 21st and the 22nd of June, Department of Physics and Astronomy, University College London - **Oral and poster presentation**
- Nova Biophysica International Conference 2019, from 4th to 6th of September, Campus de Campolide, Lisboa, Portugal - **Poster presentation**

A.2 Publications

- "Resonances in low-energy electron scattering from para-benzoquinone", Loupas, A., Gorfinkiel, J.; *Phys. Chem. Chem. Phys.*, **2017**, *19*, 18252-18261. DOI: 10.1039/C7CP02916K; URL:

https://pubs.rsc.org/en/content/articlelanding/2017/cp/c7cp02916k#!divAbstract;

- "Shape and Core-Excited Resonances in Thiophene", Loupas, A., Regeta, K., Allan, M., Gorfinkiel, J.; *J Phys Chem A*, **2017**, 122(4):1146-1155. DOI: 10.1021/acs.jpca.7b11865;

  URL: https://pubs.acs.org/doi/abs/10.1021/acs.jpca.7b11865

- "Cross sections for electron scattering from thiophene for a broad energy range", Loupas, A., Lozano, A., Blanco, F., Gorfinkiel, J., García, G.; *J. Chem. Phys.*, **2018**, 148, 034304. DOI: 10.1063/1.5040352

  URL: https://aip.scitation.org/doi/abs/10.1063/1.5040352?journalCode=jcp

- "Total electron scattering cross sections from thiophene for the (1-300 eV) impact energy range", Lozano, A., Loupas, A., Blanco, F., Gorfinkiel, J.,García, G.; *J. Chem. Phys.*, **2018**, 149, 134303. DOI: 10.1063/1.5050349

  URL: https://aip.scitation.org/doi/abs/10.1063/1.5050349?journalCode=jcp

- "Shape and core-excited resonances in electron scattering from alanine", Loupas, A., Gorfinkiel, J.; *J. Chem. Phys.*, **2019**, 150, 064307. DOI: 10.1063/1.5081813

  URL: https://aip.scitation.org/doi/10.1063/1.5081813

A.3 Prizes and Recognition

- Best poster at POSMOL2017;
- HOT topic paper of 2017 at PCCP journal.